Development of a 1D Phased Ultrasonic Array for Intravascular Sonoporation

By

Alexandru Corneliu Moldovan

A Thesis submitted in fulfilment of the requirements for the degree of Doctor of Philosophy

Centre for Ultrasonic Engineering

Department of Electronic and Electrical Engineering

University of Strathclyde

November 18, 2020

Declaration of Authorship

This thesis is the result of the author's original research. It has been composed by the author and has not been previously submitted for examination which has led to the award of a degree.

The copyright of this thesis belongs to the author under the terms of the United Kingdom Copyright Acts as qualified by University of Strathclyde Regulation 3.50. Due acknowledgement must always be made of the use of any material contained in, or derived from, this thesis.

Signed: Alexandru Corneliu Moldovan

Date: November 18, 2020

Abstract

Sonoporation represents a promising approach to increase targeted drug delivery efficiency by facilitating transport of therapeutic agents to the target tissue with the use of ultrasound. However, most of the current research in sonoporation is performed with external ultrasonic transducers, which hinders the applicability of the therapeutic procedure for treatment of conditions situated deeper into the patient's body, such as liver or intestinal tumours.

This Thesis presents the development process of a miniature-sized 1-3 connectivity piezocomposite 1D phased array for intracorporeal sonoporation. The device was to be incorporated into a capsule or catheter and hence the primary design constraint was the reduced size of the piezoelectric element, which was limited to 2.5 mm in width and 12 mm in length. To meet the needs of the intended application, resonance frequencies of 1.5 MHz and 3.0 MHz were considered. A simulation framework was developed for optimization of the miniature array in relation to the peak negative pressure attained at the focus to mitigate the low power output associated with the limited device dimensions. This was implemented through a multiparametric sweep of the 1-3 piezocomposite geometry-related parameters. Devices made with PZT-5H and PMN-29%PT were evaluated. The optimization algorithm was used to determine specifications for phased array designs based on the two materials and the two resonance frequencies. The 1.5 MHz devices comprised 24 elements and the 3.0 MHz ones had 32 elements. The piezocomposites were manufactured using the dice and fill technique and electroded using a novel method of electrode deposition employing spin coating of Ag ink. Subsequently, the prototype devices were driven with a commercial array controller and characterized with a calibrated needle hydrophone in a scanning tank.

Two simulation profiles based on finite element analysis and time extrapolation were developed to model the acoustic beams from the arrays, which were compared and calibrated with experimental data for focal distances between 5 mm and 10 mm and beam steering angles from 0° to 40°. The results showed that modelling could be employed reliably for therapeutic planning. Both the 1.5 MHz and the 3.0 MHz, PZT-5H arrays were tested *in vitro* and shown to induce and control sonoporation of a human epithelial colorectal adenocarcinoma cell layer. Finally, a 24 element, 1.5 MHz, PZT-5H array was implemented in a 40 mm long by 11 mm diameter tethered, biocompatible capsule intended for *in vivo* operation. The device was characterized in the scanning tank for steering angles in the range 0° to 56° and focal distances between 4.0 mm and 5.7 mm, and the measured beam profiles were correlated with the simulation framework. The capsule will be tested in future *ex-vivo* and *in-vivo* experiments on insulin absorption through porcine small bowel by means of sonoporation.

Acknowledgements

I would firstly like to extend my deepest gratitude to my supervisors, Prof. Anthony Gachagan, Prof. Sandy Cochran and Dr Zhen Qiu for their continuous support and guidance throughout my PhD.

I would also like to acknowledge EPSRC for providing the research funds and resources, without which I could not have been able to pursue my project. Furthermore, my thanks go to OnScale as well for providing the research license for the FEA program I used extensively throughout my work.

I am grateful for the valuable insight and assistance that David Lines offered me with respect to the DSL FIToolbox array controller and to Dr Jerzy Dziewierz for guiding me in the first year of my PhD. I also want to extend my gratitude to Dr Rolan Mansour for the training and useful advice he provided me for the spin coating procedure and to Grant Smillie for the practical suggestions and assistance he offered me with regards to materials science.

Many thanks go to my collaborator, M. Turcanu for the *in-vitro* work we performed together and for the planning of future *in-vivo* experiments with the technology that I have developed as part of this project.

I would also want to say thanks to my friends Marius Balan and Omer Elnasaney and to mention that I had great pleasure to work together with my colleagues from CUE department.

I am eternally grateful to my family, especially my parents, Moldovan Corneliu and Moldovan Daniela, for their encouragement, patience and crucial support they offered me through my most difficult times.

Finally, the completion of my project would not have been possible without the valuable help and advice from my partner, Teodora Zamfirescu, who has always been there for me.

Table of Contents

List of Figures

List of Tables

List of Terms

Abbreviations

3-DOF	Three degree of freedom
ACA	Anisotropic conductive adhesive
ARF	Acoustic radiation force
BBB	Blood-brain barrier
Caco-2	Human epithelial colorectal adenocarcinoma cell layer
CFL	Courant–Friedrichs–Lewy condition
DOF	Degree of freedom
DFT	Discrete Fourier transform
IDFT	Inverse discrete Fourier transform
FD	Fluorescent-dextran
FEA	Finite element analysis
FHMW	Full width at half maximum
Fr	French gauge size
GFP	Green fluorescent protein
GI	Gastrointestinal
GND	Ground
HIFU	High intensity focused ultrasound
HV	High voltage
IVUS	Intravascular ultrasound
MB	Microbubble
NH	Needle hydrophone
PCB	Printed circuit board
PCD	Passive cavitation detector
PDE	Partial differential equations
PDMS	Polydimethylsiloxane
PET	Polyethylene terephthalate
PI	Propidium iodine
PWM	Pulse width modulation
PZT	Lead zirconate titanate
Q_M	Mechanical quality factor
sq.	Common abbreviation of square
TDD	Targeted drug delivery
TEER	Trans epithelial electric resistance
TULSA	Transurethral ultrasound ablation
US	Ultrasound/ ultrasonic

Abbreviations for common elements or materials according to the common periodic table of elements

Symbols

α	Attenuation coefficient
α_a	Absorption coefficient
α_{W_e}	-6dB pressure magnitude beam spread half angle of the passive aperture
B	Bulk modulus
c	Speed of sound in the medium
c_e	Elastic constant of the material
c_{pq}^D	Elastic stiffness tensor coefficient at constant displacement
c_{pq}^E	Elastic stiffness tensor coefficient at constant electric field
D	Electric displacement
d	Piezoelectric strain coefficient/ distance travelled by the acoustic wave in the medium
δ	The skin depth of a conductor
Δt	Time step
Δx	Distance between two adjacent nodes in an FEA model (i.e. mesh size)
df	Deration factor
d_{n-p}	Acoustic propagation path
E	Electric field
e	Piezoelectric stress constant
ε	Dielectric permittivity
ε_{ik}^S	Electrical permittivity tensor under constant strain
ε^T	Electrical permittivity under constant stress
f	Frequency
F	Focal distance
f_a	Antiresonance frequency
f_{L1}, f_{L2}	Frequencies of the first and second Lamb waves
f_p	Parallel resonance frequency
f_r	Resonance frequency
f_s	Series resonance frequency
γ	Electrical conductivity of a wire
G	Shear modulus
I	Acoustic intensity
IPW	Inactive pulse width
I_{SPPA}	Spatial peak pulse average intensity
k	Coupling coefficient
k_{33}	Electromechanical coupling coefficient for an electric field applied in the direction of the induced poling for a tall, thin rod poled along the long side
k_t	Electromechanical coupling coefficient for a thin, wide plate oscillating in thickness mode
L	Array length
LP_e	Load protrusion in elevation
λ	Wavelength
λ_r	Wavelength corresponding to the transducer resonance frequency
MI	Mechanical index
μ_0	Free space permeability
μ_r	Relative permeability
n	Index

Nf	Near field distance
n_{elem}	Total number of elements in the array
N_C	Number of cycles
N_P	Number of pulses
$n_{pil,Y}$	Number of piezoelectric pillars in elevation
$n_{pil,X}$	Number of piezoelectric pillars per array element in active aperture direction
P	Instantaneous pressure
p	Reduced notation of ij
$P(X_P, F)$	Focus point coordinates
P_0	Initial pressure
PAR	Pillar aspect ratio
PD	Pulse duration
P_D	Dissipated power by a piezoelectric transducer
φ	Angle from the normal
P_i	Incident acoustic pressure/ Polarization tensor
PNP	Peak negative pressure
PNP_{max}	Spatial peak temporal peak negative pressure
PP	Pillar pitch
P_P	Piezoelectric polarisation vector
P_r	Reflected pressure
PRF	Pulse repetition frequency
P_t	Transmitted pressure
PW	Pillar width
Q	Heat
q	Reduced notation of kl
r	Radius of a conductor
$\bar{R}$	Average decrease in a value
ρ	Medium density
ρ_s	Surface electrical resistivity
s	Array pitch
s^E	Elastic compliance under constant electric field
S	Strain
S_P	Strain induced when the piezoelectric element is subjected to an electric field
σ	Standard deviation
T	Insonation time
T	Mechanically related stress
T_S	Period of one full beam sweep
$T_{\%ON}$	Duty cycle
τ	Ultrasonic exposure time
T_C	Curie temperature
θ_i	Angle of incidence with the normal
θ_r	Angle of reflection with the normal
θ_t	Angle of refraction (transmission) with the normal
thk	Thickness
thk_{ml}	Matching layer thickness
TI	Thermal index
T_P	Stress produced when the piezoelectric element is subjected to an electric field

T_{PT}	Phase transition temperature
U_{EE}	Electrical energy
U_{ME}	Energy coupled through the direct or reverse piezoelectric effect
U_{MM}	Mechanical energy
v	Particle velocity
VF	Volume fraction
v_l	Longitudinal velocity
v_{Lat}	Lateral wave velocity of the active phase of a 1-3 piezocomposite material
v_{phase}	Phase velocity
V_{pp}	Peak to peak voltage
V_{R_piezo}	Rayleigh velocity of the piezoelectric material
V_{R_poly}	Rayleigh velocity of the polymer phase
v_s	Shear wave velocity
W_0	Acoustic power
$W_{1\ deg}$	Acoustic power necessary to increase tissue temperature by 1°C
$w_{X,Y}$	Pillar width in the X or Y direction
W_E	Array elevation (passive aperture)
$W_{E_{-6dB}}(Z)$	-6db beam width of the acoustic field in the elevation direction at an axial distance, Z from the array face
W_{ke}	Kerf width
W_L	Array length (active aperture)
X	Direction parallel to array length (active aperture)
Y	Direction parallel to array elevation (passive aperture)
Z	Direction parallel to array thickness
Z	Acoustic impedance/ electrical impedance
Z_{axial}	Axial distance
Z_L	Load acoustic impedance
Z_M	Matching layer acoustic impedance
Z_P	Piezoelectric material acoustic impedance

1 Introduction

Ultrasound (US) is a form of mechanical energy that propagates in media at frequencies beyond the human hearing threshold, i.e. 20 kHz. The modern history of US generation started with the discovery of piezoelectricity by the Curie brothers in 1880 [1]. The first operational piezoelectric US transducer was developed by Paul Langevin in 1917 and was used for echolocation of objects hidden in the sea. Since then, the sphere of use for US has been continuously developing, with US currently playing an important role in non-destructive testing of materials, medical imaging, therapy, cancer treatment and surgery [2, Ch. 1], [3], amongst other applications. Initially employed for physiotherapy, therapeutic US grew useful in other domains, including breaking kidney stones (lithotripsy) [4] and tissue ablation by use of localized heating through high intensity focused ultrasound (HIFU) [5], with research now under way in physically targeted drug delivery through sonoporation [6].

The potential importance of sonoporation in the field of targeted drug delivery is that it facilitates transport of therapeutic agents to the biological target by permeating cell membranes [6]. This increases the membrane susceptibility to the passage of larger drug molecules that would normally be blocked from entering the region of interest. Therefore, higher drug concentrations can be attained in the targeted tissue, while healthy tissue in the surrounding region and elsewhere in the body is mostly unaffected due to therapy localization. The overall drug toxicity towards the patient is thus reduced compared to systemic administration (e.g. intravenous chemotherapy) and the therapeutic effects are increased because of elevated absorption at the target [7]. The main mechanism of sonoporation is microbubble (MB) cavitation in the vicinity of the cells [8]. Sonoporation is considered a minimally invasive procedure because it avoids open surgery by application of ultrasound externally, with focused transducers. However, the success of externally applied therapeutic US is impaired by attenuation in the tissue pathway between the transducer and the target and by the presence of media that reflect and scatter US such as the ribs [9]–[11], the skull [12], [13], and gas in the intestines [14], [15].

Currently, there is limited research on sonoporation applied intracorporeally because limitations of extracorporeal application and large transluminal treatment are still emerging. However, other therapeutic US procedures are well established with respect to internal catheters or capsules and can be used as reference in the development of intracorporeal sonoporation transducers. Examples of applications for US catheter transducers include HIFU ablation [16], transurethral [17] and transrectal prostate cancer treatment [18]. Currently, US capsule implementations are used for bowel imaging [19], and treatment [20]. The main

difference between sonoporation and imaging is that sonoporation is performed at lower US frequencies, which requires larger piezoelectric elements. The tight space constraints for catheter or capsule implementation, coupled with the requirement to avoid transducer self-heating to prevent negative biological effects due to temperature increase, lead to a challenging task in the design of intracorporeal transducers for sonoporation [21].

1.1 Objectives

This Thesis aims to explore the development of a therapeutic ultrasonic array for intracorporeal sonoporation. The leading design parameter for this type of device is the reduced space available inside the catheter or capsule. This is in opposition with the sonoporation requirement of centre frequencies <5 MHz, which leads to relatively thick piezoelectric layers, and to the therapeutic condition of moderate power transmission, which requires larger transducers and can also lead to device self-heating. Considering these requirements, the work described in this Thesis sets the following objectives:

- To produce a simulation framework for the development of improved 1-3 piezocomposite, 1D phased arrays in relation to the peak negative pressure (PNP) attained at focus through a series of parametric sweeps.
- To manufacture the simulated arrays and characterize them with respect to electrical impedance and beam profiles in water.
- To design an improved simulation framework for predicting the beam shape and pressure magnitudes achieved by the array, and to validate it with the experimental data. The purpose of this step is to demonstrate the feasibility of using finite element analysis (FEA) in therapeutic planning, which requires precise location of the beam in the target tissue and of the pressure magnitudes attained at focus.
- To validate the experimental arrays in an *in-vitro* model, including biological effects on cells.
- To develop a biocompatible capsule that incorporates the array and other necessary components as a step towards *in-vivo* trials. The capsule prototype will be used in future experiments to evaluate insulin absorption through porcine small bowel as a result of sonoporation in collaboration with M. Turcanu, University of Glasgow [22].

1.2 Contributions to Knowledge

The contributions to knowledge presented as part of this Thesis are listed below:

- The development of an automatic, cross-platform (MATLAB + OnScale) simulation algorithm based on a combination of FEA and extrapolation for the design and improvement (in PNP output) of miniature-sized, 1-3 piezocomposite, therapeutic 1D phased arrays, [23]. The program was designed to produce the full set of piezocomposite and array geometry parameters required to manufacture the arrays with the dice and fill technique and to account for manufacturing considerations such as: limitations in the lateral size and thickness of the array, limitations in the size and protrusion of the dicing blade, required resonance frequency and array element count.

- The production of parameter sets for four different types of improved miniature phased arrays, designed for being embedded into a catheter or capsule: two based on PZT-5H and two based on PMN-29%PT as active materials, with resonance frequencies of 1.5 MHz and 3.0 MHz [24], [25], followed by the manufacture of the transducers [26]. The fabricated arrays were compatible with embedding into an 8 Fr catheter sheath.

- The development and demonstration of a new method for electrode deposition on flat transducers, based on spin coating an Ag ink compound, followed by curing at lower temperature thresholds than required by the manufacturer to avoid damage to the piezoelectric material [27], [28]. The coating procedure required less specialised equipment and training, and was more cost-effective than the common transducer electroding methods such as thermal evaporation, sputtering or electron beam evaporation. The deposited electrode quality (in terms of electrical surface resistivity, layer thickness and smoothness) was evaluated and optimized for various curing temperatures through an incremental variation of spin coating parameters and dilutions of the ink. The resultant electrodes were compared with a series of electrodes (Au, Ag, Cu, Al) deposited with a standard method performed with a commercially available thin film deposition machine, and with Ag ink electrodes applied with wire bar coaters and with a brush. Subsequently, the prototype phased arrays were electroded with the developed Ag ink spin coating method and custom-designed flexible printed circuit boards (PCB) were bonded to them.

- Development of two simulation frameworks to model the beam pattern achieved by the arrays for various focal distances and steering angles, and comparison of the results with the measured data obtained with a scanning tank from the fabricated arrays [29], [30]. The first framework simulated with FEA both the array and the load, and the second framework

employed Kirchhoff time-integral extrapolation to evaluate beam propagation in the load, which led to a significant reduction in computational demand on the workstation.

- Performing an optimization of the correlation between the electrical impedance spectrum of the simulated arrays and the measured spectrum from the experimental arrays in order to improve the similarity in the elasto-electric coefficients between the simulated and the fabricated piezocomposite materials.
- Validation of the miniature phased arrays ability to induce sonoporation *in vitro*, on human epithelial colorectal adenocarcinoma cell monolayers developed on a ThinCert^{TM} porous membrane. As part of the procedure, array driving parameters were established in relation to sonoporation efficiency. A set of additional parameters were introduced to the insonation protocol compared to data from the literature due to the beamsteering capability of the arrays as opposed to the standard forward focusing transducers used in other studies. The experiments demonstrated a correlation between the size of the insonated area of the cellular monolayer and the level of sonoporation incurred by the tissue. This result was achieved due to spatial control of the beam emitted by the experimental phased arrays
- Design, manufacture and acoustic characterization of a novel, biocompatible 40 mm x 11 mm (length x diameter) tethered capsule device that incorporated the 1.5 MHz, 24 element, PZT-5H piezocomposite array and two channels for localised drug and MB delivery.

1.3 Thesis Structure

Chapter 2 provides an overview of therapeutic US employed in the field of targeted drug delivery, with a focus on sonoporation enhanced by MB cavitation. US-induced mechanisms associated with cell membrane poration are discussed and sonoporation is compared to other therapeutic modalities for treatment of cancer and other pathologies. Acoustic cavitation is described in detail due to its important role as a promoter of sonoporation, with emphasis on the various bioeffects generated by stable and inertial cavitation. Subsequently, a review of the US exposure parameters in relation to sonoporation effectiveness is provided. The chapter continues with the technical background knowledge that was employed in the development of the therapeutic miniature-sized arrays for sonoporation. The basic principles of ultrasound, piezoelectricity and ferroelectricity are introduced, followed by piezoelectric material properties and constants. The chapter ends with a review of current catheter and capsule transducer designs for therapeutic US and for imaging, which were used as a starting point for the development of intracorporeal US arrays aimed specifically for sonoporation.

Chapter 3 presents the design and optimization process of four types of miniature 1D phased arrays with a software modelling approach. The chapter begins with theory related to finite element analysis and extrapolation, followed by 1-3 piezocomposite materials and phased array design concepts. It continues with a description of the equations and constraints employed in the development of an iterative multiparametric sweep program for the miniature 1-3 piezocomposite phased arrays which are intended for incorporation into a catheter or capsule. As the transducers are designed for therapeutic US, the scope of the sweep is to determine the optimal array configuration that produces the highest PNP magnitudes at focus, given the tight space restrictions. The PNP sweep results are then correlated with the modelled electrical impedance spectra of the arrays. The chapter ends by presenting an optimization of the modelling software to reduce the computation workload.

Chapter 4 describes the manufacturing procedure for the four types of miniature phased arrays following the specifications provided by the iterative simulation approach from the previous chapter. The 1-3 piezocomposite materials are manufactured with the traditional dice and fill technique and then lapped to the required thickness. The chapter then presents an alternative method for electrode deposition, which employs spin coating, requires less specialized equipment and has lower associated costs than the more standard approaches. The process is tuned to produce an electrode layer with surface electrical resistivity and thickness similar to electrodes deposited by a commercially available thin film deposition system. The chapter ends with a description of the bonding process of a custom flexible PCB to the array electrodes, followed by transducer embedding in a 3-D printed casing and waterproofing.

Chapter 5 presents the electrical and acoustic field characterization of the manufactured phased arrays, followed by a comparison between the experimental and the simulated data. Two frameworks for the simulation of beam pattern and pressure magnitude achieved by the arrays in a water load are compared in relation to the fit with the measurement data. Both frameworks simulate the piezoelectric arrays with an implicit solver, but they differ in the solver used for acoustic propagation in the water load: one framework uses an explicit solver for the medium, and the other uses Kirchhoff time extrapolation. The experimental transducers are driven with a commercial phased array controller and beam profiling is performed in water with a needle hydrophone (NH) coupled to a three degree of freedom (3-DOF) linear scanning tank. The chapter then describes the methodology followed to minimize the discrepancies between the modelled and the measured electrical impedance of the transducers by altering the coefficients of the simulated piezoelectric materials using an optimization algorithm.

Chapter 6 describes the *in-vitro* evaluation of the experimental phased arrays on human epithelial colorectal adenocarcinoma (Caco-2) cell layers grown into films on ThinCert™ porous polyethylene terephthalate (PET) membranes in well plates. Various focusing types, beam-steering angles and US driving parameters evaluated as part of the study are described in this chapter, with reference to the degree of induced sonoporation. Several means to assess cell membrane disruption applied during and post-procedure are presented, including: trans epithelial electric resistance (TEER) and confocal and fluorescence microscopy followed by spectrometry with a fluorescence plate reader.

Chapter 7 presents the development of a tethered, 40 mm x 11 mm capsule device based on one of the experimental 1-D phased arrays evaluated in the previous chapters, intended for *in-vivo* sonoporation of porcine small bowel. The capsule is also equipped with two channels for local delivery of a suspension of drugs and MBs. This chapter provides a description of the design steps followed to engineer the capsule casing, to minimize the space required by the electrical interconnects and to ensure biocompatibility. The chapter then evaluates the beam profiles achieved by the capsule array, measured with a NH and scanning tank system, and provides a comparison with the simulation results. The chapter ends with a series of tests to allow preparation for future *in-vivo* experiments.

Chapter 8 provides the conclusions for this work and discusses further steps in the development of this project.

1.4 Publications Based on the Current Work

Peer Reviewed Papers:

J. H. Song, **A. Moldovan**, and P. Prentice, "Non-linear Acoustic Emissions from Therapeutically Driven Contrast Agent Microbubbles," Ultrasound Med. Biol., vol. 45, no. 8, pp. 2188–2204, Aug. 2019, doi: 10.1016/j.ultrasmedbio.2019.04.005.

Conference Proceedings

A. C. Moldovan, Z. Qiu, D. Lines, S. Cochran, A. Gachagan, "*Enhanced Modelling of a 1-D Phased Ultrasonic Array for Intracorporeal Sonoporation*", in *2020 IEEE International Ultrasonics Symposium (IUS)*, Sept. 2020

M. Turcanu, **A. C. Moldovan**, S. Vlatakis, D. Vllasaliu, M. Thanou, I. Näthke, S. Cochran, "*An Organoid derived Cell Layer as an in vitro Model for US-mediated Drug Delivery Studies*", in *2020 IEEE International Ultrasonics Symposium (IUS)*, Sept. 2020

A. C. Moldovan, Z. Qiu, D. Lines, A. Gachagan, and S. Cochran, "Development of a 1-D Linear Phased Ultrasonic Array for Intravascular Sonoporation," in 2019 IEEE International Ultrasonics Symposium (IUS), Oct. 2019, pp. 2056–2059, doi: 10.1109/ULTSYM.2019.8925549.

A. C. Moldovan, J. Dziewierz, A. Gachagan, S. Cochran, and H. Lay, "Virtual Prototyping of a Catheter Transducer Array for Internal Hepatic Sonoporation," in 2018 IEEE International Ultrasonics Symposium (IUS), Oct. 2018, pp. 1–4, doi: 10.1109/ULTSYM.2018.8579783.

Z. Qiu, H. Fang, R. O'Leary, A. Gachagan, and **A. Moldovan**, "*Broadband Piezocrystal Transducer Array for Non-Destructive Evaluation Imaging Applications*," in 2018 IEEE International Ultrasonics Symposium (IUS), Oct. 2018, pp. 1–4, doi: 10.1109/ULTSYM.2018.8579855.

Posters and Oral Presentations

"Enhanced Modelling of a 1-D Phased Ultrasonic Array for Intracorporeal Sonoporation", at 2020 IEEE International Ultrasonics Symposium (IUS), 6-11 Sept. 2020, Virtual Symposium.

"*Development of a 1-D Linear Phased Ultrasonic Array for Intravascular Sonoporation*", at 2019 IEEE International Ultrasonics Symposium (IUS), 6-9 Oct. 2019, SEC, Glasgow, Scotland, UK.

"*Development of a 1-D Linear Phased Ultrasonic Array for Intravascular Sonoporation*", at the 50th Annual Scientific Meeting of the British Medical Ultrasound Society (BMUS), 4-6 Dec. 2018, Emirates Old Trafford, Manchester, UK.

"Exploration in Miniature Ultrasound Devices for Therapy with Sonoporation", at EPSRC Image Guided Therapies Network+ (IGT), 31 Oct. – 1 Nov. 2018, University of Dundee, Dundee, UK.

"*Virtual Prototyping of a Catheter Transducer Array for Internal Hepatic Sonoporation*", at 2018 IEEE International Ultrasonics Symposium (IUS), 22-25 Oct. 2018, Portopia Hotel, Kobe, Japan.

2 Clinical and Technical Background

2.1 Introduction

Chapter 2 defines the biomedical and technological concepts on which this Thesis is based and provides the context for the development of an intracorporeal ultrasonic phased array for sonoporation. In outline, this chapter approaches both the medical application (intracorporeal sonoporation) and the technology employed to address it (miniature-sized US array).

The chapter commences with an introduction to the fields of US and sonoporation and their applicability in targeted drug delivery (TDD) systems. A brief history of therapeutic US is then provided, followed by a description of US-induced mechanisms that are associated with cell membrane poration. Some merits of sonoporation as a therapeutic modality compared with conventional therapies are then highlighted.

Subsequently, acoustic cavitation, which is an important phenomenon in many cases of sonoporation, is described. The difference between stable and inertial cavitation, and the effects of these forms of cavitation on the exposed tissue, are investigated in relation to US driving parameters. Microbubble (MB) mediated sonoporation is then presented as a modality to lower the cavitation threshold and increase sonoporation efficiency. Next, MBs, their interaction with the acoustic field, the bioeffects associated with their cavitation and their importance in therapeutic US are described. Having defined the methods to produce sonoporation, various means to quantify its effectiveness are thereafter presented.

The chapter then describes the technical concepts used in the development of an US array. A description of US and piezoelectricity theory is therefore provided, with emphasis on aspects employed in the subsequent modelling, improvement, manufacturing and characterisation of the phased array prototype. Design considerations for therapeutic US transducers in relation to piezocomposite materials; constitutive materials and layers; and transduction efficiency parameters are discussed.

Finally, several reasons for the development of intracorporeal US phased arrays for the treatment of various organ pathologies with sonoporation are presented, in comparison with more typical approaches based on external transducers. Subsequently, a review of current intracorporeal US transducer designs and procedures is conducted in relation to catheter or capsule incorporation. The chapter ends with a list of considerations and constraints for the design of an intracorporeal US array for sonoporation.

2.2 Ultrasound

Ultrasound is defined as an acoustic wave, with frequency over the upper audible frequency of the human ear, which is around 20 kHz. US waves are mechanical waves that propagate through a medium as an elastic deformation and kinetic displacement of the medium [3, Ch. 1]. Generation and detection of US can be performed with several methods, including optical, electromagnetic, capacitive and piezoelectric techniques, with the latter being the most common one.

Reflection of US at the boundary between two different media has made it possible to use US for echolocation and imaging by estimating the distance to an object through measurement of the time of flight between US emission and reception. US represents a practical and efficient tool for medical imaging, which carries less risks than X-rays or magnetic resonance imaging (MRI) and has lower associated costs than the other imaging techniques. Furthermore, the ability of US to generate mechanical and thermal bioeffects in living organisms, has gained increasing significance in the area of therapy in the last decades due to reduced invasiveness and lower side-effects compared to other therapeutic approaches such as conventional chemotherapy or radiation therapy.

2.3 Sonoporation

Sonoporation is a non-invasive insonation technique that facilitates targeted drug or gene delivery to a biological site of interest by creation of pores (Figure 2-1, Ref. [31]) in the cell membrane through the use of therapeutic US [32]. The biological mechanisms associated with sonoporation are mechanical in nature and they are considered to be caused by shear forces generated by microstreaming, and inertial and stable cavitation [33].

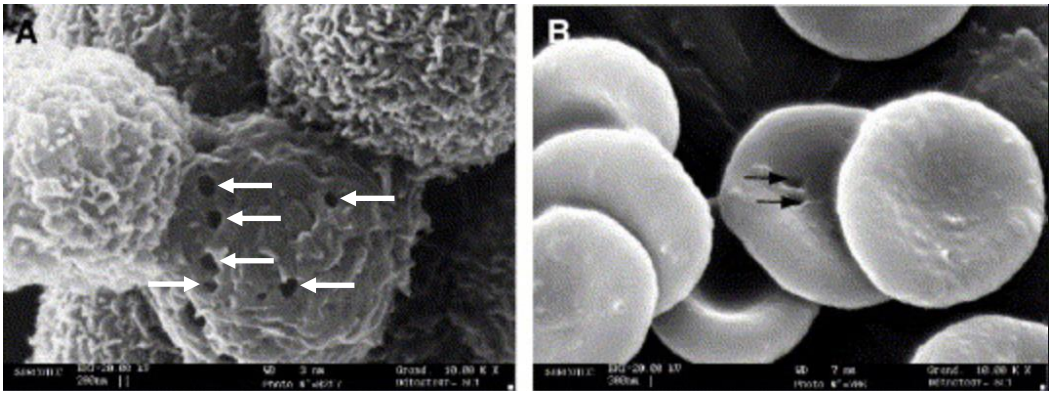

Figure 2-1 Scanning Electron Microscopy Images of Sonoporated Cells (Reprinted from Ref. [31])

2.3.1 Targeted Drug Delivery

Drug delivery systems are methods of drug or gene transport and delivery to a target biological site, including cells, tissue or even organs, by use of drug carriers. The aims in the design of

drug delivery systems are: improvement in therapeutic efficiency of the drugs, improvement of their specificity for the targeted biological site, increase in chemical stability of the compounds, and reduction in side effects caused by the therapeutic agents [34]. Drug targeting is a delivery system that focuses on concentrating increased doses of therapeutic agent in the target site. Characteristics of TDD include: therapeutic localization, increased drug absorption through the biological membrane of the target site, prolonged compound interaction with the target tissue, and reduced toxicity dissipation towards the surrounding healthy tissue [7].

Depending on the type of carrier used for the therapeutic agent, TDD can be divided into passive and active targeting. Passive targeting uses drug carrier molecules that ensure prolonged systemic circulation, a certain degree of selectivity for a given tissue (e.g. malignant tumour) and decreased accumulation in healthy cells. Active targeting increases cellular uptake of the therapeutic agent through ligands applied to the surface of the drug carriers that bind to specific receptors on the target tissue. Limitations of both methods include low drug loading capacity of the carrier (drug to carrier weight <5%); drug release before it can reach the target site, thus affecting healthy tissue; and the complexity of engineering a stable carrier-delivery system. A series of approaches including therapeutic US, hyperthermia and radiation therapy are currently used to enhance passive targeting of drugs by increasing tissue permeability as a means to achieve higher drug uptake [35].

Applications for Targeted Drug Delivery

Some areas where TDD treatment has been employed and is actively investigated for treatment are: pulmonary, colon and infectious diseases; cancer; diabetes; and brain diseases [36]. As an example, cancer is a range of diseases caused by abnormal development of malignant cells which spread uncontrollably towards other tissues or organs, often leading to the patient's death if not treated in time. According to Stewart et al. [37], approximately 14 million people developed cancer in 2012 worldwide, with predictions indicating the number will rise towards 20 million new cases per year in 2025. Currently, cancer treatment schemes include one or a combination of chemotherapy, radiation therapy, and surgical resection, each method including multiple distinct techniques and having its own advantages and drawbacks.

Conventional chemotherapy, to which TDD is most closely related, primarily affects cancer cells which have rapid division and growth, but the approach lacks selectivity and, in order to achieve sufficient therapeutic efficiency against the malignant tissue, large drug doses are administered, which lead to many negative side effects. High mortality rates of patients are often attributed to the toxicity of conventional chemotherapy towards healthy tissues and organs [38]. TDD, enhanced by therapeutic US can improve the specificity and efficacy of

chemotherapy by increasing drug accumulation in the malignant tissue, while reducing its concentration in the organism or in the surrounding tissues [39].

2.3.2 Therapeutic Ultrasound

Exploration of US for therapeutic purposes started in the 1930s. By 1950, tissue heating with US was employed in physical therapies and US imaging was beginning to be investigated for its diagnostic capabilities [40], [41]. Research in neurosurgery and cancer treatment using therapeutic US was initiated towards the mid-1950s [42]. First reports of US ablation, based on local hyperthermia induced with high intensity focused ultrasound (HIFU) appeared in 1960, and the technique gained significant clinical acceptance in the 1990s [5].

Initial attempts to introduce foreign macromolecules into living cells with US were reported in 1986 [43], and by the mid-1990s, there were already several reports published on the topic [6]. The term '*sonoporation*' was then introduced in relation to temporary membrane opening, arising from exposure to US [6]. In 1995, it was also suggested that US thrombolysis of blood clots was enhanced by acoustic cavitation of MBs, which had been previously used as contrast agents for US imaging [44]. Acoustic cavitation of MBs was linked to increased cellular membrane permeabilization in the early 2000s [45, Ch. 27]. Nowadays, the most common US mechanisms evaluated in relation to cell membrane permeabilization include: acoustic cavitation produced by US [46]–[52], microstreaming due to a vibrating tip [53]–[55] or Mason horn [56], [57], and shock waves [58]–[60] produced by lithotripters.

2.3.3 Short Description of US-induced Mechanisms Associated with Cell Membrane Permeabilization

Vibrating tips, such as needles or wires create eddy currents in the liquid around them, which leads to microstreaming without the employment of cavitation or oscillating MBs [61]. A Mason horn is an exponentially-tapered stainless steel or titanium bar attached to a vibrating source (which can be a piezoelectric US transducer) that pulses transversely vibrating waves of a given frequency through the horn. The imposed transversal motion in the horn creates microstreaming in the surrounding liquid, as in the case of the vibrating tips. Microstreaming represents a steady flow in a liquid produced by an acoustic field, which applies shear stress on objects in its path. Cells subject to shear forces are prone to membrane disruption [57]. A disadvantage of this technique is the complexity of placing the vibrating tip or horn close to the target biological site in an *in-vivo* model, making it more suitable for *in-vitro* tests.

High amplitude and short duration shock waves with low centre frequencies (~20 kHz) are generated by lithotripters. Shock wave lithotripsy is an US modality generally used to destroy

kidney stones by application of a high-intensity compressive wave (the shock front), with very high positive pressure magnitude (up to 100 MPa), followed by a high negative pressure magnitude (down to -10 MPa) [62]. The shock waves can lead to cellular membrane permeabilization [60] and their effect can be enhanced by bubble cavitation induced in close proximity to the targeted tissue [62]. Due to the nature of this therapy (low driving frequency and high-pressure magnitudes), localisation is not as good as for sonoporation and damage to the surrounding tissue is a detrimental effect.

Acoustic cavitation generated by an US field can lead to a variety of effects, including microstreaming, shock waves, radiation forces, jetting, and mechanical strain due to microbubble oscillation. Section 2.5.2 provides a detailed review of the mechanisms of cavitation-induced sonoporation. Acoustic cavitation generated by US fields benefits from good therapeutic localization due to the ability of transducers to focus US at the target site and from a large variety of transducers with different shapes, sizes and resonance frequencies.

2.3.4 Importance of Sonoporation as a Potential Therapeutic Modality

The advantages of sonoporation are its reduced or non-invasive nature because the therapy does not require tissue removal through surgery, the temporary action of membrane poration, and the possibility of accurate spatial and temporal control of the therapy, which is difficult or impossible with other methods.

One of the applications of sonoporation is to facilitate cancer treatment by locally increasing the absorption rate of therapeutic agents in the tumours. Most often tumours develop anomalous blood vessels and manifest regions of blood deprivation or have pressure gradients that complicate the supply of drugs [63]. Treatment efficiency depends on the successful spreading of drugs through the blood vessels, essentially capillaries, and on tumour cell absorbance of the agents. Cancer recurrence can happen if the therapeutic agent does not reach most of the cancerous cells in large enough doses. Furthermore, in brain cancer treatment, the blood-brain barrier (BBB) acts as a barrier for any drug intake towards the tumour, as its name suggests, adding further complexity to the treatment. Sonoporation can be employed to increase the permeability of the BBB membrane [64] and to induce higher absorption rates in the target brain tumour while maintaining a reduced overall systemic drug dose administered to the patient.

Another important application of sonoporation is in targeted gene therapy, which aims to correct defective genes by introducing nucleic acids in the target cells. DNA containing promoters or inhibitors is synthesised by the target cell into coded protein, which affects gene

expression in the cells or recombines with other proteins. This process is termed *transfection* and it aims to create genetically modified cells [65]. However, the therapeutic nucleotides are mostly blocked by the cell membrane, which acts as a barrier against exterior substances. Gene therapy is enhanced by mechanisms that increase the transfection rates of foreign DNA to the target cells, including sonoporation [50], [56].

2.4 Acoustic Cavitation

Acoustic cavitation represents the interaction between an US field and any gaseous inclusion in the medium [66]. The mechanical oscillations produced by the US field are characterized by alternating negative (rarefaction) and positive (compression) pressure magnitudes, at a frequency equal to the ultrasonic driving frequency. If a sufficiently large negative pressure magnitude is attained at a particular location in a liquid during the rarefaction section of the mechanical oscillation, the local pressure drops below the saturated vapour pressure, causing the liquid in that region to evaporate. This phenomenon is generated by a high tensile stress in the liquid under a large negative pressure magnitude, leading to a rupture in the liquid [67], followed by the formation of a void or cavity. Vapours of the liquid accumulate in the cavity and combine with any dissolved gases that enter the cavity through diffusion, leading to the creation of a gas bubble termed a cavitation nucleus [68, Ch. 1].

When the US pressure magnitude increases during the following positive section of the oscillation, the newly formed bubble contracts as a result of the local higher static pressure of the liquid, which is larger than the vapour pressure inside the bubble. Depending on the radius of the cavitation nucleus, small bubbles may disappear because of diffusion of the gas into the surrounding liquid. However, larger bubbles can survive due to increased gas pressure inside them and due to the interface (shell) created by the superficial tension of the liquid [69, Ch. 1], despite partial loss of gas to the outside through diffusion. Following the subsequent rarefaction half-cycle of the US field, the cavitation nucleus gathers more gas and vapour inside, which leads to a volumetric increase compared to the previous rarefaction. Depending on the acoustic pressure magnitude, the bubble can reach a state of steady oscillation between the compression and rarefaction half-cycles, which corresponds to stable cavitation, or it can implode violently after a small number of US cycles, corresponding to inertial cavitation.

2.4.1 Negative Pressure in Liquids

The negative pressure of a liquid is a tensile force that acts to increase its volume. Gases cannot have negative pressures but liquids and solids do [69, Ch. 1]. Applying tensile force to a liquid initially at equilibrium, reduces the density of the liquid by increasing its volume. A negative

pressure in the liquid can be described as a negative difference in pressure compared to the equilibrium pressure [70]. Negative pressures in a liquid are only temporary because the liquid is not stable at that point and they are mostly encountered during phase transitions [71].

2.4.2 Types of Cavitation Nucleation

Nucleation represents the inception of cavitation, during which a bubble, or cavitation nucleus, is formed. Depending on the presence of cavitation nuclei in the liquid, nucleation can be divided in two types: homogenous nucleation, which occurs in the bulk of the liquid, away from any surfaces or particles, and heterogeneous nucleation which is generated at the interface with a surface of a solid object (wall) or impurity in the liquid. According to classical nucleation theory, in order for a bubble to form and grow in a liquid through either type of nucleation, an external energy or force is required to overcome an energy threshold of the liquid [68, Ch. 1]. In acoustics, the *nucleation (or cavitation) threshold* is often defined as the minimum acoustic pressure magnitude that is required to initiate cavitation. A more comprehensive review of the classical nucleation theory is available in [68, Ch. 1].

The cavitation threshold depends on the liquid's equilibrium pressure, the amount of impurities in it, its temperature, the US driving frequency, and the presence of a wall bounding the cavitation region. For example, the cavitation threshold of deionized water reported in the literature for different experiments is, according to Herbert et al. [72], between -16.0 MPa and -27.7 MPa, with one study reporting the cavitation threshold as high as -140 MPa. For water saturated in air, the cavitation threshold can however drop to as low as -0.1 MPa [72]. The cavitation threshold pressure varies inversely with the US driving frequency. This is because the duration of the rarefaction phase of the acoustic field decreases with frequency, which leads to reduced time for bubble growth. To compensate for the shorter bubble growth time, higher negative pressures are required to achieve the same level of cavitation as for lower driving frequencies [69, Ch. 3].

Homogenous nucleation relies on temporary voids created in the liquid by the negative pressure, which represent the nuclei for the growth of the vapour microbubbles. These voids have a short lifetime and are generated by the thermal motion of the liquid's molecules. Dissolved gases favour nucleation as they expand easier than vapour and decrease the tensile strength of the liquid, and inherently reduce the cavitation threshold [73, Ch. 1].

Heterogeneous nucleation occurs at a lower threshold than homogenous nucleation because the interface with the wall decreases the tensile strength of the liquid by creating a rupture location for the stretched liquid. The regions on a solid's surface that have the required shape

to promote vapour bubble creation are called nucleation sites [73, Ch. 1]. In some cases, contaminant gas molecules may be trapped in crevices on the surface of the solid. Under the acoustic field, they become cavitation nuclei and start gaining volume. When these bubbles increase in size enough, they lift off due to buoyancy or radiation forces and become cavitation nuclei in the bulk of the liquid [69, Ch. 3]

An important aspect of homogenous nucleation is that it typically requires very large negative acoustic pressures to occur in the bulk volume of a liquid. However, in practice, homogenous nucleation happens in conjunction with heterogeneous nucleation at the vessel's walls and at the surface of microscopic impurities present in the liquid, which greatly reduces the cavitation threshold pressure [72], [74], [75].

2.4.3 Mechanisms for Bubble Growth During Acoustic Cavitation

Bubble growth is caused by rectified diffusion and bubble coalescence. Volume increase generated by rectified diffusion is attributed to two factors: a larger surface area of the bubble during rarefaction than when the bubble is compressed [69, Ch. 3], and a thinner liquid shell around the bubble during rarefaction due to its larger volume (consistent with Poisson's ratio) [76, Ch. 1]. The amount of gas that diffuses through the bubble shell is proportional with the surface area of the bubble. Therefore, during the rarefactional phase of the insonation cycle, when the bubble volume is larger, more gas is absorbed inside than is lost during compression, when the effective outer bubble area is smaller (Figure 2-2). This phenomenon leads to asymmetric bubble oscillations during which the bubble increases in volume following every rarefactional half-cycle.

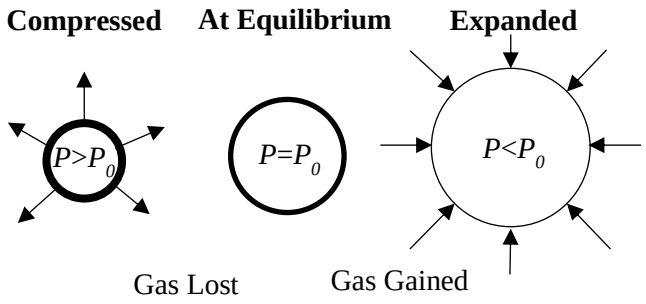

Figure 2-2 Rectified Diffusion Schematic View: P is the Time-dependent Pressure and P_0 is the Equilibrium Pressure of the Liquid

Coalescence represents the merger between several smaller cavitation nuclei, which form a larger bubble or a cloud of bubbles provided their concentration is high enough in the surrounding liquid [69, Ch. 3]. According to Maxwell et al. [77], cavitation clouds are generated by singular cavitating bubbles, which coalesce and grow along the acoustic axis in the opposite direction to the propagation direction of the waves emitted by an US source. Cloud cavitation experiences strong collapses followed by shockwaves, leading to erosion of

the exposed materials, and it happens at lower US frequencies than single bubble cavitation because of the larger resonance radius of the cloud compared to the single bubble.

2.4.4 US Driving Frequency for Cavitation

Lower insonation frequencies, in the region of 20 kHz, are associated with more violent collapses due to larger bubble sizes, leading to more destructive effects [78], while higher driving frequencies, in the MHz region, are associated with lower intensity and shorter lifetime of the cavitating bubbles [79]. This is because lower US driving frequencies lead to higher collapse velocities of the cavitating bubbles, while higher frequencies diminish the collapse velocity of the bubbles, leading to weaker effects [80]. At higher US driving frequencies, the cavitating bubble has less time to store energy during the shorter rarefactional cycle than for lower US frequencies, which have longer cycles. Therefore, bubbles exposed to higher frequency acoustic fields store less energy than at lower frequencies, which leads to smaller bubble growth and less energetic collapse. Thus, in order to achieve cavitation effects on the same scale as the ones at lower frequency, larger acoustic pressures are required at higher driving frequencies. According to Brennen et al. [73, Ch. 4], the natural resonance frequency of typical cavitation nuclei found in water lies between 5 kHz and 25 kHz, which corresponds to the strongest cavitation response. A bubble driven at its resonant frequency will manifest highly nonlinear behaviour with very large oscillations at lower driving pressures than for higher frequencies.

2.4.5 Stable and Inertial Cavitation

Cavitation nuclei develop asymmetric oscillatory behaviour at relatively low driving pressure magnitudes, i.e. tens to hundreds of kPa, depending on the US frequency, the amount of gas dissolved in the liquid and its temperature. At low driving pressures, a cavitation nucleus grows towards its resonant size, after which the bubble continues to oscillate steadily [33] (Figure 2-3 a.) for a high number of acoustic cycles, with non-destructive effects [81]. This phenomenon corresponds to stable cavitation.

However, if the negative acoustic pressure is increased above the *collapse threshold*, bubbles expand rapidly during the rarefaction phase, and then contract too much during the compression part of the US cycle. This generates their violent implosion (i.e. collapse) associated with inertial cavitation [68, Ch. 1] (Figure 2-3 b.), so called because the driving factor is the inertia of the liquid surrounding the bubble [82]. The rapid reduction in volume leads to high temperatures and pressures inside the bubble, shock waves, microjetting, formation of free radicals, and fragmentation [33].

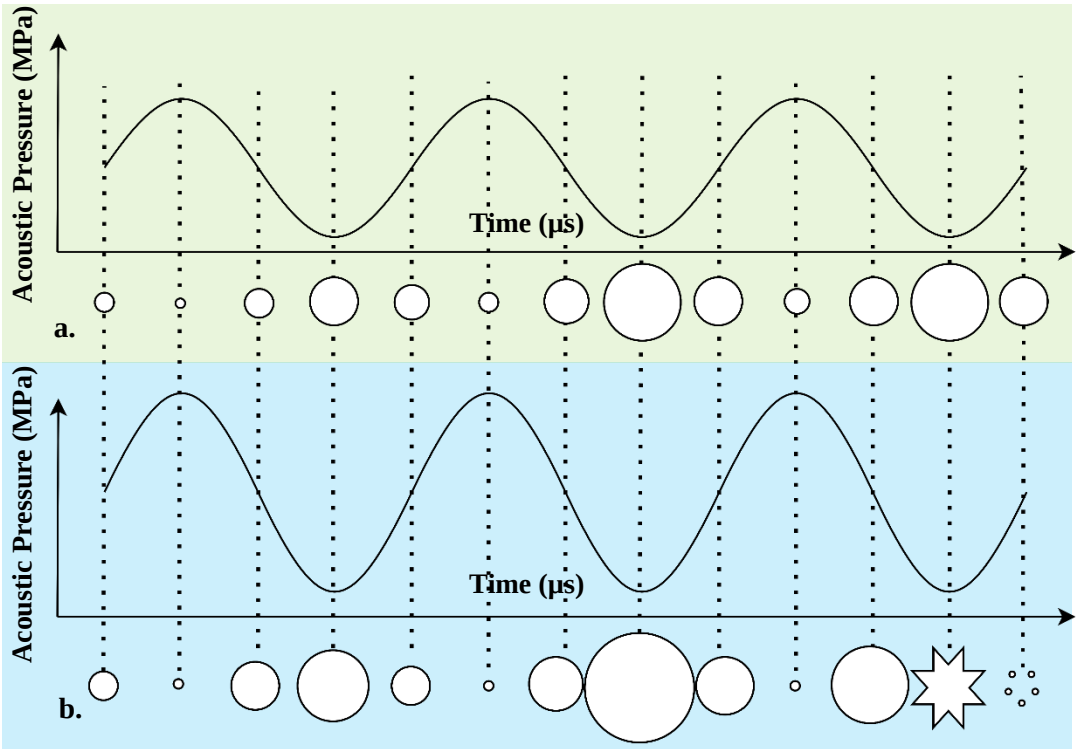

Figure 2-3 Bubble Oscillations Under Cavitating Acoustic Field: a. Bubble Reaching Stable Cavitation; b. Bubble Under Inertial Cavitation Implodes and Fragments into Smaller Cavitation Nuclei

Spherical shock waves are formed when an outward pressure wave with high amplitude, generated by an expanding bubble after its inertial collapse, overtakes the previously radiated inward pressure waves generated before the bubble collapse. This phenomenon is possible because the velocity of the outward wave produced by the fast bubble expansion is larger than that of the previously radiated waves, allowing the outward wave to overtake the former pressure waves in a progressive manner [69, Ch. 3]. The outward wave velocity is equal to the sum of the instantaneous liquid velocity of the expanding bubble and the sound propagation velocity in the medium (c), while the velocity of the former pressure waves is equal to c only. Furthermore, c of the outward pressure wave is larger than c of the previous waves because of the increased liquid pressure caused by the rapid bubble expansion (c is proportional to liquid pressure) [76, Ch. 2]. Both of these phenomena are responsible for a faster outward pressure wave.

Microjetting describes microbubble collapse which leads to the creation of a liquid jet directed by a gradient from a location of higher-pressure magnitude towards a lower-pressure magnitude. The microjet penetrates the bubble's surface at its weakest point and then advances towards its other side, accelerating liquid at high velocities (250 m/s) [83]. Generally, microjets are generated by the presence of a solid surface such as a wall or an impurity in the liquid near a cavitating bubble. The pressure gradient is lower towards the solid surface and

higher towards the bulk of the liquid, which directs the jet towards the surface. Figure 2-4, reprinted from Ref. [84], presents microjet formation, in the form of a nascent jet that penetrates the gas bubble (Figure 2-4, a.), followed by jetting, in which the mature jet is directed towards the adjacent surface (Figure 2-4, b.).

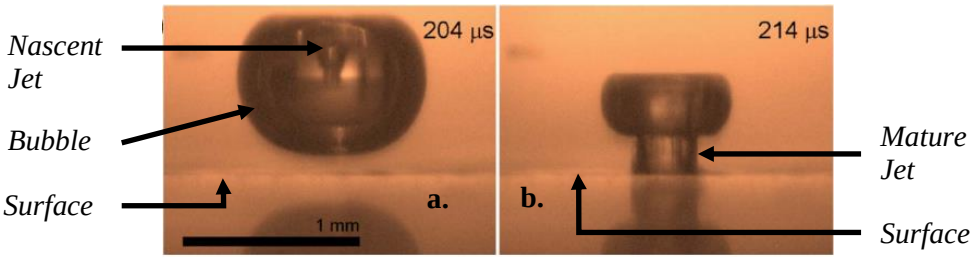

Figure 2-4 a. Microjet Penetrating the Bubble from the Bulk Liquid Towards the Adjacent Surface; b. Jetting Towards the Surface (Reprinted from Ref. [84])

Bubble fragmentation is generated by the breakage of a larger bubble into many smaller fragments upon its collapse. This phenomenon requires large bubble expansion during the rarefactional cycle before its implosion in order to break the gas bubble apart [85]. The gas fragments can then coalesce under the strong acoustic field and act as cavitation nuclei for new bubbles.

Free radicals and molecular degradation are caused by the large temperatures (>3000 K) reached upon bubble collapse. Free radicals produced by inertial cavitation are hydrogen atoms and hydroxyl radicals, which can recombine with other substances in the target liquid and create potentially toxic compounds [81].

2.5 Sonoporation Enhanced by MB Cavitation

Cavitation is one of the main promoters of sonoporation [8], [86]. In the past, high US powers were necessary to attain high enough acoustic pressures for creating and sustaining cavitation in tissue. This led to thermal damage caused by the large temperature increase as a result of US attenuation in the tissue. The problem was overcome at the beginning of the 2000s by the addition of MBs at the intended insonation site [45, Ch. 1], which lowered the cavitation threshold pressure and, inherently, the necessary US power and resultant heat, by providing nuclei for cavitation.

MB-mediated drug and gene delivery therapies rely on simultaneously injecting MBs and therapeutic agents into the systemic circulation of the patient. The targeted site is then exposed to US, which interacts with the injected MBs, leading to their volumetric oscillation or cyclic collapse. The MBs oscillations or the shock waves created upon their collapse create pores in the cell membranes, leading to an increased uptake of the drug into the target tissue [87].

2.5.1 Microbubbles

MBs are sub-capillary (< 10 μm) sized gas bodies encapsulated by a shell made of lipids, polymers or proteins [86]. Their main usage, since their introduction in the late 1960s, has been as contrast enhancement agents for US imaging due to the features of their response to US i.e. attenuation, scattering, broadband noise emission etc. [88]. In the past decades, MB use in therapeutic US has been given much research attention, especially in promoting US mediated TDD through a wide range of associated bioeffects [8].

MBs are administered intravenously, after which they spread in the circulatory system, reaching the target organ or tissue in a few minutes. However, dissemination of MBs into the circulatory system leads to restrictions in their diameter as they must pass through the capillaries of the pulmonary system, which are around 7μm in diameter [89]. Therefore, commercially available MBs are designed with mean diameters between 0.5 μm and 10 μm [86]. MB size impacts their lifetime in the blood flow, their resonance frequency, the passage mechanisms of intravenously infused drugs towards the target extravascular tissue (drug extravasation) and the drug transfer into the cells (transfection) [52].

The second restriction for the injected MBs is their survival time in the bloodstream, which must be long enough to allow for the US procedure to finalize before the encapsulated gas diffuses in the bloodstream. Ideally, MBs are expected to be indefinitely stable once injected in the circulatory system [51], but their real half-life is 3 to 5 minutes from intravenous injection [90, Ch. 8]. MB containing atmospheric gases which do not possess any means of stabilization are prone to rapid dissolution in the surrounding liquid and their lifetime can be too short either to reach the target organ or to produce the required bioeffects during US exposure. One method of slowing the dissolution process is to encapsulate the MB in an elastic shell (lipids, albumin, dextrose-albumin, sugars, gelatine or polymers) [66]. The shell reduces the compressibility of the MBs, increases their resonance frequency compared to free bubbles and increases the viscous damping [91, Ch. 2]. In addition, various gases with lower solubility or slow diffusion rate in blood, such as helium, sulphur hexafluoride, perfluoropropane and dodecafluoropropane, further reduce the dissolution rate in the bloodstream [66]. The biological environment in which the MBs are infused affects their properties and stability through the medium viscosity, temperature and hydrostatic pressure [92].

Due to the added shell stiffness, the resonance frequency of commercially-available micrometre-sized MBs ranges between 1 MHz and 10 MHz [86]. MBs subjected to large negative pressures fragment into daughter cavitation nuclei, which lower the cavitation threshold and also aid in dissipating targeted drugs contained by the MB.

Targeted Delivery with Drug Loaded MBs

In the case of TDD enhanced by acoustic cavitation, therapeutic agents are injected in the blood flow with the MBs. The mechanism of drug transfer to the target biological site is passive extravasation through the cell membrane, caused by sonoporation of the tissue. The main flaw with this approach is that therapeutic agents are transported systemically and can reach other organs, which detrimentally increases the effective drug toxicity. Recent approaches rely on attaching drugs or genes to the MB shells, thus creating hybrid therapeutic agents (Figure 2-5). The controlled release of therapeutic agents can be localized at the target region in the body by focusing the acoustic field. This approach also increases the lifetime of the therapeutic agents once they are introduced into the blood flow and facilitates their intracellular delivery [52].

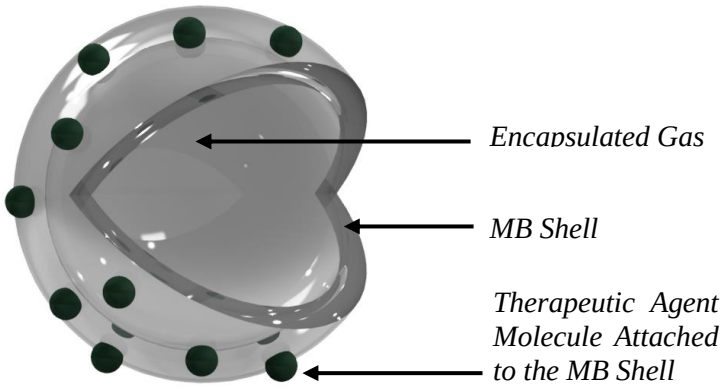

Figure 2-5 Representation of MB Shell Loaded with Therapeutic Agents

Commercially Available MBs

Contrast agent MBs can be divided in two generations. The first generation MBs were air based, they were unstable, and their size distribution varied greatly. The first commercially available contrast agent was *Echovist*; it did not survive the passage through the pulmonary system after intravenous injection, making it suitable for local studies only [66]. The following first-generation contrast agents (the most popular being *Levovist* and *Albunex*) were better stabilized, which allowed them to pass through the pulmonary capillaries. The second generation of MBs replaced the inner air with a heavier molecular weight gas, with low solubility, which greatly increased the survival time of the MBs in the systemic circulation [93]. Ref. [94] provides a list of clinically approved and tested, commercially available MBs, along with corresponding shell and size properties.

2.5.2 Bioeffects Associated with MB Cavitation

Stable cavitation is generally linked to reparable sonoporation. Mechanisms associated with cell membrane integrity disruption during stable cavitation include: fluid microstreaming

generated by MB oscillations in the proximity of a cell (Figure 2-6 a.), which applies shear stress on its membrane, and the push-pull effect of the MB oscillations (Figure 2-6 b.-c.) on the cell membrane [33], [95]. Furthermore, stable cavitation produces acoustic radiation force (ARF) which is considered to push MBs closer to the tissue, increasing the bioeffects of the oscillations. The cumulative effect of the aforementioned mechanisms leads to temporary cell membrane poration (Figure 2-7 a.) and is associated with lower US intensities [96].

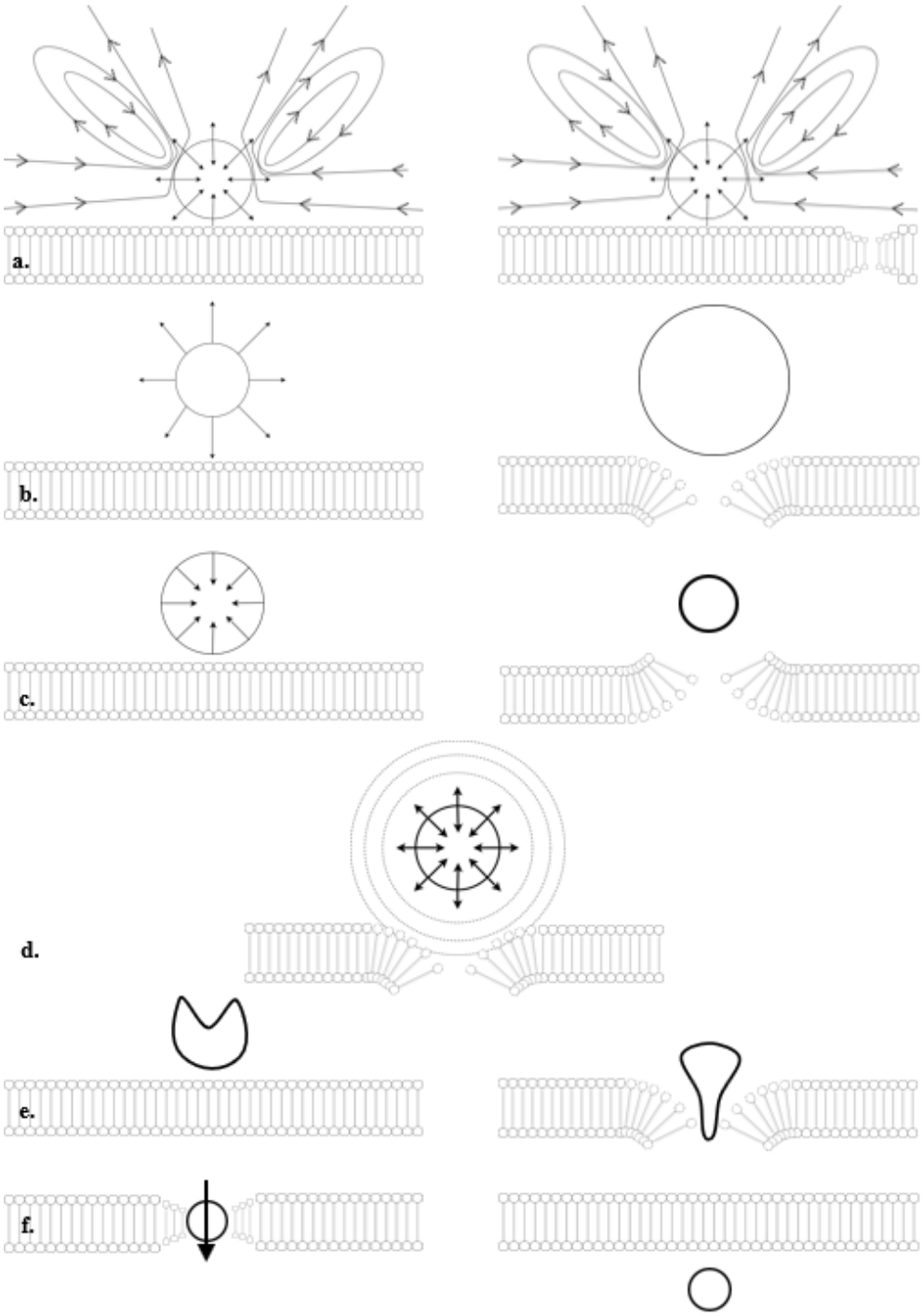

Figure 2-6 Bioeffects Associated with MB Cavitation: a. Microstreaming; b.-c. Push and Pull Effects; d. Shock Waves; e. MB Collapse Followed by Jetting; f. Translation Due to Acoustic Radiation Force

Permanent membrane poration is generated by inertial cavitation and is associated with cell lysis and eventually cell death [97]. Shock waves (Figure 2-6 d.) produced as a result of inertial MB cavitation can perturb the integrity of the cell membrane and of vascular endothelia [52]. Microjetting (Figure 2-6 e.) is related to sonoporation because it creates pores in the cell membrane, which in turn, allow for the passage of larger drug molecules inside the cell [8], [52], [86]. Free radicals resulting after inertial cavitation can recombine with otherwise passive drugs loaded onto the MB shell and create new free radicals with cytotoxic potential, e.g. for tumour treatment [98].

According to Sirsi et al. [52], inertial cavitation can also lead to disruption of the vascular endothelial tissue, by increasing the distance between the endothelial cells, which, in turn, allows drug extravasation from the inside of the vessel towards the target tissue, by means of trans-vascular delivery (Figure 2-7 b.). Bubble fragmentation can also be employed as a useful TDD method for releasing therapeutic agents carried by injected MBs [86].

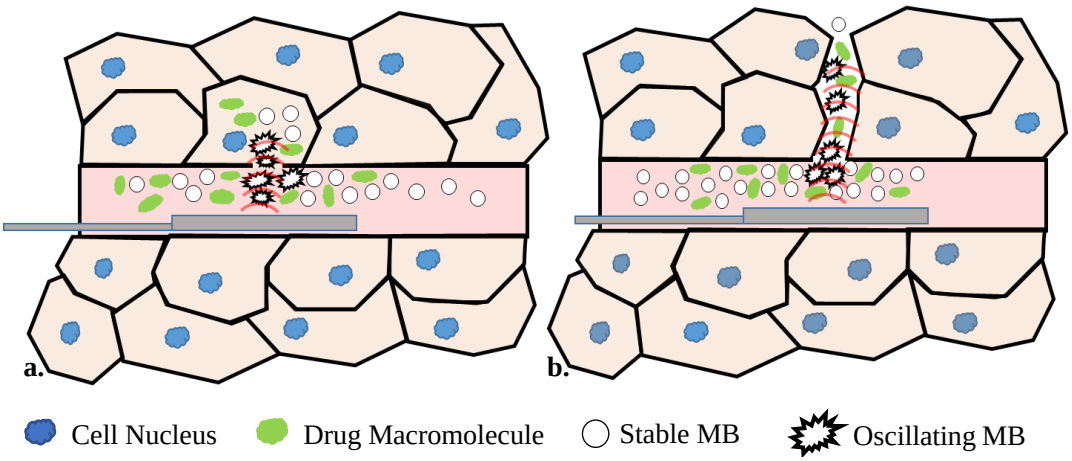

Figure 2-7 Schematic Representation of Sonoporation Mechanisms: a. Membrane Opening for Drug Delivery inside the Cell; b. Vascular Integrity Modulation Leading to Trans-vascular Drug Transport

Lastly, ARF (Figure 2-6 f.) produced by the US field causes MBs to be projected away from the acoustic source, towards the target tissue which they can porate. ARF is based on mechanical energy absorption by the microbubbles trapped in the acoustic field created by the transducer [99], [100]. This technique can increase the spatial control of sonoporation in the target biological site and increase drug affinity and specificity for the target tissue.

2.6 Sonoporation in Relation to the Driving US Field

Pulsed US carries less energy than a continuous-wave US field, resulting in reduced cell death, but still ensures enhanced drug delivery. Temporary cell membrane poration, followed by membrane repair was reported by various research groups after pulsed US was combined with administered MBs, both *in vitro* and *in vivo*. Okada et al. [101] reported cell membrane

sonoporation due to cavitating MBs under a pulsed US field, while they also recorded cell membrane repair following the procedure.

Karshafian et al. [39] explain that sonoporation can be understood, obtained and controlled efficiently if all US exposure parameters and MB characteristics are understood properly. The main US driving parameters, which affect cell permeability and viability are: peak negative pressure (PNP), centre frequency of the acoustic field (f), pulse repetition frequency (PRF), duty cycle ($T_{\%ON}$), pulse duration (PD), number of oscillations (cycles) per pulse, insonation time (T) and exposure time (τ) [39]. As sonoporation relies on mechanical rather than thermal bioeffects of US and cavitation, the therapeutic protocol requires short pulse lengths, low duty cycles and high PNPs to avoid heat deposition. This is in opposition with thermal therapies that use long pulse lengths and high duty cycles in order to raise tissue temperature through absorption [102]. Furthermore, transducer self-heating, which is generally an issue for therapeutic US, is reduced under lower duty cycle excitation due to less power dissipation.

2.6.1 Ultrasound Exposure Parameters

Several measures to quantify the potential of cavitation-induced bioeffects have been introduced in the past, especially for diagnostic US. These measures were designed to provide upper limits to the US intensity used during imaging, in order to avoid mechanical or thermal damage generated by cavitation. Before the AIUM/NEMA, 1992a standard [103], quantities such as the spatial peak pulse average intensity (I_{SPPA}) (Eq 2.1) were used to evaluate cavitation-induced bioeffects [104]:

$$I_{SPPA} = \frac{PNP_{max}^2}{2\rho c} \qquad \text{Eq 2.1}$$

where PNP_{max} is the spatial-peak temporal-peak negative pressure, ρ is medium density and c is speed of sound in the medium.

However, any quantities associated with I_{SPPA} did not include the effect of the centre US frequency, which is linked to the cavitation threshold and intensity. Therefore, the AIUM/NEMA, 1992a standard set a new measure for cavitation-induced bioeffects, based on PNP and US frequency, f, named the mechanical index (MI). MI is a unitless quantity (Eq 2.2) that reflects the probability of adverse mechanical bioeffects happening to the insonated tissue during US imaging [96].

$$MI = \frac{PNP}{\sqrt{f}} df \qquad \text{Eq 2.2}$$

where *df* = 0.3 dB/(cm*MHz) is a deration factor to account for in-situ attenuation when US propagates through tissue as opposed to water.

Similar to MI, a thermal index (TI) was also introduced in 1992 to account for the temperature increase at the target tissue during US imaging and is defined as:

$$TI = \frac{W_0}{W_{1\,deg}} \qquad \text{Eq 2.3}$$

where W_0 is the acoustic power emitted by the US transducer and $W_{1\,deg}$ is the acoustic power necessary to increase the tissue temperature by 1°C.

Generally, in sonoporation studies, MI or PNP + driving frequency are the parameters most used to quantify US dosage applied to the treated biological sites [39], [58], [105]–[108] . In this Thesis, PNP is used for evaluating the acoustic field of the prototype transducers, while MI is employed in the biological application section.

At present, the MI safety limit for diagnostic ultrasound is 1.9, while manufacturers are expected to provide justification if TI exceeds 6.0 [109]. However, clear protection standards in terms of MI and TI for therapeutic US applications do not currently exist, except for physiotherapy, because procedures such as lithotripsy or HIFU are based on the effects of high intensity US [110].

2.6.2 Review of PNP and US Frequencies Used in Sonoporation Studies

A review of sonoporation studies (Table 2-1) shows US driving frequencies in the interval 0.5 MHz to 5.0 MHz were employed, and PNP values related to reparable sonoporation were around 0.2 MPa, when MBs were introduced at the insonation site. According to Kilroy et al. [100], US enhanced drug uptake is most efficient for frequencies lower than 5.0 MHz. This limit is mostly due to the resonance frequency of MBs and to the frequency dependence of acoustic cavitation. As explained in Section 2.4.4, obtaining similar cavitation intensity at higher frequencies (i.e., >5 MHz compared to 0.5 MHz) requires much larger driving pressures. The combined effect of the elevated pressures and the increased attenuation at higher frequencies can then lead to a detrimental heat build-up in the tissue, which is not desired during sonoporation. Similar results are also reported in a comprehensive review of cellular targeted US therapies [111].

Table 2-1 Review of US Parameters in Relation to Sonoporation Efficiency and Cell Lysis, Rows Ordered by Increasing Frequency

Freq. (MHz)	PNP (MPa)	Type of Study	MB type*	Results	Ref.
~kHz	4.0	*in-vitro*	none	cells exposed to jetting were lysed	[112]
0.5 2.0 5.0	0.57 0.74 2.24	*in-vitro*	Definity	65 ± 5% permeabilized cells; 27 ± 3% dead 51 ± 2% permeabilized cells; 14% dead 36 ± 2% permeabilized cells; 19% dead	[39]
0.96	0.4	*in-vitro*	Optison	cell survival dropped from 100% at $T_{\%ON}$=5% to 73% at $T_{\%ON}$=15%	[105]
1.0	0.05-0.3	*in-vitro*	SonoVue	transfection efficiency increased from ~10% at 0.05 MPa to 30% at 0. 30 MPa, cell viability decreased from ~90% to ~80%	[106]
1.0	0.22	*in-vitro* & *in-vivo*	SonoVue	enhanced drug delivery	[107]
1.0	0.4	*in-vitro*	SonoVue	cell deformation, no lysis, but increased drug uptake	[108]
1.0	0.45	*in-vitro*	Lipid-coated (in house) (1.0-4.0 μm)	sonoporation damaged the F-actin membrane network near the pores	[113]
1.0	16-21	*in-vivo*	None	Increased transfection from 35% at 16 MPa to 61% at 21 MPa, but skin damage/ tumour haemorrhage at higher PNP	[114]
2.0	0.10 0.40	*in-vitro*	Lipid-coated (in house) (1.2-3.7 μm)	no sonoporation sonoporation always induced	[115]
2.0	0.2	*in-vitro*	None Albunex Optison	no sonoporation or lysis sonoporation + lysis much higher lysis rate	[97]
2.25	0.10 0.20 0.80	*in-vitro*	Albunex	transient permeabilization strong permeabilization + lysis increased cell lysis	[58]
3.0	-	*in-vivo*	SV-25	achieved gene transfection through sonoporation and related transfection efficiency with higher acoustic intensities	[116]

* The MB types provided in this table are indicative only. There are currently no studies that cross-compare the effectiveness of different MBs and their selection is usually dictated by their availability in the geographical region where the study was performed.

Overall, PNP values over 0.2 MPa, at driving frequencies around 1.0 MHz, lead to higher drug transfection rates into the target cells, but also to higher death rates of the insonated cells. This can be attributed to the inception of inertial cavitation at PNP > 0.2 MPa, which has damaging impact on the cells, compared to stable cavitation. In order to avoid permanent damage to the

insonated tissues, transducers designed for sonoporation are best driven at PNPs below the inertial cavitation threshold. The relation between the cavitation type of lipid-shelled MBs (excited with a 1.0 MHz US field) and PNP is evaluated by Chen et al. in [117]. They have found that a PNP of 0.25 MPa oscillated the MBs under stable cavitation; at 0.5 MPa stable and inertial cavitation coexisted; and above 1.0 MPa, inertial cavitation dominated.

2.7 Quantification of Sonoporation Effectiveness

Over the last decades, several means of evaluating sonoporation efficiency have been devised. Most of these are based on a tracer agent with similar molecular size to the targeted drugs administered in a similar manner to the therapeutic agent.

Reparable sonoporation can be evaluated by targeting fluorescent tracer molecules such as fluorescent-dextran (FD) through the cell membrane with US. FD compounds are available in different molecular masses, which can be similar to the targeted drugs, or which can be related to the dimensions of the pores created due to sonoporation [60]. After insonation, the cells are washed to remove the excess FD and suspended in a dye such as *trypan blue* [118]. Due to reparable sonoporation, the cells absorb the large FD molecules during insonation, and they do not eliminate them during washing, as their membrane reseals and traps them inside. Conversely, the cells do not become stained after their suspension in trypan blue as their membranes reclose and block the dye molecules from entering. However, lethally sonoporated cells eliminate the FD molecules during washing and they absorb the trypan blue dye because of the permanently porated membranes [18]. The cell intake of FD can be evaluated with flow cytometry [119], a technique used to measure the number of cells that exhibit fluorescence and to assess their fluorescence intensity, in order to differentiate between the sonoporated and the unaffected cells. Another tracer is *propidium iodine* (PI) which is not fluorescent. However, when bound to double-stranded nucleic acids, PI emits a reddish fluorescent light upon excitation. It is normally blocked by the cellular membrane due to its molecular size, and its presence in the cell can be related to successful sonoporation [108].

Confocal microscopy represents a means to visualise fluorescently-labelled cell membranes which have been sonoporated [120] and it has proven useful in evaluating the F-actin rupture in sonoporated cells [113]. F-actin is a filamentous protein that provides mechanical support for the cell, without which the cell cannot maintain its shape. Confocal microscopy is a type of fluorescence microscopy which allows the creation of 3-D images of the scanned samples, with resolutions down to a few hundreds of nm [121].

Haemoglobin release can be used as an indicator of cells suffering sonoporation. After the suspension containing the cells is insonated, a centrifuge removes the cells and then the amount of haemoglobin released in the suspension is measured and related to the number of sonoporated cells [61].

Finally, an electrical means to evaluate membrane poration *in vitro* is by measuring its transepithelial electrical resistance (TEER). A layer of cells creates a barrier to the passage of ions, which translates into an electrical resistance [122]. TEER measurements can be employed to measure the barrier integrity (or cell barrier function) before and after sonoporation.

2.8 Theory of Ultrasound and Piezoelectricity

The previous sections described the biomedical aspects of sonoporation and the requirements of the therapeutic approach in relation to US driving parameters. The following section discusses the general theory of US propagation and the aspects of piezoelectricity that are employed in the following chapters of this Thesis for the design, simulation and manufacture of the piezocomposite miniature-sized array for sonoporation.

2.8.1 Acoustic Impedance and Acoustic Waves

The acoustic impedance (Z) can be easily explained through an analogy with the electrical impedance [123]: the electrical impedance as defined by Ohm's law is the ratio between voltage and current. Similarly, the acoustic impedance is defined as the ratio between the pressure (P) and the velocity (v) of the particles displaced by the acoustic field:

$$Z = \frac{P}{v} \qquad \text{Eq 2.4}$$

Alternatively, Z can be expressed in terms of the medium density, ρ and the acoustic propagation velocity, c, with Eq 2.5 [124, Ch. 24] :

$$Z = \rho c \qquad \text{Eq 2.5}$$

As an acoustic wave passes through the boundary between two media with different Z at an incidence angle with the normal (θ_i), some of the acoustic pressure will be transmitted in the second medium, at a different refraction angle (θ_t). The remaining pressure will be reflected back into the originating medium at a reflected angle (θ_r) equal to θ_i as in Figure 2-8. The relation between θ_i and θ_t is given by Eq 2.6 [123]:

$$\frac{sin(\theta_i)}{sin(\theta_t)} = \frac{c_1}{c_2} \qquad \text{Eq 2.6}$$

where c_1 and c_2 are the sound propagation velocities in the first and second media.

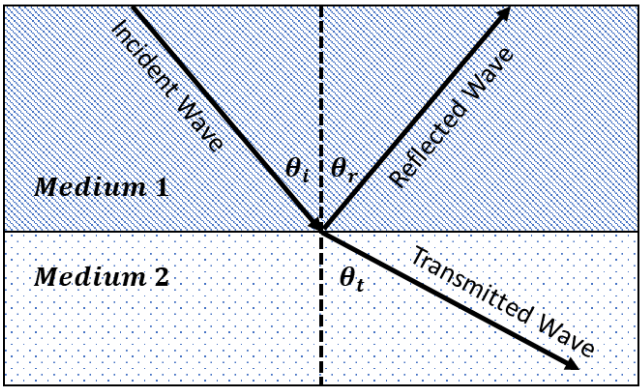

Figure 2-8 Acoustic Wave Propagation Through a Boundary Between Two Different Media

The ratio between the transmitted acoustic pressure (P_t) and the incident pressure (P_i) is given in Eq 2.7 and the ratio between the reflected pressure (P_r) and P_i is given in Eq 2.8 [123].

$$\frac{P_t}{P_i} = \frac{2Z_2 \cos(\theta_i)}{Z_2 \cos(\theta_i) + Z_1 \cos(\theta_t)} \quad \text{Eq 2.7}$$

$$\frac{P_r}{P_i} = \frac{Z_2 \cos(\theta_i) - Z_1 \cos(\theta_t)}{Z_2 \cos(\theta_i) + Z_1 \cos(\theta_t)} \quad \text{Eq 2.8}$$

For an acoustic wave with normal incidence on the boundary (i.e. $\theta_i = 0°$), the cosine terms in Eq 2.7 and Eq 2.8 are removed because they are equal to unity.

When an acoustic wave reaches the interface with a structure with different Z than the originating medium, but with size smaller than its wavelength (λ), the wave reflects in all directions. This is termed scattering and the structures that cause it are called scatterers.

Acoustic velocity is a material property, which varies as function of temperature. Typically, soft tissues have very similar *c*, with an average value around 1540 m/s and an average specific acoustic impedance around 1.64 kg/(s*m^2) [125], which allows US to pass through subsequent tissues with little distortions (i.e. reflection, refraction, scattering). The bone however has much higher *c* of around 4080 m/s and Z around 7.75 kg/(s*m^2), which leads to increased US reflections and scattering at its interface.

Furthermore, an acoustic wave that passes through a medium suffers attenuation due to absorption and scattering [109]. Absorption is the phenomenon which converts acoustic energy into heat and is associated with temperature increase in tissues during US exposure [96]. Attenuation in soft tissues is dominated by absorption (90%). The rate of heat production per unit volume (dQ/dt) as a result of US absorption is expressed as:

$$\frac{dQ}{dt} = 2\alpha_a I \quad \text{Eq 2.9 a}$$

$$I = \frac{P^2}{2\rho c} \quad \text{Eq 2.9 b}$$

where α_a is the absorption coefficient and I is the acoustic intensity expressed in terms of medium density, ρ and speed of sound, c.

Because of attenuation, acoustic pressure decreases exponentially with the distance travelled by the US wave in the respective medium [126]:

$$P = P_0 e^{-\alpha d} \quad \text{Eq 2.10}$$

where P_0 is the initial pressure, α is the attenuation coefficient and d is the distance travelled by the acoustic wave in the medium.

The attenuation coefficient is expressed in dB/(cm*MHz) and is proportional to the US frequency [109]. Figure 2-9 (reprinted from Ref.[127]) presents the approximate relation between the attenuation coefficient and frequency for three distinct types of tissue:

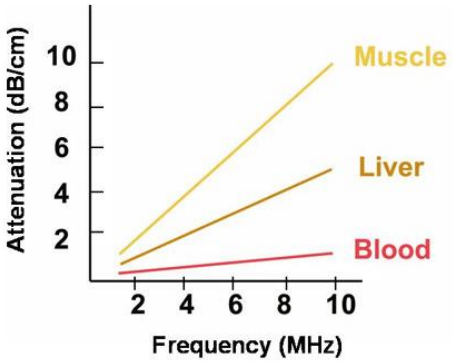

Figure 2-9 Attenuation as Function of Frequency (Reprinted from Ref. [127])

2.8.2 Piezoelectricity

Piezoelectricity is the linear and reversible property of a class of materials to transform mechanical energy into electrical energy and vice versa [128]. The electromechanical behaviour of piezoelectric materials is described by the relation between the mechanically related stress (*T*) and strain (*S*), and the electrically related electric field (*E*) and electric displacement (*D*) [129]. The direct piezoelectric effect represents the formation of an electric potential at the opposite faces of a crystal due to polarization upon material deformation, and is proportional to the amount of stress applied to the material [130, Ch. 1]:

$$P_P = dT \quad \text{Eq 2.11}$$

where P_P is the piezoelectric polarisation vector, d is the piezoelectric strain coefficient and T is the stress applied to the piezoelectric element. The direct piezoelectric effect exhibited by a quartz crystal was discovered by the Curie brothers in 1880 [1].

The reverse piezoelectric effect relates the mechanical strain (S) produced in the crystal to the electric field applied at its sides [131]. In other words, it describes the mechanical movement (oscillation) of the crystal when it is subject to an electric field [67]. It is written [130, Ch. 1]:

$$S_P = dE \qquad \text{Eq 2.12}$$

where S_P is the strain induced when the piezoelectric element is subjected to an electric field with magnitude E. Stress and strain are interrelated by the elastic constant of the material (c_e):

$$T = c_e S \qquad \text{Eq 2.13}$$

Combining Eq 2.11 and Eq 2.12 with Eq 2.13, the direct and reverse piezoelectric effects can be described as [130, Ch. 1]:

$$P_P = dT = eS \qquad \text{Eq 2.14 a}$$

$$T_P = c_e S_P = eE \qquad \text{Eq 2.14 b}$$

where T_P is the stress produced when the piezoelectric element is subjected to an electric field, and e is the piezoelectric stress constant

The influence of the electric field applied on a piezoelectric element leads to the formation of an electric displacement, which depends on the dielectric permittivity of the material (ε). The total electrical displacement of the transducer can be expressed as [130, Ch. 1]:

$$D = \varepsilon E + eS_P = \varepsilon E + P_P \qquad \text{Eq 2.15}$$

The analysis discussed above has been performed in 1-D, however piezoelectricity is a 3-D phenomenon [3, Ch. 1]. All piezoelectric materials are anisotropic which means their behaviour varies differently along different axes because they possess directionality in certain properties. Therefore, most properties that characterise piezoelectric materials are associated with a direction and relate two different quantities. As a result of crystal anisotropy, the properties in one direction are cross coupled to the other two orthogonal directions [132]. For example, strain along one direction is related by Young's modulus to the stress suffered by the material in the same direction or perpendicular to the elongation direction; also, the longitudinal and transverse strains are related by Poisson's ratio.

Thus, the electro-mechanical equations of piezoelectric materials need to be evaluated in a matrix form (over all three dimensions), which can be performed with tensors. Under linear

elasticity assumption, a deformable solid in a cartesian coordinate system (X=1, Y=2, Z=3) has six possible deformations and stresses: three longitudinal stresses and three transversal (shear) stresses. Polarization in one of the three directions (1, 2, 3) can be generated by the combined contribution of each stress or strain component [130, Appendix B]. Therefore, the polarization tensor can be approximated as:

$$P_i = d_{ijk}T_{jk} = e_{ijk}S_{jk} \qquad i,j,k = 1,2,3 \qquad \text{Eq 2.16}$$

Second order stress and strain tensors are represented by 3x3 matrices [3, Ch. 1]:

$$T = \begin{bmatrix} T_{11} & T_{12} & T_{13} \\ T_{21} & T_{22} & T_{23} \\ T_{31} & T_{32} & T_{33} \end{bmatrix} and\ S = \begin{bmatrix} S_{11} & S_{12} & S_{13} \\ S_{21} & S_{22} & S_{23} \\ S_{31} & S_{32} & S_{33} \end{bmatrix} \qquad \text{Eq 2.17}$$

In this tensor notation, the first subscript is associated with a force applied parallel to the cartesian coordinate system and the second subscript is associated with the direction of the occurring stress or strain as a result of the force. If the two subscripts are equal, the force and the reaction are in the same direction, resulting in a longitudinal effect, but if the two subscripts are different, the force and reaction have different directions, leading to transversal shear effects on the material. Considering the second-order stress and strain tensors possess symmetry (assuming the piezoelectric material is in static equilibrium), their 3x3 matrices can be written in a compressed matrix (reduced notation) form to simplify the subscript notation to 6 independent components [3, Ch. 1]: 1, 2, 3 for the longitudinal directions which correspond to the X, Y, Z coordinates and 4, 5, 6 which are associated with transversal directions. The reference system for piezoelectric materials with reduced notation is presented in Figure 2-10.

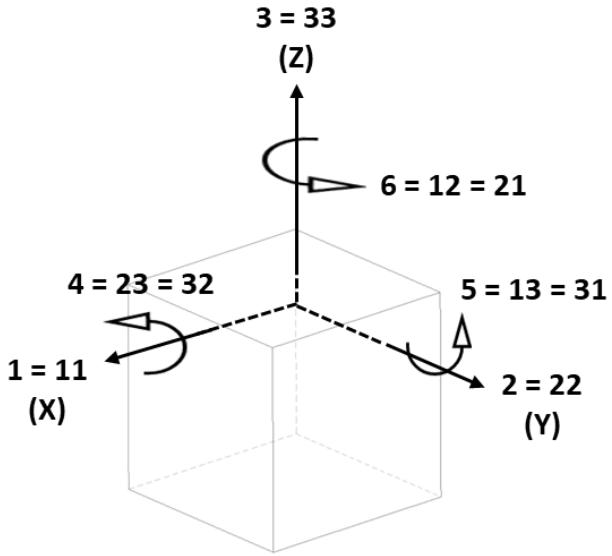

Figure 2-10 Reference Coordinate System for Piezoelectric Materials

According to the *ANSI/IEEE Std 176-1987* [133], the piezoelectric constitutive equations can be written as:

$$T_{ij} = c_{ijkl}^{E} S_{kl} - e_{kij} E_k \qquad \text{Eq 2.18 a}$$

$$D_i = e_{ikl} S_{kl} + \varepsilon_{ik}^{S} E_k \qquad \text{Eq 2.18 b}$$

or in reduced notation:

$$T_p = c_{pq}^{E} S_q - e_{kp} E_k \qquad \text{Eq 2.18 c}$$

$$D_i = e_{iq} S_q + \varepsilon_{ik}^{S} E_k \qquad \text{Eq 2.18 d}$$

where *p* and *q* are the reduced notations of *ij* and *kl; i,j,k,l* = 1,2,3 (X,Y,Z) and *p,q* = 1,2,3,4,5,6 as defined in Figure 2-10*;* $c_{pq}^{E}$is the elastic stiffness coefficient at constant electric field (*E*); ε_{ik}^{S} is the electrical permittivity under constant strain (*S*) [134].

Eq 2.18 can be expressed in matrix form as [3, Ch. 1]:

$$\begin{bmatrix} T_1 \\ T_2 \\ T_3 \\ T_4 \\ T_5 \\ T_6 \\ D_1 \\ D_2 \\ D_3 \end{bmatrix} = \begin{bmatrix} c_{11}^{E} & c_{12}^{E} & c_{13}^{E} & c_{14}^{E} & c_{15}^{E} & c_{16}^{E} & -e_{11} & -e_{21} & -e_{31} \\ c_{21}^{E} & c_{22}^{E} & c_{23}^{E} & c_{24}^{E} & c_{25}^{E} & c_{26}^{E} & -e_{12} & -e_{22} & -e_{32} \\ c_{31}^{E} & c_{32}^{E} & c_{33}^{E} & c_{34}^{E} & c_{35}^{E} & c_{36}^{E} & -e_{13} & -e_{23} & -e_{33} \\ c_{41}^{E} & c_{42}^{E} & c_{43}^{E} & c_{44}^{E} & c_{45}^{E} & c_{46}^{E} & -e_{14} & -e_{24} & -e_{34} \\ c_{51}^{E} & c_{52}^{E} & c_{53}^{E} & c_{54}^{E} & c_{55}^{E} & c_{56}^{E} & -e_{15} & -e_{25} & -e_{35} \\ c_{61}^{E} & c_{61}^{E} & c_{63}^{E} & c_{64}^{E} & c_{65}^{E} & c_{66}^{E} & -e_{16} & -e_{26} & -e_{36} \\ e_{11} & e_{12} & e_{13} & e_{14} & e_{15} & e_{16} & \varepsilon_{11} & \varepsilon_{12} & \varepsilon_{13} \\ e_{21} & e_{22} & e_{23} & e_{24} & e_{25} & e_{26} & \varepsilon_{21} & \varepsilon_{22} & \varepsilon_{23} \\ e_{31} & e_{32} & e_{33} & e_{34} & e_{35} & e_{35} & \varepsilon_{31} & \varepsilon_{32} & \varepsilon_{33} \end{bmatrix} \begin{bmatrix} S_1 \\ S_2 \\ S_3 \\ S_4 \\ S_5 \\ S_6 \\ E_1 \\ E_2 \\ E_3 \end{bmatrix} \qquad \text{Eq 2.19}$$

Depending on the type of piezoelectric crystal, the corresponding elasto-electric matrix in Eq 2.19 can be simplified due to symmetry along the poling direction of the material, zero coefficients and coefficients with interrelated values [3, Ch. 1], [134]. For example, the PZT perovskite has class 6mm symmetry. From 81 different coefficients, the diagonal axis of symmetry reduces the number of independent coefficients to 45 for PZT ceramics. Subsequently, 24 coefficients are equal to zero, and some of the remaining coefficients are interrelated, which reduces the number of independent coefficients to only 10. Figure 2-11 (reprinted from Ref. [3, Ch. 1]) shows the reduction in the elasto-electric coefficients for four types of piezoelectric materials.

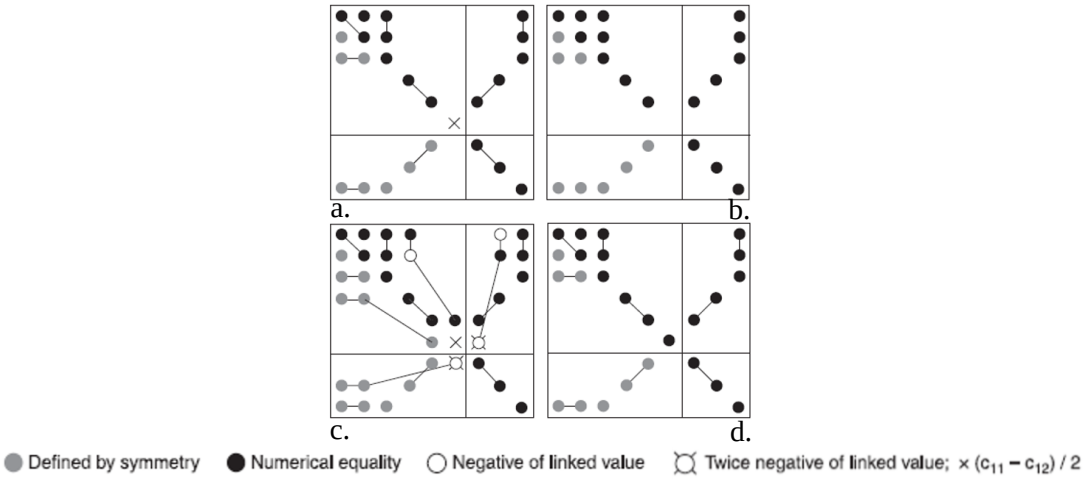

Figure 2-11 Graphical Representation of the Reduced Elasto-Electric Matrix for: a. PZT (class 6mm); b. PVDF (class 2mm); c. $LiNbO_3$ (class 3m); d. PMN-PT (class 4mm) (Reprinted from Ref. [3, Ch. 1])

2.8.3 Piezoelectric Material Properties of Interest

Resonance Frequency

According to IEEE Standard 177 [135], piezoelectric resonators have six characteristic resonances, which can be grouped as follows:

- f_r and f_a – the resonance and antiresonance frequencies. The piezoelectric material vibrates with highest amplitude free oscillations when it is excited with an electrical signal with a frequency equal to f_r. Conversely, the piezoelectric material has the lowest oscillation amplitude at f_a [136].
- f_m and f_n – the frequencies at which the piezoelectric material has minimum/ maximum electrical impedance.
- f_s and f_p – the series and parallel resonance frequencies, corresponding to maximum conductance (f_s) and maximum resistance (f_p) of the piezoelectric material.

Furthermore, according to IEEE Standard 177, for lossless or low loss piezoelectric materials, such as PZT ceramics, the following assumptions can be made:

$$f_r = f_m = f_s \; and \; f_a = f_n = f_p \qquad \text{Eq 2.20}$$

f_a depends on the piezoelectric element thickness (thk) and on the longitudinal velocity (v_l):

$$f_a = \frac{v_l}{2thk} \qquad \text{Eq 2.21}$$

Therefore, when oscillating in thickness mode, the transducer thickness can be expressed as function of wavelength:

$$thk = \frac{\lambda}{2} \qquad \text{Eq 2.22}$$

Electromechanical Coupling Coefficient

Coupling coefficients (denoted with *k*) are dimensionless quantities used to evaluate the effectiveness of a piezoelectric transducer to convert energy electromechanically [137, Ch. 2]. An ideal representation of *k*, which ignores energy losses during conversion, is provided in Eq 2.23.

$$k = \frac{U_{ME}}{\sqrt{U_{MM}U_{EE}}} \qquad \text{Eq 2.23}$$

where U_{MM} is the mechanical energy, U_{EE} is the electrical energy and U_{ME} is the energy coupled from one form to the other through the direct or reverse piezoelectric effect.

In terms of the constitutive equations, *k* can be expressed with Eq 2.24 [137], but more explicit formulations depend on the piezoelectric element geometry and polarization direction. More information on the coupling coefficients related to the geometry of the piezoelectric materials used in the development of the miniature-sized therapeutic arrays is provided in Section 3.2.3.

$$k = \frac{|d|}{\sqrt{\varepsilon^T s^E}} = \frac{|e|}{\sqrt{\varepsilon^T s^E}} \qquad \text{Eq 2.24}$$

where ε^T is permittivity at constant stress and s^E is compliance at constant electric field

Piezoelectric Coefficient

The piezoelectric strain coefficient (d_{ij}) is of particular interest in transduction because it quantifies the material displacement. As shown in Eq 2.24, the electromechanical coupling of the transducer in a given direction is directly proportional to the piezoelectric coefficient. Therefore, high electromechanical coupling is associated with high piezoelectric coefficient.

Mechanical Quality Factor

The mechanical quality factor of a transducer (Q_m) expresses the ability of the device to deliver oscillations to the surrounding media and is a function of frequency. It is a parameter that describes the energy losses in the piezoelectric material and its capacity to amplify vibrations at resonance [138], [139]. Piezoelectric materials with high Q_M are desired for therapeutic US applications due to their ability to deliver high-power acoustic fields without incurring self-heating [140]. Q_M is defined in terms of the ratio between the mechanical energy stored by the piezoelectric material (U_{MM}) and the dissipated power (P_D) with Eq. 2.25 [138].

$$Q_M = 2\pi f \frac{U_{MM}}{P_D} \qquad \text{Eq 2.25}$$

2.8.4 Material Poling

All piezoelectric materials lack a centre of symmetry (are non-centrosymmetric) which means that the unit cell of their crystal is not symmetric along all axes (Figure 2-12 a. reprinted from Ref. [141]). The non-symmetry of the unit cell leads to a non-zero net charge because the constituent negative and positive ions are not entirely balanced and form an electric dipole. A series of neighbouring dipoles with the same orientation form a Weiss domain [142]. If the Weiss domains are all aligned towards the same direction, the material is piezoelectric [143]. Figure 2-12 b.-c. (reprinted from Ref. [143]) shows an illustration of the dipoles rearrangement in the crystal structure as a result of poling with the electric field, *E*.

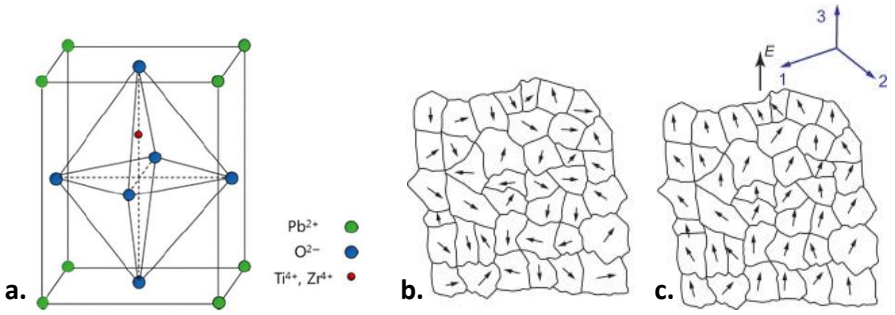

Figure 2-12 a. Perovskite PZT Unit Cell Lacking a Centre of Symmetry (Reprinted from Ref. [141]): b. Unpoled Crystal (Dipoles Oriented Randomly) c. Poled, Piezoelectric Crystal with Parallelly Aligned Dipoles (Reprinted from Ref. [143])

Polycrystalline materials are originally isotropic: they are not polarised and do not manifest piezoelectricity. Even if the single ceramic crystal grain is anisotropic and possesses a dipole moment, the macroscopic orientation of the grains is random (Figure 2-12 b.), which leads to a net charge close to zero and inherently a centre of symmetry for the overall crystal [142].

Poling is the process that induces piezoelectricity in initially isotropic crystals and relies on their ferroelectric property. Ferroelectricity is a material property that allows the polar crystal dipoles of the material to be reversed under an electric field. If the electric field is powerful enough, the poled crystal remains permanently polarised and therefore becomes piezoelectric. The poling process is analogous to the magnetisation of a metal and the name *ferroelectric* is an analogy to *ferromagnetism* [131].

During the poling process, the crystal is subjected to a powerful DC electric field at a constant, elevated temperature (i.e. the phase transition temperature of the piezoelectric material) for a certain period of time. Then the material is allowed to cool down to room temperature, while the DC field is still applied. This procedure rearranges the Weiss domains in the piezoelectric material in a direction parallel to the DC field [143], [144]. The polarization axis of a piezoelectric material is typically considered to be the thickness direction (Z direction in Figure 2-10).

The Phase Transition Temperature and the Curie Temperature

The material phase transition temperature (T_{PT}) describes the temperature at which the unit cell of the piezoelectric material incurs a change in geometry (for example from cubic to rhombohedral). The Curie point is a temperature threshold (T_C) above which the asymmetry in the ferroelectric materials disappears, leading to material depoling. Both parameters are important in determining the temperature range of operation for piezoelectric materials [140].

2.8.5 Piezoelectric Materials

Overall, there are 32 crystal classes, out of which 21 lack a centre of electrical symmetry in the unit cell. From the 21 classes, 20 can exhibit piezoelectricity and 10 out of the 20 have a unique polar axis when unstrained and they are called pyroelectric [128], [131].

Naturally occurring piezoelectric materials like Rochelle salt and Quartz crystal have been used in the past and are still used for some limited applications in the production of US actuators. More recently, synthesized piezoelectric materials with increased performance have been developed [145]. The main types of piezoelectric materials are [137, Ch. 3]: non-ferroelectric single crystals (Quartz), ferroelectric ceramics (e.g. perovskite PZT), ferroelectric single crystals (PMN), and ferroelectric polymers that possess piezoelectricity (PVDF). The first synthesized ferroelectric ceramic was barium titanate ($BaTiO_3$) in 1940 [140]. Lead zirconate titanate (PZT) ceramics were then developed, which had strong piezoelectric effects and higher Curie temperatures, making them suitable for high power US applications or imaging. PZT ceramics are to this date the most popular choice of piezoelectric materials due to the versatility in their formulations.

PZT ceramics can be divided in *soft* or *hard* ceramics. Soft ceramics such as PZT-5H have higher coupling coefficients (k_{33}~0.75) and higher piezoelectric strain coefficients (d_{33}~593) than hard ceramics such as PZT4 with k_{33}~0.7 and d_{33}~289 [140]. However, soft ceramics have lower mechanical quality factor than hard ceramics ($Q_{M\,PZT-5H} = 65$, while $Q_{M\,PZT4} = 500$). They also have higher dielectric losses and lower Curie temperatures (T_C for PZT-5H is 193°C and for PZT-4, it is 328°C). In terms of usage, PZT-5H is more suited for sensing and imaging applications, while PZT4 is more suited for high power transmission applications.

Relaxor-PT based single crystals (such as PMN-PT) provide enhanced coupling (k_{33}~0.9) and piezoelectric coefficients (d_{33}~1700) compared to PZT ceramics and increased mechanical quality factor compared to PZT-5H ($Q_{M\,PMN-29\%PT} = 150$ [140]). Yet, their more fragile structure, and lower temperature range of manipulation/operation limited by the

rhombohedral to tetragonal phase transition temperature (T_{PT}~96℃) imposes more careful manufacturing considerations than for PZT ceramics. According to Zhang et al. [140], dielectric and piezoelectric properties of PZT ceramics are mostly dependent on T_C rather than on T_{PT}, because their phase transition is almost independent of temperature. Conversely, phase transition of single crystals is highly dependent on temperature and this limits their maximum exposure temperature threshold from T_C (i.e. $135°C$ for PMN-29%PT) to T_{PT} (96℃ for PMN-29%PT). Furthermore, single crystals have lower mechanical quality factor than hard ceramics, which means they are more suited to sensing applications than power transmission. Improvements in the properties of relaxor-PT binary crystals have been obtained with the development of ternary crystals (i.e. PIN-PMN-PT), but at this date, these are not extensively available on the commercial market. PIN-PMN-PT has higher T_C (191℃) and T_{PT} (125℃), and better polarization stability than the binary crystal [140].

2.8.6 Piezocomposite Materials

Piezocomposite materials combine piezoelectric materials (the active phase) with a passive polymer material (the passive phase). They have been introduced in the late 1970s and they offer a higher degree of flexibility in tailoring transducer properties for various tasks [140]. Piezocomposite materials can address specific requirements of medical US transducers such as more efficient electromechanical energy conversion than bulk piezoelectric materials, improved acoustic matching with tissue, low electrical and mechanical losses and improved compatibility with the driving electronics [146].

Connectivity

In piezocomposite materials the active and passive phases are self-connected in one or more directions. For a two-material composite, there are 10 possible connectivity patterns (0,0), (0,1), (0,2), (0,3), (1,1), (1,2), (2,2), (1,3), (2,3) and (3,3). The first number represents the directions in which the active phase is continuous, and the second number specifies the continuity directions for the passive phase. The connectivity patterns can be visually represented by 3-D connectivity cubes, such as in Figure 2-13 (reprinted from Ref. [147]), in which the dark regions represent the passive phase and the light regions represent the active phase.

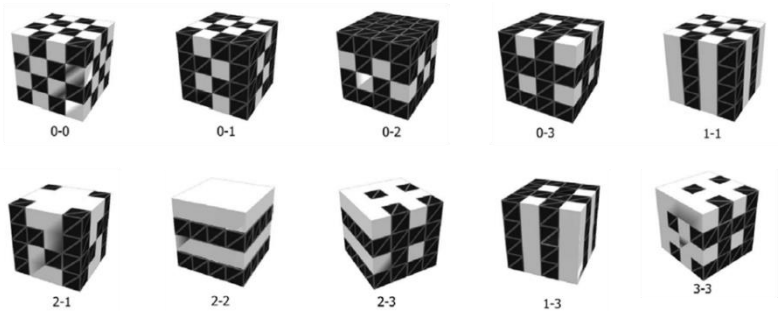

Figure 2-13 3-D Representation of the Connectivity Patterns of Two-phase Piezoelectric Systems (Reprinted from Ref. [147])

In a 1-3 piezocomposite, the active material is continuous in one dimension, and the polymer filler is continuous in all three directions, which means the active material pillars/rods are surrounded by the non-piezoelectric filler in two dimensions (Figure 2-14 a.). For a 2-2 composite, both the active and passive phases are continuous in two directions, which implies the two phases follow one after the other in one dimension (Figure 2-14 b.). Both connectivities are used in medical US transducer designs, but the coupling coefficient of a 1-3 piezocomposite is higher than of a 2-2 connectivity due to reduced lateral clamping of the pillars in Y direction (Figure 2-14).

Traditionally, 1-3 piezocomposites are manufactured with the dice and fill technique, which employs a dicing saw to cut equally spaced, orthogonal slots into a bulk piezoelectric wafer with a rotating blade, producing a matrix of free-standing piezoceramic pillars. The slots are then backfilled with an epoxy resin that represents the passive phase and which confers strength to the otherwise brittle pillars [148]. The excess material is then removed through lapping and the material thickness is adjusted to correspond with the required resonance frequency (Eq 2.21). Other 1-3 piezocomposite manufacturing methods include injection moulding and fibre manufacturing [149].

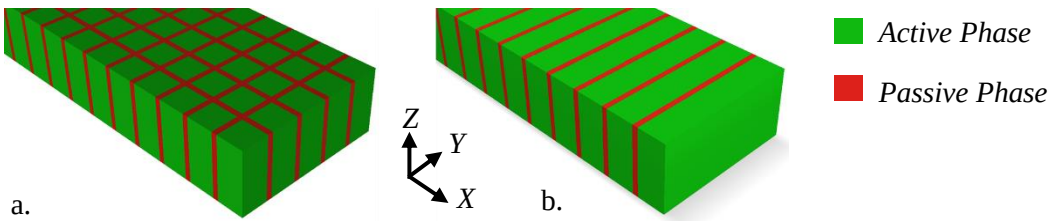

Figure 2-14 Examples of Piezocomposite Patterns: a. 1-3 Connectivity; b. 2-2 Connectivity

2.9 Transducer Modelling

In this Thesis, the US array for intracorporeal sonoporation was prototyped and improved through a simulation approach prior to its manufacture to ensure its pressure output was high enough to induce sonoporation. This section presents the base concepts that were applied for the choice of the modelling approach for the array and for the US propagation in the load.

Subsequently, the structure of a medical US transducer is described, and it will be followed in the design of the miniature-sized array.

Mathematical models and 1-D analytical approaches such as KLM [150] and Redwood-Mason [151] are useful for modelling piezoelectric transducers and US propagation in materials. However, their ability to model complex transducer geometries is limited and they do not account for 3-D geometries and material properties [152]. Alternatively, FEA allows transient, 2-D and 3-D modelling of the piezoelectric transducers and of acoustic propagation in various media, providing more accurate results in the case of complex geometries. Properties evaluated through FEA include: electrical impedance of the active material, surface displacement, US propagation, pressure magnitude, beam profiles, etc. [153].

Analysis of piezoelectric transducers is performed with a set of equations generally known as the governing equations, which comprise the piezoelectric constitutive equations described in Section 2.8.2 and the mechanical and electrical balance relations described in [154]. A change in the state of the piezoelectric material following electrical or mechanical excitation is evaluated with the partial differential form of the governing equations. The analytical method of solving the partial differential equations (PDEs) for a modelled transducer requires an exact solution at all points in the simulated space. The main issue associated with this method is the complexity of the PDEs grows with the number of features added to the model, making it impractical or impossible to find exact solutions with a purely analytical means.

FEA overcomes this problem by discretizing the PDEs of the governing equations in finite domains (or *finite elements*) [155]. The entire simulated volume is therefore divided into cells or mesh elements whose vertexes are called nodes. In a 2-D model, the cell is a four-vertex polygon and in a 3-D model, it is an eight-vertex hexahedron. FEA performs numerical approximations of the mechanical displacements and electric potentials at the nodes of the cells and interpolates them to determine solutions inside the cells [156, Ch. 2]. Therefore, instead of solving the overly-complex PDEs, FEA works on the principle of minimizing the error bounds of the approximations until the solutions at the nodes of the cells converge. The equations obtained at the nodes of all cells are then assembled into a global finite element matrix, and the solutions inside them are related with interpolation functions [154]. As the simulated time in an FEA model is divided in timesteps, the finite element matrix is evaluated at each timestep.

Commercial FEA simulation packages such as OnScale (Redwood City, CA, USA) employ a hybrid implicit/explicit solver to simulate piezoelectric transducers and US beam propagation in various media [157]. An implicit solver computes the solutions to the governing equations

for every time step, at each node of the simulated volume based on the solutions calculated at the previous time step. It also considers the effect exerted by every individual node on all other nodes. In contrast, an explicit solver does not consider interactions between nodes and it only evaluates the mechanical dynamics of the simulated space, ignoring the electrostatic phenomena. This reduces the computation size of a complex model, but can become unstable if the time step is larger than the propagation time between two adjacent nodes of the wave component with the highest frequency of interest. An implicit solver is always used to simulate piezoelectric materials because the electrical propagation velocity in the material is much faster than the mechanical one [158, Sec. 2.2], while an explicit solver can be used to simulate US propagation in other media, such as loads for example [154]. According to G.L. Wojcik et al. [159], an explicit solver can be 100 times faster than an implicit one.

However, FEA can become excessively computationally demanding if a fine mesh resolution or time step are combined with a large model size. Extrapolation can be employed as an alternative to FEA simulation of US propagation in uniform media to reduce simulation time, especially when the evaluated beam pattern is far away from the modelled transducer. It can be used to calculate either frequency or time-dependent pressure fields at specified points in a medium through an analytical, integrating approach, without simulating the entire pathway region between the US source and the evaluated site [154]. Further information about the extrapolation method used to simulate the acoustic field produced by the arrays modelled in this Thesis is presented in Section 3.2.2.

2.9.1 Transducer Structure

Typically, a medical US transducer comprises an active (or piezoelectric) layer, a ground (GND) electrode, one signal electrode or several, in case of an array, electrical interconnections to the external driving electronics, one or a series of matching layers, an acoustic lens, a backing layer, a casing and a sealing layer to provide waterproofness [160] (Figure 2-15).

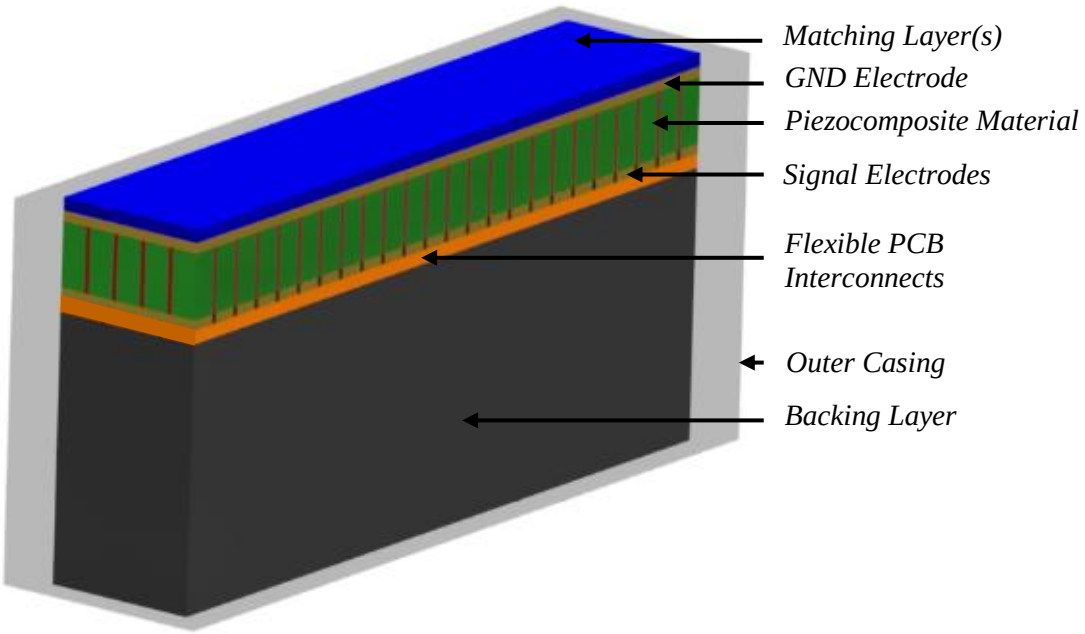

Figure 2-15 Structure of a Medical US Array

Active Piezoelectric Layer

Piezoelectric materials were introduced in Section 2.8.5 and constitute the active component in the transducer structure. The transducer depicted in Figure 2-15 is a 1D array (Section 2.10) with a piezocomposite active layer, and comprises a number of rectangular elements, each being connected to an independent signal electrode.

Electrical Connections

In medical US transducers, the electrode in contact with the load medium (the front electrode) is connected to the ground in order to provide electrical shielding, for safety reasons [3, Ch. 1]. The signal electrodes of the transducer are patterned or scratch diced with a dicing saw (Section 4.4.10) to define array elements. Subsequently, the elements are connected to the transducer's driving electronics with electrical interconnects in the form of a flexible PCB or individual cables. Most common electrode materials are Au, Ag and Cu. Electrodes can be deposited on the faces of the piezoelectric element of the transducer with a variety of methods including thermal evaporation, electron beam evaporation, sputtering or painting. The important parameters for electrode deposition are: reduced process temperature to avoid depoling or damaging the piezoelectric material, reduced layer thickness (around hundreds of nm to a few μm), consistent coating thickness and strong adhesion to the piezoelectric layer.

The Matching Layer

Because piezoelectric materials have higher acoustic impedance than tissue, energy is lost through reflection at the transducer-tissue interface. One or more acoustic matching layers can

be included between the piezoelectric element and the load in order to increase transmission of the US waves into the load. In theory, optimal transmission can be obtained for a matching layer with the following two properties [3, Ch. 1]:

$$thk_{ml} = \frac{\lambda_r}{4}, \quad Z_M = \sqrt{Z_P Z_L} \qquad \text{Eq 2.26}$$

where thk_{ml} is the matching layer thickness; λ_r is the wavelength within the matching layer corresponding to the transducer resonance frequency; Z_M is the matching layer acoustic impedance; Z_P is the piezoelectric material acoustic impedance; and Z_L is the load acoustic impedance.

Matching layers are typically a mixture of particles with high acoustic impedance such as alumina, cerium oxide or silicon oxide [161] and a low impedance polymer. Z_M can be tuned by altering the ratio of the high impedance particles in the mixture [162]. However, materials with certain acoustic impedance may not be manufacturable because the required impedance may be out of the bounds of the constituent materials, or their other related parameters (e.g. attenuation) may render them not useful. Increased matching can however be achieved by stacking a series of intermediary matching layers which are easier to manufacture. Apart from enhanced transmission, matching layers also have some disadvantages including: they are frequency dependent, they require normal incidence to avoid refraction, they attenuate US and their adhesion to the active layer can become an issue at higher US driving powers [3, Ch. 1].

Acoustic Lens

Medical imaging arrays are usually equipped with an acoustic lens attached to the matching layer, which focuses the acoustic beam and ensures good coupling with the tissue. Generally, acoustic lenses are used for focusing the US field in the elevation direction of an array in order to improve the image resolution in that direction. [163]. However, acoustic lenses are usually thicker than the matching layer, which increases the overall transducer thickness and also attenuates US, leading to unwanted heating, especially at higher driving frequencies and power levels. A comprehensive review of acoustic lenses is provided in Ref. [163].

The Backing Layer

For US imaging, the backing layer has the purpose of damping reverberations within the transducer by diminishing the reflected energy at the back of the piezoelectric element [153]. The backing layer is made of an attenuating material and is acoustically matched to the active layer in order to minimize reflections at their interface. Tungsten-loaded soft-setting epoxy is a good example of an attenuating backing material [3, Ch. 1]. However, the attenuated energy in the backing material decreases the effective power output of the transducer and leads to

heating through absorption. Air backed transducers are preferred in high power US transducers for ablation or hyperthermia purposes because no power is lost in the backing material, and reverberations are not an important concern as they are in the case of imaging [164].

Waterproof Casing and the Sealing Layer

The purpose of the casing is to provide mechanical protection and waterproofness for the transducer and the electrical connections. The sealing layer is added to prevent water ingress, to provide electrical insulation for the front-facing electrode and to increase the transducer's biocompatibility for medical US applications [165]. Water tightness of the transducer front face can also be achieved with the matching layer provided the transducer has one and the material is itself waterproof. Alternatively, an exterior sealing layer can be applied, which must be acoustically transparent (thickness $<< \lambda$) and avoid US scattering through an even thickness.

2.10 Types of Transducers

The simplest type of US transducer has a single element, flat surface resonator and is used in sonar systems, non-destructive evaluation and a range of biomedical applications [3, Ch. 1]. However, this configuration lacks efficient focusing capability and control of the US beam. Focusing with a single element transducer can be achieved by attaching an acoustic lens to the flat element or by manufacturing the active element in a concave shape. Subsequently, US beam control can be obtained by mechanically moving the transducer during the procedure.

Alternatively, beam control can be performed electronically with an US array, which comprises many individual piezoelectric elements. Beam focusing and beam steering can be achieved electronically by setting the time delays of the elements so that the emitted acoustic waves from each element arrive simultaneously at the focal point, leading to constructive interference [2, Ch. 7]. More information about phased array focusing with phase delays is presented in Section 3.2.4.

1D arrays are made of inline elements (Figure 2-16, reprinted from Ref. [2, Ch. 7]) and they can only focus along the transducer length (or active aperture), with no control of the beam in the elevation direction (passive aperture). 2D arrays can achieve focusing and steering in both length and elevation directions, but at the cost of high number of elements and interconnections. 1D arrays typically have 32 to 300 elements, while 2D arrays can have an order of magnitude more, for example 64x64 (4096) elements. More comprehensive details about arrays can be found in Ref. [2].

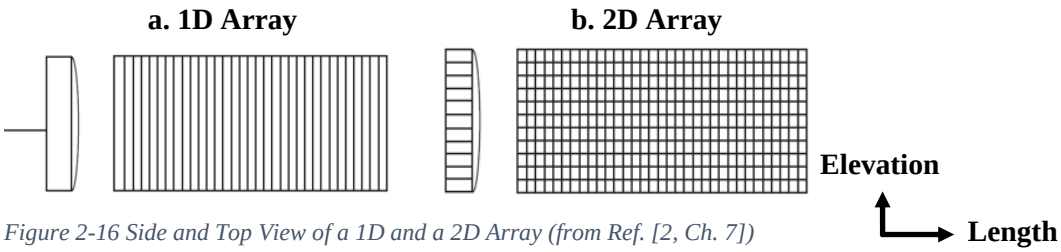

Figure 2-16 Side and Top View of a 1D and a 2D Array (from Ref. [2, Ch. 7])

2.11 Intracorporeal Transducers for Sonoporation and Other US Therapies

The aim of this section is to evaluate the benefits, the potential applications and the main characteristics of catheter and capsule transducer designs and prototypes used for US imaging or treatment which are currently available in the literature. This review was employed to provide directions for the development of the miniature-sized phased array for sonoporation.

Most of the therapeutic US procedures presented in the literature are performed with external, single element transducers. However, in some cases US-facilitated drug delivery techniques that rely on external transducers to perform treatment are affected by distortions which minimise their efficiency. Examples include treatment of: liver, kidney and pancreas (all surrounded by the rib cage) [9]–[11], brain (surrounded by the skull) [12], [13] and bowels (due to presence of gases or intestinal content) [14], [15].

External application of US for deeper target sites in the human body is hampered by attenuation in the connecting tissue between the transducer and the target biological site (i.e. the pathway or pre-focal region), and by the presence of media with significantly different acoustic properties than the surrounding tissue. As described in Section 2.8.1, US attenuation increases with distance and it reduces the pressure magnitudes attained in the target biological site. Furthermore, as attenuation and, inherently heat deposition in the connecting tissue are proportional to US frequency, the therapy resolution must be decreased in order to avoid heat damage. Another issue associated with external US therapies is organ movement during patient respiration (around 10 mm for the liver [166]), which poses issues with locking the US beam to the targeted biological site during treatment. Therefore, the US therapy requires a continuous feedback system to control array steering in order to maintain the same insonation location [166].

When targeting deeper tissues, the presence of the rib cage in the acoustic propagation path leads to high thermal deposition and US scattering, and it reduces the acoustic pressure magnitudes attained at the target [9]. US absorption in bone tissue can be as high as two orders

of magnitude compared to the other tissue at therapeutic frequencies, and the acoustic impedance mismatch leads to powerful US reflections, which highlights the importance of avoiding the ribs [167]. Various apodization techniques can be used for rib avoidance, but the disadvantage of the method is that it requires power compensation, which can increase heating in the connecting tissue. Rib avoidance through focusing was proposed with a Fermat spiral based transducer [11], which could potentially solve the power compensation issue of conventional approaches, however this modality requires complicated apodization techniques to avoid the ribs, which still require improvement.

Another connecting tissue with dissimilar acoustic properties than the target medium is the skull. This bone cannot be avoided by focusing an external US source as in the case of the ribs. Thus, US focusing inside the brain must overcome acoustic phase aberrations, wave refraction additionally to attenuation and increased heat deposition in the skull [168]. Variation of speed of acoustic propagation induced by the skull is also an issue which affects focusing capabilities [169]. In the past, a craniotomy was performed prior to US therapy in order to remove the aberrations introduced by the skull, but this invalidated the therapy non-invasiveness [12]. Currently, there is a wide range of numerical and experimental techniques for driving therapeutic arrays which allow for compensation of skull aberrations. Most of the techniques rely on previous knowledge of the bone topology and on US arrays to focus through the skull by correcting phase aberrations, but they are complex, often incur high costs and further research is required to establish an efficient, non-invasive process for US targeting of brain tissue with external therapeutic arrays [170].

Intestinal applications of US were rarely employed until recently because of gas and intestinal content that reflected acoustic waves, but due to recent advancements and expertise, US has gained importance, especially in gastroenterology due to benefits over radiology and lower costs [14]. A great disadvantage of the technique is the effectiveness of the procedure is based mostly on the operator skills to avoid and to interpret all various forms of scatterers [15].

Incorporating the US transducer into a catheter or capsule allows it to be inserted inside the patient's body, which eliminates a series of disadvantages associated with externally applied US mentioned above. One of the main advantages of this approach consists in the great reduction in the US propagation path between the transducer and the target tissue and the avoidance of obstacles in the US path such as the rib cage, the skull or gasses in the bowels. Furthermore, as the intracorporeal transducer is placed inside the target organ, the issue due to organ movement is also mitigated.

Catheter Diameter Units

Catheter diameters are most commonly expressed in French size (abbreviated as Fr), which is linearly related to the metric scale (1 Fr = 1/3 mm). Table 2-2 provides an equivalence between the most common catheter diameters (expressed in Fr) and the corresponding metric dimensions. Therefore, the sizes of the catheters discussed in this Thesis are presented using the Fr scale, but the (larger) capsules are evaluated in millimetres.

Table 2-2 Intravascular Catheter French Size Conversion Chart to Diameter (in mm), Retrieved from Ref. [171]

Gauge (Fr)	3	4	5	6	7	8	9	10	12	16	20	24
Dia. (mm)	1.00	1.35	1.67	2.00	2.60	2.70	3.00	3.30	4.00	5.30	6.70	8.00

2.11.1 Blood Brain Barrier Permeabilization

The blood brain barrier (BBB) is a biological structure construct made of blood vessels, capillaries, membranes and endothelial cells held together by tight junctions which acts as a barrier towards foreign molecules, protecting the brain from any toxic substances or pathogens [172]. However, BBB also blocks macromolecular drugs or genes from reaching any target tissue inside the brain. Only 2% of small-molecule and 0% of larger molecule drugs available commercially can pass through the BBB, which limits the treatment options for brain tumours or other diseases [173]. US in conjunction with MBs is one of the most important tools currently available to temporary increase BBB permeabilization towards therapeutic agents due to its non-invasive application and increased localization. Furthermore, therapeutic localization and MB cavitation level can be evaluated in real time with a passive cavitation detector (PCD). A comprehensive study of agents that were transported through the BBB by use of sonoporation is presented in [174]. As described beforehand, the most important issue associated with BBB disruption by sonoporation is the presence of the skull between the target biological site and the external US transducer [170]. In this case, catheter US transducers represent a promising approach for performing sonoporation from inside the skull, but size limitations and risks associated with the procedure have limited the research done so far in this domain.

2.11.2 Bowel Imaging and Therapy with US Capsule Endoscope Transducers

Capsule endoscopy is a developing approach for US inspection or treatment of gastrointestinal (GI) tract pathologies, which relies on swallowable capsules equipped with US transducers, and its aim is to reduce the invasiveness of common endoscopic procedures. Several US imaging capsules have been reported in the literature for inspection of the GI tract, but the designs are currently not autonomous and require a tethered connection. One example is

Sonocap (Figure 2-17 a., [165]), which is a 30 mm long by 10 mm diameter tethered capsule, comprising four individual imaging transducers, which was used to evaluate coupling between the capsule endoscope and tissue *in vivo*. Another example is Magnocap (Figure 2-17 b., [19]) which is a 39 mm long by 21 mm diameter tethered capsule, which was magnetically manipulated inside the GI tract and was equipped with two US imaging transducers. Lee et al.[175] manufactured a 30 mm long by 10 mm diameter tethered capsule comprising a single element, unfocused disc transducer, rotated mechanically by a stepper motor, with which they performed *in-vivo* US imaging of the oesophagus and small/large bowels of a pig.

Stewart et al. (Figure 2-17 c., [20]) prototyped a capsule endoscope (30 mm long x 11 mm diameter) equipped with a single element, therapeutic US transducer, aimed for insertion in the small bowel of *in-vivo* porcine models through a stoma. The capsule aimed to demonstrate enhanced delivery of fluorescent semiconductor nanoparticles (quantum dots) through the mucus layer of the bowel. The single element, 3.98 MHz circular US transducer was designed with an MB/drug delivery channel at its centre. Experiments were conducted both *in vitro* and *in vivo*, and demonstrated successful fluorescence agent delivery in the insonated tissue.

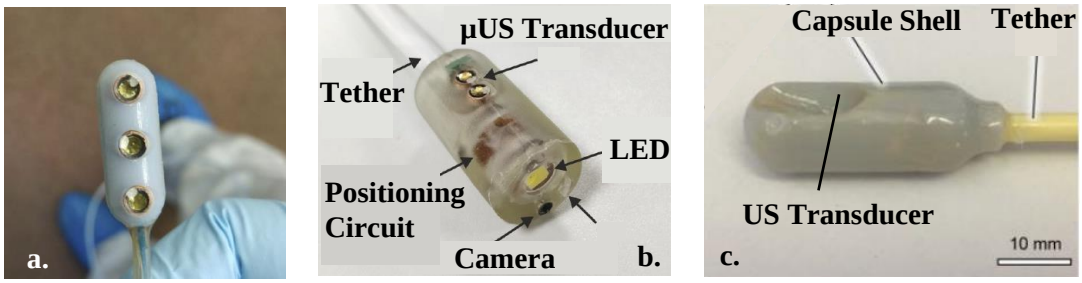

Figure 2-17 Examples of US Capsule Transducers: a. Sonocap [165]; b. Magnocap [19]; c. Small Bowel TDD Capsule Transducer [20]

2.11.3 Transurethral and Transrectal Prostate Treatment

Localized prostate tumours can be treated with minimally invasive therapeutic US delivered transrectally or transurethrally. HIFU ablation of prostate tumours applied transrectally was reported to offer effective long-term cancer control [176] and enhanced patient survival rates [177], [18]. Poissonnier et al. [177] reported high localization control of HIFU ablation with a spherical, fixed focus, 3.0 MHz transducer (Ablatherm HIFU device - EDAP SA, Lyon, France) applied transrectally and translated mechanically to insonate the entire tumour volume. An experimental 5.0 MHz transurethral transducer which was shown to ablate tissue volumes larger than 5 cm^3 is reported in [17]. Furthermore, an MRI-guided transurethral ultrasound ablation (TULSA) device was developed by Profound Medical Corp. (Profound Medical, ON, Canada), which offers real-time control of the ablation therapy through MRI imaging [178]. The US transducer used for TULSA is a 10-element ablative array, capable of

insonating the entire prostate at once. In researching this topic, no evidence of development in transrectal or transurethral sonoporation of the prostate has been found. However *in-vitro* [179], *ex-vivo* and *in-vivo* studies have demonstrated enhanced drug delivery to prostate tumour following sonoporation [180] or focused ultrasound therapy [181] performed with external US sources.

2.11.4 US Ablative Catheters

Various HIFU transducers have been designed to be incorporated into catheters with the purpose of thermal ablation of cardiac arrythmias [182, Ch. 5] . The ablative US transducers are either unfocused or in phased array configuration and their aim is to destroy arrhythmogenic tissue by heat deposition [16]. Phased arrays are better suited for non-invasive catheter ablation because of their ability to focus US [182, Ch. 5]

A catheter that contains both an US imaging system and an ablation transducer was proposed by Gentry et al. [183]. The device comprised of a 112 element, 5.4 MHz imaging array made of PZT-5H, used to image the cardiac vasculature, and a 4.5 mm diameter concentric ring PZT-4 transducer, surrounding the imaging array, operating at 10 MHz for ablation purposes. The interconnections were fitted into a 9 Fr catheter sheath, and the transducer at the front of the catheter had a diameter of 14 Fr. Figure 2-18 shows the catheter array prototypes and designs from Ref. [183]. As further research, the authors propose to use one single 2D array for both imaging and ablation which will reduce the overall size of the catheter transducer. The main issue they highlighted is choosing between PZT-5H and PZT-4 as piezoelectric material because this will either limit the ablative power or the image resolution of the device.

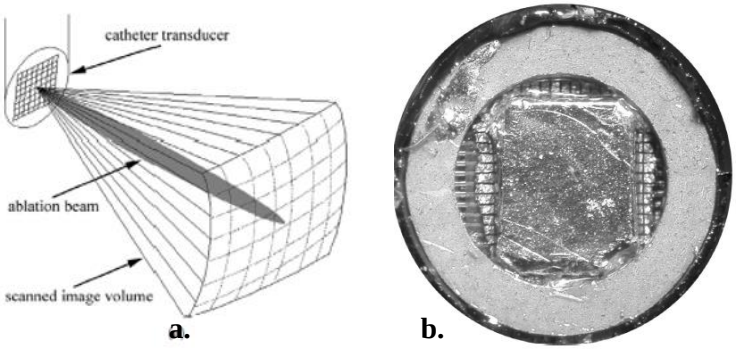

Figure 2-18 Imaging and HIFU Ablation Transducer Prototyped and Manufactured by Gentry et al.: a. Schematic View of Proposed Operation, b. Manufactured Transducer (Reprinted from Ref. [183])

Zimmer et al. [16] developed a 7 Fr planar US transducer, emitting at 10 MHz and tested it successfully *in vitro* and *in vivo*. Werner et al. [184] developed a flat, 2-D phased array operating at 1.6 MHz, with an aperture of 10.2 mm x 20.7 mm, aimed for transoesophageal insertion, for atrial and ventricular myocardium ablation. They obtained localised and

controlled ablation of the target tissue. Subsequently, a review of catheter-based US technologies for hyperthermia and ablation is presented in Ref. [185]. The work highlights that the reviewed ablative catheter transducers had US resonance frequencies between 3 MHz and 10 MHz, and the catheters had outer diameters ranging between 4.5 Fr and 7.2 Fr.

Similarities between sonoporation and HIFU ablative therapies include the use of US for therapeutic reasons and the requirement for precise control of the acoustic focal zone. However, sonoporation relies on the mechanical bioeffects of US and is performed at lower US intensities and lower frequencies than ablative HIFU in order to avoid excessive heating of the insonated tissues. Nevertheless, ablative catheter transducer designs can offer invaluable design ideas for the development of sonoporation catheters.

2.11.5 Intravascular Ultrasound

IVUS (intravascular ultrasound) is a US imaging technology that allows integration of piezoelectric transducers into catheters for the purpose of obtaining high resolution images inside the patient's body through the venous system. Furthermore, the US imaging modality can also be used to accomplish tissue characterisation [99]. One important advantage of IVUS over conventional, external US imaging modalities is the proximity to the targeted tissue or organ. Due to the smaller penetration depth, lower driving powers are required, leading to reduced tissue heating, which is especially important at the high resonance frequencies employed by the procedure (10 MHz – 40 MHz) [186]. Also, aberrations caused by the presence of obstacles in the US path between the transducer and the target are minimized.

IVUS catheters can be divided in two categories depending on the type of US imaging probe they have: mechanical (rotating) transducers and solid-state (non-rotating array) transducers. The mechanical-state catheters have a single-element transducer that is rotated to form images of the tissue surrounding the blood vessels. The solid-state transducers use electronic beam steering to perform imaging [187]. IVUS catheters used for imaging of coronary, iliac and renal vasculature usually require 5 – 6 Fr catheter sheaths (with resonance frequencies of 20 MHz to 45 MHz), but lower frequency IVUS probes (10 MHz -15 MHz) can require up to 9 Fr sheaths [187].

IVUS Design Applied in Therapeutic US

According to Kilroy et al. [99], intravascular US catheters can be modified to accomplish localised drug delivery at the vessel walls for treatment purposes. The same system can then be used for visualising the vessels as well. The research group demonstrated through a finite element analysis (FEA) simulation that the most suitable piezoelectric materials for their

design of catheter-sized therapeutic transducer were PZT-5H and PNM-PT. The prototyped therapeutic IVUS transducer (diameter < 2.0 mm), comprised a single element with a thickness resonance of 6.6 MHz, operated at the lateral resonance of 1.5 MHz for therapeutic reasons (i.e. lower frequency). The transducer was then evaluated with promising results on a flow phantom and on an *ex-vivo* porcine carotid artery.

Kilroy et al. [188] then proposed an IVUS transducer prototype (Figure 2-19, Ref. [188]) capable of displacing MBs inside the vascular walls under liquid flow velocities similar to the real blood flow in the heart. The device employed acoustic radiation forces to control MBs position inside the blood vessel. The research group manufactured two transducers operating in lateral resonance mode at 3.3 MHz and 3.6 MHz, based on hard PZT ceramic, diced in 2-2 piezocomposite configuration. Their corresponding IVUS diameters were 8.1 Fr and 6.8 Fr.

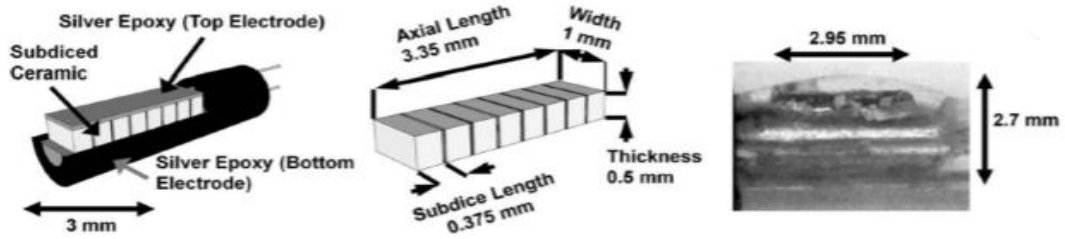

Figure 2-19 Acoustic Radiation Force IVUS Transducer Designed by Kilroy et al. (Reprinted from Ref. [188])

Furthermore, Kilroy et al. [100] were able to induce localized sonoporation *ex vivo* and *in vivo* with a rotating 5.0 MHz IVUS transducer based on a hard PZT-4 ceramic. The transducer replaced the piezoelectric element of a commercially available IVUS catheter and had a diameter of 1.0 mm. The transducer driving procedure was based on two trains of pulses, with the initial pulse having a long number of cycles and low PNP (0.6 MPa), followed by a short pulse with large PNP (2.0 MPa) and achieved satisfactory sonoporation rates. *Ex-vivo* results of the study showed localized delivery to the US exposed arterial wall and *in-vivo* therapy revealed enhanced delivery along the entire exposed artery circumference. Philips et al. [189] also reported enhanced gene transfection to a coronary artery following sonication with a 5.0 MHz modified IVUS transducer at PNPs of 2 MPa, in the presence of infused MBs.

2.11.6 Design Considerations for Intracorporeal US Transducers

The size of intracorporeal US transducers is limited by the vasculature they are intended for. Table 2-3 provides a general list of typical diameters of catheters or capsules for various intracorporeal applications. Urethral and small bowel applications allow for larger catheters, while brain-related applications limit the size drastically because of the smaller vasculature.

Table 2-3 Typical Diameters for Catheters or Capsules Depending on Application

Target Site	Typical Diameter Range (Fr)	Reference
Hepatic Arteries	6 - 24	[190]
Pulmonary Vessels	6 - 11	[191]
Coronary Vasculature	3 - 6	[99], [187]
Brain	3 - 5	[192]–[194]
Male Urethra	~ 30	[195]
Prostate Treatment	16 - 18	[195]
Small Bowel Capsule Endoscopy	15 - 39	[196]

Because the resonance frequency of piezoelectric elements is inversely proportional to their thickness, lower centre frequency transducers require thicker elements, which may not be in accordance with the catheter size limitations. However, as explained in Section 2.6.2, sonoporation is a frequency dependent process, which requires lower operating frequencies (< 5.0 MHz). As the two characteristics of an intravascular US transducer (resonance frequency and size limitations) are in opposition, careful design considerations must be taken in order to maximize the available space, while maintaining the resonance frequency within appropriate bounds for sonoporation. Apart from the active piezoelectric material, the thickness of the matching, backing and sealing layer and the dimensions of the casing also need to be considered [100]. Furthermore, as sonoporation is a therapeutic US procedure, intracorporeal transducers are expected to be robust enough to withstand higher powers and duty cycles than for imaging.

The efficiency of US mediated TDD can be increased by supplying MBs and drugs locally, near the insonation site by use of a feeder tube included in the catheter transducer. Therefore, drug concentrations can be reduced compared to the usual systemic injection, and the overall system toxicity can be decreased by localizing the drug delivery in the target biological site [191]. However, one issue associated with local delivery of MBs according to Kim et al. [191] is that bubbles not destroyed during sonication can attach to the transducer's surface and reduce its power transfer to the target tissue due to US scattering.

2.12 Discussion

Sonoporation generated by the oscillation of MBs under a US field is a feasible and continuously developing method to increase TDD efficiency, with potential life-saving applications. The reduced invasiveness of the procedure and the low post-treatment side effects are advantages over other cancer treatment modalities, which are impaired by either

reduced specificity and toxicity (in the case of conventional chemotherapy) or carcinogenic risk (in the case of radiation therapy). Due to the use of focused US, sonoporation can be highly localized in the target biological site, while most of the surrounding tissue can be spared from the therapeutic effects. The sonoporation volume can be enhanced by mechanically moving a focused US transducer, or by dynamically focusing an array. 1D Phased arrays are a good option for sonoporation purposes due to their ability to electronically control beam steering and focusing along their length, while having a much lower number of elements compared to 1.5D or 2D arrays.

However, most of the current sonoporation studies rely on externally applied US, which poses limitations on the therapy applicability for harder to reach organs including the liver, brain or bowels. Some types of US transducers have already been developed to access those organs intracorporeally by use of catheters or capsules, but the majority of them are aimed for applications such as thermal ablation through HIFU or imaging. The development of intracorporeal US transducers for sonoporation could potentially solve the issue associated with the short therapeutic range of external transducers and mitigate the detrimental effects due to the presence of scatterers in the US propagation path. The HIFU, imaging and sonoporation catheters evaluated in this chapter, can be used as a starting point for the development of a miniature sized 1D phased array for intracorporeal sonoporation.

The design of a catheter or capsule US transducer for sonoporation is defined by the available space and the resonance frequency of the active element, which is typically around 1.0 MHz, but can vary between 0.5 MHz and 5.0 MHz. The therapeutic power output is generally one order of magnitude lower than for ablation [197] and, as sonoporation relies on mechanical effects of MB oscillation rather than on heat accumulation, low duty cycles are normally employed, which reduces transducer self-heating.

3 Virtual Prototyping of the Therapeutic 1D Phased Array

3.1 Introduction

Chapter 3 presents the development of a series of miniature 1-3 connectivity piezocomposite 1D phased arrays by means of virtual prototyping using finite element analysis. The arrays were designed to be incorporated into a capsule or catheter with a diameter as small as 8-Fr (2.67 mm), with the purpose of performing intracorporeal sonoporation.

Delivering US internally as opposed to the more traditional approach that relies on external transducers offers a series of advantages, mainly due to the reduced acoustic path between the transducer and the target. For therapeutic US, this minimises exposure of the connecting, healthy tissue, reduces heating through lower attenuation and avoids scatterers, such as bones, fat or gasses. However, the size limitations associated with a practical intracorporeal transducer typically result in low power output and higher resonance frequency, which are in opposition to the requirements of sonoporation.

The advantage of using phased arrays for therapeutic US as opposed to single-element transducers lies in their ability to electronically steer and focus the US beam at different angles and depths in tissue. This capability reduces the mechanical movement of the catheter inside the patient's body, thus diminishing therapeutic invasiveness and associated risks, and offers the potential to increase the accuracy of the procedure.

In order to address the efficiency issues associated with the miniature size of the array for intracorporeal sonoporation, a multiparametric sweep of the piezocomposite parameters was performed using FEA, with the tracked model outputs being PNP magnitude and the electrical impedance spectra. The purpose of the multiparametric sweep was to determine the array configuration, constrained by the catheter dimensions, that achieved the highest PNP magnitude at focus, in a water load. PNP was chosen as the improvement goal of the sweeps because it is related to MI and inherently, to therapeutic performance of the US transducers. An FEA analysis of the electrical impedance spectrum was performed to verify the array elements operated at the desired resonance frequency and the parasitic modes were decoupled from the main resonance. The 1-3 piezocomposite materials were designed to be manufactured with the traditional dice and fill manufacturing process. Thus, some practical considerations and manufacturing constraints were considered in the development of the array model to keep consistency with the available size intervals of dicing blades and protrusions [148].

3.2 Theory

The parameter set of each prototyped 1-3 piezocomposite 1D phased array was determined analytically for each step of the multiparametric sweep and the resulting array geometry was then modelled in 3-D with a commercially available FEA software package (OnScale). The piezocomposite arrays were simulated using FEA, with an implicit/explicit hybrid solver, and their pressure distributions in the load were computed using Kirchhoff time-integral extrapolation.

Section 3.2 details the basic concepts of FEA and extrapolation that were followed to select the suitable simulation parameters for the array models and the theory employed in the development of the prototyped piezocomposite arrays.

3.2.1 Finite Element Analysis

FEA, previously introduced in Section 2.9, allows for various types of analyses including: frequency analysis (time-dependence is eliminated and unknowns become harmonic complex variables), eigenanalysis (for analysis of natural frequencies and associated mode shapes), or transient/time-domain analysis (for simulation of time-domain processes). Transient analysis is the most complex and computationally demanding type of FEA as it evaluates a broad spectrum of frequencies, and is the only method that considers nonlinear phenomena [154]. Time-domain analysis was used throughout this chapter to simulate US beam patterns achieved by the prototyped arrays in the load medium because PNP was evaluated over the full-frequency spectrum, and not only at discrete frequencies.

The base parameters required to run an FEA model are: system geometry, material properties and boundary, loading and initial conditions [155]. The numerical accuracy of the simulation depends on the time step and mesh resolution.

Boundary Conditions

Due to the finite size of the model, boundary conditions must be applied at its edges to describe the behaviour of the acoustic field when it reaches the limit of the model. Standard simulation approaches use one type or a combination of the following boundary conditions [154], [198]:

- Free boundary – the model nodes at the edges are not constrained, allowing for reflections at the edges. This boundary condition is useful to simulate the interface of the load medium with a highly unmatched medium (as in the case of water-air interface);
- Absorbing boundary – the acoustic waves continue passing through the boundary with no reflections propagating back into the model, however model accuracy near the boundary is affected. This is useful for simulating large loads, well beyond the domain of interest;

- Symmetrical boundary – assumes the model is symmetric along the symmetry axis and eliminates edge effects of the boundary. This is useful in reducing the model size and accounts for periodical geometries;
- Fixed boundary – the edge nodes are fixed leading to a full reflection of the incident waves. This is useful for cases in which the load is surrounded by a very stiff material.

Time Step in FEA Models

The solver used in FEA modelling software is a combination of implicit and explicit types due to its increased efficiency in computing the coupled mechanical-electrical problem that describes piezoelectric transducers (Section 2.9). An implicit solver is stable irrespective of the time step [154]; however the stability of the explicit solver depends on the Courant–Friedrichs–Lewy (CFL) condition [199]:

$$c\frac{\Delta t}{\Delta x} \leq 1 \qquad \text{Eq 3.1}$$

where Δt is the time step and Δx is the distance between two adjacent nodes (i.e. mesh size).

This condition ensures that an acoustic wave does not have enough time to cover the distance between two adjacent nodes of the subdomain, keeping the nodes decoupled during the period of a timestep. Sufficient accuracy and resolution is generally achieved for timesteps no larger than $T/10$, where T is the period of the highest frequency of interest [154].

Mesh Size in FEA Models

The FEA model spatial resolution is determined by the mesh size which is described in terms of λ at the frequency of interest (usually the resonance frequency of the transducer) and the number of finite elements employed per wavelength (n_{FE}):

$$\Delta x = \frac{\lambda}{n_{FE}} \qquad \text{Eq 3.2}$$

Generally, 8 to 20 finite elements per wavelength are considered to provide acceptable resolution for FEA simulations [154]. A higher mesh resolution leads to less dispersion errors but to a larger model size for computation. In certain cases when the simulated geometries have very fine features ($< \lambda/n_{FE}$), the mesh size must be set in accordance to the size of the finest feature in the model instead of λ to avoid large dispersion errors. This is because the CFL condition applies to the space domain as well through the duality of the space-time.

3.2.2 Extrapolation-based Methods

FEA can lead to very large models that may become excessively demanding in terms of computational resources or model run time if the evaluated region of the load is situated far

from the transducer. However, in the case of homogenous, elastic loads, the propagation path between the transducer and the measurement area does not require to be simulated with FEA due to the simplicity of the medium. Extrapolation offers an alternative to calculate the time-dependent pressure at specified points in a load through an integral formulation. This method only requires FEA simulation of a reduced-size load that contains a reference plane close to the transducer surface (Figure 3-1 a.). The time histories recorded at the reference plane can then be extrapolated at any chosen distance from the aperture (Figure 3-1 b.).

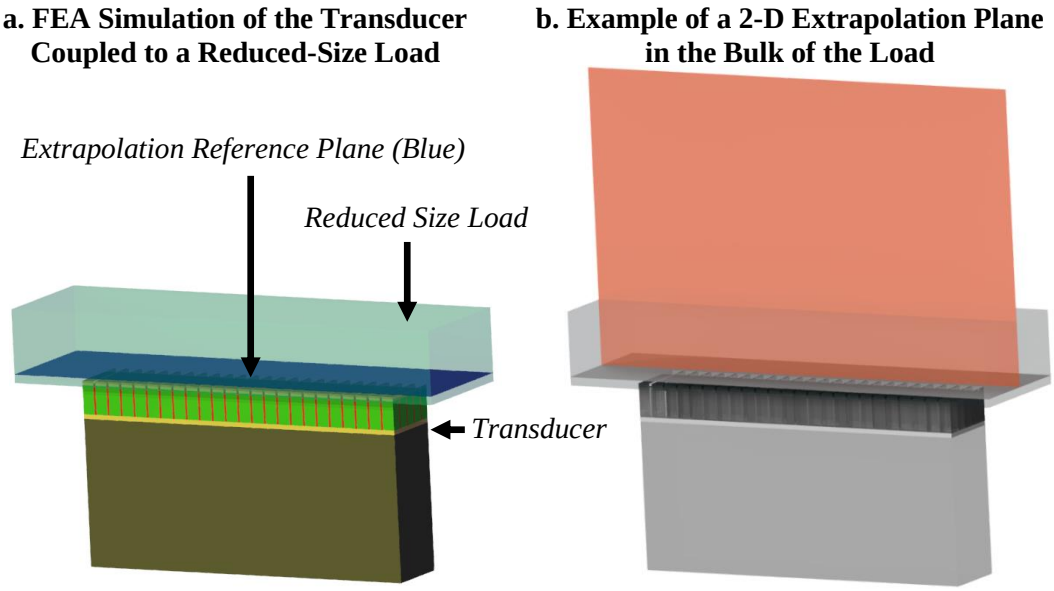

Figure 3-1 Combination of FEA and Extrapolation Used to Model a 2-D Slice of the Acoustic Field from a Piezoelectric Transducer in a Homogenous Load

One example of time-domain extrapolation that assumes dilatational waves only is the Kirchhoff integral equation, which can be used to simulate both the near and the far field of a transducer [154].

3.2.3 1-3 Piezocomposite Material Properties Used in the Development of the Phased Arrays

This section covers the theoretical aspects and equations employed in the design of the 1-3 piezocomposite materials for the prototyped phased arrays. These equations were used in the development of the program for the multiparametric sweep for array optimization.

Electromechanical Coupling Coefficient

The specific formulation of the coupling coefficient described in general terms by Eq 2.23 and Eq 2.24 depends on the elastic boundary conditions, on the applied electric field in relation to the poling direction and on the material geometry [200]. The highest thickness electromechanical coupling coefficient for an electric field applied in the direction of the

induced poling is achieved by a tall, slim rod (usually $thk > 5w_{X,Y}$) poled along the long side, i.e. *thk* (Z) direction [201] (Figure 3-2 a.) and is denoted k_{33} [202]:

$$k_{33} = \frac{d_{33}}{\sqrt{S_{33}^E \varepsilon_{33}^T}} \quad \text{Eq 3.3}$$

The lowest thickness coupling coefficient, k_t, is achieved by a thickness resonator which is a thin, wide plate (usually $10thk < w_{X,Y}$), poled in the thickness direction (Figure 3-2 b.) [201]. According to IEEE Standard 176-1987 [202], k_t is expressed as:

$$k_t = \frac{e_{33}}{\sqrt{c_{33}^D \varepsilon_{33}^S}} \quad \text{Eq 3.4}$$

Both k_t and k_{33} are a measure of energy conversion where both the electric field and the mechanical displacement are in the thickness direction of the active material, but the aspect ratio of the resonators differs.

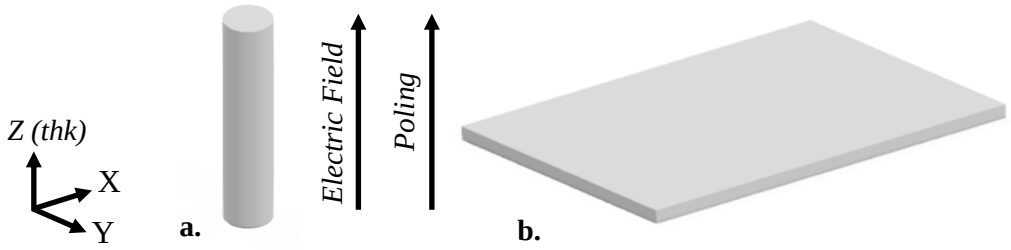

Figure 3-2 Piezoelectric Resonator Geometries: a. Tall Rod; b. Thin Plate

US transducers which operate in the MHz region, typically have reduced thicknesses compared to the effective vibrating area ($thk \ll w_{X,Y}$). If their active material is bulk piezoelectric, their coupling coefficient is k_t, which leads to lower sensitivity and lower electromechanical coupling efficiency than other geometries. This can be addressed by using piezocomposite materials, which provide higher coupling coefficients, while maintaining the same overall aspect ratio of the transducer. A 1-3 piezocomposite transducer comprising tall, thin rods embedded into a polymer phase can achieve a coupling coefficient close to k_{33} if the polymer is elastically soft and the transducer electrodes are stiff enough to force the active and passive materials to oscillate in phase [201], [1].

The electromechanical coupling coefficient can also be calculated from the parallel and series resonance frequencies for a given geometry of the active material. According to the IEEE Standard 176-1987 [202], and bearing in mind the assumptions made in Section 2.8.3 that $f_s = f_r$ and $f_p = f_a$, k_{33} is expressed as:

$$k_{33} = \sqrt{\frac{\pi}{2}\frac{f_r}{f_a}\tan\left[\frac{\pi}{2}\left(1 - \frac{f_r}{f_a}\right)\right]} \quad \text{Eq 3.5}$$

Eq 3.5 is especially useful for determining the coupling coefficient of a transducer from its simulated or measured electrical impedance response.

Volume Fraction

The volume fraction (VF) of a 1-3 piezocomposite is related to the pillar width (PW), pillar pitch (PP), and kerf width (W_{ke}) (Figure 3-3) by Eq 3.6 [203]:

$$VF = \frac{PW^2}{PP^2} = \frac{PW^2}{(PW + W_{ke})^2} \qquad \text{Eq 3.6}$$

The effective electromechanical coupling coefficient of 1-3 piezocomposites ($\bar{k}_t$) is similar to the coupling coefficient of free rods (k_{33}) for VFs in the interval [20%-80%]. However, $\bar{k}_t$ drops sharply at very low or high VFs [146]. At low VF, the polymer phase becomes dominant and its elastic loading on the piezoelectric phase increases the stiffness, thus causing the rapid drop in $\bar{k}_t$. At high VF, the active phase becomes dominant and the lateral clamping of the wider piezoelectric rods drops $\bar{k}_t$ towards k_t (Eq 3.4) [146].

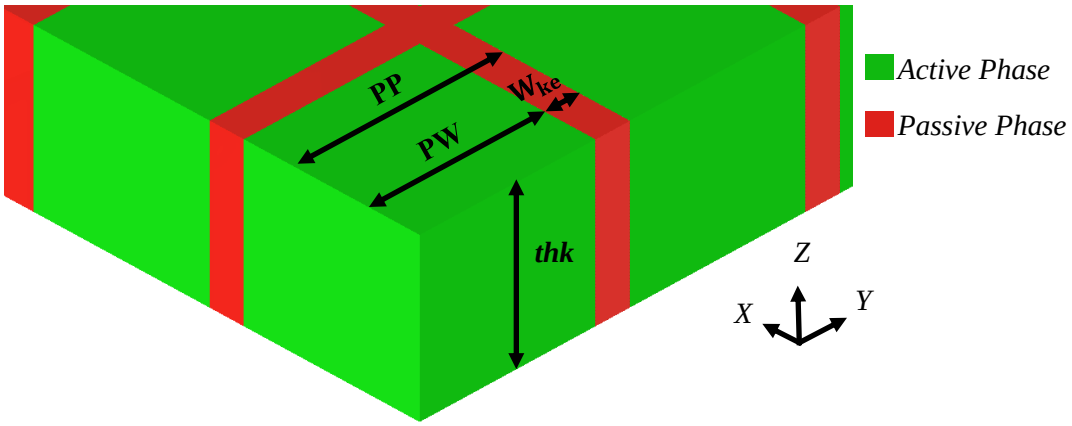

Figure 3-3 Geometric Parameters for a 1-3 Piezocomposite

According to Smith and Auld [146], the coupling coefficient of a thin piezoelectric plate transducer comprising 1-3 piezocomposite is determined by replacing the bulk piezoelectric material parameters in Eq 3.4 with the effective piezocomposite parameters ($\bar{c}_{33}^D$ and $\bar{\varepsilon}_{33}^S$):

$$\bar{k}_t = \frac{e_{33}}{\sqrt{\bar{c}_{33}^D \bar{\varepsilon}_{33}^S}} \qquad \text{Eq 3.7 a}$$

where $\bar{\varepsilon}_{33}^S$ and $\bar{c}_{33}^D$ are expressed as [146]:

$$\bar{\varepsilon}_{33}^S = VF\left[\varepsilon_{33}^S + \frac{2\,\widetilde{VF}\,e_{31}^2}{VF(c_{11}+c_{12}) + \widetilde{VF}(c_{11}^E + c_{12}^E)}\right] + \widetilde{VF}\,\varepsilon_{11} \qquad \text{Eq 3.7 b}$$

$$\bar{c}_{33}^{D} = \bar{c}_{33}^{E} + \frac{\bar{e}_{33}^{2}}{\bar{\varepsilon}_{33}^{S}} \quad \text{Eq 3.7 c}$$

$$\bar{c}_{33}^{E} = VF\left[c_{33}^{E} - \frac{2\,\widetilde{VF}\,(c_{13}^{E} - c_{12})^{2}}{VF(c_{11} + c_{12}) + \widetilde{VF}(c_{11}^{E} + c_{12}^{E})}\right] + \widetilde{VF}\,c_{11} \quad \text{Eq 3.7 d}$$

$$\bar{e}_{33}^{2} = VF\left[e_{33} - \frac{2\,\widetilde{VF}\,(c_{13}^{E} - c_{12})}{VF(c_{11} + c_{12}) + \widetilde{VF}(c_{11}^{E} + c_{12}^{E})}\right] \quad \text{Eq 3.7 e}$$

$$\widetilde{VF} = 1 - VF \quad \text{Eq 3.7 f}$$

Superscript ^{E} used for the elastic stiffness coefficient, c and dielectric permittivity, ε in Eq 3.7 denotes a piezoelectric material property and the lack of superscript ^{E} denotes a polymer property. Constants with an accent bar ($\bar{}$) represent piezocomposite parameters. All relevant material constants are described in Section 2.8.2.

Longitudinal Velocity

Knowledge of the longitudinal velocity of acoustic propagation in the 1-3 piezocomposite material is important because it relates f_a with thk of the piezoelectric material (Eq 2.21). The longitudinal velocity in the piezocomposite is expressed with Eq 3.8 a [146].

$$\bar{v}_l = \sqrt{\frac{\bar{c}_{33}^{D}}{\bar{\rho}}} \quad \text{Eq 3.8 a}$$

$$\bar{\rho} = VF\rho^{a} + \widetilde{VF}\rho^{p} \quad \text{Eq 3.8 b}$$

where ρ^{a} and ρ^{p} are the densities of the active and passive phases of the piezocomposite; and $\bar{c}_{33}^{D}$ is defined in Eq 3.7 c.

Spurious Modes

Spurious or parasitic inter and intra-pillar modes are unwanted resonances which interfere with the transducer main thickness resonance, affecting the device's transmission and reception capabilities [204].

The periodicity of the 1-3 piezocomposite structure of plate transducers favours laterally propagating Lamb waves [204], which are transmitted best in hard set polymers, and that are highly damped in soft set or lossy polymers [205]. Depending on their propagation within the plate, Lamb waves can be symmetrical, in which the top and bottom sides of the plate oscillate 180° out of phase, or antisymmetric, in which the two sides oscillate in phase (Figure 3-4 reprinted from Ref. [206]).

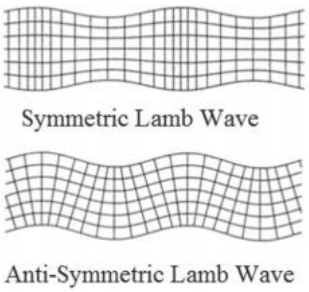

Figure 3-4 Illustration of the Symmetric and Antisymmetric Lamb Wave Modes of Propagation (Reprinted from Ref. [206])

Furthermore, in 1-3 piezocomposites, Lamb waves can propagate normal to the pillar edges, with $\lambda_{L1} = PP$, and diagonally, with $\lambda_{L2} = \sqrt{2} * PP$. The frequencies of the two Lamb waves are expressed in terms of the phase velocity (v_{phase}) of the composite plate with [207]:

$$f_{L1} = \frac{v_{phase}}{PP} \quad and \quad f_{L2} = \sqrt{2} * \frac{v_{phase}}{PP} \qquad \text{Eq 3.9}$$

v_{phase} of the symmetric and asymmetric Lamb wave modes depend on the product between the frequency of operation and the thickness of the plate (commonly denoted frequency-thickness product - *FTP*). The plot of v_{phase} against *FTP* is generally known as dispersion curve. Figure 3-5, reprinted from Ref. [208] shows the dispersion curves of a hard set polymer and of PZT-5H piezoceramic. These plots are used to determine the Lamb wave frequency and v_{phase} of the material for a desired wavelength. More information about Lamb waves and dispersion curves is provided in [208].

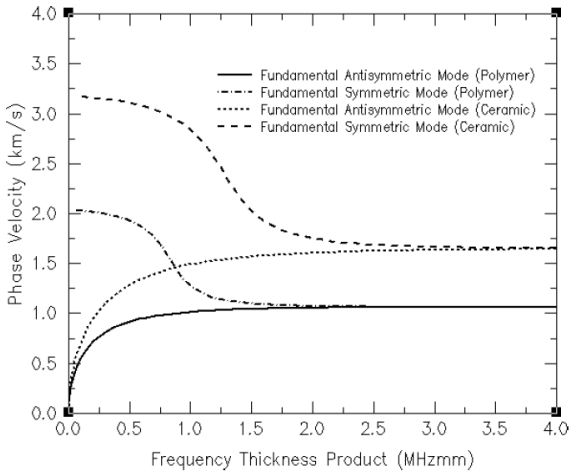

Figure 3-5 Dispersion Curves for a Hard Set Polymer and for PZT-5H Piezoceramic (Reprinted from Ref. [208])

However, as 1-3 piezocomposite materials combine two materials (the piezoelectric and the polymer phase), the dispersion curve of either of the two phases is not sufficient to predict v_{phase} of the composite. As an alternative, v_{phase} of the piezocomposite can be estimated as

function of volume fraction and Rayleigh velocities of the polymer phase (V_{R_poly}) and of the piezoelectric material (V_{R_piezo}) with Eq 3.10 [207].

$$v_{phase} = V_{R\_poly} + VF^2 * \left(V_{R\_piezo} - V_{R\_poly}\right) \quad \text{Eq 3.10}$$

The above equation assumes that in wide plate, 1-3 piezocomposite transducers, the velocity of the Lamb waves approaches the Rayleigh velocity (v_R). Finally, v_R can be expressed in terms of the shear wave velocity of the material (v_s) with [208]:

$$\frac{v_R}{v_s} = \frac{0.862 + 1.14\nu}{1 + \nu} \quad \text{Eq 3.11}$$

where ν is the Poisson ratio (ratio of longitudinal to transverse strain) of the material.

Pillar Aspect Ratio

The pillar aspect ratio (*PAR*) relates the thickness of the piezoelectric pillar to its width by:

$$PAR = \frac{PW}{thk} \quad \text{Eq 3.12}$$

Low pillar aspect ratios are preferred in 1-3 piezocomposite design to decrease the coupling between the lateral resonance mode of the pillars and the main thickness resonance. Furthermore, high PARs degrade the thickness mode vibration of the pillars through vibrational distortion in the pillar itself and through resonances in the polymer material [209].

Piezocomposites with low PAR however must be designed with small W_{ke} in order to reduce the mechanical loading of the tall, thin pillars from the passive phase. This is achieved by increasing VF, which leads to reduced inter-pillar spacing and also diminishes the parasitic modes in the passive phase by shifting the spurious modes towards higher frequencies. A beneficial aspect of composites with high VFs is that the smaller inter-pillar spacing reduces the mechanical loading at the sides of the piezoelectric pillars, which, in turn, allows for higher PAR values without impacting the transducer performance [205].

3.2.4 Phased Array Design and Steering

The following section provides a short description of the theory aspects employed to determine the maximum array element spacing and to calculate the phase delays for focusing and steering of the modelled arrays. The coordinate system used throughout this Thesis is illustrated alongside a phased array model in Figure 3-6. Z axis was chosen as the axial direction and Y axis as the elevation direction for the device coordinate system to maintain consistency with the piezoelectric domain, as discussed in Section 2.8.2.

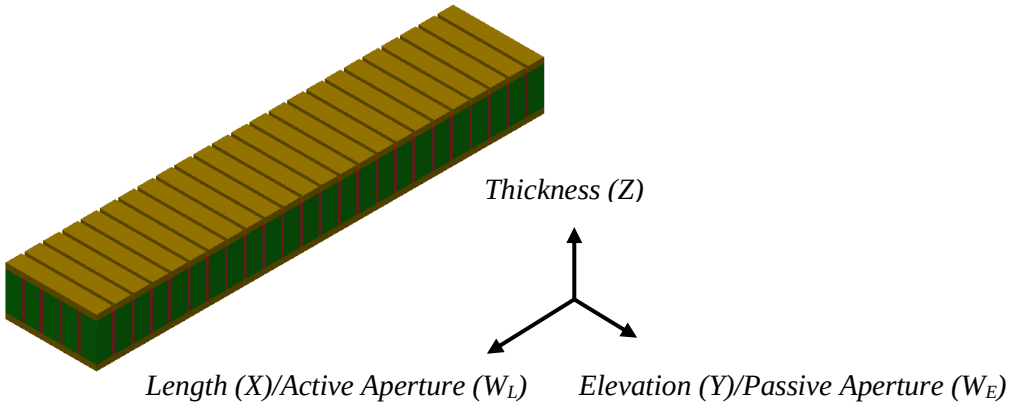

Figure 3-6 Coordinate System for the Phased Array

As introduced in Section 2.10, phased arrays combine the broad wave fields of many small elements into a concentrated acoustic beam with a directional response similar to larger-element transducers. By delaying the wave fields of the individual array elements, the interference pattern from their combined effect can be adjusted to produce both steered and focused acoustic beams. The resulting focused beam shape and pressure magnitude depends on the partial contribution of each array element, which, in turn, is influenced by the directivity function of the elements.

The directivity function represents the spread of the acoustic waves from the ultrasonic source and is dependent on the size of the transmitter [210]. Point like resonators produce spherical waves which spread evenly in all directions and thus have the largest directivity. However, as the element width (e_w) increases compared to the wavelength of the acoustic signal, its natural focus becomes stronger, which leads to a narrower emitted field (Figure 3-7 a.). This results in less energy transmitted by the array element at higher angles from its axial direction (Figure 3-7 b.). Therefore, an array with wider elements will have poorer focusing capabilities than an array with narrower elements because of the lower element directivity.

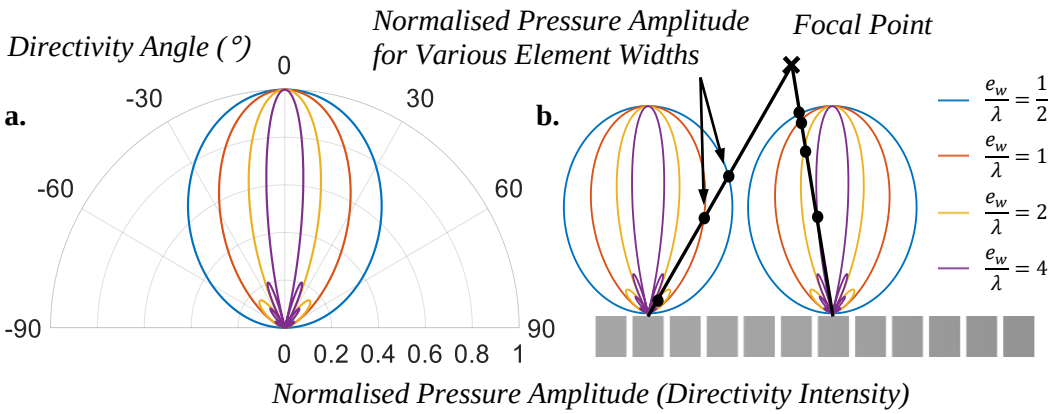

Figure 3-7 a. Directivity Function of an Array Element as Function of the Ratio Between its Width (e_w) and λ; b. Illustration of Element Directivity and Array Focusing

The beam shape produced by a phased array with a pitch (s = centre to centre distance between two adjacent array elements) smaller than λ, forward focused in the far field, is similar to that of a single element transducer of the same length. However, if the individual array element pitch is wider than λ, grating lobes appear, which represent a periodical repetition of the main lobe at higher angles than the normal beam. The existence of grating lobes affects both transmission and reception of a phased array. In the case of transmission, grating lobes cause US energy to propagate in undesired directions, limiting the effective energy of the main beam. In reception, grating lobes reduce the ability of an imaging array to determine the real position of the targets by introducing false echoes [211]. For a forward focused array, the positions of the grating lobes in terms of angle from the normal (φ) are expressed as function of λ in the load medium and s [212, Ch. 4]:

$$\varphi_n = sin^{-1}\left(\pm\frac{n\lambda}{s}\right), \quad (n = 1,2,\dots) \qquad \text{Eq 3.13}$$

If the phased array is steered at an angle $\Phi \neq 0°$ from the normal, $-90° < \Phi < 90°$, Eq 3.13 becomes:

$$\varphi_n = sin^{-1}\left(sin\,\Phi \pm\frac{n\lambda}{s}\right), \quad (n = 1,2,\dots) \qquad \text{Eq 3.14}$$

It can be observed that Eq 3.13 has no real solutions for $s < \lambda$, and Eq 3.14 has no solutions for $s < \lambda/2$. Therefore, forward focusing phased arrays do not have grating lobes if their pitch is lower than λ, but efficient steering of the arrays is accomplished for element spacing < $\lambda/2$. Apodization is generally used to reduce the grating lobes occurring in medical imaging arrays, but its drawbacks include reduction in the array output and increased main lobe width [213].

Phased Array Focusing and Steering

Phased arrays perform efficient focusing in the near field [212, Ch. 4]. When focused in the far field, they behave similarly to an unfocused aperture or a single-element transducer of similar size [214]. The near field distance (*Nf*) can be described in terms of array length (active aperture, W_L, as illustrated in Figure 3-6) and λ:

$$Nf = \frac{W_L^2}{4\lambda} \qquad \text{Eq 3.15}$$

A phased array is steered and focused by triggering its elements with different time delays. The delay laws can be calculated as function of the steering angle with the normal, Φ, and the focal distance, F, in the axial direction (Figure 3-8). Considering the focal point is $P(X_P, F)$, and the centre of the nth array element from one end of the array is $C_n(X_n, 0)$, the acoustic propagation path, from C_n to P is expressed in complex form as:

$$d_{n-P} = |d_P - d_n| = |(\tan\Phi * F - X_n) + jF| \quad \text{Eq 3.16}$$

where d_P is the distance between the centre of the phased array (**O**) and focal point (*P*), d_n is the distance between **O** and C_n , $X_n = s\left(n - \frac{n_{elem}-1}{2}\right)$ and n_{elem} is the total number of elements in the array.

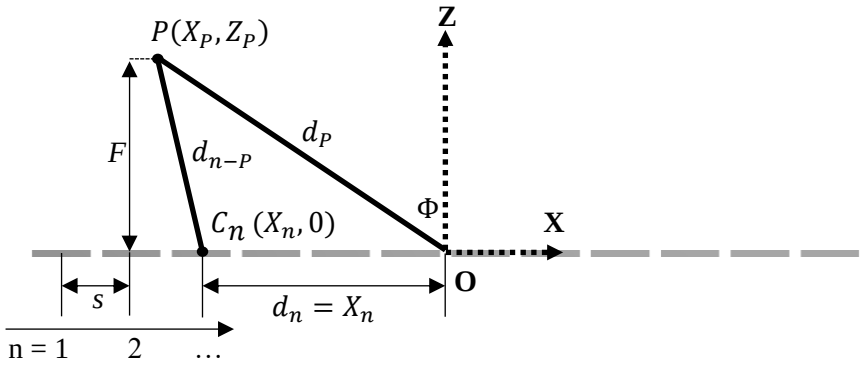

Figure 3-8 Geometrical Parameters for Calculating the Delay Laws of the Phased Array

The acoustic propagation time (t_{n-P}) from the centre of the n[th] element of the array to *P* is then calculated by dividing d_{n-P} with the acoustic velocity in the load (c_{load}). The delay times for each element are then expressed as the difference between t_{n-P} and the minimum propagation time. This method relies on the paraxial approximation and it was applied to calculate the delay laws for all arrays presented in this Thesis. A more exact method to calculate the delay laws without the paraxial approximation can be found in [212, Ch. 5].

3.3 Intracorporeal Transducer Design and Model Considerations

The constituent parts of the prototyped 1D phased array were the active layer made of a 1-3 connectivity piezocomposite material, the electrodes, and the backing layer. As the array was designed for therapeutic US, neither a matching layer nor an acoustic lens were included in order to avoid issues with layer adhesion and heating through attenuation caused by the high power operation of the transducer [3, Ch. 1], as well as, to reduce its overall thickness. The increased acoustic matching with the tissue achieved with the composite structure of the active element was considered sufficient to maintain satisfactory US transmission efficiency [215]. Furthermore, focusing in the elevation direction with a lens was not required because the therapeutic arrays developed in this Thesis were designed to operate at low distances compared to imaging devices, and therefore, beam divergence in elevation was not large.

The following section details the choice of array lateral dimensions and resonance frequency considering the space constraints of fitting inside an 8-Fr catheter. Subsequently, the choice

of materials for the active and passive phases is described in relation to the aims of this work and a series of manufacturing considerations are discussed in terms of their influence on the prototyped 1-3 piezocomposite geometry.

3.3.1 Transducer Lateral Dimension Constraints

The transducer dimensions were limited to fit inside an 8-Fr catheter which has a 2.67mm outer diameter and can be used for intravascular surgery [216], [217]. The active aperture of the phased array was designed to be placed along the length of the catheter (Figure 3-9) so that therapy would be performed longitudinally instead of at the catheter tip. This allows for a larger radiating area and more array elements to be included, which translates to better focusing capabilities and higher US power attained at the focal spot.

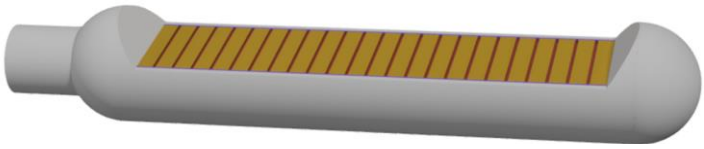

Figure 3-9 Catheter Array Concept: Lateral View

The 1-3 piezocomposite active material was designed to operate in thickness-mode and have a cuboid shape. The cylindrical design of the catheter housing (Figure 3-10) constrains the array elevation to the thickness by the following equation:

$$\sqrt{\text{elevation}^2 + \text{thickness}^2} = \text{catheter inner diameter} \qquad \text{Eq 3.17}$$

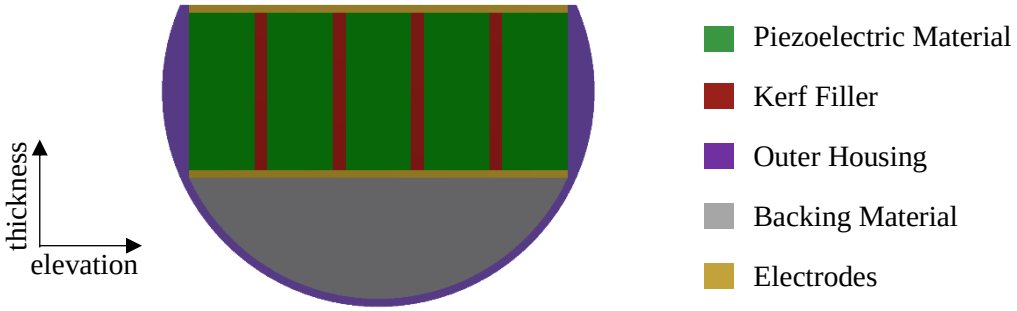

Figure 3-10 Catheter Array Concept: Cross Section

The phased array elevation (passive aperture, W_E, as illustrated in Figure 3-6) is proportional to the emitting surface of the array elements and thus, to the net power output of the device. The size of small passive apertures ($W_E << 10\lambda$), as in the current case, is inversely proportional to beam divergence [218]. The latter effect results in a diffuse focus in the elevation direction and must be reduced as much as possible in order to maintain sufficient acoustic energy at the target. The -6dB pressure magnitude beam spread half angle of the passive aperture $\left(\alpha_{W_E}\right)$ is given by the Full Width at Half Maximum (FHMW) criterion [218]:

$$\alpha_{W_E} = arcsin\left(0.5\frac{\lambda}{W_E}\right) \quad \text{Eq 3.18}$$

Eq 3.19 can be used to determine the -6dB beam width of the acoustic field in the elevation direction at an axial distance, Z from the array surface:

$$W_{E_{-6dB}}(Z) = \frac{0.5\frac{\lambda}{W_E}}{\sqrt{1-\left(0.5\frac{\lambda}{W_E}\right)^2}} * Z \quad \text{Eq 3.19}$$

The phased array length, W_L determines the number of elements included in the array, and therefore, the beamsteering capability of the transducer and its net power output. As the device was not designed to be bendable, its length was restricted to a maximum of 12.0 mm to allow safe navigation through the vasculature.

3.3.2 Resonance Frequency

The resonance frequency of the array was chosen as a compromise between sonoporation efficiency and transducer dimensions. As described in Section 2.6.2, it has been shown that cell permeabilization decreases at higher insonation frequencies and requires higher acoustic pressures [39], with insonation frequencies lower than 5.0MHz being most effective [21]. Additionally, commercial microbubbles (MBs) generally have resonance frequencies between 1.0 MHz and 3.0 MHz [219], [220]. Higher centre frequencies than the MB resonance are also linked to increased cavitation thresholds, which, in turn, relates to higher US power required to sustain MB cavitation. Higher US driving power combined with the larger attenuation at higher driving frequencies leads to increased heat deposition in the tissue, which is to be avoided during sonoporation. Considering the arguments presented above, the resonance frequency of an US transducer for sonoporation should be in the upper kHz - lower MHz range for enhanced therapeutic efficiency.

However, as transducer thickness varies inversely with resonance frequency, a device operating in the hundreds of kHz range would be too thick to be inserted into the vasculature. A large thickness would also lead to reduced array elevation because of the diameter constraint of the catheter (Eq 3.17) and inherently, to large beam divergence in the passive aperture plane. The relation between the thickness of a generic PZT-5H composite array, its constrained elevation by the 8-Fr catheter and the predicted -6dB beam width (Eq 3.19) in the passive aperture direction achieved at a focal distance of 7.0 mm, as function of resonance frequency is presented in Figure 3-11. The plot shows that for resonance frequencies lower than 1.5 MHz, the elevation of the array drops quickly because of a large increase in its thickness, leading to high beam divergence in the elevation plane.

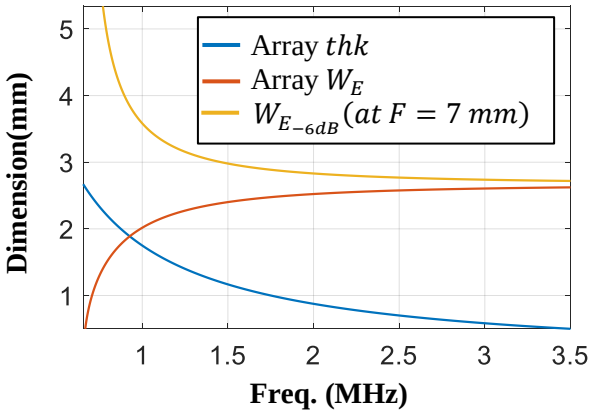

Figure 3-11 Variation of a PZT-5H Composite Array Thickness (thk), Elevation (W_E) and -6dB Beam Width ($W_{E_{-6dB}}$) at F=7.0 mm as Function of Resonance Frequency

Considering both sonoporation-related and size constraints, two resonance frequencies were selected for the arrays developed in this Thesis. 1.5 MHz was the lowest achievable frequency due to the thickness constraints, and resulted in a composite thickness of around 1.0 mm for a piezoceramic active material (PZT-5H) and 0.72 mm for a single crystal (PMN-PT). The second chosen frequency was 3.0 MHz because it corresponds to the upper resonance frequency of SonoVue™ MBs [220] that were planned for use in a biological setup (Chapter 6).

3.3.3 Choice of Piezoelectric Materials

In order to evaluate the versatility of the virtual prototyping approach, piezoceramic (PZT-5H) and single crystal (PMN-29%PT) active materials were selected and compared for application in the miniature-sized 1D phased arrays.

PZT-5H is a soft ceramic with higher piezoelectric and coupling coefficients, but lower Q_M than semi-hard or hard ceramics. The Curie temperature of PZT-5H, above which the material properties degrade, is 193°C, minimising depoling risks during the 1-3 composite manufacturing process. The choice of a soft piezoceramic, that is more preferred for imaging and off-resonance applications [1] than for high power applications, was based on the available resources for this project and on the aim of demonstrating the feasibility of the virtual prototyping approach for any type of piezoelectric material.

PMN-29%PT has superior piezoelectric and electro-mechanical coupling characteristics, and lower acoustic impedance compared to piezoceramics. However, its manipulation is limited by its brittleness, because of which the material can fracture easily during dicing and lapping, and by its first phase transition temperature which is between 80°C and 100°C [1]. The latter represents a serious limitation in the manufacturing process, especially for electrode

deposition, which generally requires higher temperatures. This material was chosen because of its superior piezoelectric characteristics compared to PZT ceramic.

The material properties employed in the FEA models were the generic ones provided by OnScale for PZT-5H, and an experimental set provided by CTS Corp. (CTS Corp., Il, USA - www.ctscorp.com) for PMN-29%PT (Table 3-1).

Table 3-1 Elastic, Piezoelectric and Dielectric Properties of the Piezoelectric Materials Used in the FEA Models of the 1-3 Piezocomposite 1-D Phased Arrays

	PZT-5H	PMN-29%PT
Elastic stiffness constants: $c_{ij}(10^{10}N/m^2)$		
c_{11}^E	12.72	12.4
c_{12}^E	8.02	11.1
c_{13}^E	8.47	10.4
c_{33}^E	11.74	10.8
c_{44}^E	2.3	6.3
c_{66}^E	2.35	3.5
Piezoelectric coupling coefficients: $e_{ij}(C/m^2)$		
e_{15}	17	10.3
e_{31}	-6.5	-3.9
e_{32}	-6.5	-3.9
e_{33}	23.3	22.3
Dielectric constant: ε_{ij}^S		
ε_{11}^S	1700	1340
ε_{22}^S	1700	1340
ε_{33}^S	1470	910
Mechanical Q_M	65	90
Density: $\rho(10^3 Kg/m^3)$	7500	8070

3.3.4 Element Count and Spacing

In order to minimize mechanical motion of the catheter inside the patient's body, the phased arrays were designed for efficient beamsteering. Therefore, the array pitch (s) was restricted to a maximum of $\lambda/2$. This constraint can be expressed in terms of PW, W_{ke} and the number of piezoelectric pillars per array element in the active aperture direction ($n_{pil,X}$):

$$s = (PW + W_{ke}) * n_{pil,X} \leq \lambda/2 \quad \text{Eq 3.20}$$

As λ in water corresponding to a 1.5 MHz resonance frequency is approximately 1.0 mm, the maximum array element count was set to 24 elements to satisfy both the inter-element spacing and the maximum array length constraints (Section 3.3.1). The wavelength in water at a driving frequency of 3.0 MHz is approximately 0.5 mm, allowing a maximum of 48 array elements before reaching the array length constraint. However, the 3.0 MHz devices were designed with only 32 elements, which corresponded to the maximum channel count of the research US phased array controller (DSL FI Toolbox – Diagnostic Sonar, no longer in business) chosen for driving the prototype phased arrays (Chapter 5). According to Eq 3.15, the maximum focusing distance of the 1.5 MHz array was 36 mm, and for the 3.0 MHz array, it was 32 mm, which are both sufficient for intravascular sonoporation applications.

3.3.5 Kerf Width Constraints

The dicing of the 1-3 piezocomposites was to be performed with a DISCO DAD3350 (DISCO, Tokyo, Japan) dicing machine using ZH-05 series blades. W_{ke} of the prototyped piezocomposite materials was therefore constrained by the dicing blades available on the market. At the time of writing this Thesis, the available kerf widths for ZH-05 series dicing blades are detailed in Table 3-2. Equally important as the blade width is its exposure, or cut protrusion. The two parameters vary proportionally, meaning that thinner blades have less protrusion, which leads to smaller dicing depths.

Table 3-2 DISCO ZH-05 Series Dicing Blade Parameters

W_{ke} (µm)	17.5±2.5	22.5±2.5	27.5±2.5	32.5±2.5	37.5±2.5	45±5.0
Exposure (mm)	0.38-0.51	0.51-0.64	0.64-0.76	0.76-0.89	0.89-1.02	1.02-1.15
W_{ke} (µm)	55±5.0	65±5.0	75±5.0	85±5.0	95±5.0	105±5.0
Exposure (mm)	1.15-1.28	1.28-1.41	1.41-1.54	1.54-1.67	1.67-1.80	1.67-1.80

Considering the 1.5 MHz piezocomposite material has a thickness around 1.0 mm and adding a 0.2 mm safety margin for the manufacturing process, the minimum blade protrusion for the task is 1.20 mm, which limits the kerf interval of the available blades to {50 µm – 110 µm}, including tolerances. The average thickness of a 3.0 MHz piezocomposite was calculated to be around 0.5 mm, which allows for a blade W_{ke} between {25 µm – 110 µm}, with tolerances.

3.3.6 Choice of Kerf Filler Material

A hard-set polymer was used as the passive phase of the 1-3 piezocomposites due to its lower viscosity than soft or medium-set epoxies, which facilitated a better coverage of the small inter

pillar gaps in the composite. Other advantages of the hard-set epoxy are the reduced curing time and temperature compared to softer polymers. The choice of kerf filler for all 1-3 composite transducers developed in this Thesis was Epofix (Struers Inc., Cleveland, OH, US), which is a hard-set epoxy. A list of material properties for the selected epoxy can be found in Appendix A.

3.3.7 Load Material

Water was used as load material in all pressure simulations to replicate experimental characterization conditions. Furthermore, soft tissues have similar density (1000 kg/m^3) and acoustic impedance ($1.6*10^6$ kg/m^2s) with water, so the transducers can be used in both media, with some additional degree of reflections and scattering expected in the tissue [221].

3.4 1D Phased Array Model Properties and Outputs

Two models of the 1D phased array were designed in OnScale to evaluate the electrical impedance of the array elements and the PNP profile of the transducer focused in a water load. The impedance model was designed for a longer simulated time (i.e. time in the simulation, not the actual computation run time) and finer meshing. Conversely, the pressure model required a great reduction in the simulated time and coarser meshing because of the additional computation demands caused by the inclusion of the load material. Both types of models were evaluated in 3-D because a 2-D model of the phased array would not simulate correctly the intra and inter-pillar spurious modes in the composite lattice and the array surface displacement in the elevation direction.

Considering the complexity of the inter-related equations for the 1-3 piezocomposite structure, its repetitive structure, the constraints on the design, and the parameter variation as part of the multiparametric sweep, the array design process was automated with a MATLAB GUI (Figure B-1, Appendix B). The program was designed to perform all calculations, to export the array geometry in OnScale compatible language and to run the OnScale model automatically. This method was less prone to design errors than the Analyst mode provided by OnScale and it combined the versatility of MATLAB programming and debugging with the FEA capability of OnScale. The method was also more dynamic than using the OnScale Designer mode where a new CAD model of the composite array would need to be created for each iteration of the parametric sweep.

3.4.1 Model Considerations for Simulating the Peak Negative Pressure Profile

Because the array model was simulated multiple times as part of the multiparametric sweep, several steps were taken to reduce the model computation time and thus increase the efficiency

of the program. Most importantly, the axial pressure magnitude from the straight-focused, unbacked phased array was simulated with a combination of FEA and Kirchhoff time extrapolation instead of with FEA only. This procedure benefitted from faster computation time of the extrapolation method, while it still modelled the piezoelectric arrays with the high accuracy of the FEA solver. Additionally, the backing layer was not added to the array model in the multiparametric sweep to further reduce computation demands of the simulation. The removal of the backing layer from the array model was considered to have minimal impact on the multiparametric sweep outcomes because it would add a constant level of damping to the piezoelectric elements throughout the entire sweep as the resonance frequency was constant.

As part of this approach, FEA was employed for the transducer and a reduced-size water load surrounded by absorbing boundaries. A reference plane to capture the time histories required for extrapolation was set in the cross section (XY) of the load, at a distance of 100 µm from the array surface (as in Figure 3-12). The water depth simulated in the FEA model was set to 2.5λ to ensure the top absorbing boundary is sufficiently far away from the extrapolation reference plane and does not influence it. Because the multiparametric sweep improvement goal was PNP at the focal spot, the time-domain extrapolation was not performed in 2-D or 3-D, but it was rather performed at 500 evenly spaced points along the line perpendicular to the centre of the array, stretching 25 mm into the depth of the load, away from the array surface (Figure 3-12).

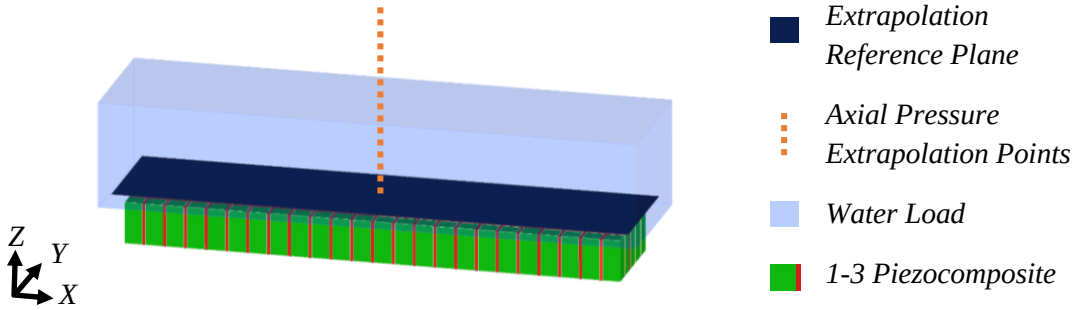

Figure 3-12 Combined FEA Model of Array and Axial Pressure Extrapolation for the Parametric Sweep

The array elements were driven with a pure 10-cycle sine wave centred on their electrical resonance frequency. This type of excitation signal was chosen to resemble the driving signal used later in the Thesis for sonoporation experiments (Section 6.1.1). Phase delays were applied to the array elements in order to obtain a straight focused beam in the near field of the transducer, 5.0 mm away from its front face. The time in the simulation was calculated as the sum of the 10-cycle US burst period and the propagation time of US from the array surface to the other end of the water load, in depth.

The FEA model used rectangular element meshing with the mesh size calculated as half of the smallest array feature dimension. This parameter was selected for meshing because it had a value lower than $\lambda/20$ in the piezocomposite material (Section 3.2.1). The meshing size ratio was set to $X:Y:Z = 1:1:3$ as the smallest dimension in the model was W_{ke}, which spanned in X and Y directions. Conversely, $thk \gg W_{ke}$, so the Z direction did not require such fine mesh resolution and the mesh size in Z was relaxed to decrease model computation demands.

3.4.2 Model Considerations for Simulating the Electrical Impedance

As stated in the introduction of this chapter, the purpose of the electrical impedance investigation using the FEA model was to ensure the resonance frequency of the array elements did not deviate significantly from the analytical prediction and to provide insight into the performance of the 1-3 piezocomposite material. A good understanding of the modes close to or at resonance, could be linked to the performance of the piezocomposite geometry in terms of PNP output. The model simulated the electrical impedance of one array element within the full array configuration (all array elements included) or partial array configuration (with several elements included). Thus, only the investigated element was excited, while the other elements were left unconnected. The unexcited elements were mechanically coupled to the assessed element in order to evaluate the effect of resonances from the entire 1-3 piezocomposite lattice on the impedance of the individual array element. The number of array elements in the simulation increased the running time, but was useful for investigating spurious modes in the composite microstructure. Half and quarter symmetry approaches were used to further reduce model size. Because of the requirement to investigate a high number of electrical impedance models to relate with the multiparametric sweep results, the computation time of an impedance model had to be reduced. Therefore, an investigation into reducing array element count and application of symmetry configurations was performed to determine the smallest model requirements that produced data similar to the full-sized phased array model.

The same X:Y:Z mesh size ratio of 1:1:3 was used for the impedance model as in the PNP model, however, the time in the simulation was fixed to a much higher value than in the PNP model to allow the transducer oscillations to ring down, with a value of 50 μs selected for all impedance simulations.

3.4.3 Parametric Sweep Automation with MATLAB

The parametric sweep procedure for improvement of the 1-3 piezocomposite arrays based on the PNP output at the focus comprised the stages described by the diagram in Figure 3-13:

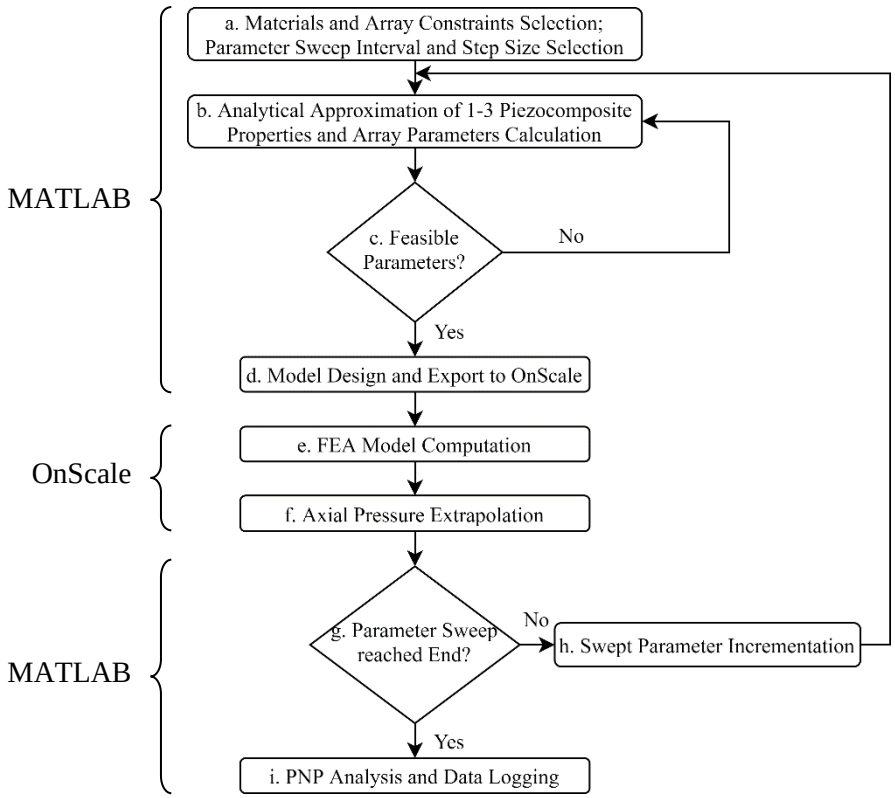

Figure 3-13 Development Stages of the Parametric Sweep

Stages a-d. were performed with a custom MATLAB GUI that used the input array properties, materials and constraints to determine the full property set required to run the FEA model of the array at each step of the parametric sweep, based on the equations described in Section 3.2. The model parameters were written as a series of text configuration files that were later used by an OnScale program (stage e.) to create and simulate the FEA model. The OnScale program was run from within the MATLAB GUI to automate the parametric sweep. The result of the FEA model was then extrapolated (stage f.) to obtain the axial pressure for each case of the parametric sweep. The extrapolation was performed with OnScale, but again automated within the MATLAB GUI.

A PNP value was extracted for each of the 500 evaluated points along the axial extrapolation line described in Figure 3-13 (stage i.). All PNP magnitudes were then plotted as function of depth in the load. This was performed by extracting the minimum pressure magnitude of each extrapolated time trace (Figure 3-14 a.). An example of axial PNP variation with depth in the load, achieved by the modelled array is presented in Figure 3-14 b. The PNP value at the focal point (~5.0 mm in this case) was then logged for each iteration of the parametric sweep and it represented the piezocomposite improvement criterion.

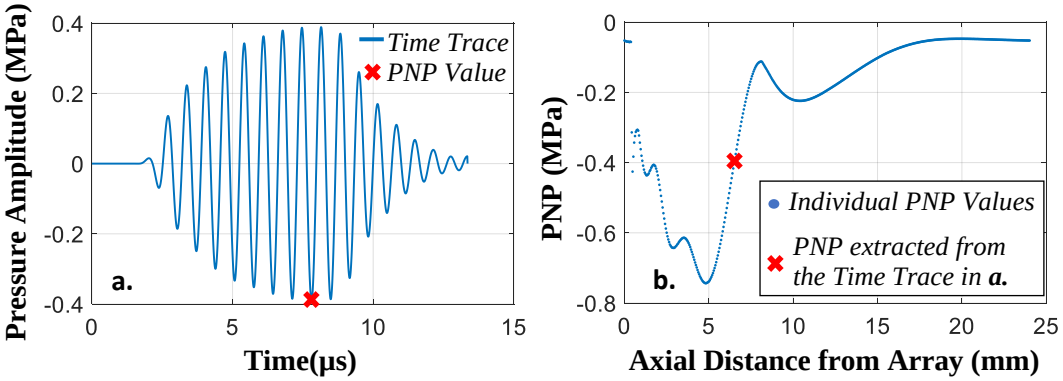

Figure 3-14 a. Extrapolated Time Trace Corresponding to 7.0 mm in Axial Depth; b. Extrapolated PNP vs. Axial Distance in a Water Load, Highlighting the Extracted PNP Value from the Time Trace in a.

Parameter and Constraint Set for the FEA Model

The full set of parameters used in the FEA model of the piezocomposite arrays at each step of the parametric sweep is detailed in Table 3-3.

Table 3-3 FEA Model Parameter Set for the Parametric Sweeps of the Piezocomposite Arrays

Piezocomposite Properties	
f_r	1.5 MHz || 3.0 MHz
Active Material	PZT-5H || PMN-29%PT
Polymer Material	Epofix
W_{ke} interval	{50 μm : 110 μm} for 1.5MHz {25 μm : 110 μm} for 3.0MHz
Swept Parameter Interval	$\boldsymbol{VF}$: {40% : 80%} || $\boldsymbol{PAR}$ interval depends on *VF*, piezocomposite thk and *PW*
Swept Parameter Increment	$\Delta VF = 2.0\%$ || $\Delta PAR = 2.0\%$
Size Constraints	
$W_E\ max$	2.5 mm
$s_{max}\ (\lambda/2\ constraint)$	0.5 mm (for 1.5 MHz) || 0.25 mm (for 3.0 MHz)
Array Parameters	
Element Count	24 elem. (for 1.5 MHz) || 32 elem. (for 3.0 MHz)
Axial Distance to Focus	5.0 mm
Excitation Pulse Type	sine, 10 cycles
Excitation Signal Voltage	10 V_{peak}
Frequency of Excitation Signal	Same as f_r
Dependent Parameters	
Active Element thk	Determined from k_{33}, f_r and composite constants
PP	Function on VF and s_{max}
W_{ke}	Determined from VF (Eq 3.6) and considering available W_{ke} interval (Table 3-2) and design constraints (Eq 3.9, Eq 3.20)
PW	$PW = PP - W_{ke}$
Pillars in Elevation ($n_{pil,Y}$)	max $n_{pil,Y}$ to satisfy: $\left(PP * n_{pil,Y} - W_{ke}\right) < W_E max$
Pillars per Array Element in Active Aperture Direction ($n_{pil,X}$)	max $n_{pil,X}$ to satisfy:$\left(PP * n_{pil,X} - W_{ke}\right) < s_{max}$
Model Related	
Load Material	Water
Load Thickness	2.5 mm
Load Lateral Protrusion	0.5 mm
Backing	No
Simulation Boundaries	All absorbing, except for Z_{min}
Mesh Size	Calculated as $W_{ke}/2$
Mesh Ratio	$X{:}\,Y{:}\,Z = 1{:}\,1{:}\,3$
Simulation time	Σ (US burst period, acoustic propagation time)
Linear Extrapolation	
Extrapolation Depth	25 mm
No. of Extrapolation Points	500

Calculation of Piezocomposite Thickness

The thickness of the active material is related to the values of f_a and $\bar{v}_l$ in the piezocomposite material with Eq 2.21. However, neither f_a nor $\bar{v}_l$ are initially known, but they can be approximated from the desired transducer resonance frequency, f_r.

For a tall, slim piezoelectric rod, f_a and f_r are related through the k_{33} coupling coefficient (Eq 3.5). Based on the results published by Smith and Auld [146], it can be assumed that k_{33} is close to the coupling coefficient of a piezocomposite plate ($\overline{k_t}$) for composites with *VF*s in the range $\{20\% < VF < 80\%\}$. This translates to: $k_{33} \approx \overline{k_t}$. Subsequently, $\overline{k_t}$ can be approximated from the active and passive material constants with Eq 3.7. Finally, $\bar{v}_l$ can also be determined from the constants of the two materials with Eq 3.8.

3.5 Transducer Design Improvement Using the Multiparametric Sweep Based on FEA

3.5.1 Parametric Sweeps Description

Two parametric sweeps were used in the design of the modelled phased arrays: *VF* and *PAR*. The VF sweep was performed first and the *VF* value that led to the highest PNP was then used as constant parameter in the PAR sweep. To avoid any confusion, the improvement parameter, PNP refers to the minimum pressure magnitude attained both spatially and temporally at, or near the estimated focal point of the modelled arrays.

Volume Fraction Sweep

VF was varied in the interval $\{20\% < VF < 80\%\}$, with increments of 2.0%. The other parameters in the modelled piezocomposite were kept constant throughout the sweep with exceptions being: pillar count ($n_{pil,X}$, $n_{pil,Y}$), *PW*, and inherently PAR. thk was also changed slightly between sweep iterations to maintain a constant f_r due to the dependency of $\overline{v_l}$ on VF (Eq 3.8). In order to minimize the variation in the radiating surface of the individual array element throughout the *VF* sweep, the array pitch was set to: $s = \lambda/2$, transforming Eq 3.20 into an equality:

$$s = (PW + W_{ke}) * n_{pil,X} = \lambda/2 \qquad \text{Eq 3.21}$$

Ideally, $n_{pil,X}$ and $n_{pil,Y}$ should not change throughout the VF sweep. However this is impossible over the entire VF interval due to the relation between PW and W_{ke} (Eq 3.6) being constrained by the available dicing blade W_{ke} interval (Section 3.3.5) and the constant pillar pitch (Eq 3.21). The alteration of $n_{pil,X}$ and $n_{pil,Y}$ is the necessary compromise to attain all *VFs* in the sweep, while adhering to all stated constraints.

Table 3-4 presents the maximum and minimum attainable *VFs* for W_{ke} in the interval $\{50\ \mu m\ -\ 110\ \mu m\}$ for the 1.5MHz arrays, as function of $n_{pil,X}$. The same maximum *VFs* are attained by the 3.0 MHz arrays for a minimum W_{ke} of 25 µm due to the proportionality of equations.

Table 3-4 VF Interval as Function of Pillar Number per Element Length, Constrained by the Dicing Blade Widths

$n_{pil,X}$	$VF\ Min$	$VF\ Max$
1	0.62	0.81
2	0.34	0.64
3	0.14	0.49

Generally, 1-3 piezocomposite transducers have at least 3 pillars per element, however, because of the manufacturing restrictions (limited dicing blade W_{ke}) and the array steering constraints presented above, the number of pillars in the design process was allowed to drop to as low as one pillar per array element in active aperture direction ($n_{pil,X} = 1$).

Finally, it must be considered that a change in $n_{pil,X}$ also affects *PW* (Eq 3.21) and PAR (Eq 3.12). The gradual increase of *VF* in the sweep should lead to a slight, gradual decrease in *PAR*, provided that $n_{pil,X}$ is constant. However, according to Eq 3.21, *PW* varies inversely with $n_{pil,X}$, which means that a change in $n_{pil,X}$ from two pillars to one, for example, leads to a doubling of *PW*, and inherently a doubling of *PAR*. Therefore, *PAR* is expected to remain almost constant within each *VF* sweep interval, in which $n_{pil,X}$ is consistent, but to vary greatly when $n_{pil,X}$ changes.

Pillar Aspect Ratio Sweep

The PAR sweep was performed for a fixed VF, which was determined following the *VF* sweep. thk was kept constant throughout the PAR sweep to maintain f_r constant. The inter-related parameters that were changed were PW and W_{ke}, with effect on the array pitch, which was no longer kept constant as in the case of the *VF* sweep. The lower and upper PAR margins in the sweep were constrained by the minimum and maximum W_{ke} intervals (Section 3.3.5).

3.5.2 Volume Fraction Sweep Outcomes

The *VF* sweep results in terms of highest PNP at focus for all four types of arrays are presented in Figure 3-15. The 1.5 MHz arrays comprised 24 elements, and the 3.0 MHz arrays had 32 elements. The models contained the same array geometry as intended for manufacturing (Chapter 4), with no symmetry applied in order to be as realistic as possible.

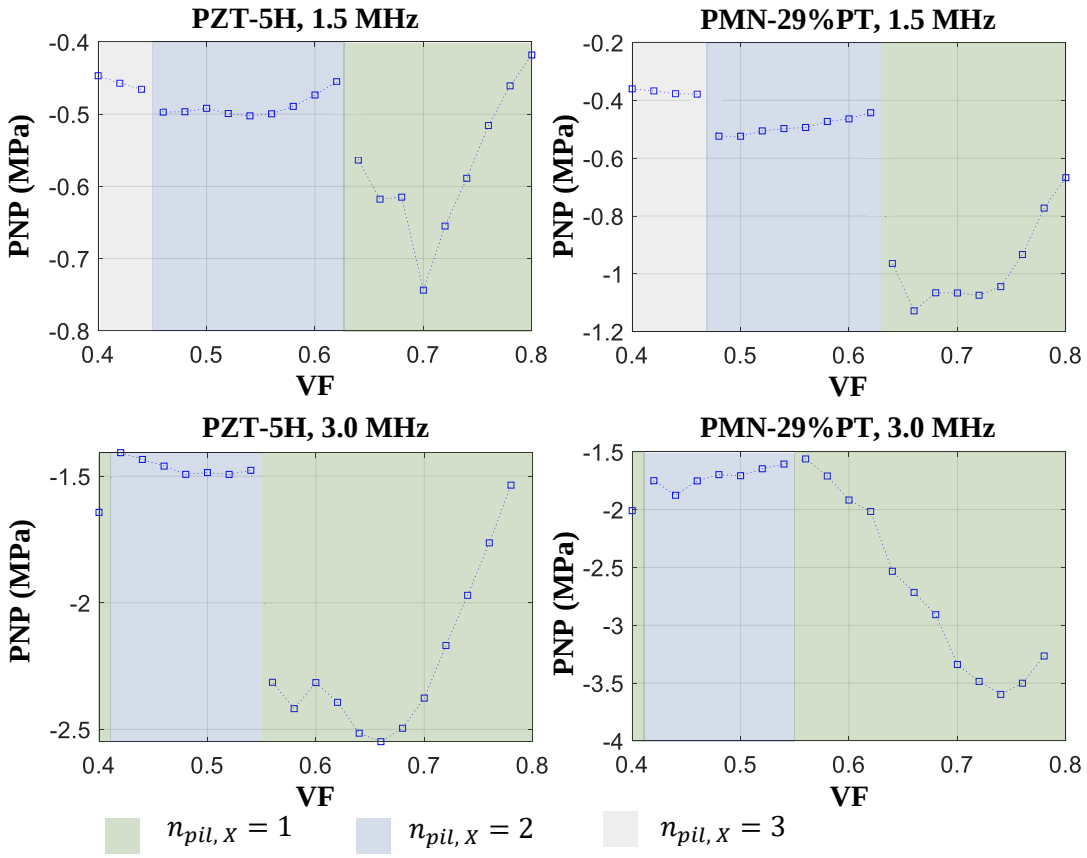

Figure 3-15 PNP at Focus as Function of VF Sweep and the Number of Pillars per Element in Array Length Direction ($n_{pil,X}$) for all Four Arrays

Figure 3-15 shows the 1.5 MHz PZT-5H array achieved the highest PNP at a VF of 0.7, which is in line with the expectation that higher VFs are more suitable for high power US transducers [222], [223]. The sweep also shows a sharp improvement in PNP at $VF = 0.7$, with the closest PNP percentage difference value of 13.5% at $VF = 0.72$. This results in a low margin of practical manufacturing variations to maintain the optimum output from the array.

The 1.5 MHz PMN-29%PT array obtained the best performance for a VF of 0.66, with less than 10% PNP difference for any VF value on the interval $\{0.66 – 0.74\}$, allowing for a larger margin of practical manufacturing variations. Similarly, the 3.0 MHz PZT-5H and PMN-29%PT arrays obtained highest PNP at focus for a VF of 0.66 and 0.74 respectively and 10% PNP difference for VF intervals of $\{0.56 – 0.70\}$ and $\{0.70 – 0.78\}$.

The grey background in Figure 3-15 corresponds to three pillars per array element width in length direction, the blue background to two pillars, and the green background corresponds to one pillar per array element width. The variation of $n_{pil,X}$ and of PAR with VF is presented in Table 3-5 for all four modelled arrays.

Table 3-5 Pillar Number per Array Element Width and PAR Variation with VF

PZT-5H, 1.5 MHz	VF	{0.40 - 0.44}	{0.46 - 0.62}	{0.64-0.80}
	$n_{pil,X}$	3	2	1
	PAR	{0.11 - 0.12}	{0.18 - 0.20}	{0.33 - 0.43}
PMN-29%PT, 1.5 MHz	VF	{0.40 - 0.46}	{0.48 - 0.62}	{0.64 - 0.80}
	$n_{pil,X}$	3	2	1
	PAR	{0.15 - 0.16}	{0.25 - 0.28}	{0.46 - 0.58}
PZT-5H, 3.0 MHz	VF	0.40	{0.42 - 0.54}	{0.56 - 0.78}
	$n_{pil,X}$	1	2	1
	PAR	0.24	{0.17 - 0.19}	{0.39 - 0.44}
PMN-29%PT, 3.0 MHz	VF	0.40	{0.42 - 0.54}	{0.56 - 0.78}
	$n_{pil,X}$	1	2	1
	PAR	0.33	{0.24 - 0.27}	{0.55 - 0.59}

Relating Table 3-5 with the PNP variation with VF (Figure 3-15), one can observe that the output performance of all arrays is better at higher VFs even if PAR is relatively high, which falls in line with the theoretical expectations detailed in Section 3.2.3. Furthermore, the best results in terms of PNP were obtained with the models that had only one pillar per array element in length direction ($n_{pil,X} = 1$). The number of pillars in the passive aperture direction varied from 15 at lower VFs to 5 at higher VFs for the 1.5 MHz arrays and from 20 pillars in passive aperture to 10 for the 3.0 MHz arrays.

An electrical impedance analysis was then performed to relate the electrical performance of the arrays at different volume fractions with the PNP outputs. The electrical impedance of the individual array element (*Z*) was evaluated at one VF value from each *VF* interval (different background colour) in Figure 3-15 for all four types of arrays (Figure 3-16). To decrease the computation time of the FEA model, the element count of all arrays was halved and quarter symmetry was applied. The central element of each modelled array was evaluated, with all other elements not excited, but present for mechanical coupling.

Comparing the PNP output of the transducers (Figure 3-15) with the electrical impedance spectra of the individual array elements (Figure 3-16) at various VFs, it can be observed that the models which achieved the highest PNP had the lowest level of interference with parasitic modes at either f_r or f_a (traces corresponding to the highest *VFs* in all four plots of Figure 3-16). For the lower *VF* values, both PMN-29%PT arrays suffered interference with a parasitic mode at f_r, which was attributed to the reduction in PNP output at the corresponding VFs. For the PZT-5H arrays, the existence of the spurious modes close to f_r at lower *VF*s is not as evident, but there is an interfering mode near f_a at the lower *VF* values.

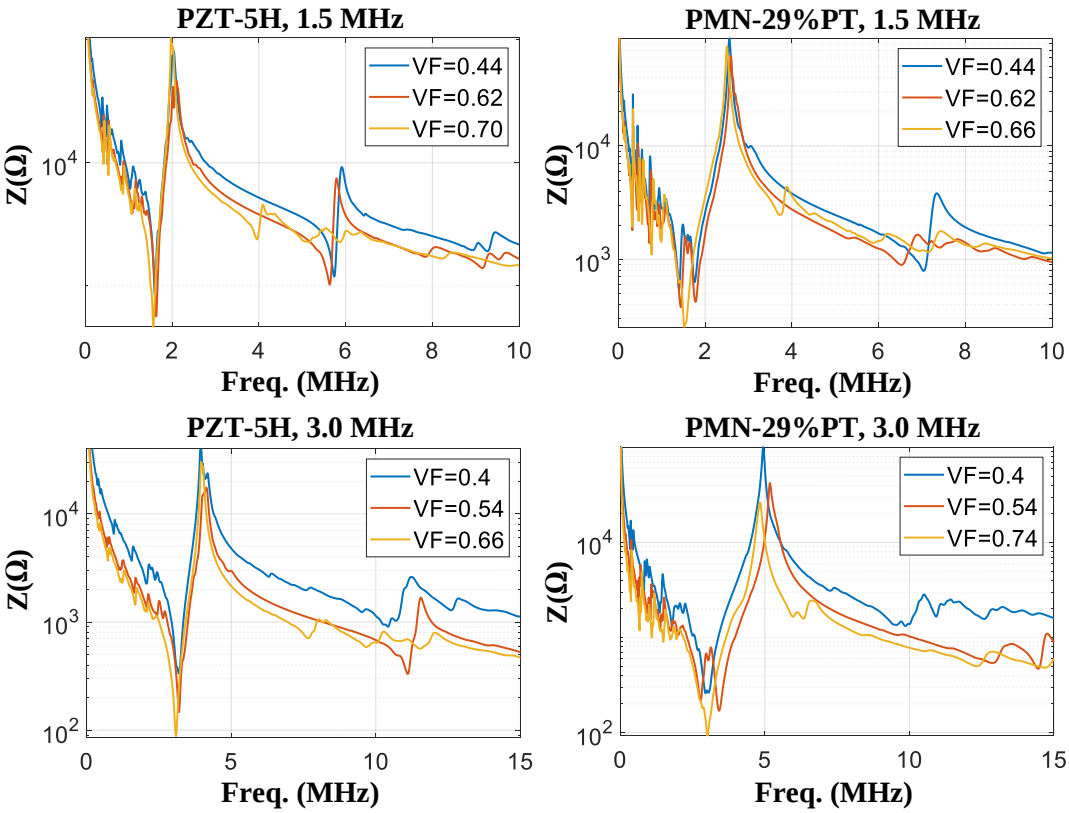

Figure 3-16 FEA Modelled Impedance of an Individual Element in Array Configuration at Different VFs

The impedance response of the individual array elements in Figure 3-16 also showed that, in the absence of parasitic modes interfering at resonance, the difference between f_r obtained with FEA and the one calculated analytically (Section 3.4.3 – Piezocomposite Thickness) was less than 5% for all modelled arrays.

3.5.3 Pillar Aspect Ratio Sweep Outcomes

Figure 3-17 relates the PNP at focus with PAR for all four types of arrays. The red cross in the graphs corresponds to the initial PAR value that was determined in the previous VF sweeps.

The PAR sweep demonstrated a further improvement in PNP was achievable in addition to the VF sweep. However, the percentage improvement in PNP between the best case provided by the PAR sweep and the initial case provided by the VF sweep alone was not very significant (< 7%).

For the 1.5 MHz, PZT-5H array case, the improvement in PNP added by the subsequent *PAR* sweep in addition to the *VF* sweep was 6.8%. This result was however obtained at the cost of a larger array pitch than λ/2 and hence, was not taken forward because the added benefit of increased PNP output was not considered of higher significance than the appearance of grating lobes at higher steering angles caused by the larger array pitch.

The *PAR* sweep for the 1.5 MHz, PMN-29%PT array led to an improvement in PNP of 5.3%, but this was obtained at the cost of an increased array elevation (2.57 mm), well over the 2.5 mm constraint, and was also not taken forward. The *PAR* sweep offered no improvement in the case of the 3.0 MHz arrays.

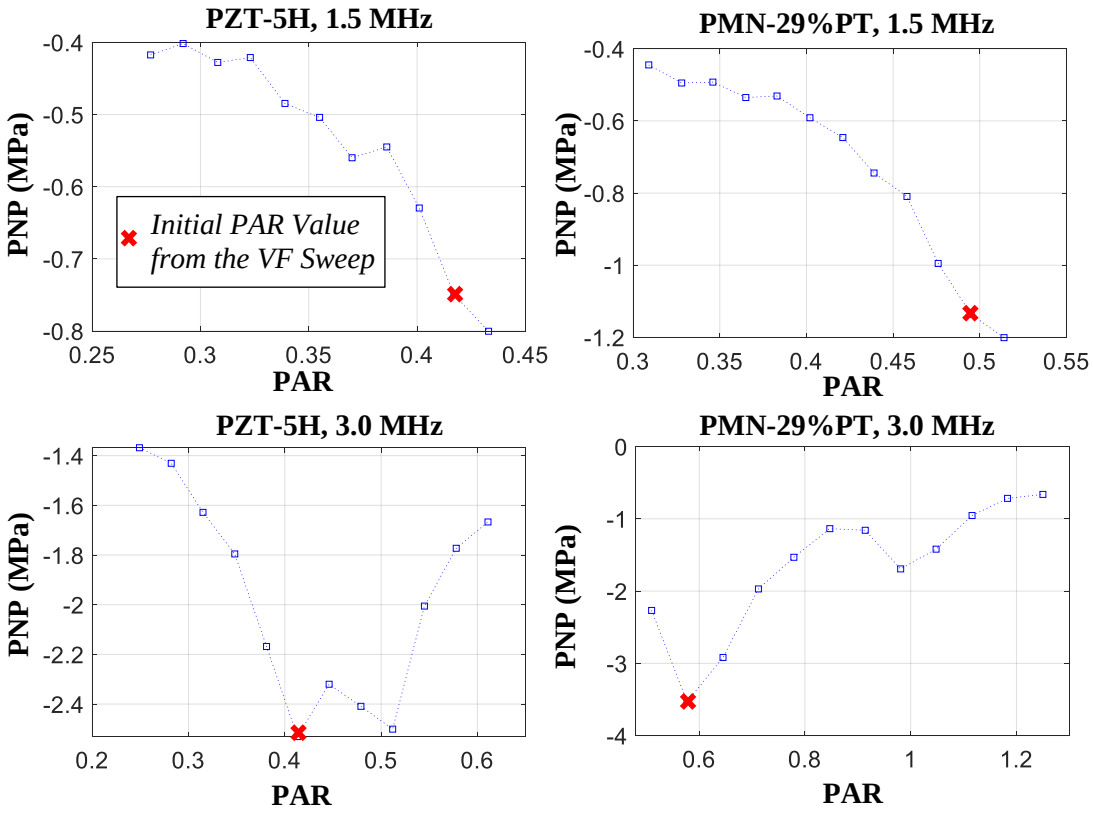

Figure 3-17 PNP at Focus as Function of PAR Sweep for all Four Arrays

3.5.4 Discussion on the Overall Outcomes of the Parametric Sweeps

As it can be seen from both Figure 3-15 and Figure 3-17, the PMN-29%PT arrays had better performance in terms of higher PNP at focus compared to the PZT-5H arrays. The main reason for this was the higher $\bar{k_t}$ of the single crystal-based composite compared to the piezoceramic one. From the impedance results of the FEA models (Figure 3-16), the PMN-29%PT transducers had $\bar{k_t} = 0.83$, and the PZT-5H had $\bar{k_t} = 0.65$. Another reason is the lower acoustic impedance of the PMN-29%PT piezocomposite material, which facilitated better matching with the water load. Considering all the outcomes of the *VF* and *PAR* sweeps, the final design and manufacturing parameters for the four types of 1-3 piezocomposite arrays are detailed in Table 3-6.

Table 3-6 Final Parameter Sets for the Four Types of Arrays Resulting from the Parametric Sweeps

Piezocomposite Properties				
Active Material	PZT-5H		PMN-29%PT	
Resonance Frequency (MHz)	1.5	3.0	1.5	3.0
Number of Array Elements	24	32	24	32
Polymer Material	Epofix			
VF	0.70	0.66	0.66	0.74
PAR	0.42	0.42	0.49	0.59
thk (μm)	983	487	700	362
Ideal W_{ke} (μm)	79.8	46.7	79.8	34.9
PP (μm)	488	250	426	250
$n_{pil,Y}$	5	10	6	10
$n_{pil,X}$	1	1	1	1
Array Parameters				
Array Pitch	0.49 λ	0.50 λ	0.43 λ	0.50 λ
Active Aperture (mm)	11.65	7.96	10.13	7.96
Passive Aperture (mm)	2.36	2.45	2.47	2.46

3.5.5 FEA Model Optimization and Size Reduction

FEA Model Optimization for the Parametric Sweep

Performing a VF sweep comprising 20 simulations of the 1-3 piezocomposite array in full-element configuration required 1-2 days on average to complete on a high-end workstation. This section describes the series of steps that were taken to reduce the computation time to a few hours and investigates their impact on the sweep outcomes and reliability.

The model size was firstly reduced by decreasing the array active aperture through a reduction in the number of array elements and, secondly, half and quarter symmetry were applied to the full-sized model. Normalized PNP values were employed instead of PNP magnitudes because the reduction in the array size affects the output of the modelled arrays. The purpose of the parametric sweep is to indicate the piezocomposite geometry that achieves the highest PNP at focus, but not to indicate the actual PNP value. Hence, this section focuses on determining whether a size reduction of the model can provide a similar trend in PNP with VF as the full-sized model, which is considered as the reference data in this study. Figure 3-18 shows the normalized PNP as function of VF for array models with different number of elements.

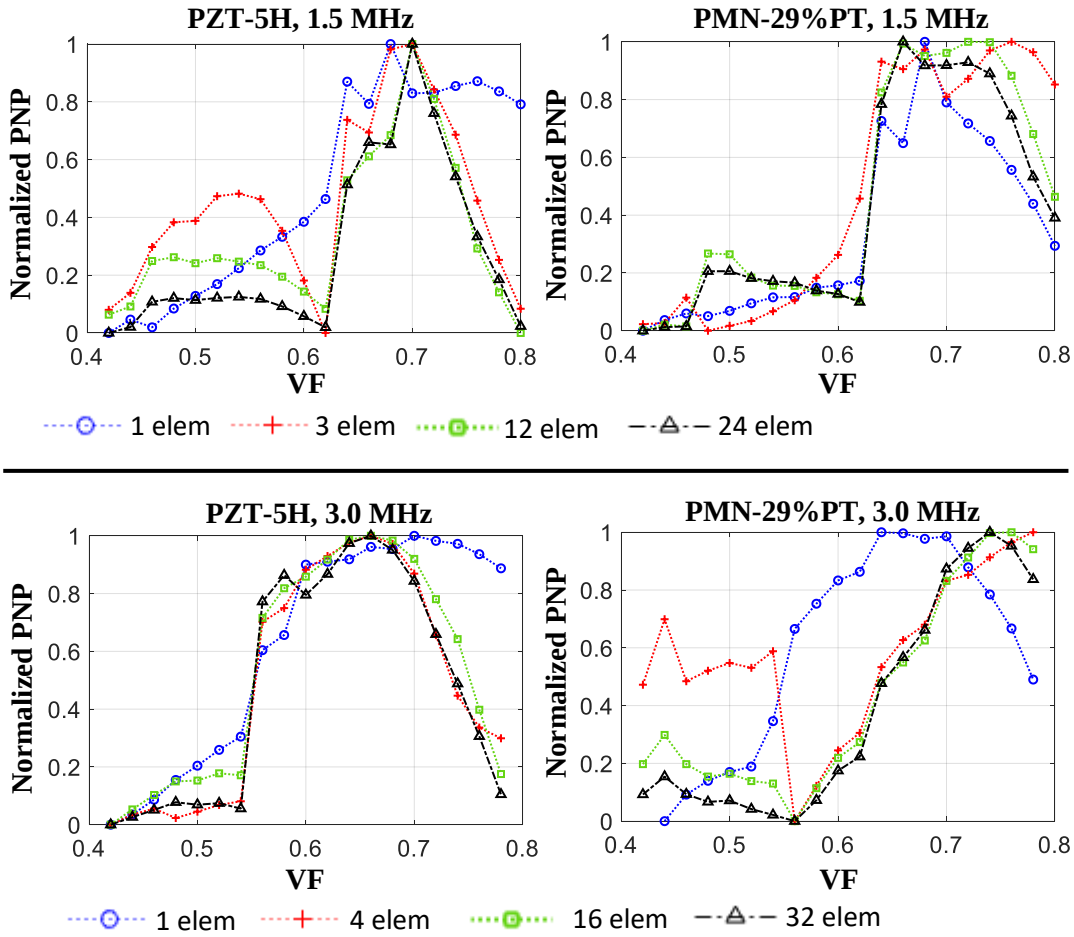

Figure 3-18 Normalized PNP at Focus as Function of VF for Various Number of Simulated Array Elements

For all four array types, it can be observed that models with half the number of array elements (12 elements in the case of 1.5 MHz arrays and 16 elements in the case of the 3.0 MHz arrays) achieved a very similar normalized PNP profile as function of VF as the full-sized models. Further decreasing the number of elements, degraded the sweep outcomes. However, for fast prototyping, evaluating even 1/8 of the total number of array elements could offer valuable insight into the performance of the piezocomposite geometry.

The only dataset that diverged excessively from the full-array configuration for all four evaluated array types was produced by the configuration with one simulated array element. The possible explanation is that the one element model did not consider any inter-pillar modes propagating in the direction of the array length and therefore, its output as function of *VF* was different than for an array configuration. Furthermore, the one element model was the only case in which focusing by phase delays was not implemented.

The VF sweeps of quarter and half symmetry models produced very similar normalized PNP plots compared to the reference full-sized, no symmetry models (Figure 3-19), which

demonstrates that symmetry can be reliably used in these types of sweeps to decrease model size and computation time. The model with half symmetry in array length (X direction) yielded the closest results with the full-sized model, while the model with half symmetry in array elevation (Y direction) deviated more from the reference at lower VFs. A possible explanation is that symmetry in Y direction interfered with the lateral modes occurring in the elevation direction of the 1-3 piezocomposite. The more pronounced discrepancy at lower VFs could be attributed to increased Lamb wave propagation due to higher ratios of the polymer phase. The quarter symmetry case (symmetry in both X and Y directions) combined the errors of both half-symmetry models and therefore had the highest discrepancy from the reference model.

The PNP magnitudes in the half-X symmetry model were approximately half of the ones provided by the full-sized model, yielding a linear relation between array size and PNP output.

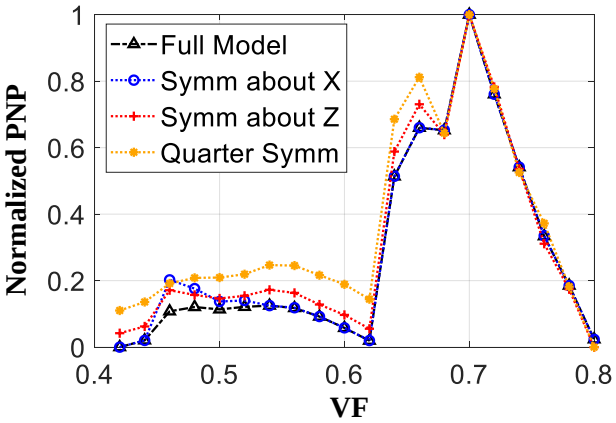

Figure 3-19 Effect of Model Symmetry on the VF Sweep Outcomes

Conversely, for half-Y and quarter symmetry, the ratio dropped below 1/2 and 1/4 respectively, with the linear relation no longer holding proportionally. It can be concluded that half symmetry in array length direction offered closer results to the full-scale model compared to the other symmetries, but, nevertheless, quarter symmetry can be reliable enough for fast prototyping, given the four-fold reduction in the model size.

FEA Model Optimization for Impedance Analysis of 1-3 Piezocomposite Phased Arrays

Several steps were taken to reduce computation time of the FEA model for electrical impedance analysis, and their impact on the impedance response of the array element was analysed and compared with the original full-sized model. For this study, the 1.5 MHz, PZT-5H array at VF = 0.7 was considered. In all simulations, the element assessed for electrical impedance was the central element in the modelled array provided the model had no symmetry applied (Figure 3-20 a.). If symmetry in the array length direction was used, then the element prior to the symmetry boundary of the FEA model was investigated (Figure 3-20 c.). All other

elements surrounding the element under test were not excited as in the full-sized impedance model.

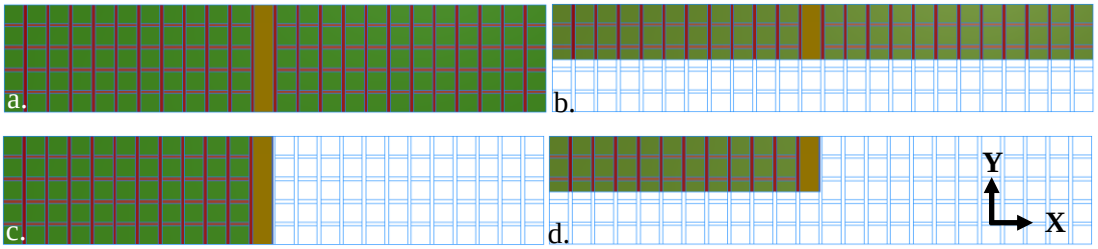

Figure 3-20 Render of Model for Impedance Analysis: a. One Element in Full Array Configuration; b. Half Symmetry in Y; c. Half Symmetry in X; d. Quarter Symmetry

Half symmetry in X direction reduced the element count from 24 to 12. Half symmetry in Y direction reduced the array elevation by a factor of two. Quarter symmetry in both directions reduced the model size by a factor of four. The impedance spectrum of the model with symmetry in X was identical with the full-sized model. The impedance spectrum from the quarter symmetry model was identical to the half symmetry in Y model, but less accurate than the full-sized model due to the presence of a parasitic mode at f_a which did not exist in the full-sized or X symmetry model. These results were in line with the observations made for the optimization of the parametric sweep program.

Subsequently, to further reduce model size, the number of array elements was then lowered to 12 and then 6 and quarter symmetry was applied. This led to a reduction in the model size by a factor of 8 for the 12 elements case and by a factor of 16 for the 6 elements case. Figure 3-21 shows a comparison of the impedance spectra of the three models. The figure shows there was a small difference in the impedance spectra between the reduced-size cases and the full-size model, with the highest degree of inaccuracy for the lower-frequency modes which were amplified in the reduced-size models. However, it is evident that the smaller-size models were useful in predicting f_r and f_a and with very small differences in the predicted coupling coefficient compared to the full-sized model.

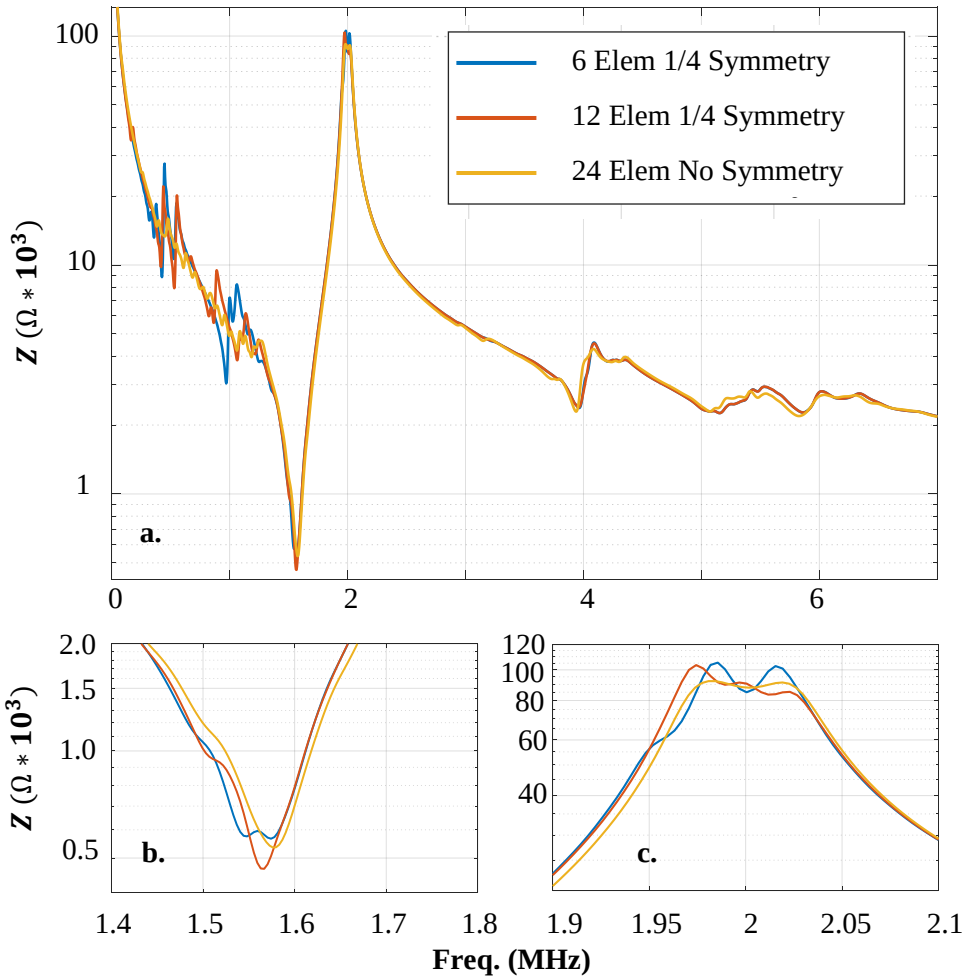

Figure 3-21 Effect of Symmetry and Reduction in Array Element Count on Electrical Impedance of an Individual Element in the 1.5 MHz, PZT-5H Array: a. Full Frequency Spectrum; b. Spectrum Close to f_R; c. Spectrum Close to f_a

Finally, the number of mesh elements per smallest array feature was varied from 2 to 4 (Figure 3-22 a.) and the X:Z mesh size ratio was changed from 1:3 to 1:2 and then to 1:1 (Figure 3-22 b.). The advantage of applying a coarser mesh and a larger X to Z ratio is reduced computation time, while the differences in the impedance spectrum are minimal at f_r and f_a. However, higher frequency modes were not simulated accurately because of the coarser meshes.

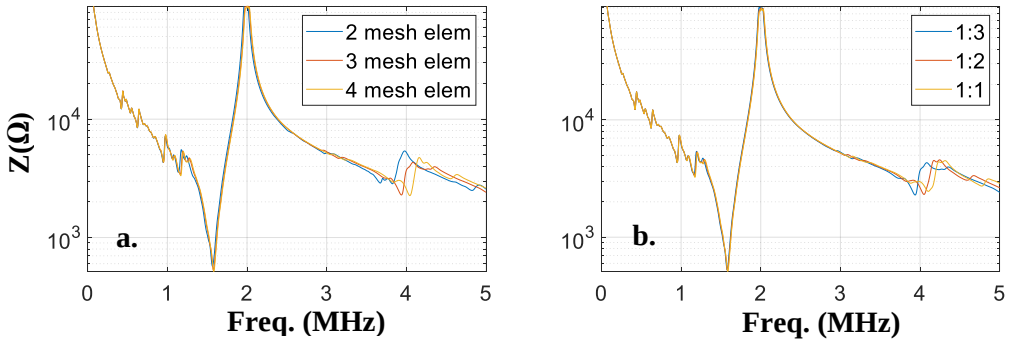

Figure 3-22 Effect of: a. Number of Mesh Elements; and b. Mesh X:Z Size Ratio on the Electrical Impedance Spectrum of the Transducer

3.6 Conclusions

Chapter 3 described the design procedure of miniature-sized therapeutic US phased arrays for intracorporeal sonoporation based on 1-3 piezocomposite materials and constrained by tight dimension limitations to fit inside an 8-Fr catheter (2.67 mm diameter). The prototyped arrays were designed for increased US transmission efficiency at resonance frequencies compatible with sonoporation (1.5 MHz and 3.0 MHz). The thickness of the active materials at the required resonance frequencies imposed strict limitations on the aperture of the arrays to maintain consistency with the catheter diameter.

To satisfy both the high efficiency requirement and the spatial constraints, a multiparametric sweep of VF and PAR was performed in order to obtain 1-3 piezocomposite array configurations that achieved the highest PNP at focus. Four array models were optimized with the multiparametric sweep method: two PZT-5H and two PMN- 29%PT arrays, with resonance frequencies of 1.5 MHz and 3.0 MHz. The multiparametric sweep was based on analytical calculations of the geometry parameters of the piezocomposite materials, performed in MATLAB and on an FEA model that simulated the resulting array prototype in OnScale.

The modelled array was coupled to a water load and was focused straight, at a distance within its near-field using phase delays. A combination of FEA and Kirchhoff time domain extrapolation was employed to evaluate the resulting pressure distribution achieved by the simulated phased array along an axial line stretching away from the centre of the array aperture into the depth of the load. PNP at the focal distance was extracted from the pressure data and was used as improvement output for the multiparametric sweep.

The VF sweep was run first and was followed by the PAR sweep. The PAR sweep provided only slight further improvements in PNP compared to the VF sweep for two out of four arrays. However, the changes following the *PAR* sweep for the two arrays were discarded because they led to higher grating lobes and a wider array elevation, with the improvement in PNP not being considered a sufficient advantage. Overall, a VF in the range {0.66 - 0.74} achieved the best results, which is in line with the literature for high power US transmission transducers. PAR values ranged between 0.4 and 0.6.

The results of the VF sweep were correlated with the electrical impedance of the modelled arrays, and the conclusion was that parasitic modes at or near resonance were the determinant factors that led to a decrease in the performance of the arrays at other VFs than the improved ones. The 1-3 piezocomposite geometry parameters and array lateral dimensions resulting

from the parametric sweeps were provided for all four types of prototyped arrays and will be used to fabricate devices for evaluation in the subsequent chapters.

Finally, a series of steps were evaluated in relation to a reduction in the FEA model size and computation time for the multiparametric sweep. The reliability of results produced by the smaller sized models was investigated in accordance with the reduction in computational demands on the workstation. It was found that for models with half symmetry in length direction, the normalized PNP trace of the VF sweep was almost identical to the reference (no symmetry) case, while providing a two-fold decrease in model size. Quarter symmetry was overall less accurate, but pointed to the same VF value as the full-size model, proving its usefulness in fast prototyping situations. Reducing the number of array elements for the VF sweep produced different outcomes than the reference model (which contained all elements), with the least impact, being for a 1/2 reduction in the element number. In terms of evaluating the electrical impedance of an element in the phased array model, a 1/4 reduction in the array element count combined with quarter symmetry offered a 16-fold decrease in model computation size, with little impact on the simulated impedance spectra at or near f_r and f_a compared to the one produced by the full-sized model.

4 Transducer Fabrication

4.1 Introduction

Chapter 4 describes the manufacturing process of the four miniature 1-3 connectivity piezocomposite, 1D phased arrays, designed and virtually prototyped in the previous chapter.

A high-level diagram of the manufacturing process described in this section is presented in Figure 4-1. While it is acknowledged that many of these processes are standard in piezoelectric transducer fabrication, it is considered that this Chapter is important from two key perspectives. First, it collates and provides high levels of detail on the associated piezocomposite fabrication processes to inform future researchers in this area. Secondly, and most importantly, it allows a clear understanding of the specific tweaks and alterations to the standard methodologies that had to be adapted in this work to successfully produce a series of miniature arrays for high power US delivery for sonoporation applications.

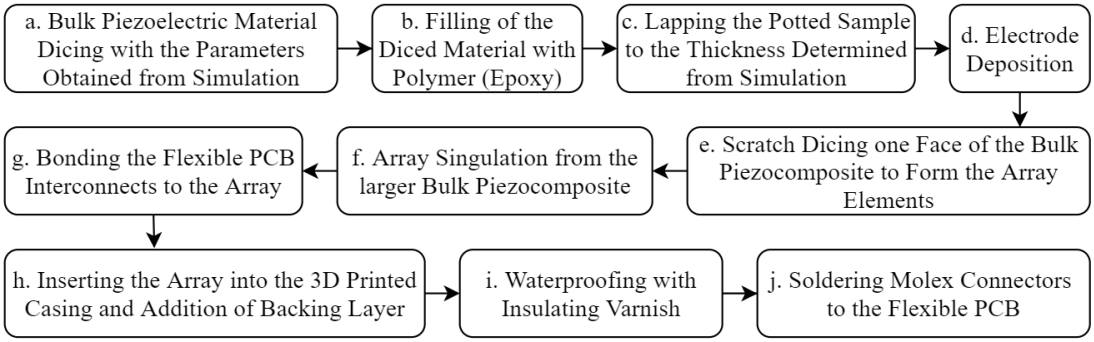

Figure 4-1 High Level Diagram of the Array Manufacturing Process

Piezocomposite materials were required for the development of the arrays and they were manufactured using well-established processes. In outline, the 1-3 piezocomposite materials were manufactured with the dice and fill technique from bulk piezoelectric wafers. The samples were then lapped to a thickness slightly larger than the value obtained through simulation in Section 3.5.4 in order to account for variations between the modelled and the real materials. Due to practical manufacturing constraints, the piezocomposite geometry of the arrays was slightly different from the model-derived dataset. Two parameters were mostly influenced: active material thickness, which was adjusted to maintain the resonance frequency of the piezoelectric materials close to the target values; and the kerf width, which depended on the dicing blade size and dicing saw accuracy.

Common methods for electroding piezoelectric materials such as thermal evaporation, sputtering or electron beam evaporation require complex equipment with purchase costs around or in excess of £50,000 and specialised training for new operators that can span over a

number of days. Additionally, the machine must be placed in a special clean room environment to avoid contamination with dust or other particles, which further increases the running costs of the equipment. This may not be an issue for industrial manufacturing of US transducers, however, it may become a limiting factor for small-scale research projects which lack the necessary equipment or funds. Therefore, a simpler and more cost-effective method of electrode deposition through spin coating of a commercially available two-part Ag ink compound, followed by elevated temperature curing was developed and evaluated. The procedure can be performed in any laboratory environment and only requires a spin coater machine, a temperature controlled oven and the ink compound, with a total estimated price around £5,000.

In order to avoid depoling the piezoelectric materials, the samples coated with the Ag ink were cured/dried in the oven at temperatures well below their phase transition thresholds, which importantly, were below the minimum curing temperatures stated by the ink manufacturer. Various spin coating parameters, curing temperatures and ink thinning ratios were evaluated in order to demonstrate the validity of the proposed electroding method and to increase the reproducibility and quality of the electrodes in relation to surface electrical resistivity, layer uniformity and layer thickness. The substrate chosen for the study, prior to coating the piezocomposite materials, was glass microscope slides. The electrodes applied with spin coating on glass slides were compared to a series of electrodes produced with the more widely used electrode deposition technique by thermal metal evaporation. Furthermore, the same Ag ink was applied on glass slides with a brush and with a series of different sized wire-bar (K-bar) coaters, and the resulting electrodes were also compared with the spin coated ones. The comparison evaluated electrode surface resistivity, layer uniformity and thickness, and its resistance to peeling from dicing machine tape used in the transducer manufacturing process. As the Ag ink spin coated electrodes were comparable with the thermally evaporated Ag electrodes, all experimental arrays were electroded using the developed spin coating method.

After both sides of the lapped piezocomposite materials were electroded by spin coating, the top electrode of each sample was scratch diced to form the phased array elements. Subsequently, the bulk, electroded 1-3 piezocomposite material was cut with the dicing saw (singulated) into the shape of the final array. Custom-designed flexible PCBs were bonded to the arrays and were then manipulated to fit inside 3-D printed casings. A backing material made of epoxy and air-filled microspheres was added to offer mechanical support for the arrays. Finally, the transducers were covered with a layer of varnish to ensure water ingress was impossible.

4.2 Materials and Equipment Used

The PZT-5H material (Ferroperm PZ29) was purchased from Meggitt Ferroperm™ (Meggitt A/S, Kvistgaard, Denmark), and had the following dimensions: 30 mm x 30 mm x 5 mm (length x width x thickness). The PMN-29%PT material was purchased from SICCAS (Shanghai Institute of Ceramics, Chinese Academy of Sciences, Shanghai, CN) and had the dimensions: 15 mm x 15 mm x 1 mm (length x width x thickness). The piezocomposite kerf filler was Epofix (Struers Inc., Cleveland, OH, US), chosen due to its reduced curing time and lower viscosity compared to softer polymers. Its increased flowability was essential because of the small interpillar spacing (as low as 28.5 μm).

As discussed in Section 3.4.1, the array models did not include the influence of a backing material in order to reduce the computation demands of the simulation. However, in the practical device, a backing layer was included to provide mechanical support for the active element, which was particularly important for ensuring its robustness. Furthermore, the backing material was chosen to maximise US transmission into the load by maximizing reverberations of the active element. This was primarily achieved by selecting a backing material with a much lower acoustic impedance than the piezocomposite, which increases US reflection at the active/backing material interface. Therefore, most of the US energy is reflected back into the piezoelectric element, rather than being absorbed into the backing layer as explained by Eq 2.7 and Eq 2.8. The choice of backing material was thus a mixture of air-filled microballoons and Epofix, with an acoustic impedance of $0.77*10^6$ kg/(m^2s). This value is approximately 25 times lower than the estimated impedance of the 1.5 MHz, PZT-5H piezocomposite and two times lower than the acoustic impedance of water (Section 3.3.7). Moreover, the proposed backing material has low acoustic damping (3.28 dB/cm measured at 1.0 MHz) compared to backing materials used in imaging transducers (Tungsten-loaded soft epoxy with an attenuation of 16 dB/cm at 1.0 MHz [3]), which further increases reverberations.

Transducer electroding was temporarily performed with Ag conductive paint (Agar Scientific Ltd, Essex, UK) during electrical impedance testing. Ag ink (118-09A/B119-44 - Creative Materials Inc., Ayer, MA, USA) was used for the final electrodes and was thinned with CMI 113-12 thinner (Creative Materials). Flexible PCB interconnects were bonded to the array with anisotropic conductive adhesive (ACA, 124-19A/B - Creative Materials), and the ground (GND) electrode was connected to the GND cable with Ag conductive epoxy (G3349 - Agar Scientific Ltd, Essex, UK).

Piezocomposite dicing was performed with a DISCO DAD3350 (DISCO, Tokyo, Japan) machine, with DISCO ZH-05 hub blades. Lapping of the materials was performed with a

Logitech PM5 machine (Logitech, Glasgow, UK), with sample thickness measurement and pressure force control via a Logitech precision jig. Off-machine thickness measurements were recorded at various points on the lapped samples with a contact measurement gauge (CG10, Logitech). Material curing was performed in a temperature controlled industrial oven (Heraeus Function Line Series - Thermo Fisher Scientific, MA, USA). Electrode deposition by spin coating was done with an Ossila spin coater machine (Ossila Ltd, Sheffield, UK). Au, Ag, Cu and Al evaporation as part of the electrode study were performed with a Thin Film Deposition System (E306, Edwards UK, West Sussex, UK).

4.3 Piezocomposite Machining

Many types of manufacturing processes have been developed for producing 1-3 and 2-2 connectivity piezocomposite materials, which include: dice and fill, rod placement, fibre insertion, ultrasonic or laser cutting, injection moulding, lost mould, co-extrusion, stacked plate, and lamination, as well as micromachining techniques for high frequency applications [203], [224]. The dice and fill technique, first reported in 1981 by Savakus et al. [225], became an important procedure in manufacturing of medical imaging transducers due to its simplicity and versatility [226]. The method relies on a series of parallel cuts performed through a bulk piezoelectric wafer with a dicing saw, in two perpendicular directions. The first cut direction produces a 2-2 connectivity piezoelectric material by separating long, parallel sheets of the material held in place by an uncut base. Rectangular section pillars are then formed by dicing parallel lines in the perpendicular direction [226]. The diced sample is backfilled with a polymer phase which offers support for the tall thin pillars after the uncut base is removed at a later stage. The composite kerf width is determined by the dicing blade width, which is restricted to a minimum of 10 µm - 15 µm, mostly limiting operating frequencies to below 20 MHz [224]. One advantage of the dice and fill technique compared to the majority of other machining techniques for the current project is that the piezocomposite materials do not require repoling after the procedure, provided the curing temperature for the polymer is below the threshold for the active material.

4.3.1 Dice and Fill Technique

The dice and fill process followed for manufacturing the 1D phased arrays presented in this chapter is described by the diagram in Figure 4-2.

Prior to dicing, the thickness of the piezoelectric wafer was measured with the precision contact gauge to determine material uniformity and the maximum thickness of the sample. This was a necessary step for determining the cut protrusion of the dicing blade. If one area of

the wafer had larger thickness than the blade protrusion, the material could be damaged, or the blade could break. Importantly, lapping of the bulk piezoelectric wafers before dicing was not required, because the uniformity measurements demonstrated that the samples were all produced with smooth, parallel faces, allowing maximal use of blade protrusion, and ensuring straight cuts.

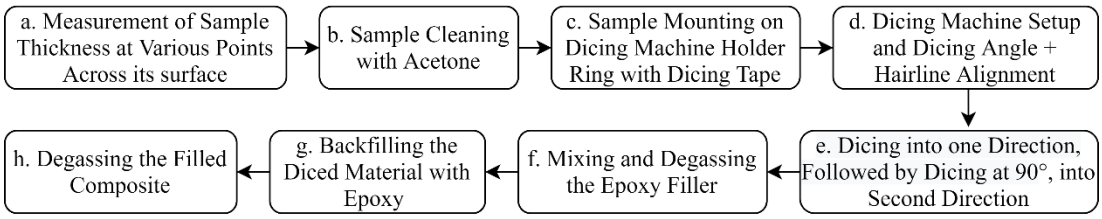

Figure 4-2 Dice and Fill Process Diagram

Sample Preparation and Mounting in the Dicing Machine

The piezoelectric wafer was first cleaned with acetone to remove any debris that could affect alignment in the dicing machine. Then, the dicing machine sample holder ring was covered with an adhesive film with low adhesion strength and the sample was mounted in the centre of the fixture on a stronger tape attached to the adhesive film (Figure 4-3). Any air bubbles trapped between the sample and the tape were eliminated to ensure correct levelling of the sample in the dicing machine.

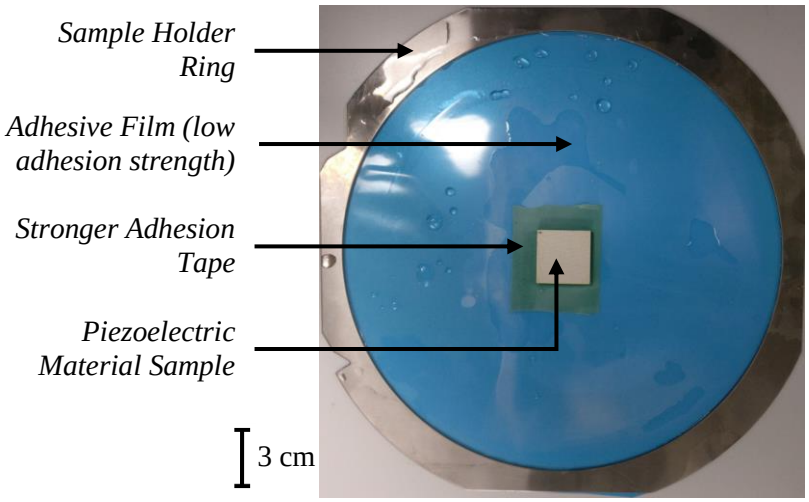

Figure 4-3 Mounting the Piezoelectric Wafer on the Dicing Machine Ring

Piezoelectric Material Dicing

The dicing machine included a control panel; a vacuum chuck table to hold the mounted sample; a spindle which rotated the dicing blade; and a water supply unit which was used to remove debris during cutting and to cool the blade (Figure 4-4).

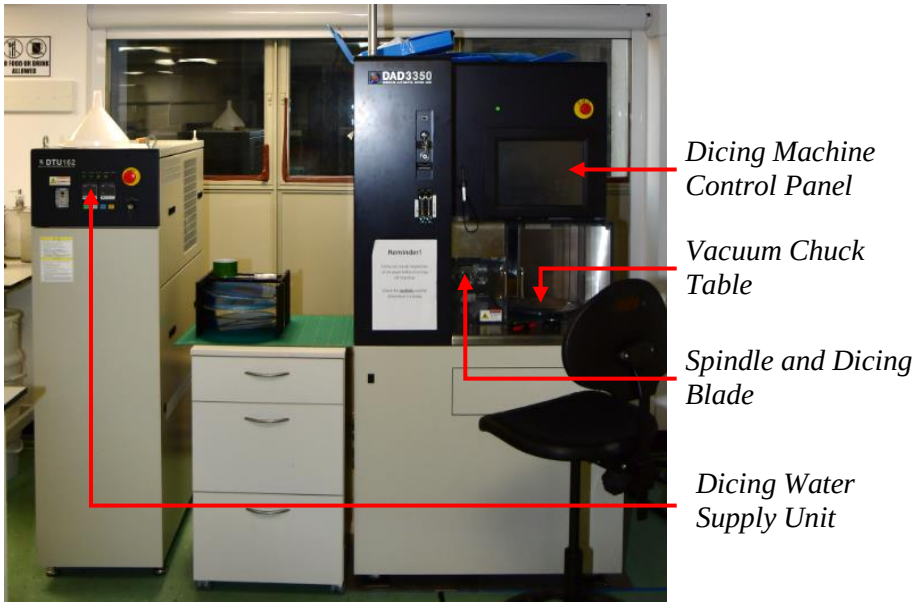

Figure 4-4 View of the Dicing Machine Constituent Parts

Dicing of the samples was performed after angle alignment, which ensured the dicing saw was cutting through the sample in the correct direction. Following the first cut, hairline alignment was performed to determine the precise position of the blade relative to the sample, as well as the cut (kerf) width. If the produced kerf was too wide compared to the blade specification, blade dressing was performed to restore its sharpness. If this process failed, the dicing blade was replaced with a new one.

The piezoceramic samples were diced with a blade feed speed (blade translation through the sample) of 0.5 mm/s, while the single crystal was diced at 0.2 mm/s. The feed speed was lowered for the single crystal samples in order to protect them from fracturing due to their increased fragility. Higher blade feed speeds lower the overall dicing time, but the force applied on the sample is larger than at lower speeds, which can lead to pillar breakage during dicing. Several trials were performed before dicing the piezoelectric materials in order to determine the optimum feed speeds, which were thus chosen as a compromise between overall dicing time and maintaining pillar integrity. Spindle revolution (blade rotation) speed was set to 35,000 RPM for the ceramic materials and to 20,000 RPM for the PMN-29%PT following previous findings from Dr Rachael McPhillips [227]. The choice considered that slow blade rotation speeds lead to larger forces on the blade and on the diced material when the blade is translated through the sample. Also, an excessively fast rotation can lead to blade oscillations, which can chip the workpiece or even lead to blade breakage. Subsequently, all samples were cut in two stages, by passing the blade through the same kerf twice: initially with half protrusion, and then at full protrusion. This technique was applied to avoid overstraining the diced material, especially for the second cut direction, in which 1-3 connectivity pillars were

cut from 2-2 geometry. Dicing in the second direction was performed without backfilling the first set of kerfs with polymer because the pillars were strong enough to withstand dicing in both directions without breaking. The blade protrusion was set to allow at least 150 µm of undiced wafer at the base of the pillars to confer mechanical support for the diced structure before the composite was backfilled with epoxy. Overall, the pillar integrity of the diced PZT-5H and PMN-P29%T samples approached 100%.

Composite Material Filling with the Polymer Phase

The completed workpiece was removed from the dicing machine ring holder by cutting a wider portion of the adhesive film to which the sample was attached. It was placed on a glass disc with the diced pillars facing upwards. Depending on the sample's lateral dimensions, one of two types of fixtures (Figure 4-5) was mounted on the glass disc surrounding the diced material and secured with silicone grease to stop polymer egress.

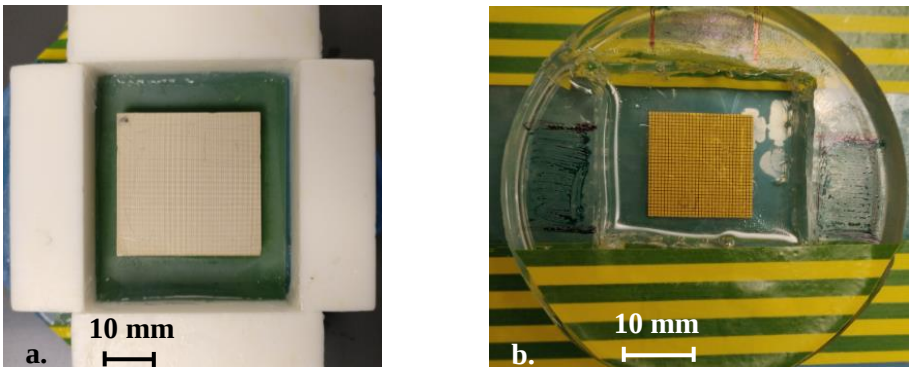

Figure 4-5 Fixtures Used for Filling the Diced Samples with Polymer: a. 3D Printed Blocks for Larger Samples; b. PDMS Fixture for Smaller Samples

Epofix was mixed with the weight ratio of 25 parts resin to 3 parts hardener in a beaker using a spatula. Care was taken to avoid introducing air bubbles into the mixture. The beaker was placed in an ultrasonic cleaner for 5 minutes to eliminate the majority of bubbles introduced into the compound during mixing. The mixture was then degassed in a vacuum chamber for 3 - 5 min. to further remove any remaining air bubbles. The degassed polymer was slowly poured into the diced sample, from a corner of the fixture. When poured from the corner, the liquid epoxy pushed the air between the pillars towards the other corner, trapping less air in the inter pillar spaces compared to when epoxy was poured directly on top of the sample. Polymer was poured in the mould until its level rose 3 – 5 mm above the top of the diced material surface, because air bubbles tended to gather in the top part of the compound. The filled composite was then degassed in the vacuum chamber for at least 10 min. to remove air bubbles trapped between the pillars. The entire filling and degassing process had to be done in less than 30 min. after polymer mixing, which is the pot life of Epofix. The filled sample was covered and left on a level surface for 24 hours to cure. Afterwards, it was placed in the

oven at 50°C for three hours to finalize the curing process. The fixtures and dicing tape were then removed and the sample was cleaned with acetone to eliminate any remaining adhesive from the tape or silicone grease from the fixture.

4.3.2 Lapping of the Piezocomposite Samples

The potted 1-3 piezocomposites were lapped with a Logitech PM5 machine which contains the following components (Figure 4-6): the rotating lapping plate; the abrasive feeder cylinder which delivers a slurry mix of abrasive powder and water onto the lapping plate; the lapping jig, which holds the sample glass carrier disc with vacuum; and the flatness monitor for the lapping plate. The sample is pressed on the extremely flat, rotating lapping plate with a controllable force by the jig. Lapping is performed by the friction between the sample and the revolving plate. The lapping procedure for the potted piezocomposite samples is described with the process diagram in Figure 4-7.

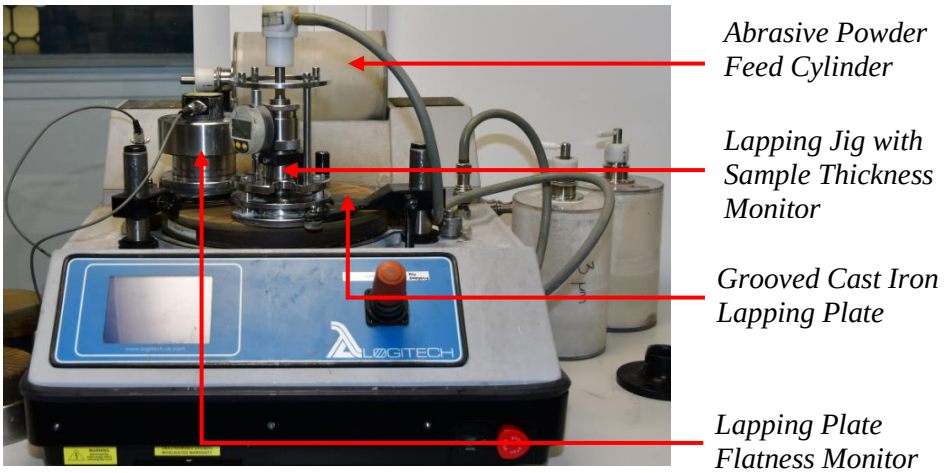

Figure 4-6 Lapping Machine Constitutive Components

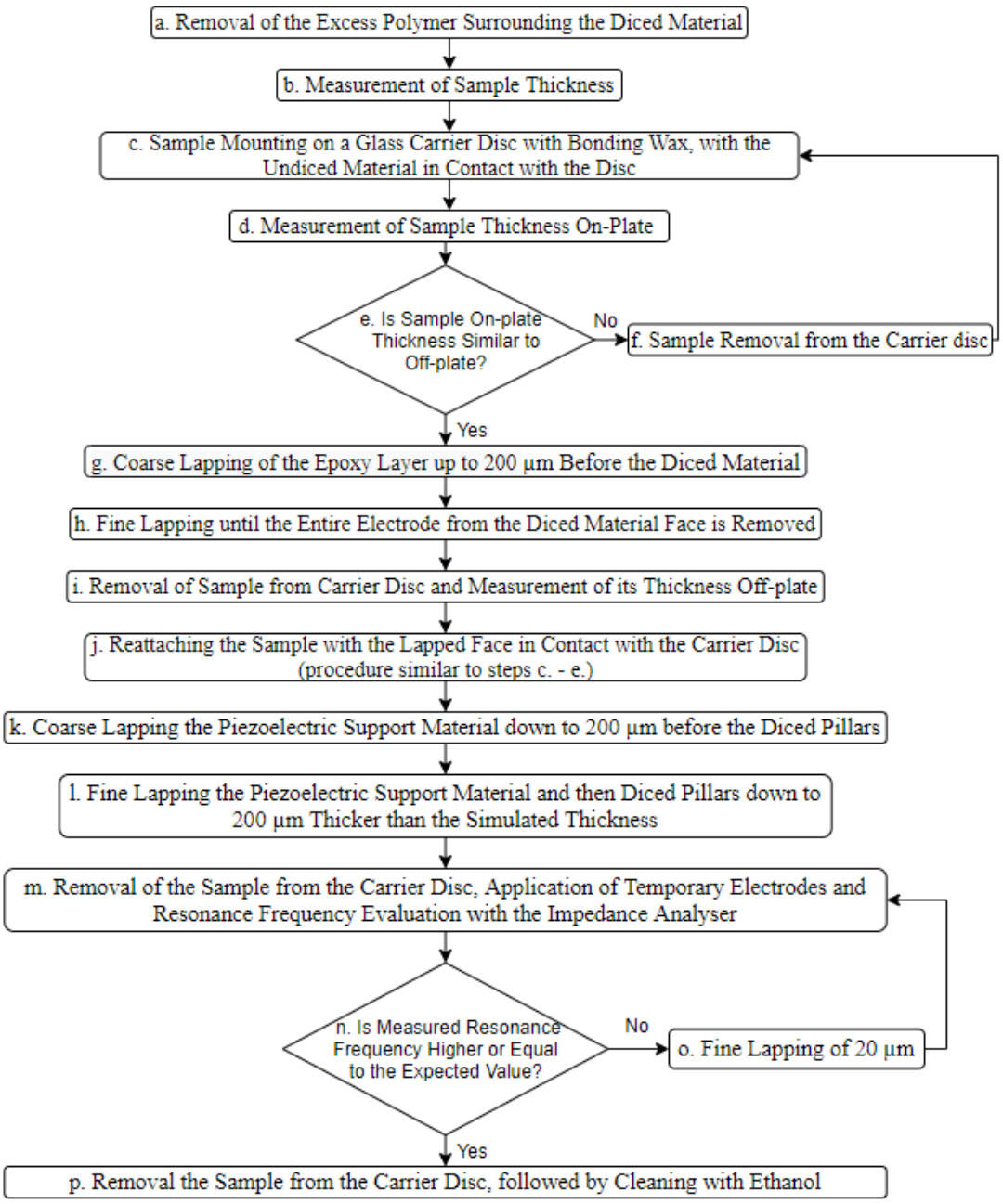

Figure 4-7 Lapping of the Filled 1-3 Piezocomposite Sample: Process Diagram

Before lapping, the excess polymer surrounding the sample was cut with a hand saw (Figure 4-8) in order to decrease lapping time by reducing the surface area of the material. The sample thickness was then measured with the contact gauge to determine the lapping thickness.

The samples were mounted on a glass carrier disc with low temperature bonding wax (Logitech, Glasgow, UK). As the melting temperature of the wax stated by the manufacturer was 50°C to 55°C, the carrier disc was preheated to 55°C on a hotplate before the sample was bonded to it. Higher wax melting temperatures were avoided in order to protect the

piezocomposite materials from unnecessary temperature strain. The sample was mounted on the carrier disc by hand and then fastened in place with a preheated spring-loaded press to ensure the composite material was level. The fixture was allowed to cool down to room temperature before the carrier disc with the sample attached was removed from the press. The composite material parallelism with the carrier disc was evaluated with the contact measurement gauge by comparing the on-plate with the off-plate sample thicknesses at various points on its surface. If any two measurements varied significantly, the composite material was removed and reattached to the carrier plate. The carrier disc was then attached to the vacuum holder of the lapping jig.

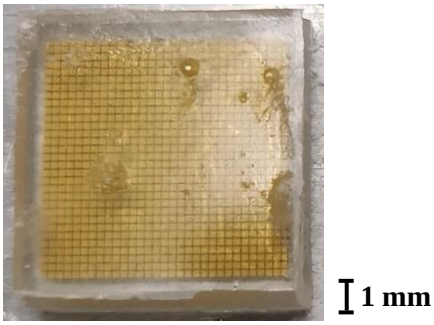

Figure 4-8 Potted Piezocomposite Sample (Top View)

Lapping of the sample always started with the excess polymer filler on top of the diced composite, while the support (undiced) piezoelectric wafer material on the bottom side of the sample was attached to the carrier plate. This was because the support material was flat, which allowed for a stronger bond with the glass carrier and better levelling of the sample due to the even surface of the base material. Coarse lapping of the excess polymer filler was performed with a grooved, radial, cast iron lapping plate (Logitech, Glasgow, UK), at 30 RPM, with 15 µm calcinated Al_2O_3 powder (Logitech, Glasgow, UK) used as abrasive. Coarse lapping was performed until the remaining layer of epoxy on top of the diced material was about 200 µm in thickness (Figure 4-9). At that point, the glass carrier plate was removed from the lapping jig and the sample thickness was measured with the contact gauge to ensure thickness uniformity and to confirm the thickness read by the lapping jig monitor was correct. The grooved plate was replaced with a radial glass plate (JMAC Technology Limited, Glasgow, UK) and 3 µm calcinated Al_2O_3 powder was used for finer lapping of the remaining layer of epoxy. The glass plate rotation speed was decreased from 20 RPM at maximum thickness to 5 RPM for the last few tens of microns left to lap.

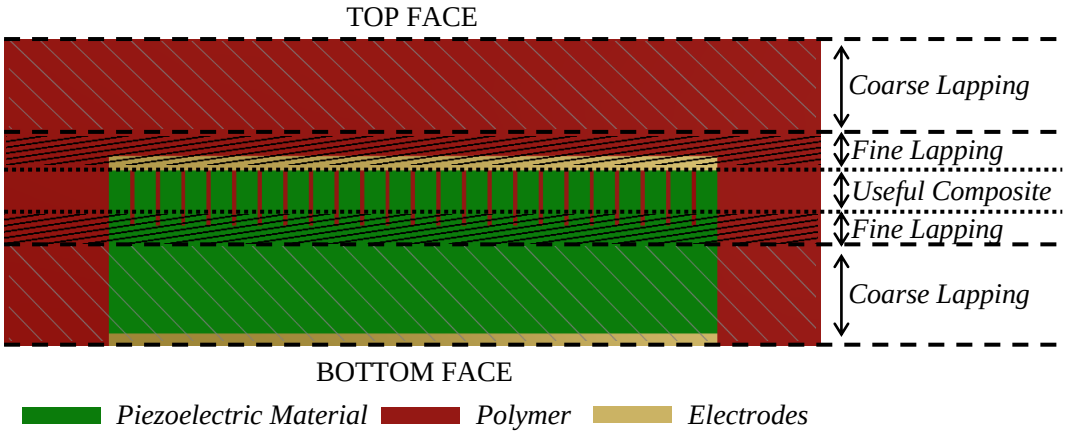

Figure 4-9 Schematic of Lapping Stages (Side View)

Fine lapping was performed until the entire electrode of the diced piezoelectric material was removed, which was an indication that all epoxy was lapped from the top sample face. During fine lapping, the carrier plate was removed from the lapping jig several times to visually inspect the electrode layer integrity and to measure sample thickness with the contact gauge. After the top face was successfully lapped, the composite material was turned over on the carrier plate and re-mounted with wax, with the undiced material facing the lapping plate. The bulk piezoceramic material was lapped up to 200 µm clearance before the diced pillars with the cast iron lapping plate and 15 µm abrasive powder. At this stage, the large 30 mm x 30 mm composite ceramic sample was cut with the dicing machine into approximately 15 mm x 10 mm pieces to allow for better control over the lapping process due to reduced surface area. The remaining 200 µm of the undiced ceramic and the excess thickness of the exposed pillars were lapped with the glass lapping plate and 3 µm abrasive powder for finer control of the procedure and to reduce material chipping. Both the undiced face and the extra thickness of the exposed pillars of the single crystal samples were lapped solely with the glass plate and 3 µm abrasive powder at lower rotation settings {15 RPM – 5 RPM} to reduce damage to the brittle material.

Considering that the thickness determined in Chapter 3 for the bulk piezocomposite materials was obtained with modelling, the simulated resonance was expected to differ slightly from the real material. Therefore, in order to ensure the composite materials were not overlapped, which is an irreversible process leading to higher resonance frequency than desired, the lapping process was halted when the diced material was ~200 µm thicker than the model. The sample was removed from the carrier plate, cleaned with ethanol, temporary Ag paint electrodes were applied to it, and its electrical impedance was measured. If the resonance frequency was too low, the sample was lapped a further few tens of microns and its impedance re-evaluated. The process was repeated until the required resonance frequency was attained. The manufactured

1.5 MHz, PZT-5H composite was on average 9.8% thicker (+90 µm) than the simulated material and the 1.5 MHz, PMN-29%PT was 15.8% thicker (+110 µm). The mean thickness of the fabricated 3.0 MHz, PZT-5H composite was 12.0% larger (+60 µm) than the modelled value, and the 3.0 MHz, PMN-29PT composite was 7.4% thicker (+30 µm) than in the simulation. The main reason for the difference in thickness between the experimental piezocomosites and the simulated ones is a mismatch in their coupling coefficients. The manufactured materials (evaluated in Section 5.4.1) have lower coupling coefficient than the modelled ones, which leads to an increased resonance frequency. Therefore, in order to reduce the resonance frequency to the desired value, the experimental piezocomposite materials had to be lapped at a larger thickness than predicted by simulation.

During lapping, it was observed that the majority of the air bubbles gathered in the excess epoxy layer on top of the diced material, which was removed through lapping. However, some bubbles also accumulated at the base of the diced material. This was caused by air trapped in the composite structure which could not escape due to the viscosity of the polymer.

4.3.3 1-3 Piezocomposite Parameters of the Manufactured Samples

Dicing blades with three different width intervals were selected to be within the requirements of the modelled array parameters described in Table 3-6. However, as the real widths of the purchased blades were slightly different from the model data, the geometry parameters of the composites were updated to reflect this change. Table 4-1 presents the updated piezocomposite array parameter set used for manufacturing all four types of arrays (in italic) and the measured parameter set following manufacturing (in bold). Both parameter sets are used to simulate the arrays and are cross evaluated in Chapter 5. The resonance frequency in Table 4-1 was determined with the impedance analyser on the bulk piezocomposite materials.

Table 4-1 Piezocomposite Array Geometry Parameter Set for all Four Manufactured Transducers (Values in Italic Are Ideal, Modelled Parameters; Values in Bold Are Real, Measured Parameters)

Piezocomposite Properties				
Active Material	PZT-5H		PMN-29%PT	
Resonance Frequency (MHz)	*1.50* | **1.53**	*3.0* | **3.07**	*1.50* | **1.57**	*3.0* | **3.23**
Polymer Material	Epofix			
VF	*0.70* | **0.71**	*0.70* | **0.73**	*0.72* | **0.72**	*0.78* | **0.78**
PAR	*0.42* | **0.39**	*0.42* | **0.39**	*0.58* | **0.50**	*0.59* | **0.55**
$thk\ (\mu m)$	*980* | **1070**	*492* | **551**	*717* | **830**	*372* | **402**
$W_{ke}\ (\mu m)$	*79.8* | **76.0**	*40.8* | **37.0**	*74.2* | **75.2**	*29.2* | **28.5**
$PP\ (\mu m)$	*489* | **489**	*250* | **249**	*490* | **490**	*250* | **250**
$n_{pil,Y}$	*5* | **5**	*10* | **10**	*5* | **5**	*10* | **10**
$n_{pil,X}$	*1* | **1**	*1* | **1**	*1* | **1**	*1* | **1**
Array Parameters				
Active Aperture (mm)	*11.7* | **11.7**	*7.95* | **7.94**	*11.7* | **11.7**	*7.97* | **7.97**
Passive Aperture (mm)	*2.36* | **2.37**	*2.46* | **2.46**	*2.37* | **2.37**	*2.47* | **2.47**

4.4 Electrode Deposition

Poling of the piezoelectric materials was avoided in the current work because of the procedural complexity and due to the possibility of avoiding the process. However, this imposed strict limitations on the temperatures to which the active materials could be exposed. PZT-5H piezocomposites were limited to a maximum temperature of 75°C to avoid softening of the polymer kerf filler, while the PMN-29%PT based composites were not allowed to exceed 50°C for prolonged time to avoid any detrimental effects in their structure.

4.4.1 Electrode Deposition Techniques

Electrodes applied to US transducers are expected to have low thickness ($<<\lambda$), which reduces the mass-damping effect on the active element, and low surface electrical resistivity, which minimizes ohmic losses and maximizes Q_M [228]. Various electrode deposition techniques are currently available, including: electron beam evaporation [229], sputtering [1] and thermal evaporation [230, Ch. 2], all of which rely on physical vapor deposition to create layers with thicknesses no higher than a few microns. Lift-off photolithography is another electrode deposition technique which employs image projection on a photoresist layer to create very fine electrodes [231]. Simpler electrode deposition approaches rely on coating with various techniques including brush painting, spin coating [232], and wire-bar coating [233].

The electrode material influences the mechanical loading of the transducer and the electrical surface resistivity. For example, Al has low resistivity and acoustic impedance, but its mechanical strength and adhesion to the sample are limited. Au has better adhesion and chemical resistance than Al, but its high density can affect transducer loading. Ag has lower resistivity, but poor corrosion resistance [228].

Ag ink coating was considered a valuable option in electroding the experimental therapeutic arrays presented in this chapter due to the simplicity of the process compared to vapor deposition or photolithography and due to good layer electrical conductivity. Merilampi et al. [234], reported that conductive layers produced with Ag ink had surface electrical resistivity in the range 0.04 - 0.13 Ω/sq. (sq. used as common abbreviation for square), which varied as function of curing temperature and time, while the lowest reported thickness of the coated layer was 12 μm.

The Ag ink used as part of this study was a two-part compound comprising the Ag ink and the hardener. Thinner was used to reduce the viscosity of the compound for a more even application. Three coating methods compatible with the Ag ink were evaluated and cross-compared on glass microscope slides: spin coating, brush painting and K-bar application. The Ag ink coatings were then compared with Au, Ag, Cu and Al electrodes deposited on glass slides through thermal evaporation under vacuum. The main parameter of interest was the surface electrical resistivity of the deposited layer. Layer thickness was also investigated for a reduced number of samples with the contact measurement gauge. The aim of the investigation was to determine the set of parameters that led to the production of a thin, even and smooth electrode, with a surface electrical resistivity lower than 1.0 Ω/sq.

4.4.2 Mixing and Preparation of the Ag Ink Compound for Coating

The two-part ink was mixed, on a glass disc with a spatula, with the weight ratio of 1 part Ag ink to 0.15 parts hardener, following manufacturer's specifications [235]. The compound was then spread over a larger area of the disc and degassed in a vacuum chamber for five minutes. The reason for spreading the mixture was to expose more of its surface, to facilitate degassing. It was observed that after one or two minutes under vacuum, some smaller air bubbles trapped in the substance burst; however, the majority coalesced in larger clusters which did not rupture readily (Figure 4-10 a.). In order to facilitate the process further, the vacuum pump was turned off midway through the procedure and air was allowed in the chamber at a fast rate. The chamber was then resealed and vacuum was reapplied for another 2.5 minutes. The change in pressure aided in the destruction of the majority of the larger air bubbles.

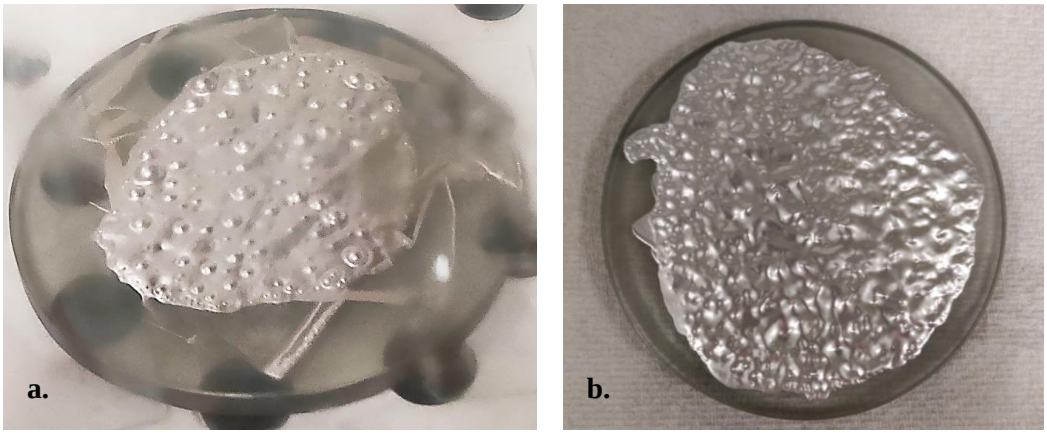

Figure 4-10 Degassing of the Mixed Ag Ink: a. In the Vacuum Chamber; b. After the Procedure

At this stage, thinner was mixed with the compound on the glass disc to make it more flowable and spreadable. The mixture was then degassed for 10 minutes, with at least four cycles of high-low pressure. A needle was used during the procedure to burst any large air bubbles that did not collapse. The resultant compound (Figure 4-10 b.) presented a series of cavities, but most of the air bubbles were removed. Degassing of the Ag ink compound was an important step in ensuring electrode continuity and smoothness.

Although the mixed Ag ink compound had an advertised pot life of four days, the addition of thinner reduced this drastically if left unsealed due the thinner volatility, which readily evaporated from the mix. Thus, after degassing, the ink was poured in 1.0 mL syringes, which were sealed afterwards. Following the application of the Ag ink on glass microscope slides, the samples were placed in a temperature-controlled oven at either 50°C or 75°C. According to manufacturer's specifications, the minimum curing temperature for the ink was 80°C, with a curing time of 4 hr. As 50°C is well below that limit, the samples were kept in the oven for a much longer period of time (i.e. 72 h) until the layer demonstrated satisfactory adhesion and low surface resistivity. The prolonged time in the oven and the 30°C lower temperature than recommended by the manufacturer for curing the compound indicate the Ag ink probably dried rather than become fully cured. However, investigation of the curing process for the Ag mix is beyond the scope of this Thesis and the satisfactory electrode properties obtained for the samples heated at 50°C were considered sufficient. The samples heated at 75°C were held in the oven for 4 hr, which was enough to cure the Ag ink and produce layers with suitable adhesion and low surface resistivity. This was due to the much lower difference in curing temperature compared to the manufacturer specification.

4.4.3 Electrode Coating with Ag Ink by Spin Coating

The Ag ink compound was introduced with the syringe onto the middle of a glass microscope slide, which was previously mounted in a levelled and calibrated spin coater machine. The

following process parameters were evaluated in relation to the electrical resistivity of the electrode: thinner to ink ratio, quantity of ink on the glass slide, rotation speed, spin time, and curing temperature. The amount of Ag ink was measured in terms of volume rather than weight, due to the simplicity of reading the syringe gradations, compared to evaluating the ink weight added to the spin coater machine. Table 4-2 presents the spin coating conditions evaluated for electrode deposition. Each condition was evaluated with at least three repeats. The exception was the 1000 rpm case, which had only one repetition per condition due to the insufficient ink spread and elevated thickness, rendering the layer not useful.

Table 4-2 Curing, Mixing and Spinning Parameters Evaluated for Electroding by Spin Coating

<table>
<tr><th>Curing Temp. (°C)</th><th>Curing Time (hr)</th><th>Ink – Thinner Weight Ratio</th><th>Ink on Slide (mL)</th><th>RPM (1000/min)</th><th>Spin Time (s)</th></tr>
<tr><td>50</td><td>72</td><td>100 : 4.35</td><td>0.06</td><td>1, 2, 3,4
6</td><td>10, 15, 25, 45
5, 10, 15, 35</td></tr>
<tr><td rowspan="4">75</td><td rowspan="4">4</td><td rowspan="2">100 : 4.35</td><td rowspan="2">0.06</td><td>1,2,3,4</td><td>10, 15, 25, 35, 45</td></tr>
<tr><td>6</td><td>5, 10, 15, 25, 35</td></tr>
<tr><td>0.01, 0.03</td><td>3</td><td>15</td></tr>
<tr><td>100 : 2.03
100 : 5.80
100 : 10.2</td><td>0.06</td><td>3</td><td>15</td></tr>
</table>

4.4.4 Electrode Application with Brush and K-bar

For all brush painting and K-bar test conditions, the ink to thinner ratio (by weight) was 100 : 4.35, while the amount of ink placed on the glass slide was 0.06 mL. The curing temperatures and times were the same as for spin coating. Four K-bars were used for the study, with the following wire diameters: 6 µm, 12 µm, 18 µm, 40 µm. At least three repeats were performed for each condition.

4.4.5 Electrode Deposition by Metal Evaporation

Four different metals were deposited with thermal evaporation onto glass microscope slides or Acetal sheets: Au, Ag, Cu, Al. For the first three metals, a 20 nm base layer of Cr was first evaporated on the slide to increase layer adhesion. One sample was coated with an 83.3 nm layer of Au, another sample with 220 nm of Au, and each of the Ag, Cu and Al electrodes had a thickness of 200 nm. The deposited layer thickness was measured during evaporation with a quartz crystal microbalance placed inside the machine. In order to remove any contaminants and to improve layer adhesion, the samples were cleaned with plasma discharge prior to the thermal deposition.

4.4.6 Surface Finish and Coverage Results

Spin coating was the most efficient procedure to apply Ag ink electrodes to the glass microscope slides compared to K-bar applicators or brush painting. The coating finish was reproducible, with its coverage and thickness depending on the concentration of mixed ink, amount of added thinner, rotation speed of the slide and spin time. Increasing the spin speed led to a thinner layer, while the spin time did not affect the layer thickness significantly. Figure 4-11 shows the thickness variation of the coated samples cured at 75°C as function of spin speed and time. The measurements were performed with the precision contact gauge at various spots on each sample. For the 50°C heated samples, the 3000 RPM, 15 s spin time condition produced an Ag ink layer of 4.71 µm thickness, with a standard deviation of 0.84 µm, similar to the condition evaluated at 75°C.

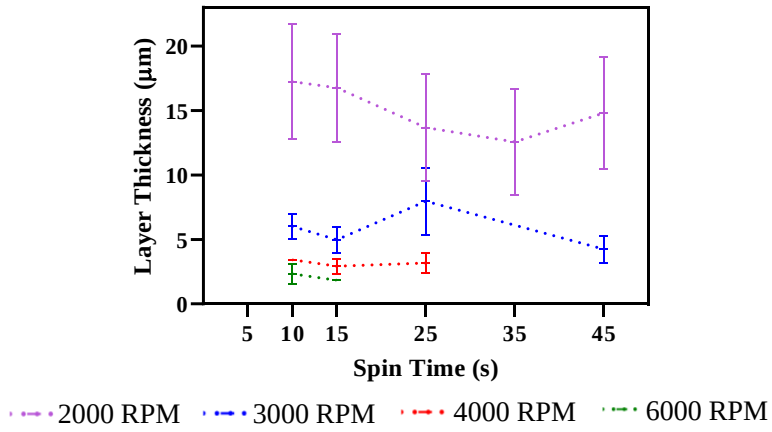

Figure 4-11 Average Ag Ink Layer Thickness as Function of Spin Time and Rotation Speed

In terms of layer uniformity, the ink produced a tiny blob at the slide's axis of rotation, and the highest layer thickness was also attained in the same region. Figure 4-12 a. depicts an example of an electrode deposited on the glass slide by spin-coating. It is worth mentioning that spin coating is limited to flat samples and cannot be used for electroding a cased array.

The brush painted layer was non-uniform in thickness (Figure 4-12 b.), which could lead to US beam scattering or unnecessary mechanical loading of the transducer. This issue was attributed to the increased viscosity of the Ag ink, even after being mixed with thinner, which hampered the process due to a non-even spread. However, the method was advantageous over spin coating for covering recessed corners or non-uniform surfaces that could not be coated by spinning and was considered effective for repairing any flaws in the ground electrode of the cased transducer.

The 40 µm K-bar coaters produced a layer with pronounced grooves (Figure 4-12 c.), while the finer K-bars produced a smoother layer (Figure 4-12 d.) but with grooves still visible. This coating method also relied on surface flatness for good electrode deposition. The layers

deposited by evaporation were uniform and had a tenfold lower thickness than the spin coated samples with Ag ink.

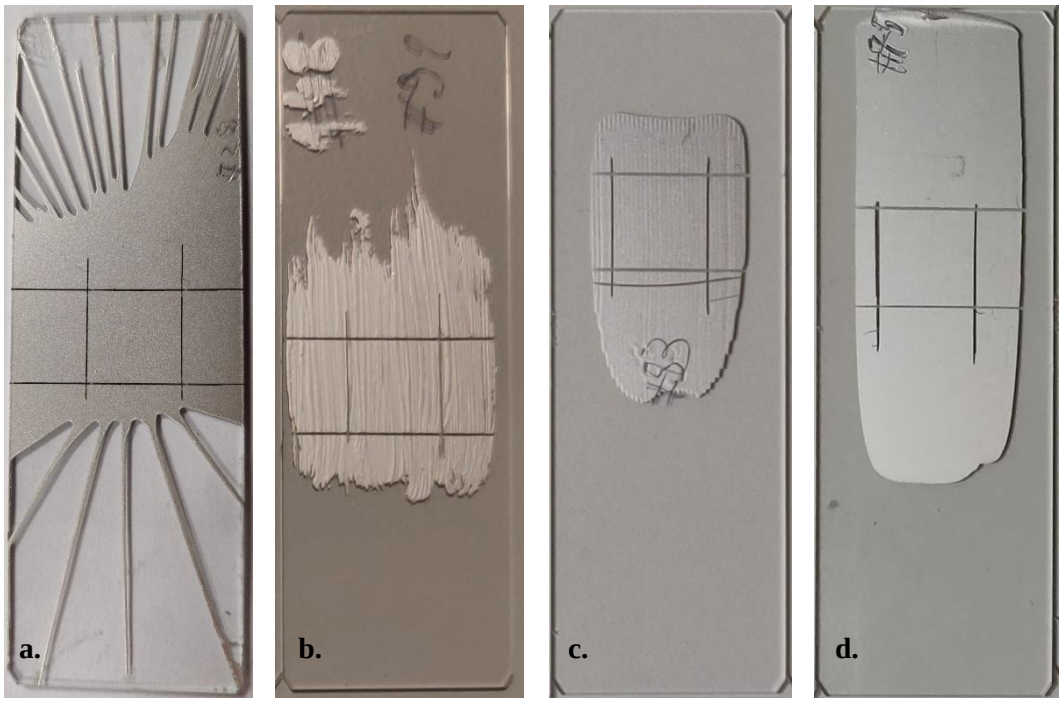

Figure 4-12 Ag Ink Applied Electrodes on Glass Microscope Slides by: a. Spin Coating; b. Brush Painting; c. 40 µm K-bar; d. 12 µm K-bar

In order to evaluate the electrode bond strength to the substrate, a number of spin coated samples from both curing temperature batches were subjected to a peel test with the dicing tape. This test was critically important because the piezocomposite samples would be fixed to the dicing tape for scratch dicing and array singulation after they had been electroded.

The electrode bond strength test was performed by attaching dicing tape to the surface of the spin coated glass slides, followed by the slow peeling of the tape from the samples, in a similar manner to removing the processed arrays from the dicing tape following scratch dicing and singulation. Both the 50°C and the 75°C cured Ag ink layers deposited on glass slides proved enhanced robustness to peeling from the dicing tape.

4.4.7 Electrode Layer Surface Resistivity Measurements

Electrical surface resistivity measurements of the deposited layers were performed with a custom-made, 3-D printed jig connected to a calibrated RLC meter (HM 8018 - Rhode & Schwartz, MD, USA). The surface resistivity of each sample was obtained by measuring the electrical resistance of a square (1 cm x 1 cm) piece of the electrode, singulated from the deposited Ag layer on the glass microscope slide (Figure 4-12). The surface resistivity is a useful measure of electrode surface resistance because it eliminates the effect of the electrode's

surface size, being expressed as Ω per sq. According to ASTM D4496-13 standard, surface resistivity can be expressed as [236]:

$$\rho_s = R_s \frac{W}{L} \qquad \text{Eq 4.1}$$

where ρ_s is the surface resistivity, R_s is the surface resistance measured with the meter, W is the layer width, and L is the layer length.

Surface resistivity measurements were performed with a custom-made contact probe containing two thin, 1 cm long Cu tracks, separated by a 1 cm gap. The two tracks were bonded to a flat glass microscope slide, which was attached to the 3-D printed jig with a four-spring system that ensured equal pressure applied to all samples. The two Cu tracks were connected to the RLC meter with a two-wire system (Figure 4-13). Prior to electrode measurements, the RLC meter and contact probe were calibrated with a thin 1 cm x 1 cm solid Cu block.

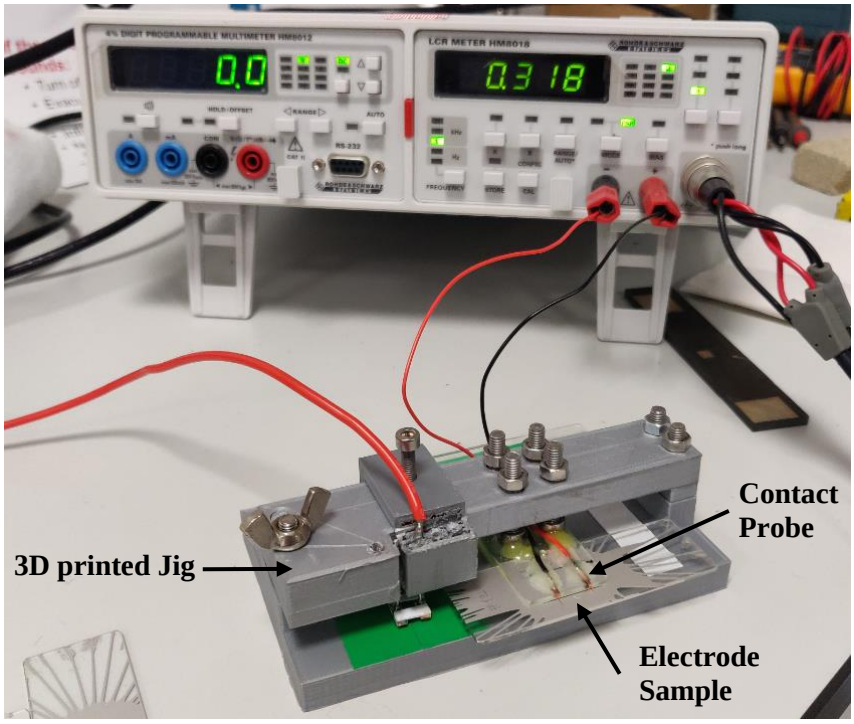

Figure 4-13 Measurement System for Surface Resistivity of Deposited Electrode

Surface resistivity measurements of the electrodes were performed three times over a period of a week after drying/curing: 30 minutes after the samples were removed from the oven, one day, and then 7 days after sample removal from the oven in order to evaluate the influence of time since drying/curing on the electrode resistivity.

Surface Resistivity of the Spin Coated Samples

The effect of spin time and rotation speed on the surface resistivity is presented in Figure 4-14 for both curing temperatures. The values were averaged for each sample over the three resistivity measurements performed at different times after curing. The plots show the rotation speed had greater influence than the spin time on the surface resistivity. Resistivity varied proportionally with the spin time only in the interval 5 - 15 s, while for longer spin times, ρ_s did not vary significantly from the value at 15 s. For both curing temperatures, it can be observed that the surface resistivity of the electrode increased with the rotation speed, which can be related to a decrease in the layer thickness. Lower spin speeds led to thicker layers, which inherently had lower resistivity.

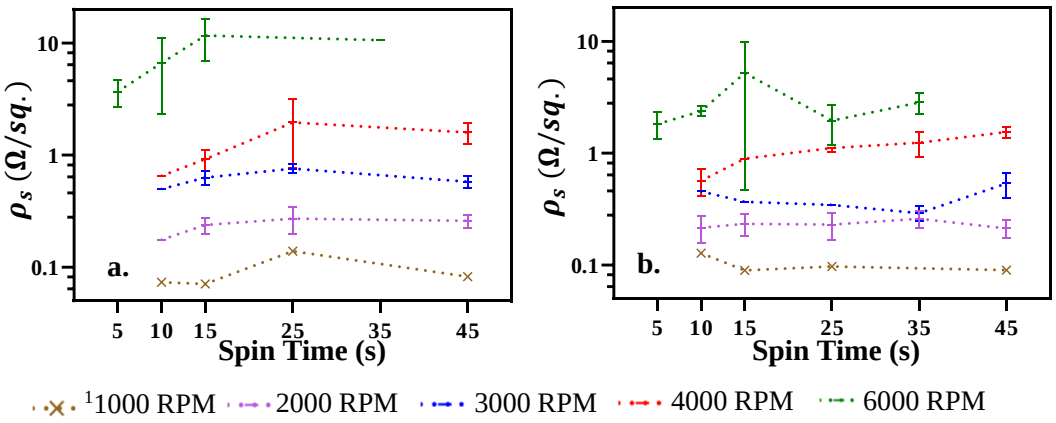

[1]*1000 RPM samples only evaluated with one repeat per condition*

Figure 4-14 Surface Resistivity of the Spin Coated Ag Ink Electrode as Function of Spin Time and Rotation Speed for Samples Cured at: a. 50°C; b. 75°C

The influence of the quantity of ink applied on the glass slide in relation to the surface resistivity is presented in Figure 4-15 a. The plot shows that resistivity does not vary significantly with the quantity of ink applied on the sample. ρ_s was slightly elevated for the 0.01 mL quantity because the amount of applied ink was very low and the electrode coverage was also significantly reduced. 0.06 mL was determined to be the lowest amount of ink that could entirely cover a 10 mm x 10 mm sample.

Adding thinner to the ink compound was important for decreasing the viscosity of the Ag ink, which allowed for more even and uniform coverage during spin coating. Figure 4-15 b. shows the thinner to ink weight ratio of 4.35 parts thinner to 100 parts ink achieved the lowest ρ_s. Higher concentrations of thinner led to higher ρ_s and thinner electrodes, which were related to lower viscosity of the spun material and to an increased spread of the Ag flakes within the thinned ink compound.

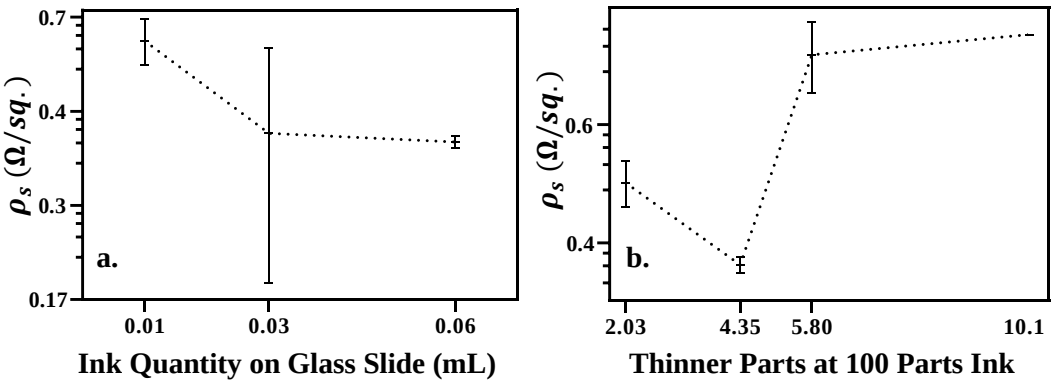

Figure 4-15 Surface Resistivity of the Spin Coated Ag Ink Electrode (Cured at 75°C) as Function of: a. Quantity of Ink on the Sample; b. Thinner to Ink Weight Ratio

Surface Resistivity of the Samples Coated Using the K-bars

The surface resistivity of the Ag ink layer applied with a K-bar coater on the glass slides varied inversely proportionally to the K-bar groove size and layer thickness (Figure 4-16). The resistivity values measured from the samples coated with the 12 µm, 18 µm and 40 µm K-bars were similar to the spin coated samples. The 6 µm K-bar produced a very thin layer of ink that was discontinuous and its electrical resistance could not be measured for either of the three samples cured at 50 °C and for two out of the three samples cured at 75°C.

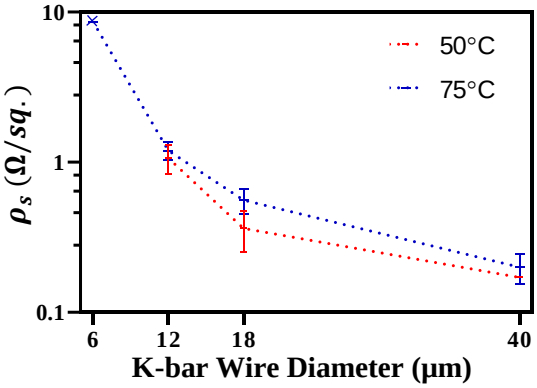

Figure 4-16 Surface Resistivity of the Spin Coated Ag Ink Electrode as Function of K-bar Wire Diameter

Surface Resistivity of the Samples Painted with the Brush

The average surface resistivity of the brush painted electrode across 12 samples cured at 75°C was 0.51 Ω/ sq., with a standard deviation of 0.25 Ω/ sq. One outlier was removed from this evaluation due to its large resistivity of 17.93 Ω/ sq. The average surface resistivity for the ink cured at 50°C, across 8 samples was 1.21 Ω/ sq. and the standard deviation 0.74 Ω/ sq. The higher surface resistivity at the lower curing temperature was associated with less efficient curing of the electrodes at that temperature. This effect was not as evident for the spin coated

samples because they had lower thickness and were more uniform, which allowed for more even sintering, even at the lower temperature setting.

Effect of Time Elapsed Since Curing on the Resistivity of the Ag Coated Samples

The decrease in ρ_s with time since curing was evaluated as the percentage ratio between the surface resistivity of a sample measured after one or 7 days since its removal from the oven and the resistivity measured 30 minutes after removal. An average value of the decrease in resistivity ($\overline{\rho_s}$) and its associated standard deviation (σ) was calculated over all samples coated with the same process (Table 4-3). Overall, the average surface resistivity of the electrodes ($\overline{\rho}$) deposited by spin coating decreased more after a week than after one day from removal from the oven, indicating that the ink compound continued to cure even after its removal from the oven. However, the standard deviation of the data was larger than the decrease in average resistivity for all evaluated cases.

Table 4-3 Effect of Elapsed Time Since High Temperature Curing on the Average Surface Resistivity ($\overline{\rho_s}$) of the Ag Ink Electrodes

Procedure	Cure Temp. (*C)	Initial $\overline{\rho_s}$ $(\Omega/sq.)$	One Day		7 Days	
			$\overline{\rho_s}$ (%)	σ (%)	$\overline{\rho_s}$ (%)	σ (%)
Spin Coating	50	2.14	-1.46	8.32	-8.22	10.1
	75	0.97	0.10	15.9	-5.81	20.2
K-Bar Application	50	0.61	-0.83	3.11	-10.3	13.4
	75	0.71	0.34	8.01	-7.09	7.21
Brush Painting	50	1.32	-12.3	15.5	-21.6	13.6
	75	0.56	-7.76	11.1	-24.4	18.8

Surface Resistivity of the Thermally Evaporated Samples

The 83.3 nm layer of Au had a surface resistivity of 1.77 Ω/ sq. and the 220 nm layer had a resistivity of 0.70 Ω/ sq. The Ag electrode presented the lowest surface resistivity of all evaporated metals at 0.10 Ω/ sq., the Cu electrode had a resistivity of 0.30 Ω/ sq., and the Al electrode had 0.75 Ω/ sq.

4.4.8 Comparison of Electrode Deposition Methods

The electrode coated with Ag ink at a spin speed of 2000 RPM for 15 s was 2.4 times thicker than the electrode produced by spinning at 3000 RPM for 15 s, while the surface resistivity was similar in the two cases (0.23 Ω/ sq. at 2000 RPM and 0.37 Ω/ sq. at 2000 RPM). For higher rotation speeds than 3000 RPM, the surface resistivity increased (Figure 4-14), and the decrease in thickness was less significant (Figure 4-11). Considering both of the above

arguments, 3000 RPM was regarded the most suitable spin rotation for transducer coating. Furthermore, as shown in Figure 4-11 and Figure 4-14, the spin time did not influence the layer thickness and surface resistivity significantly, and 15 s was considered a suitable value.

The thermally evaporated layers had the smoothest surface finish and the lowest thickness. However, spin coating produced comparably smooth layers, but their average thickness (4.84 μm) was an order of magnitude higher than the evaporated electrodes. This did not represent an issue for the arrays developed in this Thesis as $\lambda >> 4.84$ μm at their resonance frequency. The Ag electrode deposited through thermal evaporation had an average surface resistivity of 0.1 Ω/ sq., comparable to the 0.37 Ω/ sq. average surface resistivity of the electrode produced by spin coating Ag ink at 3000 RPM for 15 s, followed by curing at 75°C for 4 hours. The surface resistivity of the samples spin coated with Ag ink at the same rotation speed and time setting as previous, but cured at 50°C for 72 hours was elevated, with an average value of 0.64 Ω/ sq.

The finer K-bars (6 μm and 12 μm) produced smoother and thinner surfaces than the larger ones (18 μm and 40 μm), but grooves were present in all coated samples, making the surface finish of the electrodes rougher than of the spin coated layers. Furthermore, the average surface resistivity of the samples coated with the finer K-bars was larger than of the spin coated electrodes. Brush application of Ag ink produced the most uneven surface finish and had the largest deviation in surface resistivity compared to the other coating methods evaluated in this section.

Considering the arguments above, spin coating was regarded a more effective approach for electroding the experimental piezocomposite materials than using K-bars or brush coating. Furthermore, the spin coated electrodes were comparable in terms of surface resistivity and layer smoothness (upon visual inspection under optical microscopy) with the thermally evaporated ones, which were considered the reference standard. In view of the lower procedure cost and increased simplicity compared to thermal evaporation, all arrays developed in this Thesis were electroded by spin coating Ag ink.

The selected process parameters for spin coating were: rotation speed of 3000 RPM, for 15 s, with at least 0.06 mL of ink, and with an ink to thinner weight ratio of 100 : 4.35. Following spin coating, the PZT-5H composite materials were cured at 75°C for 4 hours and the PMN-29%PT samples were cured at 50°C for 72 hours. Any retouches to the front electrode of the assembled arrays were also performed with Ag ink, but applied with a brush.

4.4.9 Piezocomposite Material Coating with Ag Ink

Piezocomposite Sample Preparation for Coating

Prior to coating, the piezocomposite material was cleaned of the previous Ag paint electrode used for electrical impedance evaluation with a lint-free tissue soaked in acetone. The sample was then dipped in a container filled with acetone, which was placed in an ultrasonic cleaning bath for 15 s. The material was then dried with a lint-free tissue, then dipped in a container filled with ethanol and placed in the ultrasonic cleaner for 45 s. The sample was dried again and then placed in a container filled with DI water and kept in the ultrasonic cleaner for 3 min. The piezocomposite material was wiped with a lint free cloth and allowed to dry in a dust-free enclosure for one day prior to coating.

Piezocomposite Sample Coating

Afterwards, the sample was secured to a clean glass slide with temperature resistant PVC tape, and the slide was placed in the spin coater. Using a syringe, 0.1 mL of the thinned Ag ink mixture was introduced onto the material to cover a wider region of its surface (Figure 4-17). The spin coater was set to 3000 rpm and 15 s spin time. Following transducer coating, one or two other glass slides were coated with the same Ag ink mixture and the same spin coating parameters for control. The piezocomposite samples were then placed in the oven and allowed to cure with the temperature and time parameters corresponding to the type of active material. The coating process was repeated for the other side of the sample.

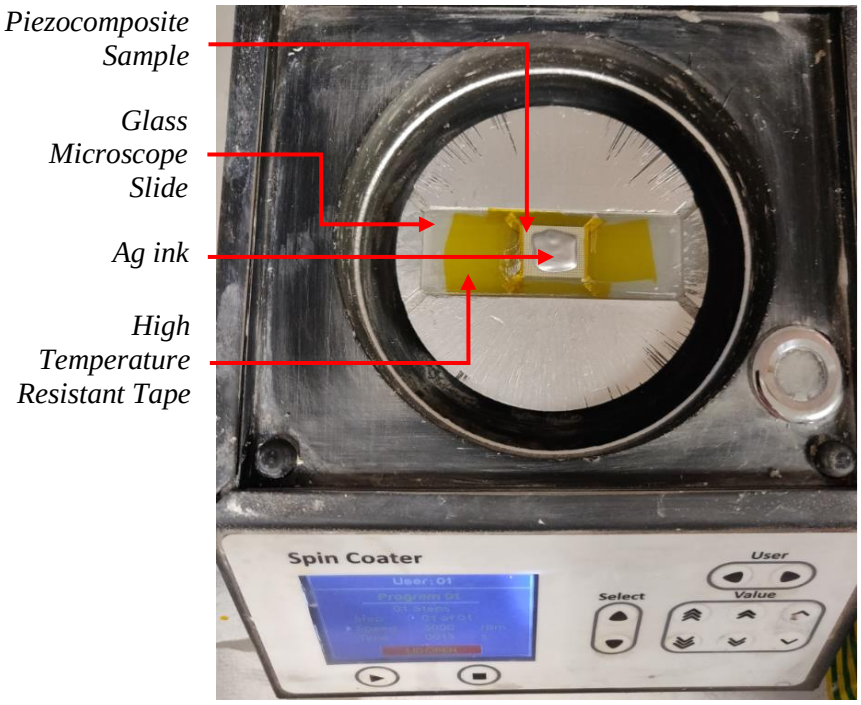

Figure 4-17 Electroding the Piezocomposite Material by Spin Coating with Ag Ink

4.4.10 Scratch Dicing and Array Singulation

Scratch Dicing of the Array Elements

After the sample was coated with Ag ink on both sides, one of its faces was scratch diced in order to separate the array elements. The entire bulk piezocomposite material workpiece was scratch diced in one direction prior to being singulated into several transducers. The same blade was employed for this process as the one used for initial dicing of the bulk piezoelectric wafers because the array elements had the same width as the piezoelectric pillars and were separated by the same kerfs.

Before being mounted on the dicing tape, the coated sample thickness was measured at various spots on its surface with the contact gauge. The initial blade protrusion for scratch dicing was set to 10 µm from the highest measured thickness value and the entire sample was diced. Due to slight thickness variations of the sample, it was common to find several regions which were not scratch diced during the initial run upon inspection with the machine's microscope. Without altering the saw's alignment, the blade protrusion was increased by 5 µm and scratch dicing was restricted to the areas which could not be diced in the previous run. The process was repeated until all the bulk piezocomposite material was scratch diced.

Upon inspection of the first scratch diced sample, it was observed that air bubbles trapped in the polymer phase were coated on the inside with Ag ink (Figure 4-18 a-b.). Scratch dicing did not break the inter-element connection created by some larger air bubbles because the blade protrusion was smaller than the bubble depth. An evaluation of the lateral section of the piezocomposite materials revealed that most air bubbles in the polymer filler accumulated at the bottom side of the samples. Therefore, instead of increasing the protrusion depth of scratch dicing to break the inter-element short circuits caused by the coated air bubbles, which could affect the piezocomposite integrity, the problem was mostly mitigated by scratch dicing the array elements on the top side of the sample, which had less or no air pockets.

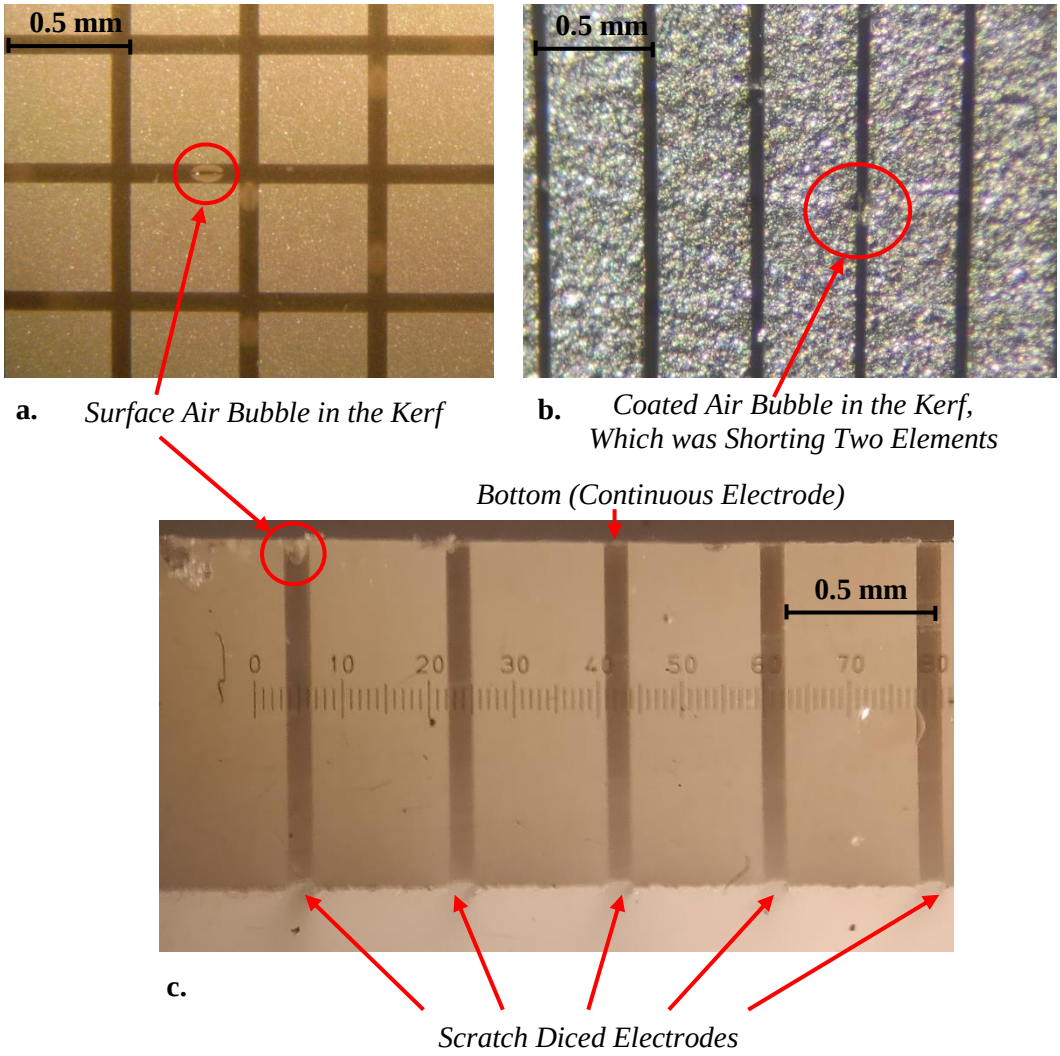

Figure 4-18 Inter-element Short Circuit Produced by a Coated Surface Air Bubble in the Kerf Filler: a. Surface Air Bubble in the Unelectroded Piezocomposite (Top View); b. Air Bubble Coated with Ag Ink (Top View); c. Bubble Protrusion in Side View

Array Singulation

Array singulation was performed with the dicing machine. The transducer was placed with the ground electrode (the continuous electrode side of the material, which was not scratch diced) in contact with the adhesive tape of the holder ring. The blade protrusion was set to 10 µm deeper than the thickness of the sample, which was measured before the application of the Ag ink electrodes. This step carried the risk of damaging the dicing machine chuck table if the blade was lowered too much. However, the total clearance from the array bottom to the chuck table was 135 µm, due to the combined thickness of the two adhesive tapes holding the sample, which reduced the risk to an acceptable level. Examples of singulated arrays are presented in Figure 4-19.

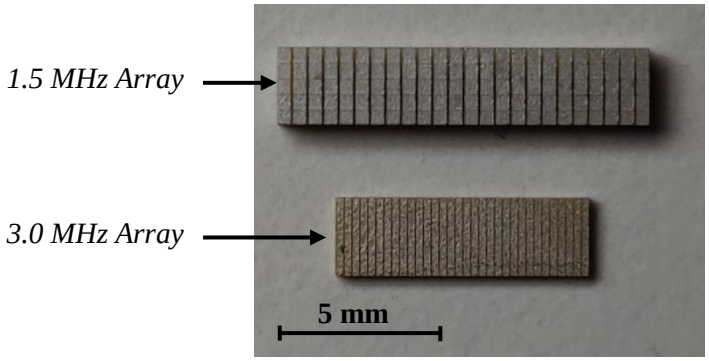

Figure 4-19 Singulated Arrays

Removal of the Singulated Arrays from the Dicing Tape

Removing the array from the dicing tape had the potential to destroy the transducer back electrode. The electrodes deposited on the PZT-5H piezocomposite materials were much stronger than the ones deposited on the single-crystal composite and resisted well from peeling off the dicing tape. Removing the PMN-29%PT samples from the dicing tape, however, led to electrode damage (Figure 4-20) when the action was performed under room-temperature conditions, contrary to the test results obtained with the coated glass microscope slides (Section 4.4.6). This was attributed to the much lower Ag ink curing temperature (50°C) than the minimum recommended by the manufacturer (80°C), and to the reduced adhesion of the Ag ink to the single crystal material compared to the glass slides.

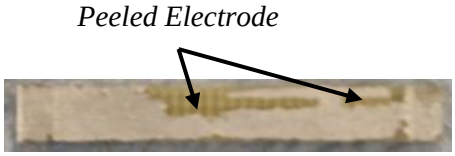

Figure 4-20 Electrode Detached from a PMN-29%PT Sample as a Result of Removal from the Dicing Tape

The solution that offered the best outcome in terms of electrode preservation was to detach the singulated PMN-29%PT arrays slowly from the dicing tape while pouring water at ~45°C, mixed with 20% ethanol (by weight ratio) over the tape. Concentrated solvents were avoided due to the risk of chemically attacking the deposited electrodes.

Inter-element Short Circuit Detection

In order to ensure no short circuits between array elements were present, adjacent electrodes were tested under the microscope for continuity with two fine wires connected to a multimeter. Any eventual short circuit was removed with a fine needle (Figure 4-21).

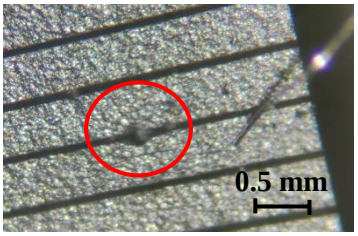

Figure 4-21 Inter-element Short Circuit Mitigation

4.5 Array Interconnects

The ground electrode of the array, which was continuous over the entire transducer face, was chosen as the front element for electrical safety (in line with Section 2.9.1) and simpler bonding to only one ground wire. The array elements were individually controlled through a flexible PCB connector, bonded to the scratch diced electrodes on the back face of the device.

4.5.1 Design of the Flexible Array Interconnects

The array interconnects were designed with Autodesk Eagle (Autodesk, CA, USA) and manufactured externally. The flexible polyimide substrate had a thickness of 130 µm, and the 35 µm thick Cu traces were plated with a 0.03 µm Au layer through electroless Ni immersion. Two flexible PCB designs were manufactured for the four types of arrays because the devices with the same resonance frequency had the same element pitch. The flexible circuits (Figure 4-22 a.) comprised a bonding area, with 24 parallel pads at 490 µm pitch for the 1.5 MHz arrays and with 32 parallel pads at 250 µm pitch for the 3.0 MHz arrays. The width of the pads was set to 125 µm to leave sufficient inter-element clearance. The pads were connected to two 34 way, 1.54 mm pitch Molex connectors soldered on the flexible PCB via independent traces on the top face of the PCB. The Molex plugs ensured easy connection with cables from the phased array controller. The bottom face of the flexible PCB was fully coated with Cu and was connected to the electrical ground (Figure 4-22 b.).

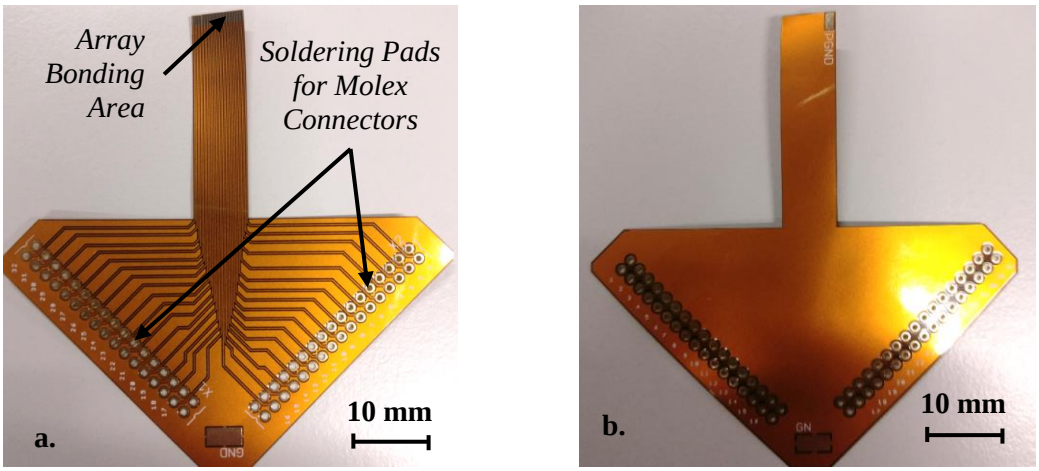

Figure 4-22 Flexible PCBs for Bonding to the 3.0 MHz Arrays: a. Top Face (Bonding Side); b. Bottom Face (GND Layer)

The flexi connectors for the 3.0 MHz arrays were manufactured first, and presented a flaw related to the ground layer on the back face spanning over the bonding area with the array. The added stiffness of the Cu electrode mechanically loaded the array unnecessarily and it also impaired flexi alignment with the array elements. The problem was mitigated without reordering new flexis by completely lapping the Cu electrode from the back face of the PCB with the radial glass plate and 3 µm fused Al_2O_3 powder. An image of the resultant flexi array bonding area is presented in Figure 4-24 b. The flexible PCBs for the 1.5 MHz arrays were designed without a ground electrode coinciding with the array bonding area and did not require lapping.

4.5.2 Bonding the Interconnects to the Array

Flexi PCB Positioning Jig

As the alignment of the flexi PCB pads in the centre of the array elements had too fine a scale to be performed by hand, a custom-built positioning jig was designed to aid in the process (Figure 4-23 a-b.).

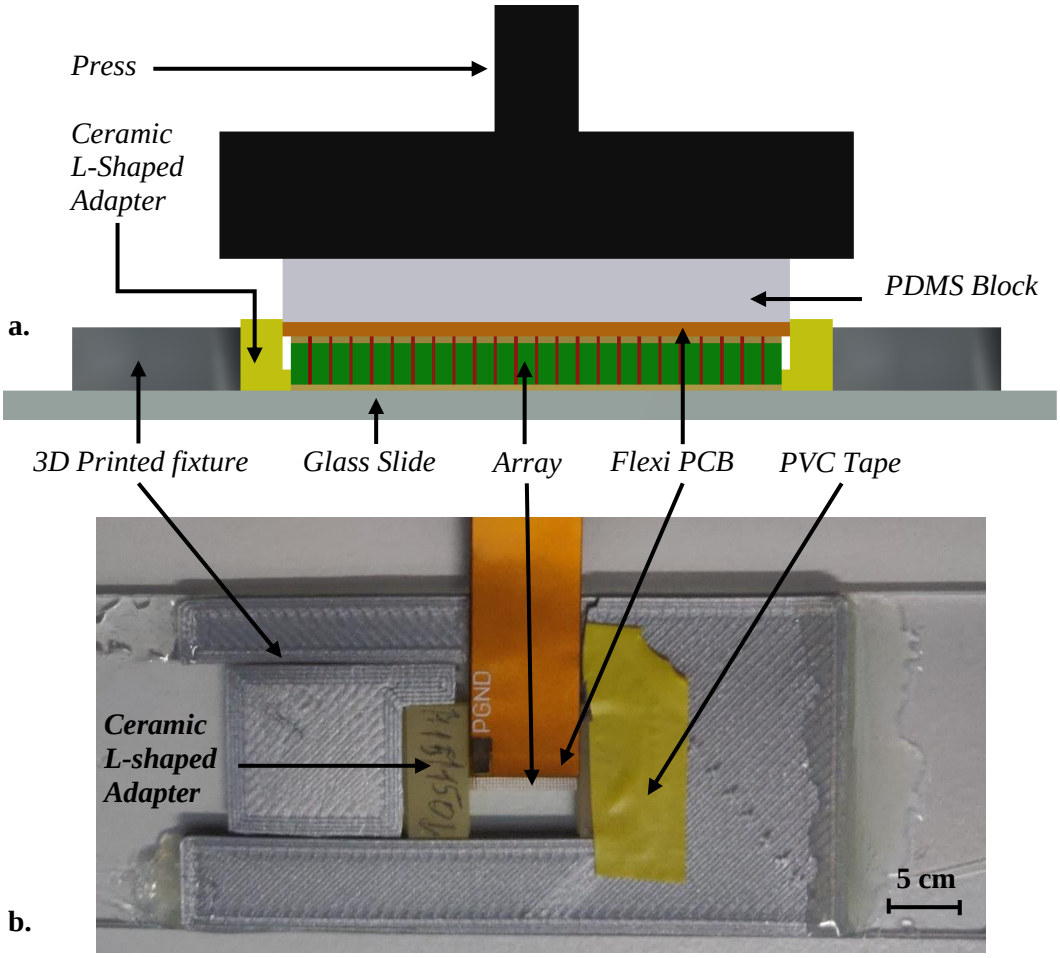

Figure 4-23 Fixture for Flexible PCB Bonding to the Array: a. Schematic Side View; b. Top View

The jig comprised a glass microscope slide as the base, to which a 3-D printed locking mechanism was fixed with two-part epoxy (Araldite Rapid - Huntsman Advanced Materials, Basel Switzerland). The flexible PCB protruded by 0.115 mm from both sides of the array in the length direction, and its alignment with the transducer was accomplished with two L-shaped adapters (Figure 4-23). The adapters could not be 3-D printed because of their very fine features, so they were cut from ceramic material to the desired shape with the dicing machine and then fixed to the 3-D printed locking mechanism with PVC tape (Figure 4-23 b.).

Bonding Process Description

Before flexi-bonding, the array elements were cleaned with a lint-free cloth dipped in deionized water, followed by a jet of high-pressure N_2 gas to remove any remaining water or debris. The array was then inserted into the positioning jig and a thin layer of anisotropic conductive adhesive was applied to the bonding area of the flexible PCB. The flexi was then positioned on top of the array, guided by the ceramic holders. Pressure was applied to the bond with a press (Figure 4-24 a.), through a PDMS (polydimethylsiloxane) block (Figure 4-23, a.) until the adhesive cured. The PDMS block was added between the press plate and the composite transducer to balance the pressure applied to the transducer and because of its low reactivity with adhesives, which allowed its easy removal after curing. The press holding the array was placed in the oven at 50°C for one hour to cure the adhesive and improve its electrical conductivity. Figure 4-24 b. depicts the array bonded to the flexi PCB after its removal from the holders.

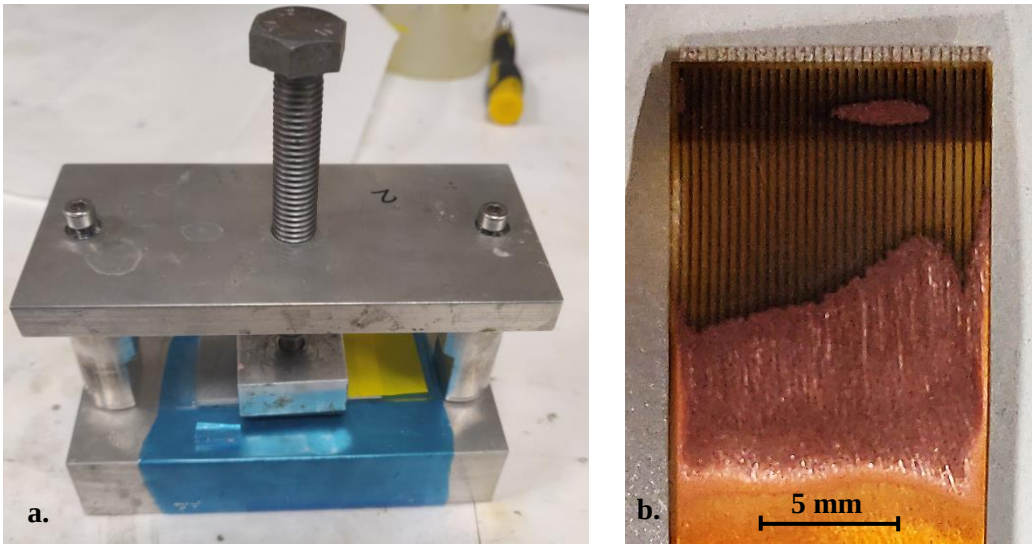

Figure 4-24 a. Press for Flexible PCB Bonding to the Array; b. Flexible PCB Bonded to the Array

4.6 Backing Layer, Transducer Casing and Final Assembly

4.6.1 Transducer Casing Design

The array casings were designed as hollow cuboids and were 3-D printed by additive manufacturing with an Ultimaker 2 Pro printer (Ultimaker B.V., Utrecht, NH) using polylactide filament. All casings had a depth of 11 mm to allow approximately 10 mm of backing layer. The inner dimension of the casings in the array elevation direction was designed with a 1.5 mm clearance to allow bending the flexible PCB connector at 90° inside (Figure 4-25). The inner clearance of the casing in the array length direction was set to 0.1 mm at each side of the array, to allow insertion of the transducer.

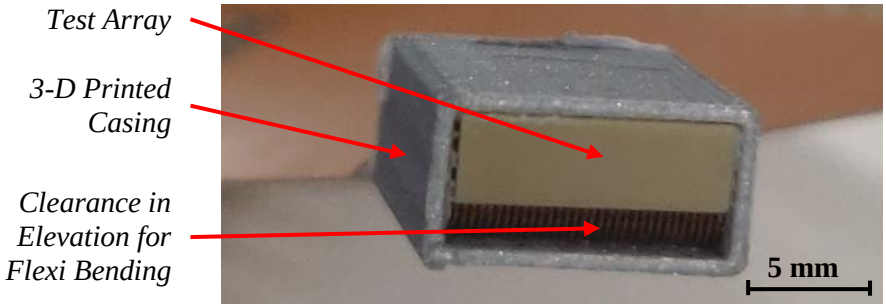

Figure 4-25 Transducer Casing with Clearance for Flexi PCB Bending

4.6.2 Addition of the Backing Layer

Epofix was mixed with hardener in a beaker following the same weight ratio as for the kerf filler (Section 4.3.1). Air-filled microballoons were then added slowly into the beaker, under continuous stirring with a spatula. When the mixture thickened, stirring with the spatula became inefficient and was replaced by kneading. Microballoons were added until the compound became saturated (i.e. had a grainy texture). Saturation was noticed at a mixing ratio of 5 mL of microballoons to 1.09 g Epofix. For consistency, the same mixing ratio was applied to the backing layers of all manufactured arrays presented in this Thesis. The resulting material was acoustically characterized, and the constants required for modelling it are presented in Table 4-4.

Table 4-4 Measured Constants for the Epoxy with Air-filled Microballoon Spheres Backing Layer

Frequency	$\rho\ (Kg/m^3)$	$^1v_l(m/s)$	$^2v_s(m/s)$	$^3\alpha_{long}(dB/cm)$	$^4\alpha_{shear}\ (dB/cm)$
1.0 MHz	382	2027	1186	3.28	7.03
2.25 MHz	382	2015	1178	10.64	18.41

^1v_l = longitudinal velocity, ^2v_s = shear velocity, $^3\alpha_{long}$ = longitudinal attenuation, $^4\alpha_{shear}$ = shear attenuation

After placing the array and its interconnects inside the 3-D printed casing, the backing material was added by hand. The array was held parallel to the casing face with the low-strength

adhesive film used for the dicing machine ring while backing material was pressed into the casing from the bottom. The assembly was left for 24 hours to cure the epoxy and then the film was removed. The front gap where the flexi PCB was bonded inside the casing (Figure 4-25) as well as any other empty space around the array were then covered with the same mixture of air-filled microballoons and epoxy and then left to cure for another 24 hours.

4.6.3 Ground Electrode Wire Bonding

The ground electrode of the array was bonded to an external connector with Ag conductive epoxy after the transducer was cased and the backing layer was added. The epoxy bonding site was placed at one side of the array to minimise unnecessary loading of the piezoelectric element. The ground connector was a 5.0 mm wide Cu band, specifically chosen to diminish the skin effect (Section 7.2.3) and to have low electrical resistance. The transducer was then placed in the oven at 50°C for one hour to cure the conductive epoxy.

4.6.4 Final Transducer Assembly

The last two stages in transducer manufacturing comprised soldering the Molex connectors to the flexible PCB and application of a layer of varnish on the transducer front face and on the ground connector in order to ensure no ingress of water. The varnish layer was applied with a brush, and then the transducer was left to cure for 24 hours. The finalized arrays are presented in Figure 4-26.

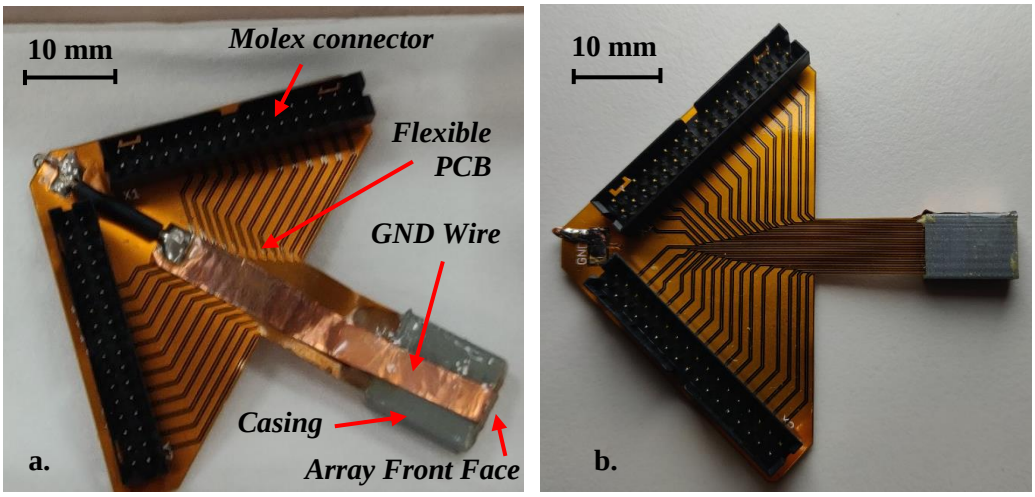

Figure 4-26 Finalized PZT-5H Arrays: a. 1.5 MHz; b. 3.0 MHz

The approximate manufacturing time for one array was around two weeks and its estimated fabrication cost, including use of laboratory resources and raw materials, was around £500. However, it is worth mentioning that the manufacturing time and price per array could potentially decrease several times if the devices were fabricated in larger numbers.

4.7 Conclusions

Chapter 4 described the manufacturing process employed to produce four types of miniature, therapeutic ultrasonic 1D phased arrays, based on 1-3 connectivity piezocomposites. The devices are designed to interface with the array controller through flexible PCBs and were cased and waterproofed for the characterization and functional trials which are discussed in detail in Chapters 5 and 6.

The transducer active materials were piezoceramic (PZT-5H) and single crystal (PMN-29%PT), while the kerf filler was Epofix. The geometry parameter set of the manufactured 1-3 connectivity piezocomposite materials was kept as close as possible to the optimum set determined with the simulation presented in Chapter 3. However, because of manufacturing restrictions, the parameter set of the experimental arrays diverged slightly from the modelled set. The two leading causes were the differences between available dicing blade widths and the simulated kerf widths, and the higher thickness of the manufactured piezocomposite samples than the modelled ones, chosen in order to maintain the correct resonance frequency. The modified parameters led to a slight change in the composite volume fraction and aspect ratio, which is investigated in Chapter 5.

The arrays were electroded by spin coating a layer of Ag ink, which had low surface resistivity and reduced thickness. The spin coating parameters that produced the best compromise between resistivity and thickness were determined to be 3000 RPM and 15 s spin time for two curing temperatures, 50°C and 75°C, while the Ag ink was thinned with 4.35% parts thinner (by weight). The piezoceramic-based samples were cured at 75°C for four hours and had an average surface resistivity of 0.37 Ω/ sq. and an average layer thickness of 4.98 μm. The lower curing temperature, chosen for the single crystal materials, led to a similar layer thickness (4.71 μm), but higher surface resistivity of 0.63 Ω/ sq., even after a prolonged curing time of 72 hr at 50°C. The layers deposited on glass slides demonstrated good robustness to peeling from dicing machine tape. The Ag ink electrodes also had good adhesion to the PZT-5H composites, but the single crystal samples lost parts of the electrode when removed from the dicing tape and required later repair with a brush.

The backing layer was designed to have low acoustic impedance and damping, and thus to maximize ultrasonic transmission towards the load. The material was a saturated mixture of air-filled microballoons in Epofix. Prevention of water ingress was ensured by application of a thin layer of varnish on the face of the array and on the ground connector.

5 Transducer Characterization and Applications

5.1 Introduction

Chapter 5 presents the experimental characterization of the four 1D phased arrays in terms of electrical impedance and ultrasonic beam profiles in degassed water. The experimental data is then cross compared with FEA modelling results to assess the feasibility of implementing array driving parameters derived from software models into therapeutic protocol.

Electronic beam steering of the manufactured transducers was performed with a 32-channel DSL FI Toolbox phased array controller based on hardware from National Instruments (Austin, TX, USA). Several modifications were applied to the standard FI Toolbox machine to repurpose it from an US imaging system to driving therapeutic arrays.

Experimental beam profiling of the acoustic field from all phased arrays presented in this chapter was performed with a three degree of freedom (3-DOF) flatbed configuration linear stage (Galil Motion Control Inc, Rocklin, California, USA) coupled to a 0.2 mm diameter needle hydrophone (NH) (Precision Acoustics Ltd, Dorchester, United Kingdom). As sonoporation is closely related with MI, and inherently, with PNP, an accurate relation between the array driving voltage magnitude and both the beam profile and PNP output was required. In order to increase the accuracy of the measurement system, a complex (magnitude-phase) sensitivity deconvolution method was applied in post-processing to extract the PNP magnitudes from the NH voltage dataset recorded by the scanning tank system.

The simulation of the beam profiles was performed with OnScale, employing either a combination of FEA modelling and Kirchhoff time-domain extrapolation, similar to the one described in Section 3.4.1, at equally spaced points in a 2-D slice of the load, or by means of an FEA-only model with an explicit solver for the load. The two types of simulations were then compared in terms of beam profile and PNP magnitude fit with the experimentally measured data, for all four types of arrays, at various steering angles, focal depths in the water load and driving voltage amplitudes.

Finally, the material coefficients of the PZT-5H and PMN-29%PT used in the simulations were altered as result of an optimization algorithm that minimized the correlation between the FEA modelled and the measured electrical impedance of the transducers. The simulated beam profiles achieved by the arrays with the modified piezoelectric materials were then compared, in the same manner as before, with the experimental data and with the data from the original FEA simulations.

5.2 1D Phased Arrays Experimental Characterization: Procedures and Methods

The manufactured 1D phased arrays were characterized in terms of electrical impedance with an HP 4194A Impedance/ Gain-Phase Analyzer. Measurements were performed at various stages of the manufacturing process to identify and correct flaws in the process, but also for comparison with the FEA models. Further electrical impedance measurements of all array elements were performed as verification before and after beam characterization in the scanning tank to ensure the transducers operated as expected.

Beam pattern characterization was performed in a large tank filled with deionized and degassed water, with the front face of the arrays positioned just below the water surface. The transducers were fixed to the tank with a 3-D printed fixture, while 2-D scans of their acoustic beams were recorded with a NH coupled to a custom-made 3-DOF linear stage. The scanning tank program, developed in-house, controlled both the transmission and reception of the US signal by means of a common sync line. The principle of operation was that once the NH was brought to the scan position, the phased array controller was triggered, followed by data acquisition with the NH. Then, the position of the hydrophone was translated to the next scan point and the process was repeated until the entire scan area was covered.

5.2.1 Importance of Beam Shape and dB Profile Plots for the Characterization of the Prototyped Phased Arrays

Beam profile characterization provides insight into the shape of the sonicated area and the pressure magnitudes attained. It is an important step in the characterization of experimental therapeutic transducers and in therapy planning, especially in sonoporation, where MI must be controlled accurately to avoid causing irreversible damage to the tissue. Because of variations in material properties and manufacturing, noise in driving electronics, propagation nonlinearities or temperature dependence of processes, FEA modelling requires thorough correlation with experimental measurements to produce highly accurate beam patterns.

In order to quantify and compare the simulated and the measured beam profiles of the manufactured arrays, two types of data plots were used: a 2-D colour plot (Figure 5-1 a.) that offered information about the beam shape and PNP magnitude distribution across the imaged slice, and a dB profile plot with three contour levels at: -1 dB, -3 dB and -12 dB (Figure 5-1 b.). The -1 dB contour was considered to enclose the area of most therapeutical relevance and was used to quantify the PNP and MI levels achieved by each array at different driving voltages. The -3 dB profile was considered to be the lowest margin of relevance for therapeutic

purposes and therefore was used to determine the steering angle separation in a sonoporation sequence spanning over a wider treatment region (more details about the *in-vitro* sonoporation procedure are presented in Section 6.2). The -12 dB profile was mainly used for the comparison and alignment between the experimentally measured and the simulated beam profiles.

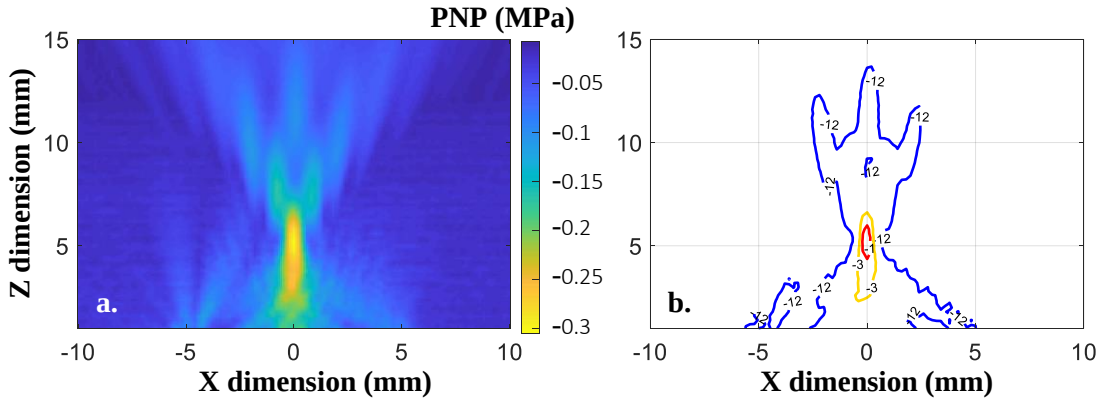

Figure 5-1 Beam Slice form the 1.5 MHz, PZT-5H Array, Recorded with the NH, and Represented as: a. 2-D PNP Colour Plot; b. dB Contour Plot

5.2.2 Transducer Driving with a Phased Array Controller

A DSL FI Toolbox was used for driving the 1D phased arrays due to its operational versatility and integrated LabView-based control software. The array flexi circuits were connected to the transmitter board of the FI Toolbox with a custom-made cable comprising 32 mini coaxial cables with 2.6 mm outer diameter and 50 Ω matched impedance. One additional cable was included to connect to the ground (GND) electrode of the array. The cable length was 1.0 m, being long enough to allow for positioning the arrays in the scanning tank, but short enough to minimize transmission line effects. For the 24 element phased arrays, the FI Toolbox was configured to neglect 8 channels in order to allow the reuse of the same cable.

DSL FI Toolbox

The DSL FI Toolbox is an array controller designed for US imaging and data acquisition. The device transmits excitation signals for up to 32 channels through a DSL 32T FlexRIO adapter module, while reception is performed on a DSL 32R board. The transmit module contains 32 pulser channels, capable of delivering a maximum voltage of ±90V per channel. A pulser is an electronic component based on transistor logic that shifts the output voltage between a series of predefined DC voltage levels. The resulting square wave is used to drive the US array. A more comprehensive description of a pulser circuit is provided in Ref. [237].

The output signal waveform from the DSL 32T is a pulse width modulated wave, with three amplitude levels that enable transmission of coded excitation signals [238]. Electrical power is supplied to the pulsers from a configurable high voltage (HV) power supply, integrated into

the machine. The FI Toolbox software allows the creation of arbitrary pulse streams and enables the individual control of pulse-width modulation (PWM) for each channel. The RMS voltage of the pulsers is comparable to the RMS amplitude of a sine wave for a PWM duty cycle of 70%. Multiple transmit/receive modules can be added into the same chassis to increase the instrument's channel count.

Changes Made to the DSL FIToolbox

As the FI Toolbox was designed for imaging applications, several hardware and software modifications were performed to optimize it for driving the manufactured phased arrays both during their evaluation with a scanning tank system and for therapy. A full raw data capture module of the FI Toolbox software was the closest program to the purpose of the project because it allowed simultaneous transmission on the entire array aperture. The receiving part of the FI Toolbox control software was redundant, but could not be completely switched off. However, the scan range and delay time between successive bursts were reduced to a minimum in order to increase the pulse repetition frequency (PRF) of the machine during therapy.

Furthermore, the FI Toolbox required a common sync line with the scanning tank system for the beam characterization of the phased arrays. As the array controller had no dedicated trigger input port for this purpose, the solution adopted for this work was to connect the scanning tank trigger line to a digital I/O pin of the DSL 32T and configure the machine to consider the pin connected to an encoder. By setting the encoder counter step to two, the DSL 32T could be triggered on one edge of the trigger signal sent by the scanning tank controller.

5.2.3 Beam Pressure Mapping with a Needle Hydrophone and a 3-DOF Linear Stage Scanner

Acoustic beam pattern characterization of medical transducers is most commonly performed in a scanning tank filled with deionized and degassed water, with a NH attached to a linear two or three DOF manipulator. Beam pattern plots of the acoustic field are acquired at discrete spatial points in the scanned volume by means of a pitch-catch method. At each spatial point, the NH records the pressure magnitude time trace in the form of a voltage waveform. Traditionally, the pressure waveform is estimated by dividing the measured voltage with the sensitivity of the hydrophone at the main resonance frequency of the transducer [239].

In order to assess the beam patterns from the arrays under test, three types of 2-D scans were performed with the linear stage. The most relevant scan was the XZ slice, with Y direction fixed in the centre of the array elevation. This scan provided insight into the beam width in the active aperture plane, the steering angle, the focal distance and the PNP values of the main

beam. The XY scan was usually centred in the focal distance of the array (on the Z axis) and it evaluated the cross section of the beam, with relevance in assessing the active sonoporation area. Lastly, the YZ scan was performed at the centre of the array length and it revealed the passive aperture focal distance and the beam dispersion in that direction. This type of scan was useful for improving the accuracy of the simulation with respect to the experimental data (Section 5.4.4).

The general reference frame for all beam plots provided in this chapter is presented in Figure 5-2. The load depth direction, away from the array surface, is considered the +Z axis in order to maintain consistency with the piezoelectric material thickness direction and with the previous notation used in Chapter 3.

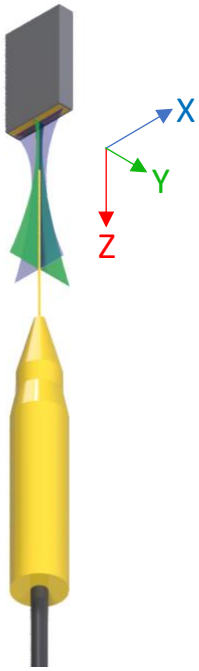

Figure 5-2 NH Scan Reference Frame

As part of beam pattern evaluation, a fixed voltage of 15 V_{PP} was used as excitation for all arrays under test, and it corresponded to the lowest voltage output from the FI Toolbox power supply. The array controller was set to output a 10-cycle burst for the 1.5 MHz transducers and a 15-cycle burst for the 3.0 MHz case. The number of cycles in the burst was determined experimentally to be small enough to avoid US back wall reflections, but large enough to allow the DSL 32T pulsers to reach full voltage amplitude swing for at least 5 cycles.

NH Size and Spatial Resolution of a NH Scan

The NH is a piezoelectric device that transforms the acoustic pressure at its tip into a complex voltage waveform which is recorded by the measurement system. The complex amplitude-phase pressure measured by the NH is integrated over its active area, which can lead to measurement errors if the NH size is larger than the wavelength of interest. According to the IEC TS 62556:2014 standard [240], in order to minimize measurement uncertainties due to phase and amplitude averaging over the NH active area, its effective radius should be equal to, or less than $\lambda/4$. Therefore, the maximum NH diameter for measuring acoustic fields in water, emitted at a frequency of 1.5 MHz, should be approximately 0.5 mm. The maximum NH diameter should be reduced to 0.25 mm for characterizing acoustic waves at 3.0 MHz. To ensure compliance with the IEC TS 62556:2014 standard, a NH with a diameter of 0.2 mm was selected for beam pattern characterization of all arrays evaluated in this Thesis and the spatial resolution of the beam profile scans was set to 0.2 mm in all three directions.

Beam Alignment

The purpose of beam alignment as part of the beam profile characterization of the arrays was a crucial aspect because it ensured the acoustic magnitude was maximized in the passive aperture scan direction (i.e. the fixed direction in the XZ scan) and the scan was centred on the beam axis.

The axial distance (Z_{axial}) between the NH and the transducer surface was calculated in terms of the speed of sound in water and the time of flight (Δt_f) between the electrical excitation of the array and the reception of the acoustic wave with the NH. In order to avoid confusion and eliminate any potential measurement errors due to propagation delays, the arrays were not focused during this procedure, with no phase delays applied.

Next, as the 3-DOF linear stage used in the beam characterization of the phased arrays was custom-built, the scanning software and the beam alignment procedure were developed in-house, using NI LabView. Snapshots of the two programs (Figure B-2 and Figure B-3) are provided in Appendix B. The description of the software is beyond the purpose of this Thesis, however the beam alignment algorithm is summarized below.

The initial step of the alignment procedure was to focus the phased array forward (i.e. 0° steering) at the desired distance in the load (Z_F), and to position the NH at an axial distance from the array surface equal to Z_F (i.e. $Z_{axial} = Z_F$). Beam alignment in the cross-section (XY) plane was then performed, with the aim of maximizing the beam in both the active (X) and the passive (Y) aperture directions. The beam was firstly maximized in the X direction, followed by a maximization in the Y direction. The origin of the NH system was updated to the new X, Y coordinates and then the NH was translated away from the transducer in Z direction, by one half of Z_F, without altering the phasing of the array.

XY beam alignment was performed again at the further axial distance ($Z_{axial} = 3/2 * Z_F$) and the array was manually rotated until the new point of maximum in the cross-section plane aligned with the previous alignment (performed at $Z_{axial} = Z_F$). This step ensured the array was perpendicular on the hydrophone axis, which implied the forward-focusing beam was maximised. Often, the alignment methodology required several repeats to decrease the alignment errors systematically. The beam alignment methodology is described schematically in Figure 5-3.

The measured accuracy of the beam alignment procedure was around 0.2 mm in any direction. The X and Y accuracy was mostly influenced by the spatial averaging of the 0.2 mm diameter NH, while the Z accuracy was dependent on the velocity of sound propagation in water. The

former was determined with the Lubbers and Graaff's simplified equation [241], and was dependent on the atmospheric pressure and water temperature. The step size of the scanning tank linear stage was not a significant error source as it was only 0.6 µm.

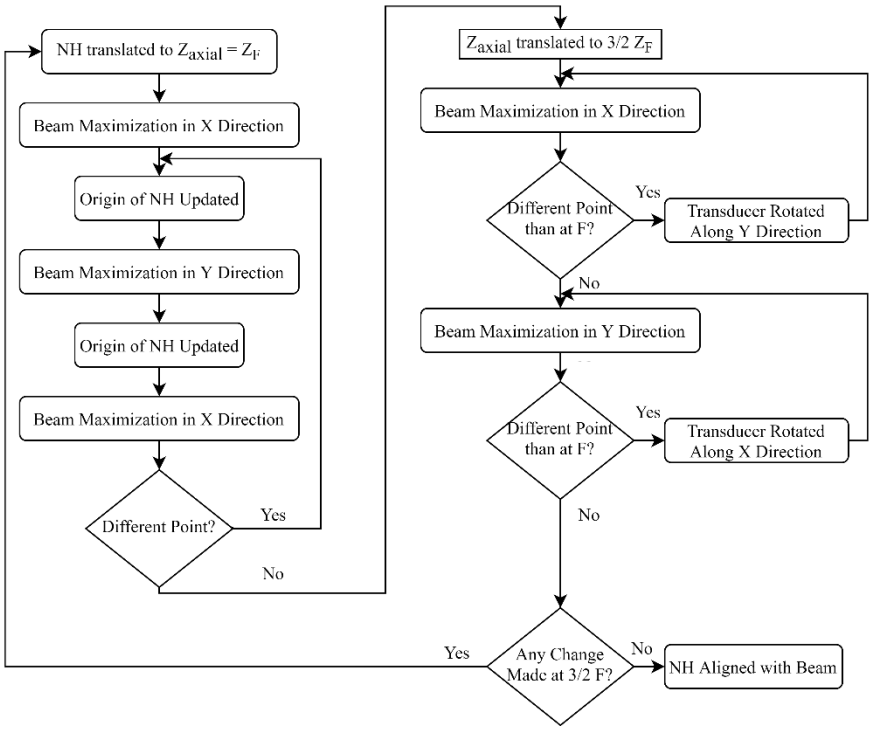

Figure 5-3 Beam Alignment Procedure for the Scanning Tank

5.2.4 Complex Deconvolution of the Needle Hydrophone Sensitivity

As sonoporation efficiency is closely related to PNP and driving frequency, an accurate relation between the driving voltage and the PNP achieved by the transducer at focus is essential. A source of measurement uncertainty when performing beam characterization is due to the traditional approach of considering the NH transfer function as a constant. Thus, its value is taken as equal to the sensitivity magnitude of the NH at the resonance frequency of the transducer under test. However, this method adds uncertainty to the measurement because it does not consider the variation of the NH magnitude and phase sensitivity with frequency. Even if the characterized transducer is narrowband, other frequency components may appear in the scanned beam due to nonlinear effects of acoustic propagation in the load, cavitation emissions if PNP is high, higher transducer harmonics or spurious modes.

The reliability of the PNP measurements can be increased by deconvolving the complex sensitivity of the NH over its calibration spectrum. Generally, hydrophones are calibrated with respect to magnitude only due to the higher complexity and costs associated with phase calibration. According to [242], phase calibration data for the hydrophone is as important as the magnitude data for the accuracy of the deconvolution process.

Because the NH used for beam characterization of the arrays contained only magnitude sensitivity calibration data, a mathematical approach was employed to obtain the missing phase sensitivity data required to faithfully reconstruct the pressure waveform [242]. The voltage time trace (v) recorded from the NH was transformed into single-sided spectral data (V) using a discrete Fourier transform (DFT) approach. Then, the complex (magnitude-phase) sensitivity transfer function (TF) of the NH was deconvolved from the voltage spectrum, yielding the raw pressure spectrum (P) recorded by the NH. An ideal low-pass filter was applied to remove high frequency ripple, and an ideal DC band-stop filter was added to remove the DC bias from the signal. Lastly, an inverse discrete Fourier transform (IDFT) was used to transform the reconstructed PNP from frequency domain into time domain data. Figure 5-4 describes the stages of the process used to reconstruct the PNP time domain data from the voltage recorded by the NH, and is based on the methodology from [239] and [242]. The use of lower-case letters on top of the arrows in Figure 5-4 depicts the time-domain pressure or voltage datasets, and the upper-case letters depict the frequency domain datasets or variables. Furthermore, sensitivity calibration data is expressed as magnitude $|S|$ and phase φ_S.

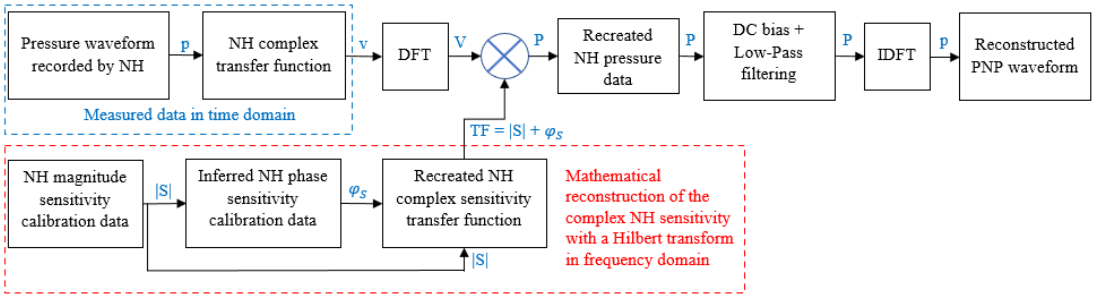

Figure 5-4 Schematic Representation of the NH Sensitivity Complex Deconvolution and Filtering Performed in Post-processing

Inference of the Phase Sensitivity Transfer Function of the NH

The calibration data for the 0.2 mm diameter NH was provided as discrete sensitivity magnitude values at frequency increments of 1 MHz on the interval {1 MHz – 30 MHz}. The phase data, $\varphi_S(\omega)$, was inferred by applying an inverse Hilbert transform on the original (frequency domain) magnitude sensitivity calibration data, $|S(\omega)|$ [239]:

$$\varphi_S(\omega) = H^{-1}\{\ln(|S(\omega)|)\} \qquad \text{Eq 5.1}$$

Because the inverse Hilbert function, $H^{-1}\{\ }$, is a continuous-frequency function, it could not be used on discrete-frequency calibration data available for the NH under use, but it could be inversed to a direct Hilbert transform, which is discrete-point, with the relation [243]:

$$H\{H\{f(x)\}\} = -f(x) \qquad \text{Eq 5.2}$$

which yields:

$$\varphi_S(\omega) = -H\{\ln(|S(\omega)|)\} \quad \text{Eq 5.3}$$

According to [242], the inverse Hilbert transform can only be applied to approximate the phase sensitivity data of the NH if the system is minimum phase. This is achieved if the transmitted signal is narrowband, which is true in the case of all the arrays under test presented in this chapter.

The described phase inference method was tested on calibration data from a reference 0.2 mm NH, similar to the one used in this work, but calibrated in both magnitude and phase. Figure 5-5 compares the inferred and the measured phase sensitivities of the reference NH. The plot shows the two traces are in good accordance, especially on the {0 MHz -15 MHz} interval of frequencies relevant to the arrays characterized in this work, proving the validity of the method.

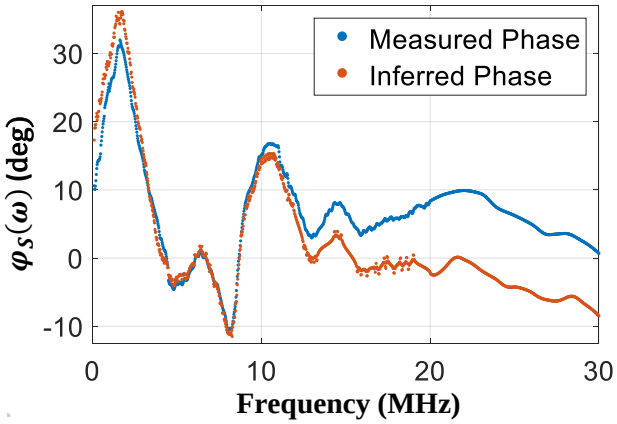

Figure 5-5 Comparison Between the Calibration Phase Sensitivity and the Inferred Phase Data with the Hilbert Transform Method Described by Wear et al. [229]

NH Complex Sensitivity Deconvolution in the Frequency Domain

The deconvolution procedure was performed in the frequency domain, on discrete data. This required the voltage dataset and the discrete NH complex sensitivity function to have an identical frequency base for the division operation in the frequency domain to have mathematical significance. Firstly, the NH calibration data was provided as single sideband, which required the voltage data to be reduced to $(N/2) + 1$ samples, according to Nyquist theorem for accurate reconstruction [242]. Secondly, as the NH calibration data was sampled at lower resolution than the voltage dataset, it was interpolated with spline interpolation to create a sensitivity calibration vector with magnitude and phase points corresponding to the same frequency values as the points in the voltage signal. To account for the voltage data that was not in the NH calibration bounds (<1 MHz and >30 MHz), the NH sensitivity magnitude was set to the calibration magnitude at the minimum frequency for $f < f_{min}$, and to the

calibration magnitude at the maximum frequency for $f > f_{max}$ [242]. All phase values out with of the calibration interval were set to zero [242]. Figure 5-6 a. shows the magnitude sensitivity and the inferred phase sensitivity of the 0.2 mm NH used for characterising the phased arrays as function of frequency. Figure 5-6 b. shows the relationship between the normalized frequency spectrum of a voltage dataset recorded by the 0.2 mm NH and the normalized sensitivity magnitude of the hydrophone.

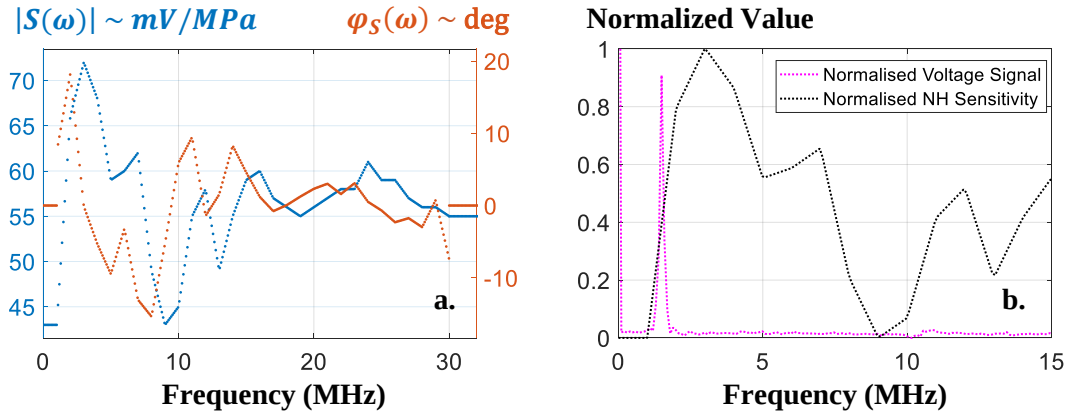

Figure 5-6 a. 0.2 mm NH Sensitivity Magnitude and Inferred Phase; b. Relation Between the Measured Voltage Signal and the NH sensitivity Magnitude in Frequency Domain

Figure 5-7 displays the differences in the reconstructed pressure magnitude from the voltage dataset recorded with the NH between the deconvolution method (red trace) and the traditional fixed sensitivity division (yellow trace). In this case, the percentage difference in PNP between the deconvolution and the fixed sensitivity approach was 7.5%. Filtering the DC bias from the NH voltage (blue trace) led to a percentage difference in PNP of -33.1% from the pressure reconstructed with deconvolution only.

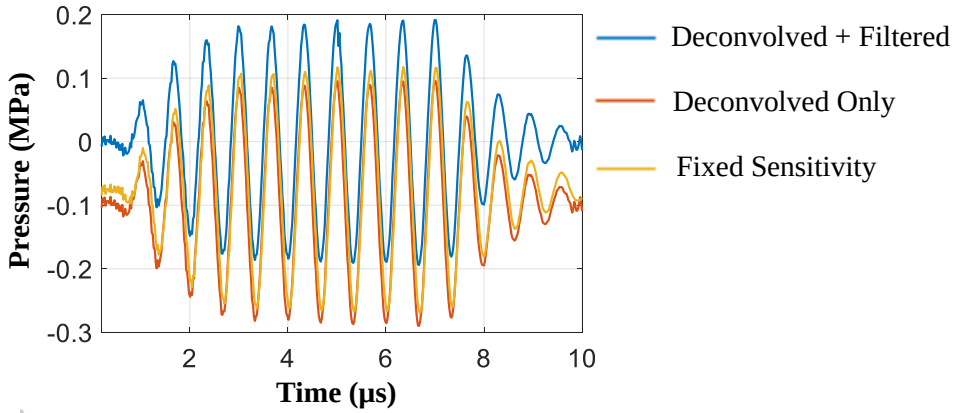

Figure 5-7 Comparison Between the Deconvolution Methods and the Division by Fixed Sensitivity Method for Pressure Reconstruction from the NH Voltage

The pressure waveforms were evaluated at various points from the centre of the array main beam. It was observed that the pressure difference between the methods increased with increasing the lateral distance from the centre of the main beam. This phenomenon led to

differences in the dB pressure profiles of the 2-D slice scan obtained with the different pressure magnitude reconstruction methods (Figure 5-8). The dB profiles obtained with the deconvolution + filter approach were smoother and better defined than the less accurate (according to [242]) pressure reconstruction method relying on fixed sensitivity division. Hence, the complex deconvolution method with filtered DC bias was used throughout this work for reconstructing the pressure magnitude from the voltage data recorded by the NH.

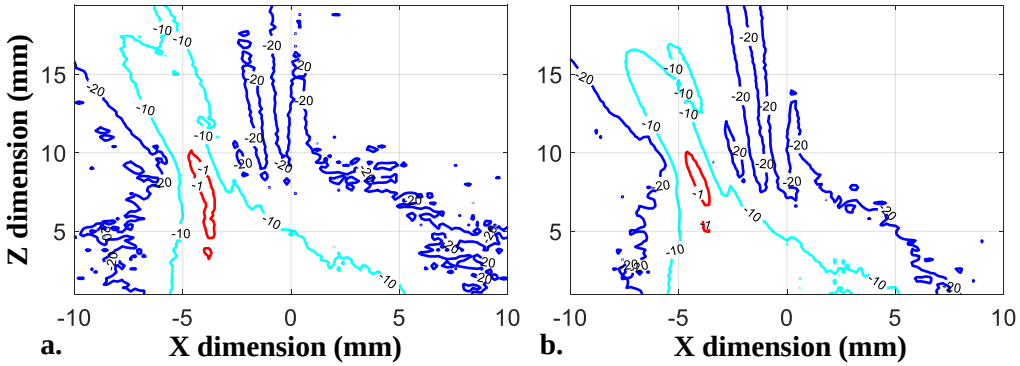

Figure 5-8 Normalized Pressure Profiles for Effective Comparison Between: a. Fixed Sensitivity, and b. Deconvolution + DC Bias Filter Reconstruction Methods

5.3 FEA Model Development for Impedance and Beam Pattern Characterization

Beam pattern simulations with FEA were performed for all arrays under test and the resulting data was correlated with the experimental results. Where necessary, the array models were adapted for better fit in terms of the steering angle, focus distance or PNP thresholds achieved in the water load. Efficient model calibration was important to prove that accurate software models could be safely employed to determine the array driving parameters as part of therapeutic planning, thus reducing the number of NH scans prior to therapy. The ultimate purpose of the software models is to reliably predict ultrasonic beam patterns in tissue, where a NH cannot be readily inserted.

5.3.1 2-D Beam Pattern Modelling

A similar approach as in Section 3.4.1 was employed to simulate a 3-D FEA model of the array coupled to a reduced size water load, combined with a time-domain Kirchhoff extrapolation of acoustic propagation in the remaining load. The water depth was set to 2.5 λ, and it extended by a further 0.5 mm in the elevation direction from both sides of the array, as in the previous approach (Table 3-3). The load lateral protrusion in the length direction was increased from 0.5 mm to 3.0 mm at both array sides in order to allow sufficient space for beam steering. However, the main difference between the current model and the one presented in Section 3.4.1 was the extrapolation was performed for a 2-D slice, rather than a line.

A second method was developed which modelled the entire 3-D array and load with FEA-only. Pressure magnitude time histories were saved at all points of the same 2-D slice as evaluated with the extrapolation model. The beam patterns produced by both methods were compared in terms of the fit with the experimentally measured datasets. The array models also included a full-size backing layer for the 1.5 MHz arrays, and a reduced size backing in the case of the 3.0 MHz arrays due to the large computation size at the finer time step. The acoustic properties of the backing material used in the models were the ones for the air-filled microballoon loaded epoxy (Table 4-4). Four-micron thick Ag electrodes were also added to the simulated arrays as a *Shell* element [244], rather than as an FEA continuum element because of their reduced thickness, which would have unnecessarily increased the mesh resolution of the models.

FEA Model Improvement to Conform with the Experimental Setup

Initially, the modelled arrays were excited with an ideal 10 or 15 cycle sine-wave burst, with an RMS value equal to an average RMS value of the excitation signal measured from the FI Toolbox. However, this simplistic representation of the driving voltage differed from the pulsed excitation signal from the array controller (Figure 5-9 a.), which was richer in frequency content (Figure 5-9 b.) than the ideal sine wave. The additional resonances present in the excitation signal from the DSL 32T could possibly lead to other vibration modes of the arrays. Furthermore, the effect of the connecting cables was not considered in the initial model either.

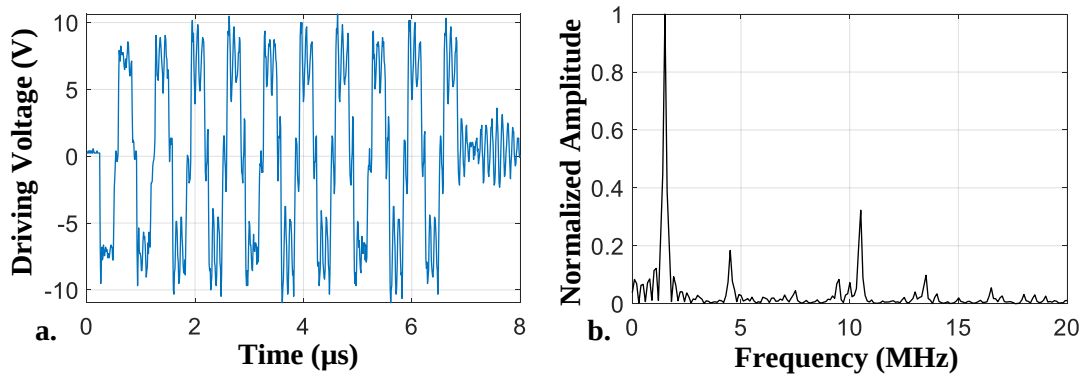

Figure 5-9 a. Typical DSL 32T Output Waveform Measured on One Channel of a 1.5 MHz, PZT-5H Array; b. The Corresponding Frequency Spectrum of the Measured Signal

The first modification to the original model was to include the real driving voltage measured from the array controller for each test condition (steering angle and focal distance). In order to do so, an oscilloscope synched with the scanning tank was connected through a 10 MΩ probe in parallel to one channel of the DSL 32T board. The transducer under test was connected to the array controller and dipped into the water during the voltage measurement procedure to provide mechanical loading. The voltage measurement could not be performed

at the transducer terminals directly because of the 3-D printed enclosure and the closeness to the water. This issue led to a second model update which comprised the inclusion of connecting cables to the transducer. This was done in the form of an RLC circuit simulated in series with each array element. The RLC values of a mini coaxial cable and associated connector used to deliver power from the FI Toolbox to a phased array element were measured with a calibrated RLC meter (RS Pro, RLC 6002). The series resistance of the cable assembly was measured at 10 Hz by placing the meter probes at the two ends of the coaxial cable inner core, with the GND sheath unconnected. The series inductance of the cable was measured in the same way as the resistance, but with the RLC meter set at 2 kHz. The shunt capacitance of the cable was measured at 2 kHz, with one probe connected to the inner core, and the other to the GND sheath at one end of the coaxial cable, while the other end was left unconnected. The measured components of one cable assembly (considering all cables were identical) were: $R = 0.654\ \Omega, L = 2.08\ \mu H, \mathrm{C} = 100.2\ \mathrm{pF}$.

5.3.2 Electrical Impedance Simulations of the Arrays

In order to obtain better insight into the differences between the PNP levels provided by the FEA models and the experimental data measured with the NH, a comparison between the electrical impedance of the modelled and the manufactured transducers was established. The main points of the comparisons were: the presence of spurious modes in the manufactured piezocomposite that may not have been highlighted by the simulations, the difference in the coupling coefficient, the deviation of f_r and f_a, and the difference in electrical impedance magnitude, especially at f_r.

Initially, the impedance spectra of the bulk composite materials were obtained by simulating a wide piece of the material and applying symmetrical boundaries in X and Y directions. Four-micron Ag electrodes were also applied to the models in order to increase their match to the real materials. The impedance of the simulated bulk piezocomposites was then correlated with the experimental data from the spectrum analyser. The purpose of comparing the impedance of bulk piezocomposites as opposed to the impedance of the finalized transducers was to keep the system simpler in order to obtain insight into the active material and the composite structure properties and interactions. In this manner, several sources of errors between models and real transducers were avoided or reduced including: the clamping effect at the edges of the array due to the small number of pillars in the elevation direction, the effects of the electrical interconnects, the electrically conductive epoxy layer, the transducer casing, the backing material, the wire-bonded cable to the ground electrode or the varnish layer for waterproofing.

The second electrical impedance model investigated one element in array configuration. This model included a full backing layer of air-filled microballoon loaded epoxy in the case of the 1.5 MHz arrays, and a reduced size backing for the 3.0 MHz arrays, with the same dimensions as the pressure models. As the backing material greatly increased the model size, the number of array elements in the impedance model was reduced to half for the lower frequency arrays and to a quarter for the higher frequency ones, with symmetry in X direction applied in all models. According to the results in Section 3.5.5, this necessary size reduction should not have greatly impacted the accuracy of the results. The purpose of this approach was to evaluate and compare the influence of the backing material on transducer damping and of the reduced array dimension in elevation direction between the modelled and the experimental data. The array interconnects, the electrically conductive epoxy, the insulating varnish layer or the 3-D printed casing were not included in the simulation because of their complexity and manufacturing variations.

Optimization of the Electrical Impedance Spectrum Correlation between the Simulated and the Real Piezoelectric Materials

Finally, the thickness of the active material in the FEA models was set to the average thickness of the manufactured material in order to minimize the inconsistencies between the models and the real transducers (Section 4.3.3). This led to a change in the resonance characteristics of the simulated arrays compared to the experimental ones and was attributed to a mismatch in the 1-3 piezocomposite properties. The mismatch was minimised by optimizing the correlation in f_a, f_r and $\overline{k_t}$ between the simulated piezocomposites and the experimental materials by varying the elasto-electric coefficients of the modelled piezoelectric materials. The purpose of the optimization was to align the piezoelectric properties of the simulated arrays with the manufactured ones in order to increase the reliability of the modelled beam profiles in terms of beam shape, and most importantly, PNP magnitude.

To reduce procedure complexity, the elastic coefficients of the epoxy kerf filler were not changed because the hard polymer properties are not substantially prone to manufacturing variations and their characteristics are well-known [245]. The optimization algorithm (based on previous work of Nicola Fenu, University of Glasgow) minimized the differences in f_r and f_a between the FEA simulated impedance magnitude and the experimentally measured electrical impedance, with the latter being the reference. The bulk 1-3 piezocomposites used in the optimization procedure comprised either PZT-5H or PMN-29%PT as active material and Epofix for the passive phase, and had a resonance frequency of 1.5 MHz.

The material coefficients that were modified as part of the optimization were: c_{11}^E, c_{12}^E, c_{33}^E, c_{66}^E, e_{31}, e_{32} and e_{33}. According to OnScale, [246], the reduced parameter set for defining a piezoelectric material requires the following constants: material density, 6 stiffness or compliance parameters (c_{11}^E, c_{12}^E, c_{13}^E, c_{33}^E, c_{44}^E, c_{66}^E), three piezoelectric coefficients (e_{15}, e_{31}, e_{33}), two relative permittivity constants (ε_{r11}^T, ε_{r33}^T) and the mechanical Q-factor, Q_M. The remaining part of the elasto-electric matrix is determined by the OnScale postprocessor automatically.

In order to maintain self-consistency of the reduced elasto-electric matrix required by OnScale, a series of restrictions on the piezoelectric material coefficients were considered in the optimization algorithm. As PZT-5H has class 6mm hexagonal symmetry (Section 2.8.2), c_{66}^E is constrained by the following relation [247]:

$$c_{66}^E = \frac{c_{11}^E + c_{12}^E}{2} \qquad \text{Eq 5.4}$$

The PMN-PT material used in the piezocomposite arrays had <001> poling, with tetragonal class 4mm symmetry, and independent c_{66}^E coefficient.

Furthermore, in order to maintain crystal stability of the piezoelectric materials, the strain energy density must be positive, with the following derived restrictions on the stiffness parameters [134], [248], [249]:

$$c_{11} > |c_{12}|, \qquad (c_{11} + c_{12}) * c_{33} > 2c_{13}^2, \qquad c_{44} > 0, \qquad c_{66} > 0 \qquad \text{Eq 5.5}$$

Lastly, the signs of the piezoelectric stress coefficients for the class 4mm and 6mm symmetry types are restricted to [250]:

$$e_{31} < 0\ ,\ e_{32} < 0\ ,\ e_{33} > 0 \qquad \text{Eq 5.6}$$

Once the modelled piezoelectric materials have been optimised, they could be used to analyse the predicted beam profiles for the phased arrays comprising the modified materials with the same analysis as described in Section 5.3.1.

5.4 Results of the Cross Comparison Between Simulation and Experimental Data

5.4.1 Electrical Impedance Comparison

Effect of the Backing Material on the Impedance of an Individual Array Element

The effect of adding the air-filled microbaloon loaded epoxy backing material in the FEA model, to replicate the case of the manufactured transducer, led to damping of the electrical impedance spectrum. Figure 5-10 shows the damping added by the backing material is proportional between the FEA model and the experimental dataset. No significant spurious resonances were introduced by the backing material in either the simulated or the measured electrical impedance spectra.

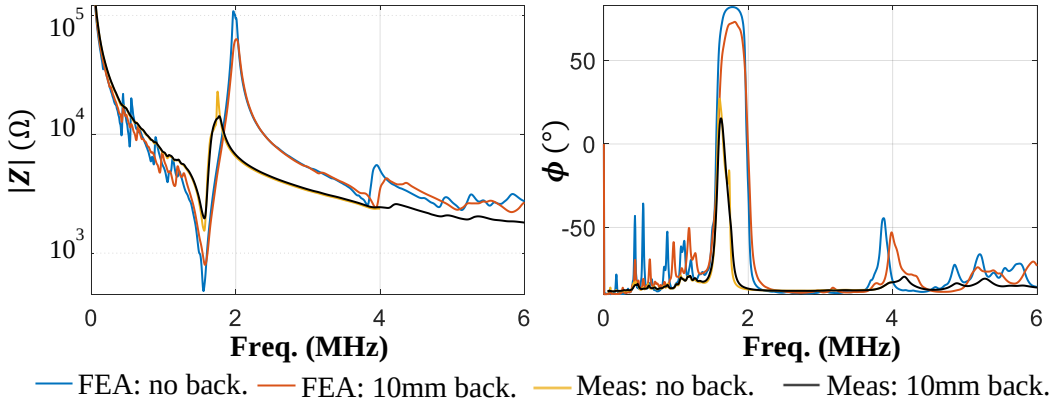

Figure 5-10 Damping Effect of the Backing Material in Both the Simulated and the Measured Array Element Impedance (Z) and Phase (ϕ) Response (1.5 MHZ, PZT-5H Array)

Electrical Impedance Correlation and Optimization Outcomes

The correlation between the experimentally measured electrical impedance and the FEA simulation of the original and optimized modelled materials is presented in Figure 5-11 for both bulk 1-3 piezocomposite materials and for an individual element from the array.

Generally, the bulk 1-3 piezocomposites modelled with the original active material properties had a much higher $\bar{k_t}$ than the manufactured samples, with f_a shifted towards a higher frequency, and f_r close to the modelled frequency. The correlation in the case of individual element impedance in array configuration showed higher discrepancies than in the case of the bulk materials. The main sources of errors were attributed to the differences between the modelled and the real piezoelectric material properties and to the degradation of the piezoelectric properties during the manufacturing process. Dicing and lapping of PMN-PT single crystal materials is known to produce highly stressed or damaged surfaces, impacting the performance of the material [251]. Also, mechanical degradation has been previously shown to cause shifts in resonance peaks and to affect $\bar{k_t}$, especially in the case of softer

piezoceramics as in the case of PZT-5H [252]. The further decrease in $\bar{k}_t$ and the higher resonance frequency shift incurred by the finalised arrays was credited to additional mechanical and thermal degradation associated with the remaining manufacturing stages, as well as lateral clamping from the casing and interference from the bonded flexi interconnects, backing material and the insulating varnish membrane.

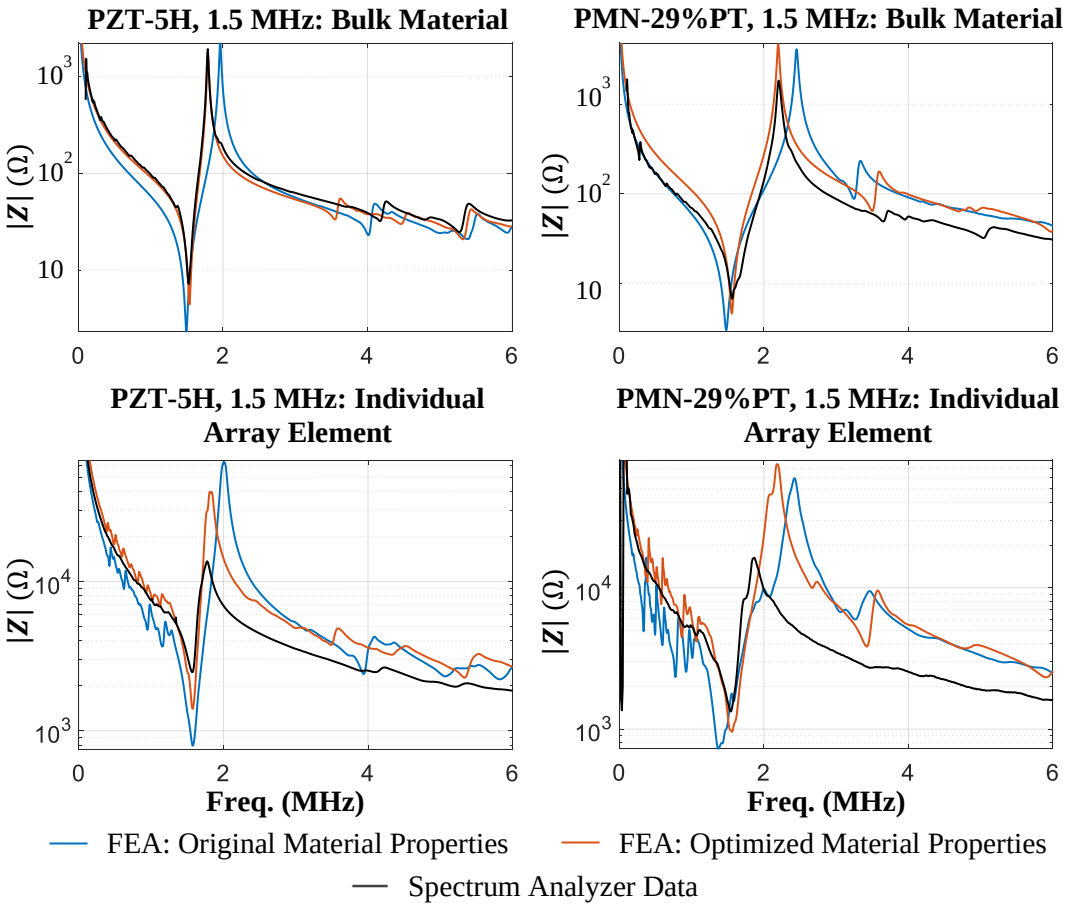

Figure 5-11 Outcomes of the Optimization on Electrical Impedance Magnitude Correlation Between the Simulated and the Experimental Data

Table 5-1 presents f_r and $\bar{k}_t$ for the bulk 1-3 piezocomposite materials and for the individual array elements determined experimentally, for both 1.5 MHz and 3 MHz devices, and their correlation with the FEA model results for the original and the modified piezoelectric materials.

Table 5-1 Resonance Frequencies and Thickness Coupling Coefficients Determined Experimentally and Their Correlation with the FEA Determined Parameters

		Measured $f_r(MHz)$	Original [1]$\Delta f_r(\%)$	Modified Δf_r (%)	Measured k_t	Original Δk_t (%)	Modified Δk_t (%)
PZT5H	Bulk	1.53	-1.91	0.80	0.56	21.6	-1.81
		3.07	-4.94	-3.39	0.49	40.0	11.8
	Array Elem.	1.57	0.70	0.50	0.50	33.3	10.6
		3.05	0.51	0.32	0.49	34.9	13.0
PMN-29%PT	Bulk	1.57	-5.96	-0.58	0.74	12.2	0.35
		3.23	-11.3	5.05	0.76	7.54	-5.06
	Array Elem.	1.55	-10.9	0.93	0.60	41.0	22.2
		2.78	11.8	22.7	0.75	5.97	-4.55

[1] $\Delta(\%)$ = (FEA Parameter – Measured Parameter) / Measured Parameter x 100

The optimization procedure decreased the discrepancy in f_r and $\bar{k_t}$ between the fabricated piezocomposite and the one modelled with FEA in all cases, except for one outlier: the individual array element impedance of the 3.0 MHz PMN-29%PT device. The frequency shift incurred in this case compared to the bulk material case was probably due to damage suffered during the manufacturing process. One important aspect to consider when analysing the optimization procedure results is the modified dataset also accounted for the measured 1-3 piezocomposite material thickness, whereas the original models had significant thickness discrepancies.

The modified elasto-electric coefficients of the modelled PZT-5H and PMN-29%PT materials as a result of the optimization procedure are presented in Table 5-2.

Table 5-2 Elasto-electric Material Coefficients Modified as Result of the Impedance Correlation Optimization

Material	PZT-5H			PMN-29%PT		
Coefficient	Original	Modified	[1]$\Delta(\%)$	Original	Modified	[1]$\Delta(\%)$
$c_{11}(10^{10}\,N/m^2)$	12.72	10.12	-20.47	12.40	11.79	-4.93
$c_{12}(10^{10}\,N/m^2)$	8.02	8.01	-0.13	11.10	7.83	-29.49
$c_{33}(10^{10}\,N/m^2)$	11.74	14.32	22.02	10.80	13.44	24.46
$c_{66}(10^{10}\,N/m^2)$	2.35	1.05	-55.17	3.50	1.98	-43.41
$e_{31} = e_{32}(C/m^2)$	-6.50	-6.57	1.08	-3.90	-6.67	70.90
$e_{33}(C/m^2)$	23.30	17.30	-25.75	22.30	18.40	-17.48

[1] $\Delta(\%)$ = (Modified - Original) / Original x 100

Array Bandwidth Measurements

In order to ensure the prototype arrays were transmitting at the desired frequency, the bandwidth of the devices was measured with a pitch-catch method. Each array element was individually excited with a narrowband pulse generated by a JSR DPR300 Pulser/Receiver (Imaginant, Inc., NY, USA) and the resultant acoustic field was measured, in water, with a 0.2 mm NH placed at the far field of the element. The complex sensitivity of the NH was then deconvolved from the measured dataset using the approach described in Section 5.2.3. Subsequently, the average frequency response of all array elements was calculated from the deconvolved time domain signals (Figure 5-12) and was employed to determine the centre frequency and -6dB fractional bandwidth of the prototype devices (Table 5-3) with the following equation [253]:

$$BW_{-6dB} = \frac{f_u - f_l}{f_c} * 100\% \qquad \text{Eq 5.7}$$

where f_l and f_u are the lower and upper -6dB frequency thresholds and $f_c = \frac{f_l + f_u}{2}$ is the transducer centre frequency.

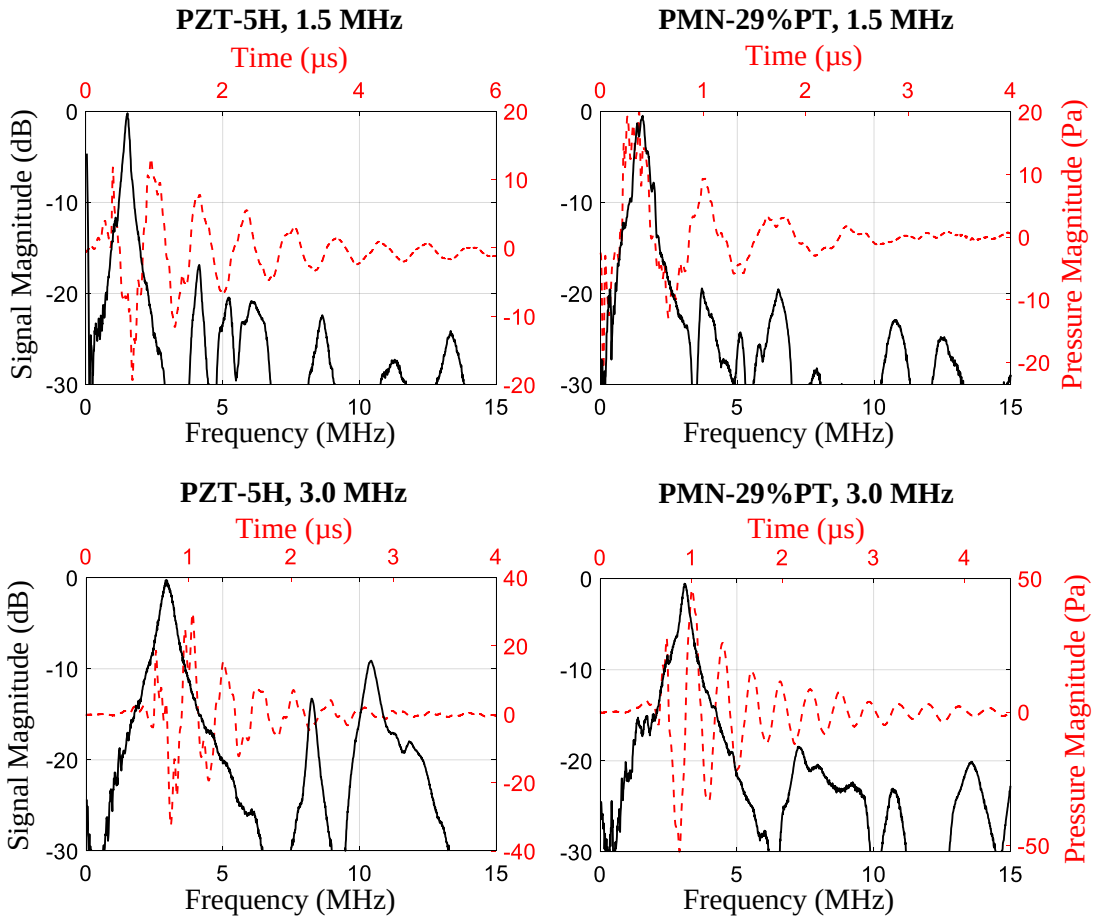

Figure 5-12 Deconvolved Pressure Signal Recorded with the NH (Red Trace) and Frequency Response Averaged Across all Array Elements (Black Trace)

Table 5-3 Average Centre Frequency and -6dB Fractional Bandwidth of the Manufactured Arrays

Array Type	PZT-5H		PMN-29%PT	
	1.5 MHz	3.0 MHz	1.5 MHz	3.0 MHz
f_c (MHz)	1.52	2.94	1.54	3.09
BW_{-6dB}(%)	21.2	26.1	37.9	18.1

The measured centre frequencies of the four arrays (Table 5-3) are in good correlation with the electrical impedance measurements presented in Table 5-1. Furthermore, the low fractional bandwidths of the prototype transducers are related to the long ring down time of their piezoelectric elements. This is caused by the microbaloon-filled epoxy backing material, which has much lower acoustic impedance than the active material and low attenuation in order to maximize transmission efficiency and to reduce device self-heating.

5.4.2 Experimental Beam Profiling and Array Element Directivity Measurements

Beam profiling with the scanning tank was performed for all four types of phased arrays at two focal distances and four different steering angles (Table 5-4).

Table 5-4 Beamsteering Angles and Focal Distances Used for Beam Profiling

Array Resonance Frequency	Focal Distance (mm)	Steering Angles (°)
1.5 MHz	5.0	0, 15, 30, 40
	10.0	0
3.0 MHz	5.0	0, 15, 30, 40
	8.0	0

As previously described in Section 5.2.3, the phased arrays were driven with an excitation voltage of 15 V_{PP}, which corresponded to the lowest output of the FI Toolbox. However, at this voltage, the PNP levels achieved by the 3.0 MHz PMN-29%PT array at focus were higher than the safety limit for the needle hydrophone. Thus, the duty cycle ($T_{\%ON}$) of the excitation voltage was reduced from the standard 70% used for the other transducers (Section 5.2.3) to 20%. A detrimental effect of lowering $T_{\%ON}$ of the pulse excitation by such a large amount was an increase in the noise level of the driving signal. Table 5-5 presents the maximum PNP levels at focus achieved by the four types of arrays.

Table 5-5 Maximum PNP Measured at the Focal Distance for Various Steering Angles

Focal Distance in Z (mm)		5				10
Steering Angle		0°	15°	30°	40°	0°
Array Type		PNP (MPa)				
1.5 MHz	PZT-5H	0.29	0.30	0.26	0.22	0.22
	PMN-PT	0.38	0.39	0.35	0.30	0.24
3.0 MHz	PZT-5H	0.67	0.57	0.39	0.28	0.51
	PMN-PT[1]	0.63	n/a[2]	0.38	0.25	0.49

[1] Duty cycle of excitation voltage reduced to 20% to avoid damage to the NH

[2] Value not included due to an error with the measurement

As expected, PNP decreased with steering angle and focal distance. Two slight variations from the general trend occurred at the steering angle of 15° for both types of 1.5 MHz arrays, which achieved higher PNP magnitudes at 15° steering than at 0°. This phenomenon can be explained by evaluating the directivity of the individual array elements at a radius of 5 mm from their centre. Figure 5-13 shows that the average directivity of the elements increased up to 7% at angles between 5° and 28° compared to the central axis, which can thus be related to the increase in PNP at 15° steering.

Average Directivity of the Array Elements

The directivity of each array element was determined from the acoustic pressure magnitude, simulated at equally spaced points along a semicircle centred on the middle of the element. The transducer and a reduced size water load were simulated in 3-D with FEA, while the pressure at the points on the directivity semicircle was determined with time-domain Kirchhoff extrapolation. Only the investigated array element was electrically excited in each simulation, while the other elements were included in the model to account for cross coupling and laterally propagating vibration modes. The directivities of all array elements were then averaged to determine the mean element directivity of each prototype transducer.

The element directivity patterns were evaluated at radii of 5 mm and 100 mm (Figure 5-13). The shorter radius corresponded to the focal distance of 5 mm evaluated as part of the array beam profiling methodology presented earlier in Table 5-4 and the longer radius was evaluated to demonstrate the average array element behaviour far from the transducer aperture. The directivity plots of all four types of arrays show their elements have wide beams, with sidelobes close to zero, which is due to the $\lambda/2$ element spacing.

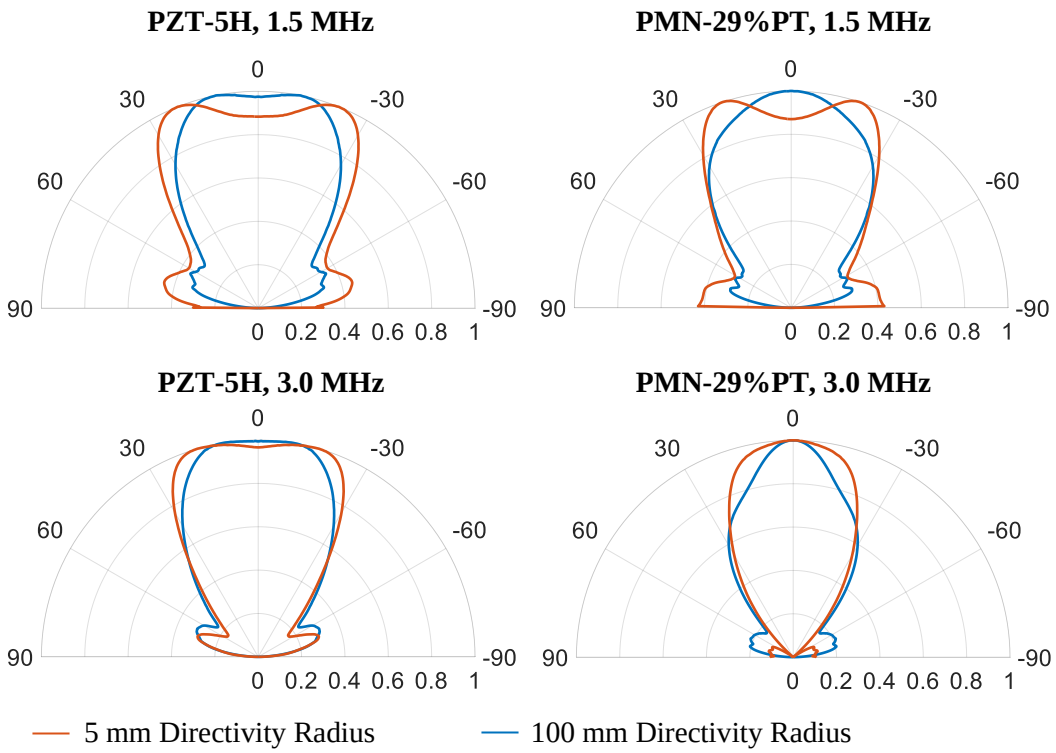

Figure 5-13 Simulated Average Array Element Directivity at a radius of 5 mm and 100 mm

5.4.3 Comparison of the Beam Profiles and PNP Magnitudes between Simulation and Measurement

Beam profiles produced by the two simulation frameworks described in Section 5.3.1 (FEA combined with time extrapolation and FEA-only) were then cross compared with the experimental data for all beam-steering cases in Table 5-4. Each framework was further subdivided in simulation profiles that evaluated and cross compared the following:

- Driving voltage type: ideal sine burst or waveform imported from one channel of the FI Toolbox array controller;
- Effects of electrical interconnects: not included or simulated as RLC (with component values measured experimentally);
- Piezoelectric material properties: original and modified set (following the optimization procedure described in Section 5.3.2). The modified set was only evaluated in conjunction with the FI Toolbox driving voltage.

A total of 12 different simulation profiles (6 profiles for the FEA + Extrapolation, and 6 profiles for the FEA only framework) were compared with the experimental data and their structure is presented schematically in Figure 5-14. Furthermore, it should be noted that because of the reduced kerf size of the 3.0 MHz, PMN-29%PT array, the computation size of

modelling the full-FEA load was larger than the available computational resources, and therefore, that framework could not be used to simulate the array.

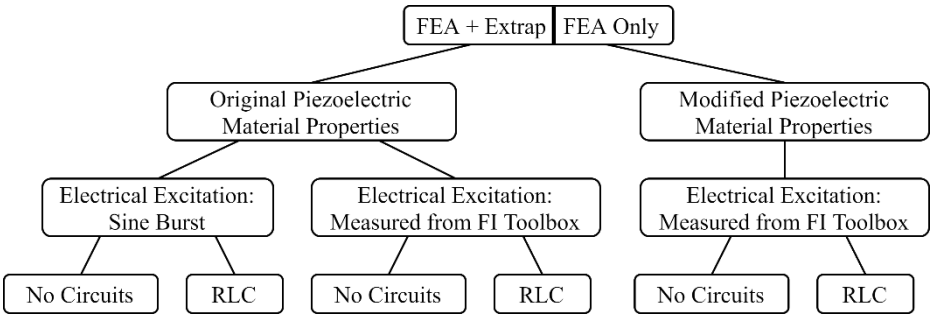

Figure 5-14 List of the 12 Different Simulation Profiles (6 Profiles for FEA + Extrap, and 6 Profiles for the FEA Only Framework) Compared to the Experimental Data

1-D Phased Array Focusing: Beam Profile Comparison between the Manufactured and the Simulated Arrays

In order to compare the experimental and modelled beam profiles in the XZ plane, the -1 dB, -3 dB, and -12 dB contours of the pressure distributions were overlaid on the same graph, as illustrated in Figure 5-15. The two main outcomes of the comparison are the evaluation of errors in the steering angle and in the focal distance of the simulated beams. These two aspects are important in assessing the feasibility of implementing array driving parameters (phase delays and driving voltage amplitudes) derived from software models directly into therapeutic planning.

To correctly overlay the dB contour plots, a series of steps were implemented with a MATLAB GUI (Figure B-4, Appendix B). Firstly, as the X and Z scanned dimensions were not always the same as the model dimensions, the larger dataset was reduced to the dimensions of the smaller one. Secondly, because the FEA model step size was smaller than the scanning tank resolution, the former data matrix was interpolated to the same spatial resolution as the simulation and then both magnitude datasets were normalized and transformed into logarithmic scale. Finally, in order to account for small errors in the X or Z beam alignment of the NH scan, the program was designed to allow for linear translation of one plot with respect to the other. Figure 5-15 provides an example of overlaid beam profile plots between the two simulation frameworks (FEA-only and FEA + time extrapolation) and the beam profile measured with the scanning tank, for the 1.5 MHz, PZT-5H array, focused at 5.0 mm and steered at 0° and 40°.

As observed in Figure 5-15, both simulation frameworks provided very good agreement with the beam profiles measured using the scanning tank, highlighting even minor beam features at the -12 dB level. Furthermore, the -1 dB contours, which were of the highest relevance to

the study, demonstrate excellent correlation, highlighting the potential to use simulation to accurately predict the array focal region and steering angle.

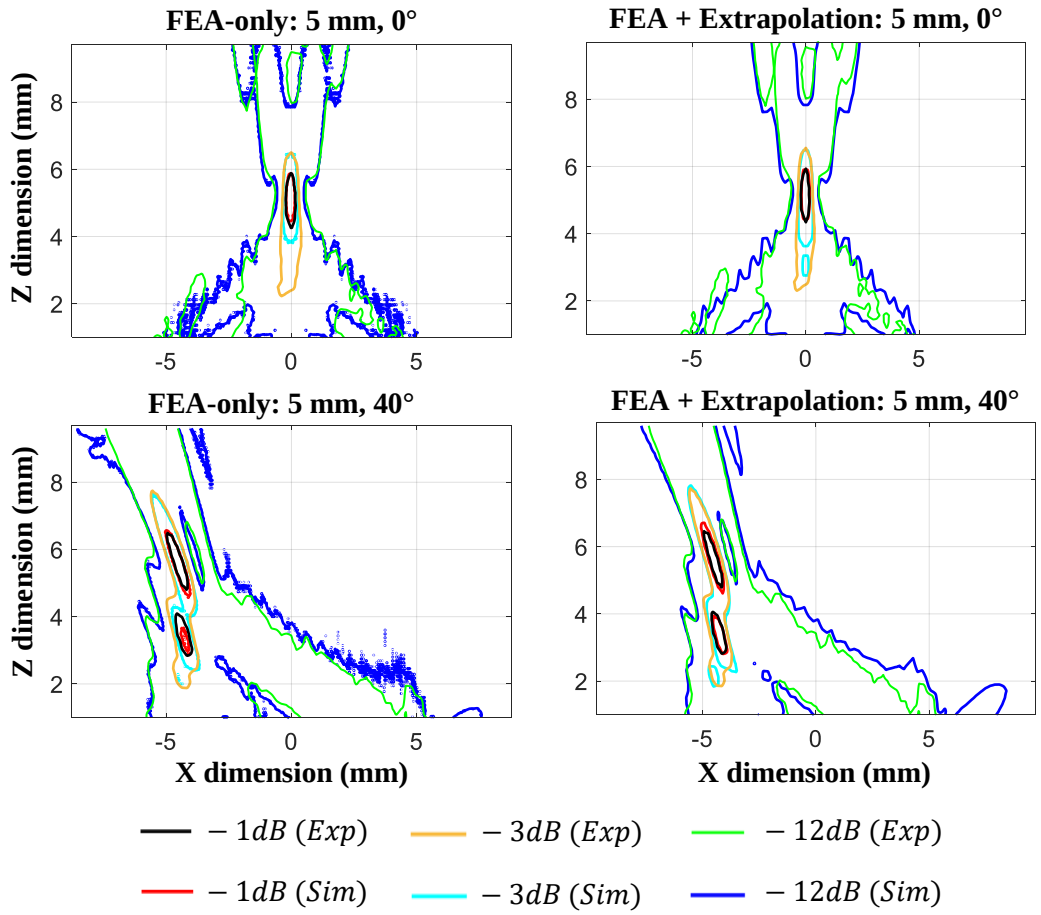

Figure 5-15 dB Profile Comparison Between the Simulated (Sim) and the Experimentally (Exp) Measured Acoustic Beam Profiles for the 1.5 MHz, PZT-5H Array, Focused at 5.0 mm

The beam profiles of both the FEA + time-extrapolation and the FEA-only frameworks were also very similar with each other. The FEA-only method had a certain degree of noise, especially at lower PNP values, as in the case of the -12 dB contour. The reason for this negative effect was the uneven mesh size ratio of $X{:}\,Y{:}\,Z = 1{:}\,1{:}\,1.5$ applied to reduce model size, which led to divergence of the FEA constitutive equations. It was determined that for a mesh size ratio of $1{:}\,1{:}\,3$, the noise became much higher, impacting the -1 dB and -3 dB beam contours as well, while a mesh size ratio of $1{:}\,1{:}\,1$ would not simulate because of the model size being too large to process. Therefore, all simulations were set to the mesh size ratio of $X{:}\,Y{:}\,Z = 1{:}\,1{:}\,1.5$.

The same type of comparison was performed for all 12 simulation profiles, with similar results in terms of the beam shape comparison. One exception occurred however for the simulation of the PMN-29%PT, 3.0 MHz array, driven by the 20% duty cycle excitation signal, through

coaxial cables. The combined effect of the noisier excitation signal imported from the FI Toolbox and the connecting cables led to variations in the shape of the simulated beam profile compared to the measured data, which were not as obvious when the cables were not included in the simulation (Figure 5-16).

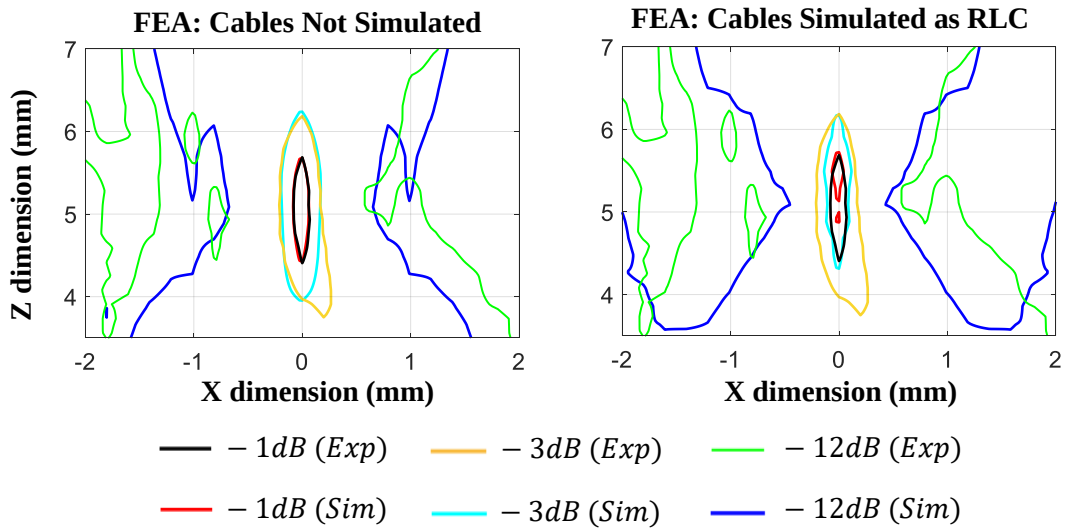

Figure 5-16 dB Profile Comparison Between the Modelled (Sim) and the Measured (Exp) Beam Profiles with and without the Inclusion of Connecting Cables in the Simulation, for a Noisy Driving Voltage

The RLC equivalent circuit of the cables acted as a low-pass filter, with a resonance frequency around 11 MHz. The resonance of the RLC was close to a higher-frequency spectral component of the 20% duty cycle excitation voltage used to drive the array, which led to an amplification of that frequency component (Figure 5-17). The respective frequency component was also near a spurious resonance of the modelled PMN-29%PT, 3.0 MHz phased array, which amplified that mode of vibration, affecting the beam profile produced by the simulation.

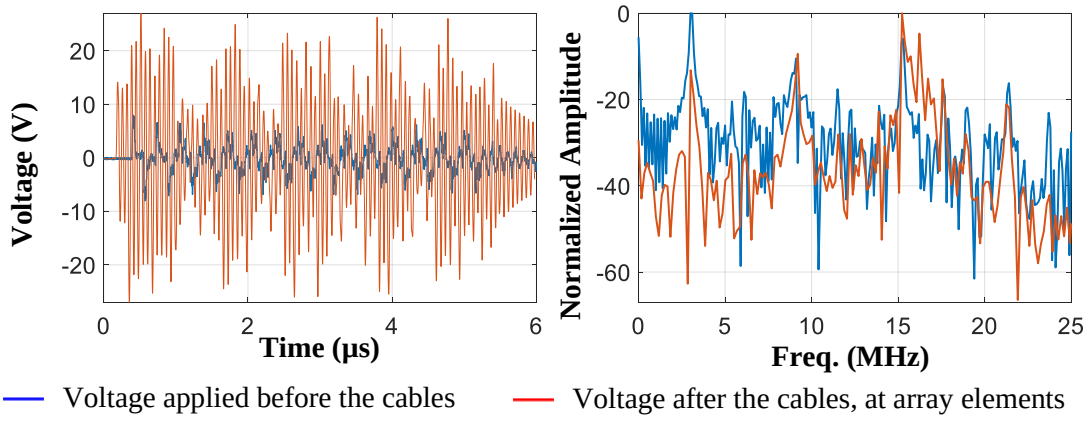

Figure 5-17 FEA: Combined Detrimental Effect of the Connecting Cables and Noisier Driving Voltage Imported from the FI Toolbox

This observation was further backed by an investigation of the simulated pressure waveforms in the frequency domain. In the case of no cables simulated, the power of the frequency mode around 15 MHz was less than half of the power at the main resonance of 3.0 MHz, however, when the cables were included in the simulation, the high frequency mode was the dominant peak in the spectrum by a factor of greater than two compared to the main 3.0 MHz resonance. On the other hand, this phenomenon was much weaker in the manufactured array due to its lower electrical impedance than in the simulation, which damped the effect of the cables. The influence of the RLC cable resonance on the driving voltage was not as significant in the other simulations.

Regarding simulation processing time, the FEA method required an average of 1hr45m computation time, and the FEA + time extrapolation required about 1hr00m for the 1.5 MHz arrays. FEA-only required 4hr00m, and FEA + time extrapolation required an average of 2hr30m for the 3.0 MHz transducers. Therefore, the FEA combined with time-extrapolation framework proved to be computationally faster than the FEA-only method and it provided good match with the experimental data. Additionally, the use of time extrapolation rather than FEA for simulating US propagation in a uniform load such as water or tissue was much less demanding in terms of RAM memory usage, allowing for larger loads to be evaluated.

PNP Comparison between the Simulated Beam Profiles and the Experimental Data

The comparison between the simulated and the measured pressure magnitude data was performed on the average PNP value enclosed by the -1 dB profiles (PNP_{-1dB}) from both cases. This comparison parameter was chosen instead of the maximum PNP value in the beam because the -1 dB profile corresponded to the area of therapeutic relevance, whereas the spatial maximum PNP value was measured only at one single point in space. Table 5-6 provides the comparison outcomes for all four array types given as the average ($\bar{R}$) and standard deviation (σ) of the ratio between the simulated and the measured PNP expressed as percentage for all steering angles and focal distances enumerated in Table 5-4.

$$\bar{R} = \frac{\sum_1^N R_i}{N}\,, \qquad \sigma = \sqrt{\frac{\sum(R_i - \bar{R})^2}{N}} \qquad \text{Eq 5.8}$$

where $R_i = \frac{PNP(i)_{-1dB\ Measured}}{PNP(i)_{-1dB\ Simulated}} * 100$, $N = 5$ (total number of steering angles and focal distances evaluated per simulation profile).

Table 5-6 Average Percentage Ratio ($\bar{R}$) and Standard Deviation (σ) Between the Measured and the Simulated PNP_{-1dB} for all Simulation Profiles

			Original Materials				Modified Materials	
			Sine Burst		DSL Waveform		DSL Waveform	
			No Circuits	RLC	No Circuits	RLC	No Circuits	RLC
PZT-5H 1.5 MHz	FEA + Extrap	$\bar{R}$	67.5	66.7	60.9	60.2	99.3	98.3
		σ	1.76	1.73	1.92	1.93	2.82	2.75
	FEA only	$\bar{R}$	64.8	64.0	58.5	57.7	93.4	92.1
		σ	2.34	2.32	2.13	2.10	2.97	2.89
PMN-PT 1.5 MHz	FEA + Extrap	$\bar{R}$	67.9	67.5	57.8	57.5	95.1	93.9
		σ	3.79	3.75	2.94	2.85	2.86	2.85
	FEA only	$\bar{R}$	64.8	64.5	55.9	55.6	90.6	89.3
		σ	2.57	2.56	2.07	2.13	3.23	3.21
PZT-5H 3.0 MHz	FEA + Extrap	$\bar{R}$	44.9	43.0	37.2	35.5	57.0	54.2
		σ	3.83	3.76	3.09	3.08	4.69	4.43
	FEA only	$\bar{R}$	43.0	41.0	35.2	33.6	55.1	52.5
		σ	5.97	5.78	5.08	4.97	8.02	7.61
PMN-PT 3.0 MHz	FEA + Extrap	$\bar{R}$	N/A[1]		80.7	74.1	181.0	122.0
		σ			8.64	7.08	23.12	14.57

[1] The 3.0 MHz PMN-PT array was not simulated with sine wave excitation because the $T_{\%ON}$=20% excitation signal could not be directly equated to an RMS equivalent value for the sine wave signal

An analysis of the data in Table 5-6 shows the average difference in $\bar{R}$ between the FEA-only and FEA + time extrapolation frameworks was only -2.93%, and the difference in σ was 0.73%. The results demonstrated that the FEA + time extrapolation framework produced comparable outcomes in comparison to the sole FEA-based method in simulating both the beam profile and the actual PNP magnitude in uniform loads. The added benefits of using extrapolation to model ultrasonic propagation in the load are the reduction in computational demands on the workstation and the ability to simulate larger loads than with FEA only.

The second observation is the modified piezoelectric materials used in the simulations led to an average PNP_{-1dB} fit ($\bar{R}$) of 94% with the pressures measured from both types of 1.5 MHz arrays under test. The active material properties were modified following the impedance correlation optimization for the bulk 1-3 piezocomposite materials, with resonance frequency of 1.5 MHz. However, the average $\bar{R}$ was only 54.7% in the case of the 3.0 MHz, PZT-5H array with the modified piezoelectric material properties, which was attributed to manufacturing degradation, especially during lapping to a more reduced thickness. The large

increase in $\bar{R}$ and σ for the 3.0 MHz, PMN-29%PT array with modified material properties was mainly credited to errors in the FEA simulation of the noisier excitation voltage, which was richer in higher-frequency spectral components.

PNP Comparison between Measurements and Simulation at Various Driving Voltages

The comparisons in PNP presented in Table 5-6 were evaluated for a driving voltage of 15 V_{PP}. In order to obtain a full understanding of the correlation between the simulated and the fabricated arrays, the effect of varying the driving voltage amplitude also required investigation. This final comparison evaluated the fit in PNP_{-1dB} between simulation and measurement for the two 1.5 MHz arrays, focused at 5.0 mm, with 0° steering, driven with different excitation voltages from the FI Toolbox. Each voltage level was measured and logged with an oscilloscope following the same procedure as detailed in Section 5.3.1. The voltage waveform was then included in the FEA-only framework for the 1.5 MHz, PZT-5H and PMN-29%PT arrays, and the resulting beams were compared with the NH data (Table 5-7). $\bar{R}$ dropped for both arrays when the excitation voltage was changed from 15 V_{PP} to 20 V_{PP}, but it then remained almost constant (around 80%) with further increases in voltage. This demonstrates that the driving voltage has limited impact on the accuracy of the simulation.

Table 5-7 Percentage Ratio in PNP_{-1dB} Between Measurement and Simulation at Various Driving Voltage Amplitudes

	$\bar{R}$ (PZT-5H, 1.5 MHz)	$\bar{R}$ (PMN-29%PT, 1.5 MHz)
15 V_{PP}	89.4%	88.3%
20 V_{PP}	80.3%	82.5%
25 V_{PP}	79.7%	81.6%
30 V_{PP}	79.9%	81.6%

5.4.4 Discussion and Further Observations

Effect of Lateral Load Size on the Beam Profile and PNP of the Simulated Arrays

As previously discussed in Section 3.4.1, the simulated water load was surrounded by absorbing boundaries to avoid US reflections at the edges of the model. Initially, the load width extended a further 0.5 mm from either side of the array in the elevation direction (Section 5.3.1), which corresponded to $\lambda/2$ at 1.5 MHz and λ at 3.0 MHz. The load protrusion in the transducer length direction was much larger, with 3.0 mm added at each side of the array to allow for beam steering.

The reduced load protrusion in elevation (LP_e = 0.5 mm) led to a compression of the beam in the passive aperture plane (YZ) of the simulated array, impacting both the beam shape and

PNP. LP_e was then increased from 0.5 mm to 2.5 mm, and the results for the PZT-5H, 1.5 MHz array, focused at 9 mm are presented in Figure 5-18.

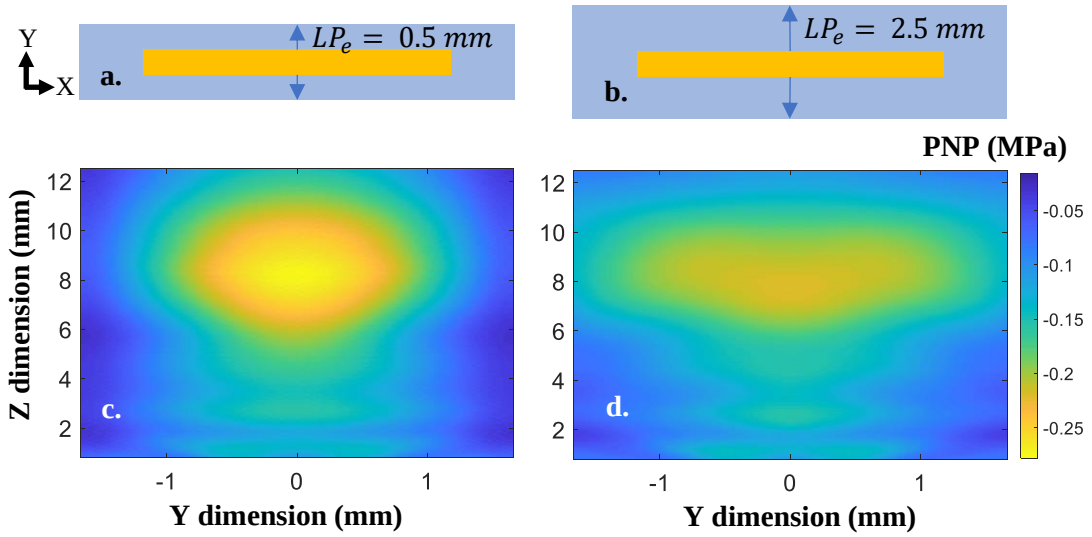

Figure 5-18 Effect of Varying Load Protrusion Size in Elevation (FEA Model of PZT-5H, 1.5 MHz, Focused at 9 mm): a.-b. Model Top View, Highlighting the Load Protrusion Size in Elevation; c.-d. Resulting Beam Profiles in the Elevation – Depth (YZ) Plane

For the 1.5 MHz, PZT-5H array, the average percentage difference in PNP_{-1dB} between the LP_e = 0.5 mm and the LP_e = 2.5 mm cases, evaluated for all steering angles and focal distances described in Table 5-4, was 13.2%, with a standard deviation of 8.2% in the case of the FEA-only framework. For the FEA + time extrapolation framework, the difference in PNP_{-1dB} was 3.1% and the standard deviation 0.7%. A further increase of the load protrusion in elevation (LP_e > 2.5 mm) did not bring any significant change in the simulated beam profile or PNP compared to the LP_e = 2.5 mm case, but only increased the computation size of the model.

The increased pressure magnitude and the more compressed beam shape provided by the LP_e = 0.5 mm case shows the simulated US field was affected by the absorbing boundaries of the load, which were set too close to the beam. The first argument to support this observation is that load elevation protrusions larger than LP_e > 2.5 mm provided almost identical beam patterns as the LP_e = 2.5 mm case, but significantly less compressed than the LP_e = 0.5 mm case. Secondly, as the acoustic field diverged with depth from the array surface, the FEA-only framework was more affected by the absorbing load boundaries than the FEA + time extrapolation, which is indicated by the lower percentage difference in PNP_{-1dB} for the extrapolation case. The reason is the latter framework only employed FEA to simulate a small load depth, while the extrapolation in the remaining load (where the acoustic filed diverged towards the model edges) did not consider boundary effects. Considering the above observations, all 1.5 MHz models in this chapter were run with a load protrusion of 2.5 mm at each side of the array in the elevation direction.

As λ in water halved at 3.0 MHz, the LP_e = 0.5 mm did not lead to a significant compression of the beam compared to a larger evaluated case of LP_e = 1.0 mm. Above LP_e = 1.0 mm, the model could not be simulated due to increased computational size. The load protrusion in elevation was therefore kept at 0.5 mm for the 3.0 MHz arrays throughout this chapter in order to reduce simulation time.

Model Accuracy in Relation to the Manufactured Transducers

In order to have similar resonance frequency, the manufactured transducers were lapped to an average 11.4% larger thickness than predicted by the initial FEA models (Section 4.3.2). Furthermore, the thickness coupling coefficient of the manufactured arrays was lower than the simulated $\bar{k_t}$ by an average of 20.6%. The lower $\bar{k_t}$ of the fabricated transducers was an important source of error that led to the large PNP mismatch between the simulation and the measured datasets. The optimization algorithm for the electrical impedance correlation used the average measured transducer thickness and varied the piezoelectric material coefficients to align the coupling coefficient of the modelled 1-3 piezocomposites with that of the actual materials. The optimization was performed only on bulk piezocomposites, with a resonance frequency of 1.5 MHz, as ideally, the piezoelectric material coefficients should be constant, and not differ for the thinner materials resonating at 3.0 MHz. The PNP fit between simulation and measurement improved significantly for the 1.5 MHz arrays with modified material parameters, and improved moderately for the piezoceramic composite array resonating at 3.0 MHz. A better PNP fit would have been achieved if the 3.0 MHz, PZT-5H composite material was optimized in a similar manner as the 1.5 MHz one. Whereas, the 3.0 MHz single crystal array suffered from large manufacturing variations between the bulk material and the finalized transducer, poorer performance in terms of noise because of the lower duty cycle excitation signal required to protect the NH, and hence, was not a good candidate for this optimization method.

The general observation was the manufacturing process led to variations in the properties of the active material, mostly through degradation of its properties, but also through clamping from the polymer phase in the 1-3 piezocomposite and added stiffness from the electrodes. Optimizing the correlation between the impedance of the finalized bulk 1-3 piezocomposite and the simulated material through modification of the modelled piezoelectric material coefficients led to an improved PNP fit between the fabricated array and the simulated one.

Beam profiles are related to the geometry and the mechanical characteristics of the transducers and the load, rather than the piezoelectric properties. Therefore, the beam shape is mostly influenced by: resonance frequency, modes of vibration, lateral array geometry and acoustic

impedance. The optimization algorithm did not significantly change the resonance frequency or lateral geometry of the array (only the thickness was modified), and the spurious modes also remained well detached from the frequency of the main resonance or of the driving voltage. Therefore, the beam profiles did not vary considerably between the optimized FEA models and the initial ones, and their fit with the scanning tank data was in all cases very good. The 3.0 MHz, PMN-29%PT array was the only exception because the combined detrimental effect of the simulated connecting cables and noisy excitation voltage led to the amplification of higher frequency lateral modes that interfered with the main resonance, altering the shape of the beam.

The PNP magnitude achieved by an array in the load is dependent on both the beam profile and on the electrical characteristics of the transducer and controller (piezoelectric properties, driving voltage, driving circuits). A mismatch in the piezoelectric properties of the transducer leads to an altered efficiency and, inherently, to variations in PNP magnitudes in the load between simulation and the fabricated array case, while the beam profile is not affected, provided lateral modes are still decoupled. Therefore, the gains of modifying the piezoelectric properties of the modelled transducer to optimize the electrical impedance fit with the measured one are the achievement of a more realistic model of the array under test, and the better correlation in PNP magnitude output with the real case.

However, the optimization algorithm is not entirely necessary if a deep understanding of the transducer behaviour is not intended, and the purpose of the simulations is solely to predict the beam profile and the PNP magnitudes attained at focus. Given the average standard deviation in PNP_{-1dB} between both FEA frameworks and the experimental measurements was only 3.41% (excluding the 3.0 MHz PMN-29%PT array case), a correction factor of the form $C_F = \bar{R}$ multiplied to the simulated PNP would suffice.

The effect of including the connecting cables as an RLC circuit in series with the array elements (excluding the 3.0 MHz, PMN-29%PT case) consisted in an average decrease in $\bar{R}$ of 1.9% compared to simulation profile that did not consider them. The inclusion of the driving electrical signal from the FI Toolbox into the FEA models made the simulations more realistic and led to an average decrease in $\bar{R}$ of 6.8% compared to using a pure sine wave burst with $V_{RMS} \approx V_{RMS-\,FI\,Toolbox}$. The beam profiles changed slightly between the two simulation cases due to the higher frequency content of the real driving voltage. The worst case was for the 3.0 MHz, PMN-29%PT array, with simulated cables, in which the simulation amplified a spurious mode that was not as evident in the measured dataset, affecting both the beam profile fit and $\bar{R}$.

Sources of Errors between Simulations and Measurements

The array elements located at the edges of the manufactured transducers had a damped electrical impedance response compared to the other elements due to increased lateral clamping with the epoxy filler surrounding the casing. Furthermore, because of imperfect flexi bonding, some array elements had either slightly shifted resonance behaviour (i.e. f_r of element 1 in the 1.5 MHz, PZT-5H array was 110 kHz, or 7% lower than the average f_r) or higher electrical impedance (the impedance of element 1 was around 1.7 times higher than the average element impedance). These two error sources led to slight variations in beam steering between simulations and the scanning tank data and also to a possible drop in the measured PNP. However, none of the arrays had any dead elements, which minimized this error source.

Machining of the piezoelectric materials led to degradation of their properties through dicing and lapping. Exposure to elevated temperatures, leading to piezoelectric degradation, was also required at various stages in the array manufacturing process: 1-3 piezocomposite potting, curing of the Ag ink electrodes, curing of the electrically conductive adhesive for flexi circuit bonding, as well as melting the wax holding the composite material on the lapping machine glass holder.

The driving voltage recorded from the FI Toolbox for inclusion in the FEA simulations was averaged and great care was taken to minimize impedance mismatch with the data logging system to reduce errors. However, a 1-2% drop in the FI Toolbox power supply voltage was noted after prolonged operation time, probably due to heating of the device's internal electronics. This issue could have led to a decrease in the array pressure output during beam characterization within the scanning tank. Another significant error source was due to the impedance mismatch between the FI Toolbox and the array elements. The simulated array elements had a higher electrical impedance at resonance than the manufactured transducers. The optimization algorithm reduced the mismatch, thus decreasing the error.

A large source of uncertainty in the pressure magnitude measurement with the scanning tank was the needle hydrophone. Even if a complex deconvolution method was employed to extract the pressure amplitude waveform from the NH voltage more faithfully than fixed sensitivity division, the NH sensitivity calibration had a 14% uncertainty according to the manufacturer. However, it is worth noting that this error source did not affect the shape of the recorded beam profile contours since it is related to the frequency of the signal, and therefore applies evenly to all the spatial points in a beam profile scan.

Great care was taken to keep the aforementioned sources of error at a minimum and, where possible, to integrate variations in the FEA models (through the optimization algorithm) and account for instrumental errors (the inclusion of the FI Toolbox driving voltage or NH deconvolution procedure). However, due to the random nature of some error sources, they could not be accounted for in the simulation frameworks, leading to differences in impedance spectra, beam profiles and PNP values. Importantly, a significant number of comparisons were performed to understand the errors and to determine solutions to mitigate them, in order to obtain a strong correlation between the simulations and the fabricated arrays.

5.5 Conclusions

Chapter 5 evaluated the correlation between the measured and the simulated acoustic beam patterns in water from the four experimental therapeutic 1D phased arrays. The experimental beam pattern characterization process was performed with each transducer dipped in deionized and degassed water, using a NH coupled to a 3-DOF linear scanner. In order to increase the accuracy of the measurements, the complex (magnitude-phase) sensitivity transfer function of the NH was deconvolved from its output voltage waveforms to recreate the acoustic pressure. The arrays were driven with a 32-channel DSL FI Toolbox controller based on hardware from National Instruments. Several modifications were brought to the array controller software in order to repurpose it from imaging applications to a more therapeutic oriented driving, namely, to increase PRF by minimizing the scan range and the time delay between successive bursts. A trigger line was also added to the machine in order to synchronise it with the scanning tank during beam characterization.

Two simulation frameworks were developed to simulate the acoustic beam patterns in water achieved by the modelled arrays. The first framework used a combination of FEA modelling (for the transducer and a reduced part of the water load in its vicinity) and Kirchhoff time extrapolation for the majority of the load. The other framework used FEA for the entire model. The simulated beam patters were compared to the ones measured with the scanning tank with two parameters of interest investigated: beam shape fit (expressed as -1 dB, -3 dB, -12 dB contours) and PNP_{-1dB}, corresponding to the average PNP value enclosed by the -1 dB profile. The comparisons yielded good results in terms of the beam shape fit, but the average ratio, $\bar{R}$ between the measured and the simulated PNP_{-1dB} was slightly larger than one half.

In order to improve the simulation reliability, the driving voltage measured from the array controller was included in the model and the connecting cables to the arrays were measured and simulated as an RLC circuit. The combination of the two led to a further decrease in $\bar{R}$.

As an important reason for the low value of $\bar{R}$ was the large difference in coupling coefficient between the modelled and the fabricated transducers, an optimization algorithm was employed to minimize the differences in f_r and f_a by modifying the piezoelectric material constants, based on the correlation of electrical impedances. The algorithm also accounted for the difference in the active material thickness between the initial FEA models and the manufactured transducers. The inclusion of the modified 1-3 piezocomposites in the pressure models led to an increase in $\bar{R}$ to an average of 94% for the 1.5 MHz arrays, on which the optimization was performed in the first place. The 3.0 MHz arrays had a greater difference in $\bar{R}$ because of the manufacturing variations and noisier driving signals (in the case of the PMN-29%PT). It was assumed that an optimization performed on the bulk materials of the higher frequency arrays, as in the case of 1.5 MHz piezocomposites, would bring $\bar{R}$ closer to a better fit.

The combined FEA and time extrapolation model produced similar outcomes with the FEA-only model, with even a lower standard deviation between all test cases, rendering it a good option for simulating larger, but uniform loads, where FEA would become too computationally demanding. Given the low standard deviation in PNP_{-1dB} of 3.41% between simulation and measurement, enforced by the large number of assessed cases and variables, the PNP fit can be improved towards 100% by simply multiplying the simulation output with a correction factor equal to $\bar{R}$.

Considering the results of this chapter, it is safe to state that a good correlation between simulation and measurement can be established, allowing FEA models to be employed in determining array driving parameters (phase delays and driving voltage characteristics) for therapeutic ultrasound procedures. Simulations could therefore be used to predict therapy dosage and localization, given tissue and array parameters are known well.

6 *In-vitro* Sonoporation

6.1 Introduction

The two experimental PZT-5H, 1D phased arrays with resonance frequencies of 1.5 MHz and 3.0 MHz were used to sonicate human epithelial colorectal adenocarcinoma cells (Caco-2 cells, ATCC, Rockville, USA) developed on ThinCert^{TM} porous PET membranes (Greiner Bio-One, Austria). The *in-vitro* procedure was aimed to evaluate the ability of the transducers to sustain cellular membrane disruption through sonoporation, and to perform targeted drug delivery. The experiments were performed in collaboration with M. Turcanu from Glasgow University, who designed the *in-vitro* procedure setup.

MBs (SonoVue, Bracco, Milan, Italy) were introduced in the test medium to promote cavitation and improve therapeutic effectiveness. The arrays were focused on the membrane and steered at different angles along the direction of the active aperture in order to maximize the sonicated area. As an alternative, a diffuse focus method was investigated in relation to therapy effectiveness, and was implemented by setting the focus of the array behind the active layer. Various parameters related to electrical driving and US pressure magnitude at the target were evaluated in the study, including duty cycle ($T_{\%ON}$), pulse repetition frequency (PRF), and MI.

Therapeutic effectiveness was assessed in real-time, during insonation by measuring the transepithelial electrical resistance (TEER) of the cell layer. The post-therapy assessment included confocal and fluorescence microscopy to assess the insonation effects on the cellular structure, and spectrophotometry with a plate reader to evaluate the amount of fluorescein dextran (FD, here FD3 or FD4) that extravasated through the cell layer as a result of the US therapy.

6.1.1 Experimental Setup and Equipment

The experimental 1D phased array was dipped into the culture insert of the ThinCert^{TM} (Figure 6-1 a.), facing the Caco-2 monolayer on the bottom of the insert (Figure 6-1 b.). The inner (apical) chamber was filled with a suspension of 5% MBs and 100 µg/mL FD3 or FD4 in Hank's Balanced Salt Solution (HBSS), while the exterior (basal) chamber was filled with HBSS only. A syringe pump was set to supply 4 mL/min of suspension into the culture insert, and overflow was avoided with an aspirator pump. This arrangement was necessary in order to ensure a fresh supply of MBs during the entire period of insonation and to reduce the temperature increase generated by the transducer operation. TEER measurements were performed between the apical and basal chambers of the cell well during insonation, while

temperature readings of the medium in the culture insert were made with a thermocouple placed in the proximity of the cell monolayer.

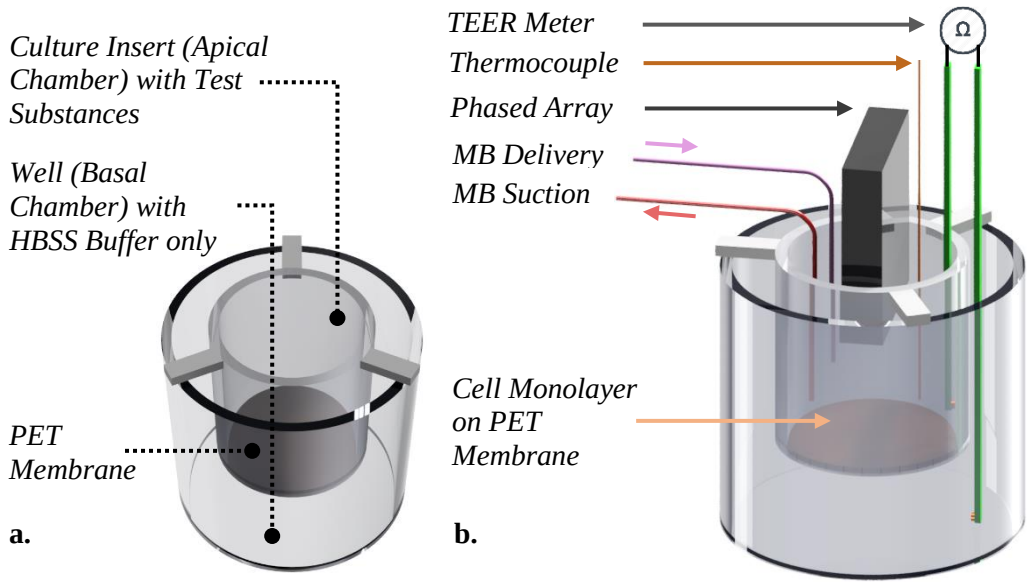

Figure 6-1 a. ThinCert™ Cell Well; b. in-vitro Sonoporation Experiment Setup (Designed by M. Turcanu)

At the end of the procedure, the HBSS solution in the basal chamber was sampled by M. Turcanu and then analysed with a plate reader (SpectraMax i3x, USA) to determine the amount of FD that extravasated through the cell monolayer as a result of the US therapy. The sonoporated samples were then optically inspected with macro imaging. Finally, confocal and fluorescence microscopy of the samples were performed by M. Turcanu at the Dundee Imaging Facility (www.lifesci.dundee.ac.uk/technologies/dundee-imaging-facility, University of Dundee, Dundee, UK). Phalloidin was used to label the cells prior to confocal microscopy due to its affinity for the filamentary actin (F-actin) found in the cellular cytoskeleton. A reduction in the stained F-actin fluorescence at the sonicated site represented an indication of the rupture of F-actin fibres and inherent changes in the cellular cytoskeleton structure due to membrane disruption following therapy [113].

ThinCert™ Cell Wells

The ThinCert™ well comprises two cylindrical chambers, separated by a PET porous membrane which can support epithelial and endothelial cell cultures (Figure 6-1 a.). The well represents the exterior chamber, while the apical chamber, positioned inside the well, is the culture insert. The latter contains the PET membrane on its bottom surface, which lies between the suspension in the culture insert and the control medium in the well. A multiwell plate contains 6 to 24 wells to allow multiple conditions to be assessed simultaneously. Generally, the basal chamber contains a buffer solution that ensures cell stability, while the apical

chamber contains the drugs under test. Applications of the ThinCert™ include studies of transport, secretion, diffusion and migration through the cell layers developed on the PET membrane, cytotoxicity and TEER measurements [254].

TEER Measurements

The electrical resistance of a cell is given by its resistance to the passage of ions, acting like a barrier [255]. The integrity of a cell layer can therefore be assessed by measuring the electrical resistance between the fluids in the two chambers of the well. An intact cell layer acts as an electrical insulator between the two media, leading to an elevated electrical resistance. Membrane disruption of the cell monolayer during insonation reduces the resistance of the barrier to ions, which in turn leads to a decrease in electrical resistance. The TEER meter is a volt-ohm meter that measures the electrical resistance between two chopstick-like electrodes placed in the two media separated by the cell layer (Figure 6-1 b.) [255].

Substances Used in the Experiment

The buffer solution (in this experiment, HBSS) has the purpose of maintaining a balanced PH level around the cells, preserving their chemical stability. Due to that property, HBSS was used as the MB and FD carrier medium, and as the control medium in the basal chamber of the ThinCert™.

FD3 and FD4 are fluorescent tracer molecules that do not readily enter through a healthy cell membrane due to their dimensions. The number following 'FD' describes the molecular weight of the dextran molecule, expressed as kilodalton, and it can be related to the molecule size. The accumulation of FD inside the cell or in the buffer solution from the basal chamber of the well is an indication of increased permeabilization of the cell membrane. A fluorescence plate reader is used to assess the amount of FD in the sampled medium by measurement of the fluorescence intensity.

The SonoVue MBs used in the experiments are lipid-based MBs, with a mean radius of 1.5 μm and with 95% of their size distribution under 10 μm [256]. The main usage of MBs in medicine is to act as contrast agents for US imaging; however, their range of applications extends to sonoporation and drug delivery [257]. The purpose of the MBs in the current study was to enhance the bioeffects of the US therapy and to act as cavitation nuclei, reducing the cavitation threshold for the acoustic field emitted by the array. A syringe pump was used to continuously deliver a suspension of MBs and FD in the culture insert during the therapeutic procedure in order to replace the depleted MBs resulting from insonation.

Feasibility Study Prior to the Array Implementation

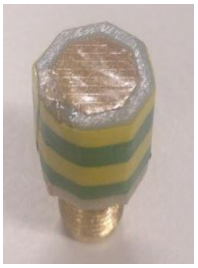

Figure 6-2 1.0 MHz Octagonal Transducer

An octagonal 1-3 piezocomposite single element, flat surface, 1.0 MHz transducer (Figure 6-2) was designed with the procedure detailed in Section 3.4 and manufactured in a similar manner as the 1D phased arrays. The single element transducer was used prior to the phased arrays to test the feasibility of the *in-vitro* setup based on the ThinCert™ due to its simpler operation and its similarity with other sonoporation studies in literature. Appendix C provides a short description of the manufacture and characterization of the experimental single element therapeutic transducer used in the initial feasibility experiments.

M. Turcanu performed *in-vitro* trials with the octagonal transducer, with the same experimental biology setup as for the phased arrays. The study results proved satisfactory and provided confidence to move onto the sonoporation array evaluation. The initial studies with the single element transducer are not described in detail here as they are outwith the primary scope of this Thesis. A comprehensive description of the study can be found in [22] and [258].

Choice of 1D Phased Arrays

The PZT-5H arrays were chosen over the PMN-PT ones due to the increased robustness of the piezoceramic compared to single crystal and due to better electrode bonding (Section 4.4.10). Additionally, as Section 5.4.2 demonstrated, the piezoceramic arrays obtained satisfactory MI levels for sonoporation even at a driving voltage as low as 15 V_{pp}, making them suitable for the *in-vitro* study. Both resonance frequencies of 1.5 MHz and 3.0 MHz were evaluated as part of the study in order to examine the relation between the driving frequency and the therapeutic effectiveness.

6.2 Methods

The 3.0 MHz array was placed at a distance of 7.0 mm from the ThinCert™ membrane, while the 1.5 MHz array (which has a larger active aperture) was placed at 9.0 mm from the membrane due to lateral size restrictions of the culture insert. The focal distance of each array was set to the distance between the transducer and the cell monolayer. Three insonation patterns were investigated, depending on the beam succession rate and on the focus type. The first procedure was studied in detail, while the other two were briefly tested for feasibility.

1. A continuous sweep of focused beams over a series of steering angles in order to cover the entire diameter of the ThinCert™ membrane in the array length direction (Figure 6-3). The procedure involved emitting a small number of bursts of focused US (pulses) at one

steering angle and then incrementing to the next angle, in a continuous loop. Shifting the steering angle after short insonation periods allowed time for fresh MBs to reperfuse the previously insonated areas and increase therapeutic effectiveness. Furthermore, the application of short US pulses at one spot of the cell monolayer followed by a longer time without sonication was adopted to avoid excessive damage caused by prolonged sonication of the same region, and potentially allow for reparable sonoporation.

2. A fixed-time focused-beam sweep, in which US was also emitted in pulses, similar to the continuous sweep method, but the steering angles were incremented only once. Therefore, each beam was active for an amount of time equal to the total insonation time over the number of beams employed in the sweep. The local reperfusion of MBs was more limited than for the previous method and the treated areas were exposed to a more concentrated dose of US.
3. A diffuse (divergent) beam, achieved by assuming the focus of the array is located at a virtual point behind the active aperture (-25 mm on the central Z-axis). The arrays were driven in pulses, similar to the previous focused methods, and the diffuse focus was expected to sonicate the entire treatment area simultaneously.

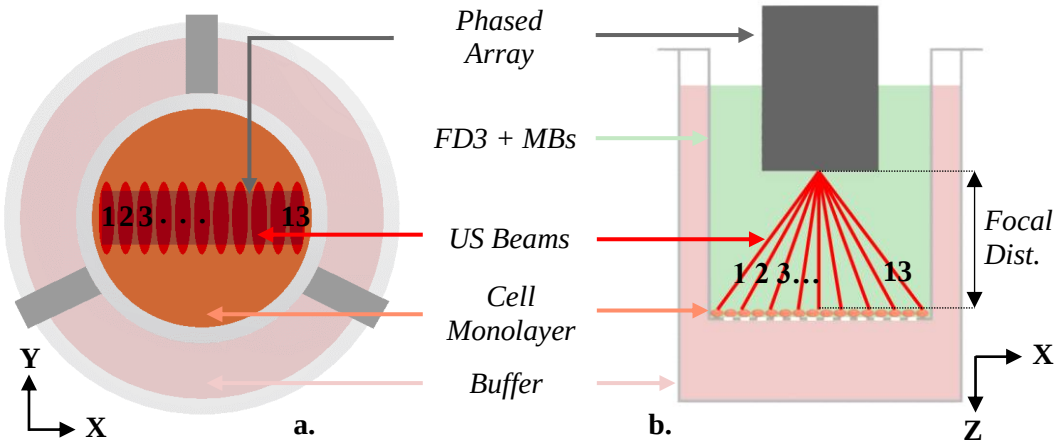

Figure 6-3 Beam Steering Inside the ThinCert™ Culture Insert: a. Top View; b. Side View

The focused US procedures concentrate the US energy in the vicinity of the cell monolayer, which is an advantage over the diffuse focus due to better localization of MB cavitation (Figure 6-4). Therefore, MB depletion in regions too distant to be therapeutically relevant is more limited in the case of a focused beam than for the diffuse focus. In addition, scanning tank measurements proved the diffuse focus method was not efficient for load penetration depths larger than 5.0 mm, which required the array to be brought closer to the ThinCert™ membrane (Figure 6-4 b.), rendering the use of the 1.5 MHz array not suitable for this method. Furthermore, the pressure distribution resulting from the diffuse focus was uneven, which added uncertainty when assessing the sonicated region of the cell monolayer or setting the driving power for the transducer.

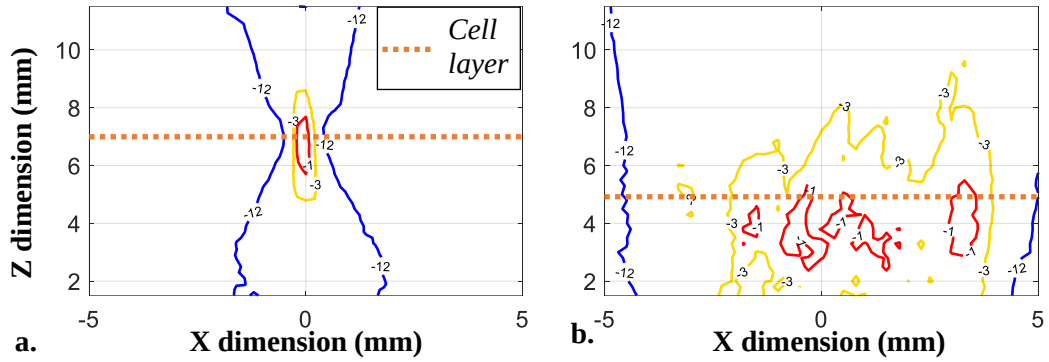

Figure 6-4 Sonoporation Protocols Employed for the 3.0 MHz Array: a. Central Focus at 7 mm; b. Diffuse Focus

Selection of Transducer Driving Parameters in Relation to Therapeutic Relevance

Trans-membrane drug delivery into cells depends on the acoustic cavitation of MBs in the vicinity of the cell membrane. Depending on the mechanical index, MB cavitation can be stable for low MIs or inertial at higher MIs. Generally, inertial cavitation leads to higher doses of drug delivery, but it also increases the rate of cell disruption and death. For sonoporation, the MI is chosen to minimize cell damage while maximizing bioeffects [257]. van Rooij et al. found that MIs of 0.3 and 0.5 were sufficient to achieve sonoporation in human endothelial cells, while an MI of 0.15 did not yield significant drug uptake at a 1.0 MHz insonation frequency [259]. They also showed that cell death was proportional to the sonoporation level. Other studies also show that relevant MI levels for MB-enhanced sonoporation are in the region of 0.15 to 0.5 [260], [261]. Furthermore, MI is closely related to the driving frequency as the cavitation threshold increases with frequency. In [262], it was found that sonoporation was 2.5 times more efficient at a 1.0 MHz insonation frequency than at 2.25 MHz for a constant PNP of 0.33 MPa, but at the cost of increased cell death at the lower frequency.

Considering the mechanical indexes presented in the literature, the MI levels tested as part of the current study were set in the interval {0.1 - 0.3} for the 1.5 MHz array and {0.1 - 0.4} for the 3.0 MHz device, investigated at increments of 0.1. Because the *in-vitro* medium was more similar to water than solid tissue, the deration factor of 0.3 dB/(cm*MHz) in Eq 2.2 was not considered in the calculation of the MI from PNP in this experiment. Another therapeutically important parameter is the number of insonation cycles, which varies proportionally with cell death and sonoporation effectiveness [262]. The number of insonation cycles is also related to the MB life, with research showing that MBs can oscillate for up to 20,000 cycles at lower acoustic pressures (0.1 MPa) but that the lifespan of MB decreases to 100 oscillations at 0.4 MPa. [260]. A reperfusion time between insonations is therefore required to allow for fresh MBs to replace the depleted ones. The derived single-element transducer driving parameters are the number of cycles per pulse (N_C), PRF and the total insonation time (T) [263]. The

variation in N_C and PRF leads to different MB cavitation behaviours, influencing MB distribution size and number, which, in turn, affects therapeutic effectiveness.

Due to the multi-beam insonation pattern achieved with the phased arrays, the structure of the electrical excitation signal had to be further sub-divided than the pulsed US provided in the literature for single-element transducers. Therefore, one full beam sweep (T_S) comprised the succession of 13 different steering angles (beams), followed by an inactive period for MB reperfusion. All beams in the sweep contained the same number of pulses (N_P = 10 or 100). Finally, each pulse was broken down into the active insonation period, termed here the pulse width ($PW = N_C/f_r$), followed by an inactive pulse width (IPW). The 1.5 MHz array was driven with N_C = 5, 7 or 10 cycles / pulse, while the 3.0 MHz array was driven with N_C = 5 or 7 cycles / pulse. The pulse duty cycle ($T_{\%ON}$) was varied between 10.6% and 20.7% for the lower frequency transducer, and between 7.0% and 13.0% for the 3.0 MHz transducer. PRF is related to PW, IPW and $T_{\%ON}$ by:

$$PRF(kHz) = \frac{T_{\%ON}}{PW} = \frac{1}{PW + IPW} \qquad \text{Eq 6.1}$$

The 1.5 MHz transducer was generally driven with a PRF of 30 kHz, but 22.8 kHz was investigated for one test condition to assess the effect of PRF on therapeutic effectiveness. The 3.0 MHz array was intended to be driven at a PRF of 60 kHz to maintain the same $T_{\%ON}$ as for the lower frequency transducer, but the maximum operation frequency of the FIToolbox controller restricted the PRF to 57 kHz. The insonation time for all conditions was set to 11 minutes, to allow sufficient time for passive drug diffusion to occur through the insonated tissue, following several trials performed by M. Turcanu. Subsequently, the array, the suspension delivery and the aspiration were turned off but TEER measurements were continued for another 9 minutes to assess cell recovery. The last parameter investigated in relation to therapeutic effectiveness was the sonicated area, altered by reducing the number of active beams from 13 to 9, 6 and finally 3.

Focused US: Beam Selection and Characterization with FEA

In order to determine the insonation area per beam and the number of beams required to cover the entire diameter of the ThinCert™ membrane, FEA combined with time extrapolation simulations (with the same framework as described in Section 5.3) were performed for both arrays steered at 0°. The 1.5 MHz device was focused at 9.0 mm and the 3.0 MHz one was focused at 7.0 mm. The 1.5 MHz array produced a -3 dB beam width of 0.83 mm in the length (X) direction and 3.30 mm in the elevational (Y) direction. The 3.0 MHz array had a -3 dB

beam width in X direction of 0.47 mm and 1.35 mm in Y direction. As the ThinCert™ membrane had a diameter of 13.65 mm, a decision was made to use 13 beams equally spaced at 1 mm in the X direction. Therefore, the -3 dB profiles of two consecutive beams were kept well separated, which ensured two adjoining beams would not overlap on the cell monolayer, thus avoiding doubling of the sonication time for those regions. Throughout this chapter, beam numbering starts at the outermost left beam (Beam 1) in Figure 6-3 a. and ends at the outermost right beam (Beam 13), with Beam 7 corresponding to the central beam. The limits of steering angle for the 1.5 MHz array were ±34.0°, while for the 3.0 MHz array, they were ±40.6°.

The widths of the other beams were initially determined through simulations to ensure satisfactory separation. In order to reduce modelling time, only the odd beams were simulated, with the properties of the other beams being interpolated. Assuming steering symmetry about the central axis of the active aperture, the simulated beam number was further halved to the leftmost three beams: 1, 3, 5, plus the central beam. The models showed the -3 dB beam width in X increased with steering angle by a maximum of 33.8% for Beam 1 compared with the central beam (Beam 7) for the 1.5 MHz array, and by 52.7% in the case of the 3.0 MHz array, maintaining satisfactory separation between adjacent beams. As expected, beam width in the elevational direction remained fairly constant, with an average of 3.26 mm for the 1.5 MHz array and 1.40 mm for the 3.0 MHz device across the simulated steering angles.

Beam Pattern Characterization and MI Measurements with the Scanning Tank

Beam profiling was performed within the scanning tank, with the same procedure as presented in Section 5.2.3, and the arrays were driven with the DSL FI Toolbox controller. The comparison of beam profiles between the scanning tank data and the simulations demonstrated good correspondence for both arrays (Figure 6-5).

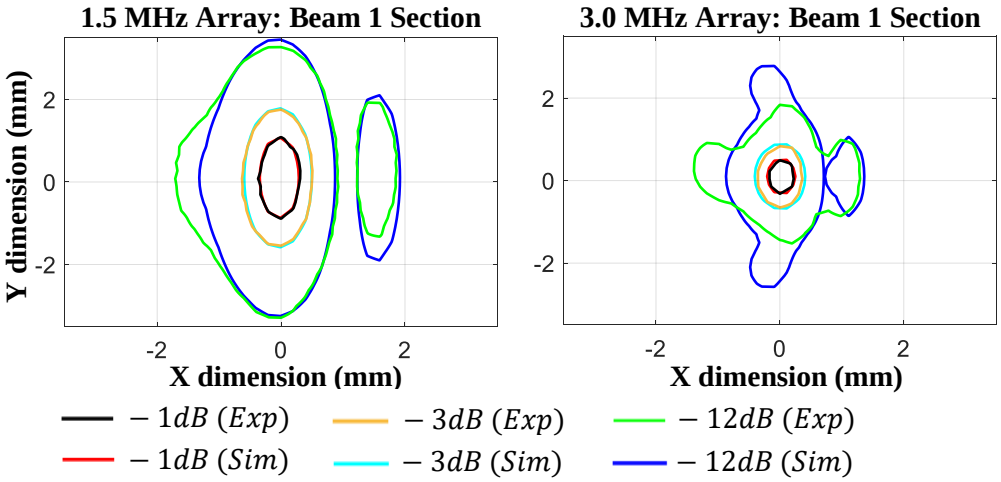

Figure 6-5 Comparison of the Simulated and Measured Cross Sections of the Beams at Maximum Steering Angle (Beam 1) for the 1.5 MHz and the 3.0 MHz Arrays (Cross Sections Recorded at the Focal Point in Z Direction and Centred on the Respective Beam in X Direction, not on the Central Axis of the Array)

As part of experimental beam profiling, the arrays were driven with constant 15 V_{pp}, irrespective of the steering angle. Figure 6-6 a. shows the MI at the focal point decreased with steering angle, but also symmetrical beams about the central axis had similar MI levels. Subsequently, the initial *in-vitro* experiments revealed that, in order to obtain sonoporation at higher steering angles, the increased MI at the more central beams became too high, leading to the generation of permanent damage (holes) in the ThinCert™ membrane (Figure 6-6 b.).

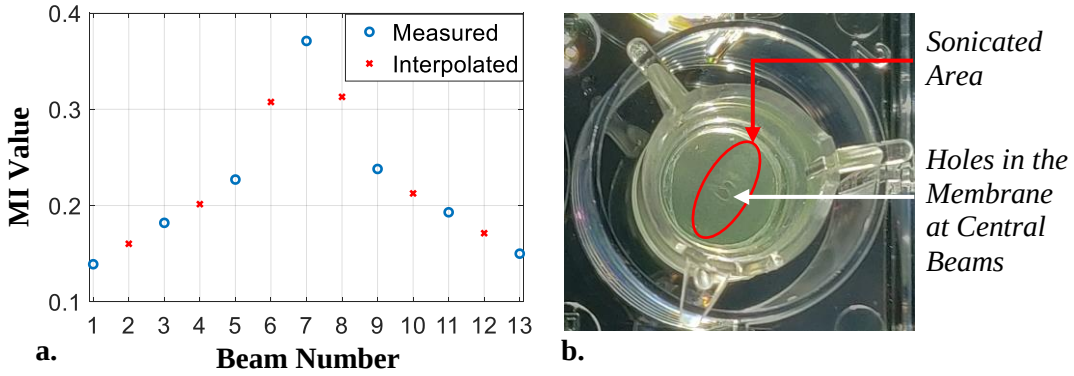

Figure 6-6 a. MI Achieved by the PZT-5H Array at Focus as Function of Beam Number for Constant Driving Voltage; b. Formation of Holes in the ThinCert™ Membrane as a Result of Uneven MI Distribution

Ideally, the MI imbalance would be mitigated by decreasing the electrical power delivered to the array for the central beams. However, the FIToolbox power supply voltage could not be adjusted with the same high frequency as the sweep between the steering angles. The issue was resolved by altering the electrical power applied to the transducer by controlling the PWM duty cycle ($T_{\%ON\ PWM}$) of the FIToolbox's pulsers, while keeping the supply voltage constant over all swept beams. This was implemented on the array controller by employing custom excitation signals, based on 3-level pulse files, created with a proprietary DSL software tool (*Signal-to-PWM.vi*). Figure 6-7 presents an example of array driving signal amplitude control with PWM for a fixed DC supply voltage of 15 V_{pp} applied to the FIToolbox's pulsers, and the ideal equivalent waveform driving the transducer. The method presented here for the FIToolbox can be potentially implemented on any type of commercial array controller.

$T_{\%ON\ PWM}$ for each steering angle was determined experimentally, with the array dipped in the scanning tank and the NH placed at the focal point of each beam. The first step of the procedure was to steer the array at the maximum angle, corresponding to Beam 1 (which had the lowest efficiency in terms of MI, similar to its counterpart – Beam 13). $T_{\%ON\ PWM}$ was set to its nominal value (70%), and the FIToolbox power supply voltage was varied until the desired MI level was reached. The driving voltage was then kept constant, and $T_{\%ON\ PWM}$ was varied for each subsequent beam to achieve an MI with a 5% tolerance compared to the MI at the focal point of Beam 1. Considering steering symmetry about the central axis, beams 13 to 8

were assigned the same $T_{\%ON\ PWM}$ as their counterparts from beams 1 to 6. The procedure was then repeated in order to create a pulse table for each MI level tested as part of the *in-vitro* experiment. Table 6-1 provides the relationship between the power supply voltage (Vpp) applied to the FI Toolbox pulsers and the MI achieved by the arrays after PWM control, as well as the ratio in $T_{\%ON\ PWM}$ between beam 7 and beam 1 to keep MI constant.

Table 6-1 Relation Between Driving Voltage Amplitude, MI at Beam Focus, and $T_{\%ON\ PWM}$ Ratio Between Beam 7 (Highest Efficiency) and Beam 1 (Lowest Efficiency) to Maintain MI Constant

$f_R(MHz)$	1.5			3.0			
MI	0.1	0.2	0.3	0.1	0.2	0.3	0.4
Vpp (V)	21.0	37.0	57.0	18.2	30.2	44.2	59.2
[1]$T_{\%ON\ PWM}$ ratio	0.44	0.48	0.50	0.60	0.50	0.57	0.55

[1]$T_{\%ON\ PWM}$ ratio = $T_{\%ON\ PWM}$(Beam 7) / $T_{\%ON\ PWM}$(Beam 1), considering Beam 1 has maximum $T_{\%ON\ PWM}$

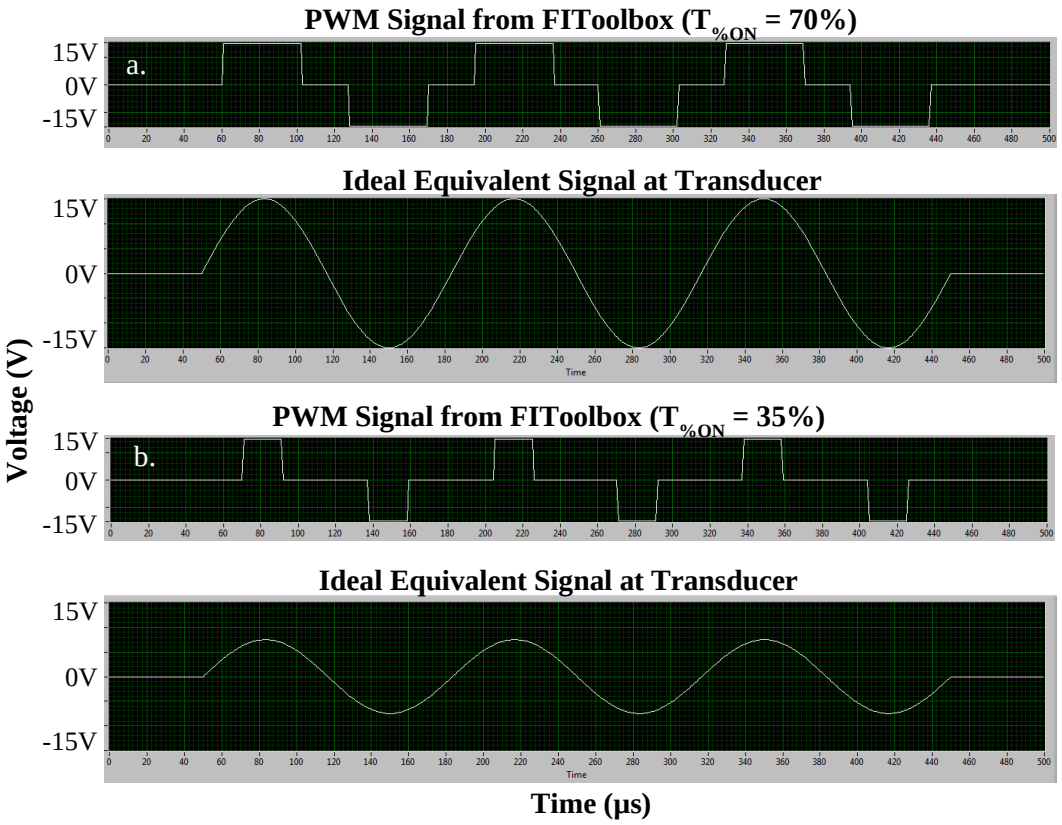

Figure 6-7 PWM Control of the Array Excitation Signal and the Ideal Equivalent Waveform at the Transducer for: a. Nominal Duty Cycle (70%); b. Half Duty Cycle (35%)

Control Measurements and Experimental Conditions

In order to evaluate the effects of US without the action of MBs, the 3.0 MHz array was driven at an MI of 0.3, but with no suspension delivery, while TEER was recorded as for the previous methodology. The other control test assessed the effect of the suspension delivery and suction on TEER and FD intake, but with the transducer turned off in that instance.

Afterwards, a total of 25 different conditions were tested by varying the following parameters: focus type, f_r, N_P, N_C, PRF, number of active beams, $T_{\%ON}$ and MI. Three repeats were performed per each condition for statistical significance. The number of test conditions does not represent permutations of all the evaluated parameters, but it was rather dictated by the limited availability of cell cultures and by the therapeutic outcomes. An initial parameter set was used for the first test condition and evaluated in relation with the measured level of induced sonoporation. For the following condition, one parameter (or a reduced set of parameters) was modified for consistency reasons and was again related to the sonoporation level. Once a satisfactory outcome was found, the parameter (or parameter set) was fixed and another parameter was evaluated.

6.3 Experimental Results

TEER and temperature measurements were performed every minute from the time the insonation started, and ceased 9 min. after the end of treatment, for a total period of 20 min. The decrease in barrier function for each test condition was evaluated as the percentage difference between the minimum TEER value attained in the 20 min. interval ($TEER_{min}$) and the TEER value recorded at the start of treatment ($TEER_{initial}$), averaged over the number of repeats ($n_{repeats}$) performed for each condition:

$$\overline{\Delta_{TEER}} = \frac{\sum\left(\frac{TEER_{initial}(i) - TEER_{min}(i)}{TEER_{initial}(i)}\right) * 100\ \%}{n_{repeats}} \qquad \text{Eq 6.2}$$

where i denotes the index of the repeat.

The average standard deviation in TEER per test condition was calculated as the mean value of the standard deviations between all repeats of the same condition, determined at every time point (t) recorded during the measurements:

$$\overline{\sigma_{TEER}} = \frac{\sum \sigma_{TEER}(t)}{20} \qquad \text{Eq 6.3}$$

where $t \in [0, 20]\ min$.

Any outlier that deviated more than 20% from the other repeats was removed from $\overline{\Delta_{TEER}}$ and $\overline{\sigma_{TEER}}$ of the corresponding test condition. The temperature increase was calculated similarly to the TEER. The medium in the basolateral chamber was sampled twice: firstly, immediately after the TEER measurements were completed (20 minutes after the start of the procedure), and secondly, one hour after the procedure start. As the FD compound concentration had larger deviation between repeats of the same condition, outliers that deviated more than 5 times from the average were removed.

Control Measurements

The application of US without MB delivery and *vice versa* resulted in an average cell barrier function decrease of only 5%. The low therapeutic effects resulting from the lack of MBs highlighted their importance in promoting sonoporation at low acoustic pressures. The lack of insonation demonstrated the MB delivery and aspiration systems did not cause interference with the cell monolayer. The TEER measurements were confirmed by similar results obtained with the fluorescence plate reader, and no visual marks on the ThinCert™ membranes were observed when they were inspected with macro imaging.

Continuous Sweep Procedure

The continuous sweep procedure was evaluated in detail, in contrast to the other two methods, because it made use of the full steering potential of the arrays and it allowed MB reperfusion time between subsequent insonations of the same treated area. The correlation between $\overline{\Delta_{TEER}}$, $\overline{\sigma_{TEER}}$ and the corresponding set of driving parameters for each test condition is presented in Table 6-2. A larger $\overline{\Delta_{TEER}}$ value was attributed to a larger decrease in cellular barrier function.

Table 6-2 Relation Between Electrical Driving Parameters Applied to the Phased Arrays and the Induced Decrease in Cellular Barrier Function, Expressed as $\overline{\Delta_{TEER}}$, and the Average Standard Deviation Between Subsequent Repeats of Each Test Condition, $\overline{\sigma_{TEER}}$

f_r	1.5 MHz											
N_P	100										10	
N_C	5			7					10		7	
PRF (kHz)	30			22.8	30				30		30	
Beams no.	13			13	13	9	6	3	13		13	
$T_{\%ON}$ (%)	10.6			10.4	13.7	14.4	13.7	13.7	20.7		13.5	
MI	0.1	0.2	0.3	0.2	0.2	0.2	0.2	0.2	0.2	0.3	0.2	0.3
$\overline{\Delta_{TEER}}$ (%)	7.00	25.8	78.1	61.6	59.0	55.4	38.6	22.8	72.5	71.6	10.0	52.2
$\overline{\sigma_{TEER}}$	0.94	5.83	3.38	11.2	8.06	6.33	4.94	2.49	8.62	12.1	4.74	10.4

f_r	3.0 MHz							
N_P	100							
N_C	5					7		
PRF (kHz)	90*	57				57		
Beams no.	13	13				13	9	6
$T_{\%ON}$ (%)	7.0	10.0				13.0	13.0	13.0
MI	0.3	0.1	0.2	0.3	0.4	0.2	0.2	0.2
$\overline{\Delta_{TEER}}$ (%)	57**	2.8	21.7	52.9	59**	45.8	22.5	16.7
$\overline{\sigma_{TEER}}$	-	1.81	2.86	8.55	-	6.57	6.16	7.38

* PRF of 90 kHz only attained for lower $T_{\%ON}$ due to FI Toolbox limit

** data from one repeat only

An analysis of the results in Table 6-2 shows that higher MIs generally achieved a greater decrease in TEER. However, for the 1.5 MHz array, for a higher number of cycles per pulse (10) and an increased $T_{\%ON}$ (20.7 %), the difference between an MI of 0.2 and 0.3 was insignificant in terms of barrier function decrease, being well below the measurement variation. As the $T_{\%ON}$ could not be increased to 20.7 % for the 3.0 MHz array, due to FIToolbox limitations, a similar correspondence could not be identified for that frequency.

10 pulses per beam led to a much lower decrease in barrier function compared to using 100 pulses per beam. This could imply that 10 pulses at lower MI (0.2) were insufficient to insonate one area of the cell monolayer, before the array was steered to the next beam. However, an increase in MI from 0.2 to 0.3 led to a higher decrease in barrier function, suggesting that 10 pulses per beam could be used in conjunction with higher MIs to achieve satisfactory results.

Using a lower number of insonation cycles per pulse generally led to lower barrier function decrease than a higher number of cycles at the same MI. Due to limitations of the FIToolbox, a higher number of cycles could not be investigated. The 3.0 MHz array achieved a lower TEER drop than the 1.5 MHz one for the same MI, indicating that the 1.5 MHz resonance frequency was more efficient for cellular membrane disruption.

A lower number of beams, corresponding to a narrower area of insonation of the cell monolayer led to a lower TEER drop than in the case of more beams used. This result proved the array's ability to spatially control the therapy. Furthermore, it showed the TEER drop was not caused by a single insonated area but was rather a function of the cumulative effect of all sonoporated areas.

The maximum instantaneous temperature increase during therapy was 1.3°C, caused by the 3.0 MHz array, driven at an MI of 0.3, with one outlier removed. The average temperature increase at the end of the 11 minutes of sonication was 0.5°C, which was not substantial, considering that a temperature increase of > 5°C is associated with cell damage *in vivo* [264].

Diffuse Focus and Fixed Time Sweep Procedures

The diffuse focus method was evaluated with the 3.0 MHz array, continuously driven with PRF = 12.5 kHz, $T_{\%ON}$ = 8.33% and MI = 0.15 for 11 minutes. TEER dropped by 55.8% from the initial value at the end of insonation, and continued to drop to a maximum reduction of 59.0% after the next 9 minutes without US. The continuous drop in TEER after the end of insonation was a clear indicator of irreversible sonoporation. The average standard deviation of the measurements was 4.3% and the average temperature increase in the ThinCert™ was 1.0°C, towards the end of the US therapy.

The fixed time sweep method was also evaluated with the 3.0 MHz array, driven with $N_C = 20$, PRF = 12.5 kHz, $T_{\%ON}$ = 8.33% and MI = 0.21 with 8 active beams. The percentage decrease in TEER from the initial value at the end of insonation was 30.4%, and continued increasing to 41.5%, measured after 9 minutes from the end of therapy. The large decrease in barrier function that occurred after insonation indicated severe damage to the cell monolayer, probably caused by the long, continuous insonation time (50 s) over the same area of the cell membrane before incrementing to the next beam. The average standard deviation between the three experimental runs was 4.4%. The maximum temperature increase during therapy was 0.77°C.

The FD4 extravasation through the cell membrane, measured with the plate reader was not significant in either case, indicating a low effectiveness of the two procedures.

Correlation Between TEER and Plate Reader Results

Generally, a similar trend was obtained between the TEER data and the FD transport into the basal chamber as a result of insonation, after the outliers from the plate reader data were removed. Figure 6-8 presents the comparison between TEER and FD4 results for the most relevant test cases that evaluated: the control measurements, the sonoporation amplitude in relation to the insonated area (set by the number of active beams), and the US frequency.

As it can be seen in Figure 6-8, TEER and the concentration of FD4 extravasated in the basal chamber vary inversely proportional. The cause of this phenomenon is the decrease in the barrier function of the cell monolayer as a result of sonoporation, which leads to a higher layer permeability. The higher permeability of the cell membrane leads to a drop in TEER and an increased rate of FD4 extravasation from the apical chamber into the basal chamber.

Both control tests (i.e. array inserted in the apical chamber followed by delivery of MBs + FD4 suspension, but no US applied; and US applied, but suspension delivery not containing MBs) showed insignificant TEER reduction/FD4 extravasation in the basal chamber. Hence, the results indicated successful sonoporation required both US and MBs, and that the presence of the array in the apical chamber and the delivery of suspension did not influence the permeability of the cell monolayer. Subsequently, reducing the area of insonation by using less beams resulted in lower TEER decrease and lower FD4 extravasation compared to insonating a larger area by using more beams. This indicated that the amount of drug extravasated through the insonated tissue could be controlled by varying the size of the treated area. Finally, the higher frequency array achieved less TEER decrease/FD4 extravasation than the lower frequency one, which falls in line with other research [39].

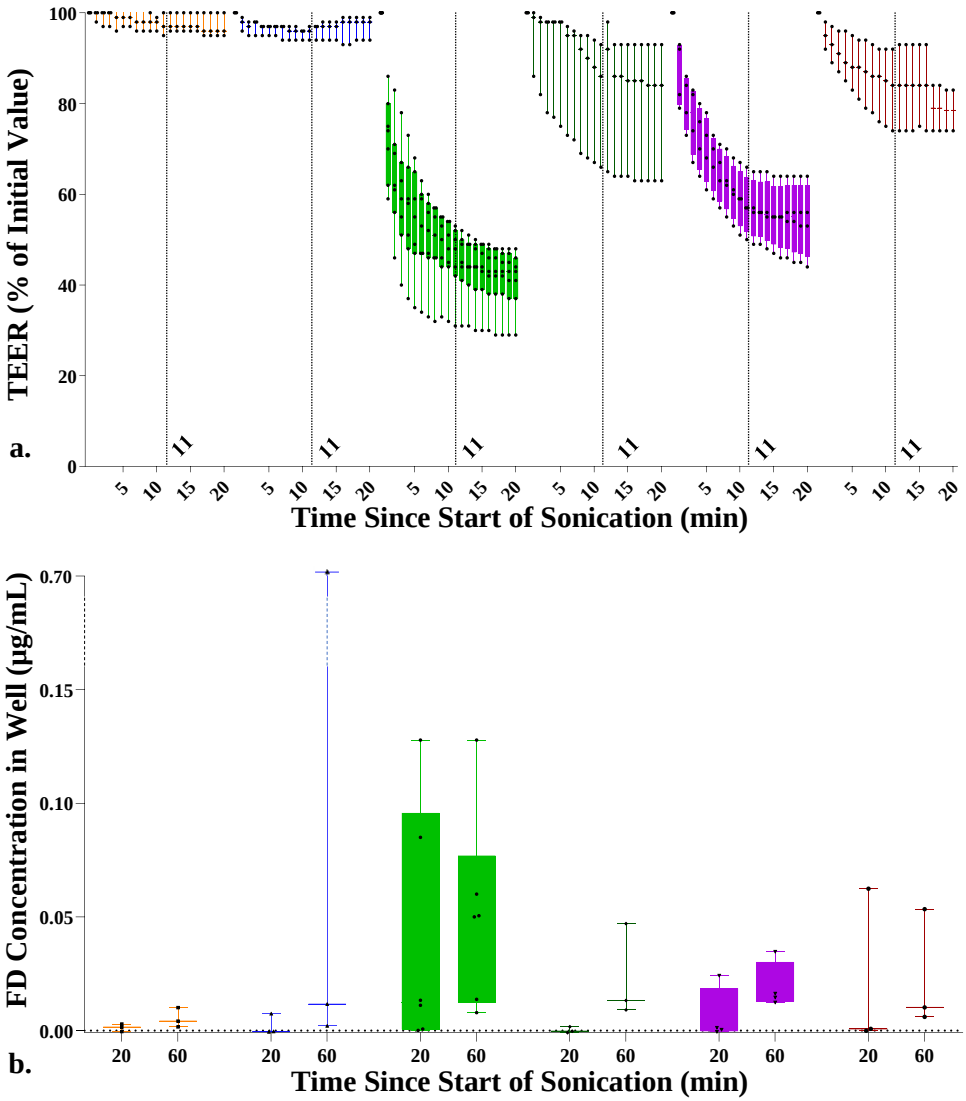

Figure 6-8 Correlation Between TEER Decrease and FD4 Intake Through the Cell Monolayer for Background Experiments and for the Variation of the Sonoporated Area as Function of the Number of Active Beams, Evaluated at Two Resonance Frequencies. a. % Decrease in TEER from Initial Value; b. FD4 Intake into the Basal Chamber

Imaging of the Treated Cell Monolayers

Macro imaging of the ThinCert™ membrane after insonation showed the treated regions presented discolouration, with a similar shape as the characterized cross sections of the US beams from the phased arrays. This could be attributed to a change in the cellular structure. The area of discolouration was generally proportional to the TEER decrease, and it was larger for higher MIs and lower f_r (Figure 6-9).

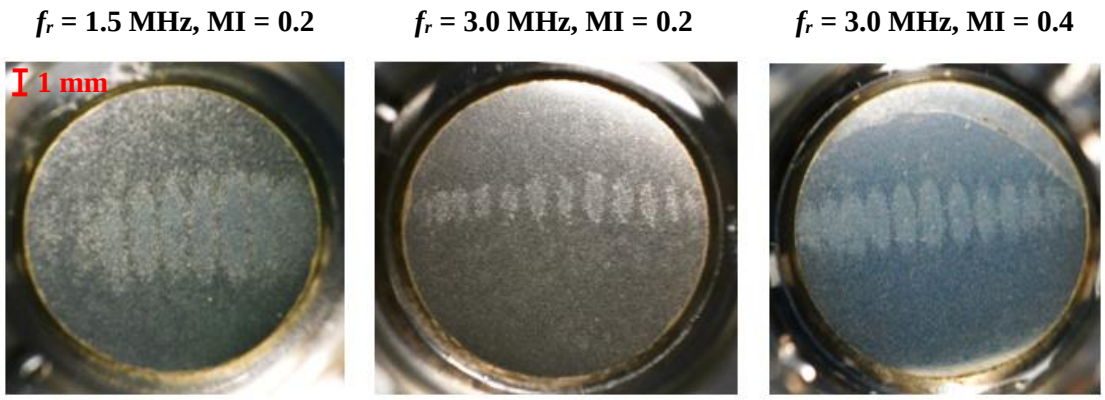

Figure 6-9 Macro Imaging of the Cell Monolayers After Sonication

Confocal microscopy further revealed the concentration of stained F-actin in the cytoskeleton of the sonoporated cells was reduced compared to the regions not subject to ultrasound. The red zones in Figure 6-10 a. represent normal accumulation of phalloidin in the F-actin of the cytoskeleton, while the darker, blue zones indicate rupture of the actin filaments. Moreover, the blue zones also corresponded to the cross section of the phased arrays beams. Furthermore, fluorescence microscopy of the samples highlighted disruption in the tight junctions of the sonoporated cells, leading to micron-sized holes in the monolayer (Figure 6-10 b.).

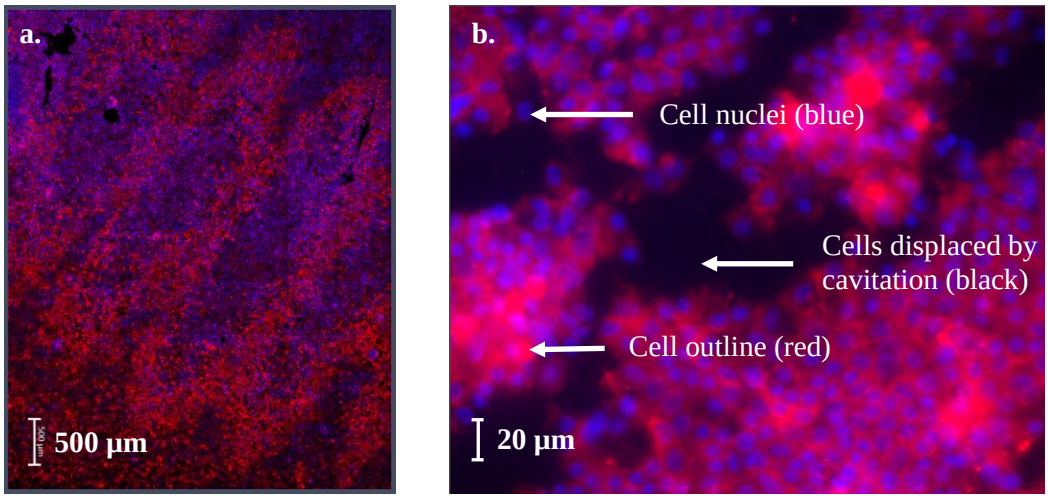

Figure 6-10 Therapeutic Results: a. Confocal Fluorescence Microscopy Indicating Internal and External Modification of Cellular Structure; b. Fluorescence Microscopy Depicting Cellular Tight Junction Disruption; Image Analysed by M. Turcanu at Dundee Imaging Facility Following Insonation with the Experimental 1D Phased Array

Sources of Error

The variations in TEER readings and FD concentration in the basolateral chamber can be attributed to both biological variability (e.g. variability of the Caco-2 cells) and experimental errors, which include:

- The fluid height in the ThinCert™ was not always at the same level, which led to small differences in the pressure exerted by the weight of the liquid on the cell monolayer, affecting the extravasation of FD compound into the basolateral chamber;
- Overflow of the medium from the apical chamber into the basal chamber due to low suction;
- Capillary action from the suction pump led to a reduced level of liquid at the end of the procedure (and inherently low FD concentration) in the culture insert;
- Air bubbles formed on the face of the phased array when it was dipped into the ThinCert™, affecting the US field;

The experimental errors enumerated beforehand fall into the observational error field, and they depend on the researcher's ability to control the process. They can be mitigated in future experiments by automating the MB suspension delivery and suction with the aid of fluid level sensors in the two chambers of the ThinCert™. A second type of experimental error can be attributed to reflections and standing wave formation from the back walls of the culture insert and of the cell well. This error is inherent, but can be reduced by applying an acoustic absorber under the basal chamber. However, since the experimental results suggested good spatial discrimination of the US therapy, any reflections and standing waves must have been negligible in this experimental arrangement.

6.4 Discussion

TEER measurements performed following the end of insonation indicated the barrier function did not recover in any of the test conditions, which could be related to irreversible sonoporation of the tissue. However, this result does not imply that *in-vivo* tissue will also be irreversibly sonoporated with the procedure described in this chapter because cell repair mechanisms may differ between an *in-vitro* culture and an *in-vivo* tissue [265], with the latter being more robust and possessing more efficient healing capabilities.

The larger decrease in barrier function when all 13 beams were employed, compared to a lower number of beams, demonstrated the capability of both arrays to control sonoporation spatially, not just to produce it. Furthermore, the decrease in barrier function could be controlled to a satisfactory degree by the application of different electrical driving parameters to the array.

PWM control of the excitation signal applied to the transducer during the continuous beam sweep allowed for similar MI levels to be achieved across all steering angles. This resulted in a more uniform treated area (Figure 6-9), and visible holes in the ThinCert™ membrane created by the central beams (Figure 6-6 b.) were successfully avoided.

As the FIToolbox was mainly designed for imaging, PRF could not be increased to more than 57 kHz at 3.0 MHz, without decreasing $T_{\%ON}$ (to lower than 13.0%) or the number of cycles per pulse. The array controller was further slowed down by a software limitation which required data capture as part of the imaging algorithm, which was unnecessary in the current experiment. Increasing one parameter of Eq 6.1 often required a decrease in the other parameters, in order to maintain a correct output signal. A further increase in parameters often led to errors in the output pulses caused by DRAM memory overflow. Therefore, variation of a driving parameter for a new test condition often required changes to several other parameters to keep within the specification of the instrument. Also, as a result of the FIToolbox limitation, higher duty cycles or numbers of cycles per pulse could not be investigated.

The driving parameters that were most favourable in terms of barrier function decrease of the cell monolayer were: f_r = 1.5 MHz, N_c = 7 cycles per pulse, $T_{\%ON}$ = 10 - 15%, PRF = 30kHz, MI = 0.2 and 13 active beams. The insonation at those parameters did not produce visible holes in the ThinCert™ membrane, while the TEER dropped by 59% from the initial value, indicating satisfactory barrier function decrease, without extensive damage to the cell layer.

6.5 Conclusions

The *in-vitro* experiments demonstrated the experimental 1D phased arrays could achieve satisfactory control of tissue damage and decrease in the membrane barrier function, potentially through sonoporation. The level of tissue permeabilization could be controlled through the electrical parameters used to drive the transducers, and satisfactory therapeutic localization was achieved via focusing and beam steering. No significant barrier function recovery was observed, indicating the cells were irreversibly sonoporated.

The effectiveness of the therapeutic procedure was evaluated with two different approaches: real-time by measuring the barrier function decrease with a TEER meter, and post-treatment with a fluorescence plate reader. Generally, the two procedures were in good accordance, with a higher TEER drop corresponding to larger drug extravasation through the insonated cell monolayer, measured with the fluorescence plate reader from the test medium sampled from the basal chamber of the ThinCert™. The results were further confirmed by macro imaging,

confocal and fluorescence microscopy, which revealed changes in the cellular structure and membrane rupture following therapy.

A decrease in barrier function was correlated with: a higher MI level, a higher number of cycles per pulse and a higher number of pulses per beam. Furthermore, the 1.5 MHz phased array was more effective in decreasing the barrier function of the cell layer than the 3.0 MHz one at similar driving parameters. This was mainly due to the lower frequency of resonance, which is correlated with higher cavitation intensity (Section 2.4.4). Neither transducer incurred significant heating over the 11 min. insonation period, which was advantageous in avoiding unwanted thermal effects on the insonated cells.

Subsequently, a set of driving parameters were identified as being the most suitable for achieving a satisfactory degree of membrane disruption, while avoiding excessive damage (i.e. visible holes) to the insonated cell monolayers.

Finally, due to the satisfactory outcomes of the *in-vitro* experiments, a decision was made to manufacture a capsule phased array transducer, for a future follow-up *in-vivo* trial, and this is the focus of Chapter 7.

7 Capsule Array Implementation

7.1 Introduction

Chapter 7 presents the development of an intracorporeal ultrasonic transducer based on the 24 element, 1.5 MHz, PZT-5H phased array that was successfully tested *in-vitro* in Chapter 6. The intracorporeal transducer was designed as a 40 mm long by 11 mm diameter (33 Fr) capsule attached to a tether cable which contained the array electrical interconnects and two delivery channels for in-situ drug and MB suspension delivery. The device is aimed for *in-vivo* cavitation-enhanced drug delivery through porcine small intestine and is intended to be inserted into the bowel through a stoma. The porcine model was chosen due to the resemblance of its small bowel anatomy with humans [266, p. 240], [267]. The capsule array designed, manufactured and characterized in this chapter is aimed to be tested *in vivo* by a research team from University of Strathclyde, University of Glasgow and University of Edinburgh at the University of Edinburgh, Bioresearch & Veterinary Services facility (https://www.ed.ac.uk/bioresearch-veterinary-services). Due to the 2020 Covid-19 pandemic, the *in-vivo* tests have been rescheduled for summer 2021 and it is intended to disseminate these results and the capsule array developments contained in this Chapter through both journal and conference publication routes.

The capsule dimensions were chosen as a compromise between size, manufacturability and array focusing efficiency. The phased array was embedded into the capsule casing which provided an open region between the transducer and the small bowel tissue where the delivered MBs could oscillate in the focused acoustic field. FEA was employed to simulate the array and the capsule walls surrounding it in order to determine the best geometry to minimize US reflections. One of the major challenges in manufacturing the intracorporeal array was fitting all the necessary electrical interconnects and the two suspension delivery channels into the 12 Fr tube attached to the capsule, which was originally intended for nasogastric feeding. Biocompatibility was attained by coating with a thin layer of Parylene C.

After manufacturing, the capsule was characterized in the scanning tank before and after Parylene coating, and the results were compared with the FEA simulations. The array was driven using the same FIToolbox controller as for the *in-vitro* trials, but the internal power supply for the controller's pulsers was replaced with a bench power supply. This offered better voltage and current control of the excitation signal and produced less noise.

7.2 Capsule Design and Manufacturing

The constitutive parts of the intracorporeal device were: the capsule, housing the phased array, the nasogastric (tether) tube containing the electrical cables and the two delivery tubes, and the bench equipment consisting of the array controller and the syringe pump for drug and MB suspension delivery. The capsule array design and manufacturing process is schematically described in Figure 7-1.

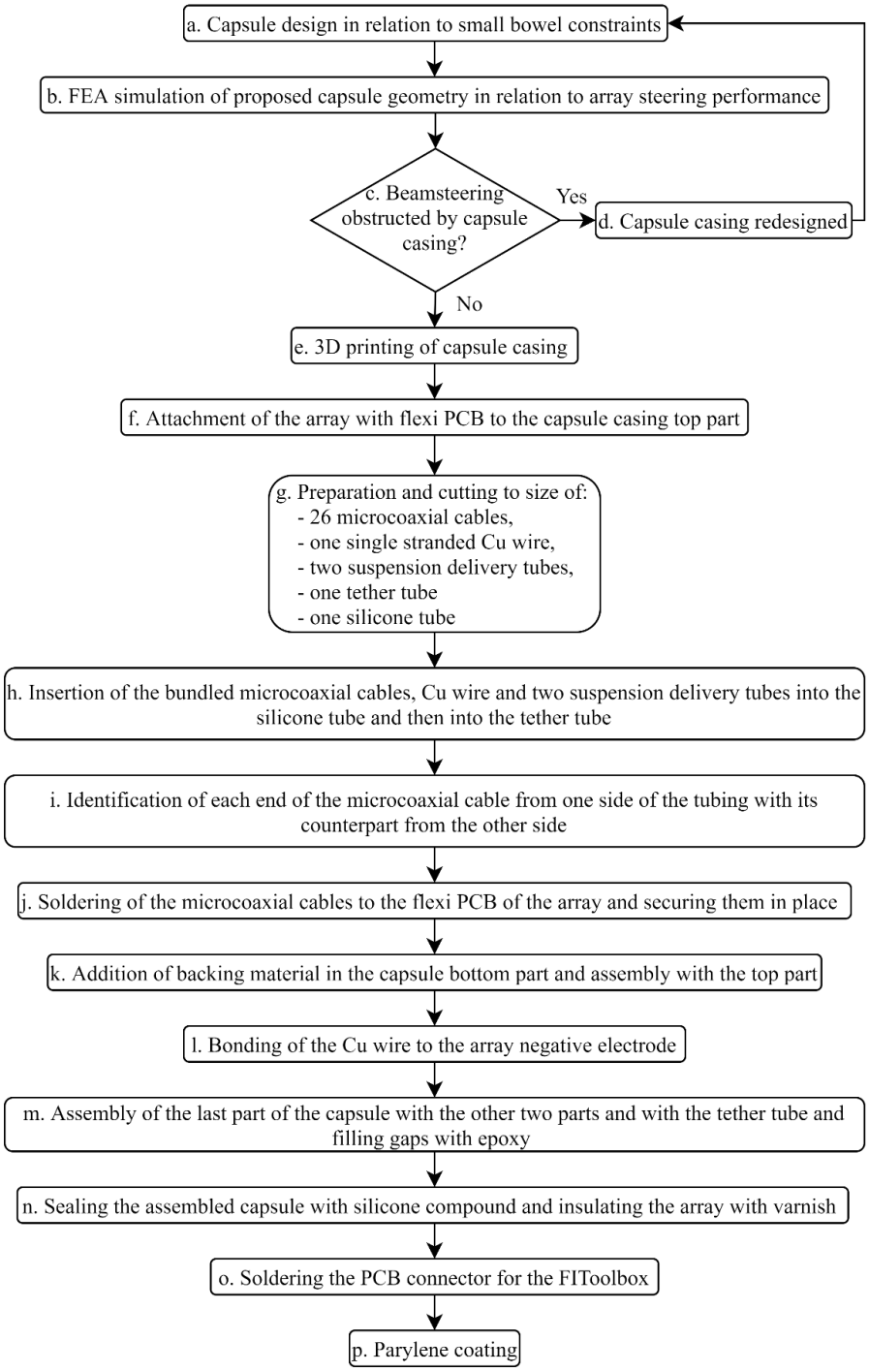

Figure 7-1 Capsule Array Design and Manufacturing Process Diagram

7.2.1 Design of the Capsule and its Constraints

The porcine small intestine diameter varies between 25 mm and 35 mm [268, p. 354]. C N Beale et al. [269] demonstrated that a 14 mm diameter cannula could be successfully implanted into the porcine duodenum and used to deliver drug capsules. Furthermore, Yongqiang Qiu et al. successfully tested *in vivo* a 10 mm x 30 mm (diameter x length) capsule for US imaging, inserted into the small intestine through a stoma in the pig's lateral side [270]. Another study trialled an 11 mm x 26 mm capsule endoscope for imaging porcine small intestine *in vivo* [271]. Considering the anatomy of the porcine bowel, the literature in small intestine endoscopy, and manufacturing restrictions, the maximum dimensions of the capsule array were set to 11 mm x 40 mm (diameter x length). The length would make this device difficult to swallow but does not affect use when inserted in tethered form, through a stoma.

The capsule was designed to perform sonication of the small bowel epithelium. However, the array was not meant to be directly coupled to the tissue, but to use the liquid medium in the small intestine for US propagation and beamforming. The casing was thus designed to maintain a gap between the transducer aperture and the tissue to allow efficient focusing of the US beam close to the epithelium, where the MBs can be driven into cavitation under the focused acoustic field. Therefore, in order to achieve a transducer/bowel separation of around 4.0 mm, the capsule enclosure was designed with raised edges around the phased array (Figure 7-2). Finally, two channels placed at the sides of the array length ensured the delivery of drugs and MBs in the vicinity of the treated area.

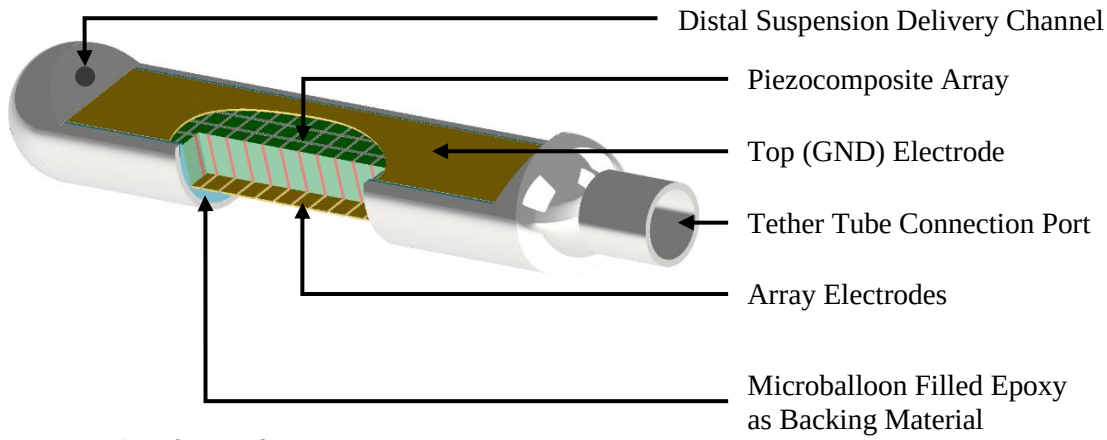

Figure 7-2 Capsule Transducer Design

A simplified 3-D FEA model (Figure 7-3 a.) of the array surrounded by the capsule walls was designed to evaluate the best geometry of the walls with respect to minimizing US reflections, especially at higher steering angles. The maximum steering angle investigated was 56°, at a focal distance of 4.0 mm from the transducer aperture. Figure 7-3 b. shows no significant side lobes existed in the beam pattern at this large steering angle and the capsule walls did not

produce unwanted US reflections. FEA was used to model both the array and the load because of the angled capsule walls which could not be simulated with extrapolation. The simulation framework was similar to the one described in Section 5.3 and used the modified PZT-5H material constants for the active material. Modifications from the previous model included: a thinner backing layer due to the limited space inside the capsule, the addition of the capsule walls surrounding the array and the update of the equivalent RLC circuit of the connecting cables with the values for the new interconnects.

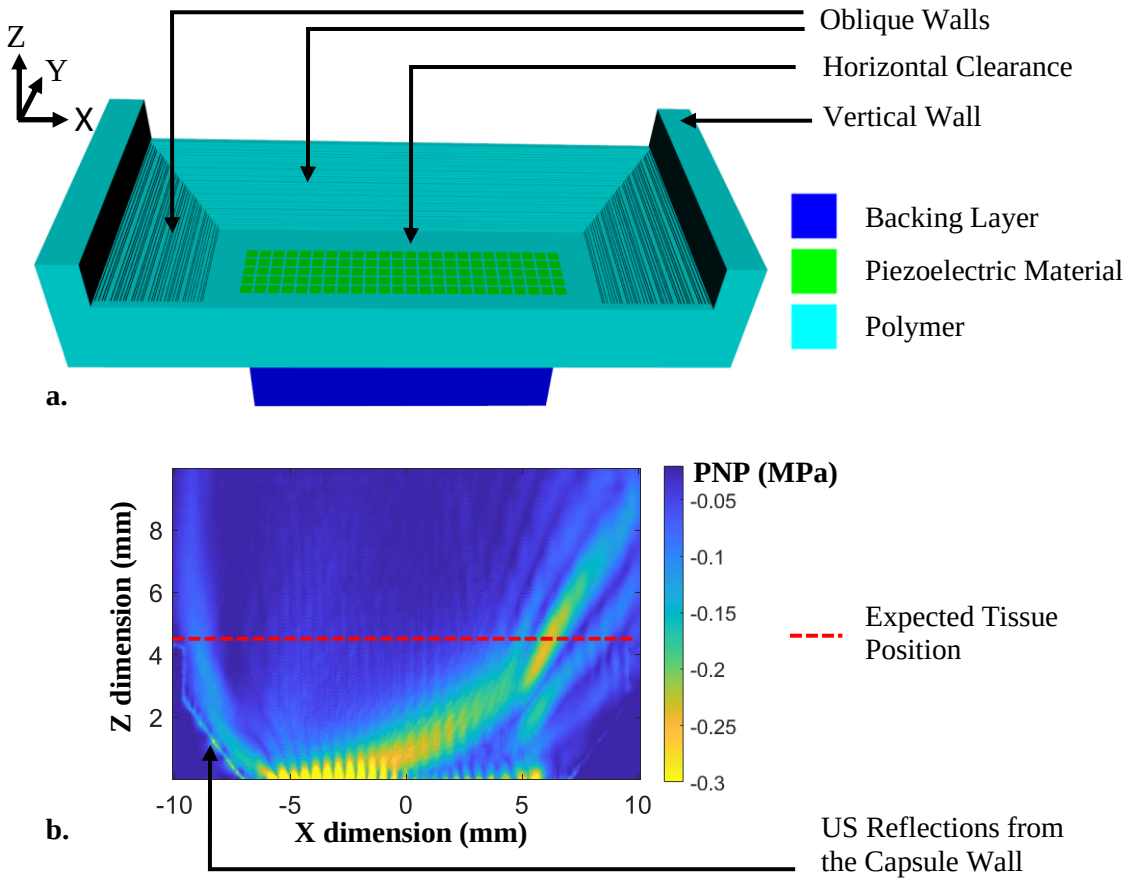

Figure 7-3 a. FEA Model of the Phased Array Surrounded by the Capsule Walls; b. Simulated XZ Beam Section for the Array Focused at 4.0 mm and Steered at 56°

The minimum horizontal clearance in both X and Y was found to be 1.26 mm. The oblique profiles started after the clearance section in both X and Y directions and had a height of 2.56 mm, while a vertical section with a height of 4.26 mm from the array aperture was added after the oblique walls in the active aperture (X-direction) only. In the manufactured capsule, both the backing material and the capsule walls had a cylindrical shape, further reducing the walls' impact on US reflections and beam scattering.

7.2.2 3-D Printing of the Capsule Casing

The capsule casing was designed in collaboration with M. Turcanu, who prepared the final CAD models for 3-D printing. The casing was divided into three independent pieces to allow

mounting of the phased array, soldering of the microcoax cables to the flexi PCB attached to the array, filling with backing material and attachment of the tether. The three components of the capsule were designed to be fastened with a lip/groove system to reduce moisture ingress (Figure 7-4). The width of the locking features was 0.525 mm, making them the finest features of the capsule casing. The exterior dimensions of the capsule were 44.6 mm in length (including the 4.6 mm tether connection port) and 11.0 mm in diameter. Internally, the capsule had a diameter of 8.0 mm and a useful length of 30.0 mm. The maximum depth available for the transducer backing layer was approximately 4.0 mm, with a cylindrical geometry.

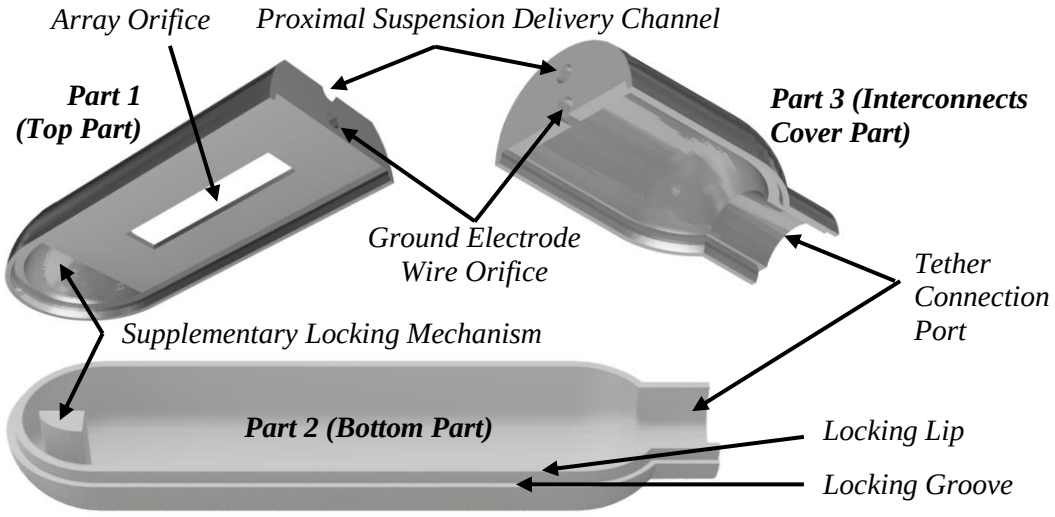

Figure 7-4 The Three Constitutive Parts of the Capsule Casing

Various 3-D printing techniques were assessed for manufacturing the capsule casing with respect to feature resolution, surface smoothness of the finished product, biocompatibility and resource availability. Two available procedures were identified as suitable: digital light processing (DLP) 3-D printing and Polyjet due to the fine print resolution and smooth surface finish. Both are additive manufacturing processes which use light to solidify a UV-curing polymer. DLP 3-D printing uses a stereolithography process in which a 2-D image of the part's cross section is projected into a tank filled with liquid photopolymer resin. The layer of photopolymer is solidified under the effect of light, taking the shape of the projected image. This process is repeated incrementally until the entire part is printed. Printing resolution of commercial DLP 3-D printers ranges between 25 and 50 µm [272]. Polyjet technology deposits the liquid photopolymer layer by layer by jetting it on the part to be constructed, in a similar manner with an inkjet printer, and then cures the layer with UV light. The layer resolution achieved with this process can be as low as 14 µm.

DLP 3-D printing was performed with an Asiga PICO2 (Asiga, Sydney, Australia) using a base monomer material (polyethylene glycol diacrylate – PEGDA MW 250), a photoinitiator

(phenylbis (2,4,6-trimethylbenzoyl) phosphine oxide – Irgacure 819) and a light absorber (Sudan I) to control the light penetration depth in the material. The weight concentration ratios of Irgacure and Sudan were 1% and 0.2% of the total mass, following the details of the procedure described in [272]. The biocompatibility of the resulting 3-D printed material was low due to the presence of Sudan I, which has known carcinogenic effects [273].

Polyjet 3-D printing was performed with an Objet Eden 350V (Stratasys, MN, USA), using a VeroBlack photopolymer. The outer surface of the capsule was made with the printer's *gloss* mode active in order to obtain a smoother finish to reduce the risk of tissue irritation and diminish friction inside the bowel. Vero materials have been previously used in manufacturing of US capsule endoscopes tested *in vivo*, on porcine models, with increased biocompatibility achieved through an external coating with Parylene C [165].

The DLP 3-D printed capsule had a smooth finish and small features (< 0.5 mm) had the desired shape and size. However, because of the material brittleness, the small features of the printed components (i.e. locking lips or array holder edges) broke during every assembly trial. Furthermore, the 3-D printed parts suffered extensive bending and shrinking in the 24 hr period following printing, leaving nonuniform gaps in the assembled capsule, which could allow water ingress.

The Polyjet printed capsule also had a satisfactory smooth and glossy finish and all small features were successfully printed. The material was less brittle and the lip/groove system locked well without any breakage. Any imperfections in the parts were sanded with fine grain sanding paper. Finally, in terms of cost and printing time, both processes were similar, with an estimated cost around £20 per capsule and required about 30 minutes to complete. Considering the flaws observed in the DLP 3-D printed capsules and the toxicity of the Sudan I component of the material, it was decided that the Polyjet process was better suited for printing the array casing.

7.2.3 Electrical Interconnects and Tether Tube

A custom flexible PCB was designed in CAD (Autodesk Eagle^{TM}) to fit into the tight space inside the capsule and was sent for manufacturing to a specialized company. The flexible circuit board had a substrate thickness of 130 µm, the Cu traces were 35 µm thick, plated with 0.03 µm Au through electroless Ni immersion. The trace width was 70 µm, and the bonding pads with the array were 150 µm wide. Pads for soldering to the microcoax cables were placed on both sides of the PCB and the two layers were connected with plated vias. The diameter of the vias was 200 µm, sufficient to allow a microcoaxial cable to be inserted through the pad

for a stronger solder connection. The distance between two pads was set to 1.0 mm to facilitate soldering. The flexible PCB was fanned out in two arms which contained both the pads for soldering and their corresponding traces in order to allow easier bending of the flexi inside the capsule casing (Figure 7-5). A GND plane was added on the bottom layer of the flexi board, spanning over both arms, to reduce interference. The ground planes of the two PCB arms were terminated with pads for soldering to microcoax cables connected to the ground of the phased array controller. The area of the flexi that was bonded to the array was not covered by the GND plane in order to avoid unnecessary mechanical loading of the array by the metal layer. The PCB was bonded to the array with anisotropic conductive adhesive (124-19, Creative Materials Inc., Ayer, MA) and cured for 1 hr at 50°C.

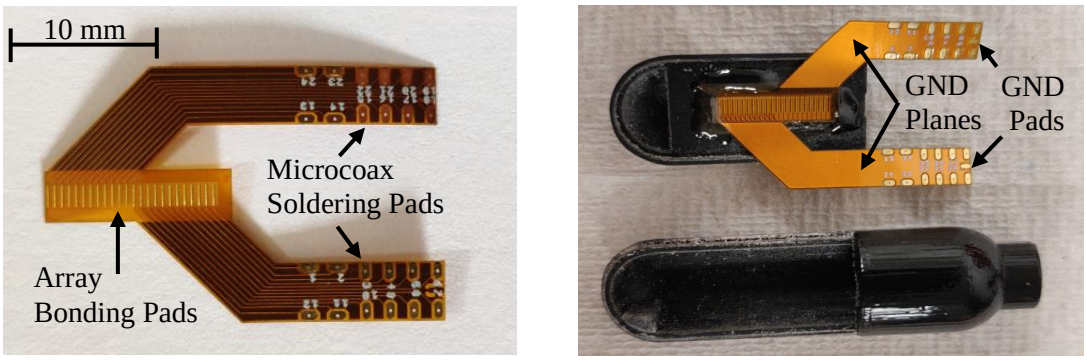

Figure 7-5 a. Top View of the Flexi PCB; b. Bottom View of the Flexi PCB Bonded to the Array and to the Capsule Casing

The electrical interconnects between the flexible PCB of the array and the controller were made with 42 AWG microcoaxial wires (Alpha Wire, NJ, USA). 24 microcoax cables were used to independently control each channel of the 1.5 MHz phased array and two more were used for the GND planes of the flexi. The cables were cut to a length of 2.7 m, in order to allow sufficient reach for the capsule array during the *in-vivo* experiments.

The ground electrode of the array was connected to a single-stranded, 0.315 mm diameter Cu enamelled wire. The choice of wire was made considering the ampacity of the cable, the DC resistance per unit length and the resistance due to the skin effect, which is predominant in single-core wires at higher AC frequencies. Choosing suitable cable for the ground electrode of the array was important because it collected the current from all 24 elements and if its resistance was excessively large, it could overheat or impact the performance of the transducer. The choice of wires, considering the limited space in the tether, was between two microcoaxial cables connected in parallel, with the inner cores and outer sheaths also connected, or a single threaded Cu wire.

The DC resistance of the two cable choices was measured per 2.7 m, with a calibrated RLC meter. The parallel DC resistance of the two microcoax cables was 1.85 Ω, while the DC resistance of the Cu wire was 0.64 Ω. The AC resistance, R_{AC}, per meter of the single-cored Cu wire due to the skin effect was calculated with the following equation [274]:

$$R_{AC} = \frac{1}{\pi\gamma\delta\left(1 - e^{-\frac{r}{\delta}}\right)\left[2r - \delta\left(1 - e^{-\frac{r}{\delta}}\right)\right]} \quad \text{Eq 7.1}$$

where γ is the electrical conductivity of the wire, r is the conductor's radius and δ is the skin depth of the conductor, determined with:

$$\delta = \sqrt{\pi f \mu_r \mu_0 \sigma} \quad \text{Eq 7.2}$$

where f is the frequency of the AC signal, equal to the array driving frequency, f_r; μ_r is the relative permeability of the wire material; and μ_0 is the free space permeability.

For the 2.7 m long, 0.315 mm diameter single-stranded Copper wire, at 1.5 MHz, R_{AC} = 1.1 Ω, resulting in a combined wire resistance of 1.74 Ω. The microcoax cables are not notably affected by the skin effect due to their multi-strand architecture, and their total resistance was considered approximately equal to their DC resistance. Even if the difference in resistance between the two cable choices was minimal, the decision in favour of the Cu wire was made due to the larger ampacity of the cable. According to *NFPA 79, Electrical Standard for Industrial Machinery*, [275], the ampacity of a 28 AWG (~0.32 mm diameter) Cu cable is 0.8 A. While the 42 AWG microcoaxial wire is not specifically considered in this standard, its cross-sectional area is a factor of 25 smaller compared to the 28 AWG Cu wire and hence, it was considered to have lower ampacity. For FEA simulation purposes, the impedance components of a 2.7 m long Cu wire soldered to the inner core of a 2.7 m microcoaxial cable were measured with a calibrated RLC meter, using the procedure described in Section 5.3.1. The inductance was 3.58 μH, the capacitance was 371.9 pF and the resistance was 18.73 Ω.

The tether was selected so that its inner diameter could accommodate the 26 bunched microcoax cables, the ground electrode wire and the two suspension delivery tubes. The external diameter of the suspension delivery tubes (Smiths Medical, MN, USA) was 0.96 mm. The bundle diameter was calculated as a function of the number of identical wires (N_{wires}) and their respective diameter (D_{wire}) with the bundled wires formula:

$$D = 1.2 * \sqrt{\sum_{i=1}^{n} N_{wires}(i) * D_{wire}(i)} \quad \text{Eq 7.3}$$

where n = the number of different types of wires in the bundle

The resulting ideal bundled diameter of the wires was 2.38 mm. In order to allow for easy insertion of the wire bundle into the tether, a 12 Fr, 109 cm nasogastric feeding tube, with inner diameter of approximately 2.6 mm was chosen (CORFLO, Avanos Medical, GA, USA).

7.2.4 Assembly of the Capsule

Prior to soldering to the flexi PCB, the 26 microcoax cables were bunched together with the single strand Cu wire and were soldered to the tip of the catheter stylet provided with the tether tube. The two suspension delivery tubes were then glued to the stylet. As the length of the nasogastric tube was not sufficient to allow testing *in vivo*, taking into account the circumstances of the test as identified in previous work [270], another 150 cm of silicone tubing (Masterflex Transfer Tubing, Cole-Parmer, UK) were used to cover the remaining length of the 2.7 m cabling. The extension tube will not be inserted into the pig and therefore does not need to be biocompatible; it can thus be chosen from a wider range of possibilities, and its diameter was chosen to be larger (4.76 mm inner diameter) to facilitate the insertion of the bunched cables. The interiors of the tether and silicone tubes were lined with chalk powder to allow for easier insertion of the bundled cables, which were pulled through the tubing with the aid of the stylet. The extra length of the bunched cables outside the nasogastric tube, towards the capsule, was 5 - 7 cm to allow manipulation during soldering. The stylet was then removed, the microcoax cables were stripped with fine tweezers, and their GND sheath was cut at the array end of the cables.

The ends of the 26 microcoax cables at the array side were correlated with their corresponding terminations at the other side of the tubing with a continuity tester and labelled accordingly. The inner core of each microcoax cable was soldered to the corresponding pad on the flexi PCB and the label was then removed from that end only to allow later assembly of the capsule. The cables were soldered in pairs and then tacked (with LOCTITE 382™ TAK PAK) to the flexi circuit in order to minimize the risk of them breaking loose while soldering the other interconnects. Adjoining pairs were soldered on opposite faces of the flexible PCB to minimize the risk of short circuits (Figure 7-6). After all the microcoax cables were soldered and tacked to the flexi, a thin layer of two-part epoxy (Araldite Rapid) was added to confer extra strength to the soldered connections.

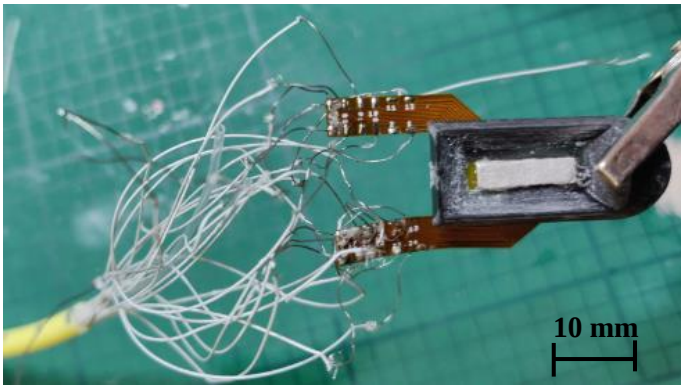

Figure 7-6 Soldering of the Microcoax Cables to the Flexi PCB

One of the two suspension delivery tubes was inserted into the distal orifice of the capsule top part and bent into a 180° curve to fit into the bottom part. The bottom part of the capsule was then covered with polyvinylidene chloride (PVDC) sheet and filled with a mix of epoxy (Epofix, Struers, UK) and air filled microballoons with weight to volume ratio of 1.09 g epoxy for 5 mL of microballoons (full procedure detailed in Section 4.6.2). The mixture was placed by hand in the bottom part of the capsule due to its powdery texture, which did not flow through a syringe needle. Afterwards, the two parts of the capsule were assembled and pressed, while the arms of flexi PCB were bent to fit inside the bottom part of the assembly (Figure 7-7 a.). A more flowable mix of epoxy and microballoons, obtained by adding a lower concentration of microballoons, was introduced with a syringe through a 1.0 mm diameter needle around the edges of the array to provide water tightness (Figure 7-7 b.). The assembly was fastened with zip ties and the epoxy was allowed to cure at room temperature for a minimum of 12 hr.

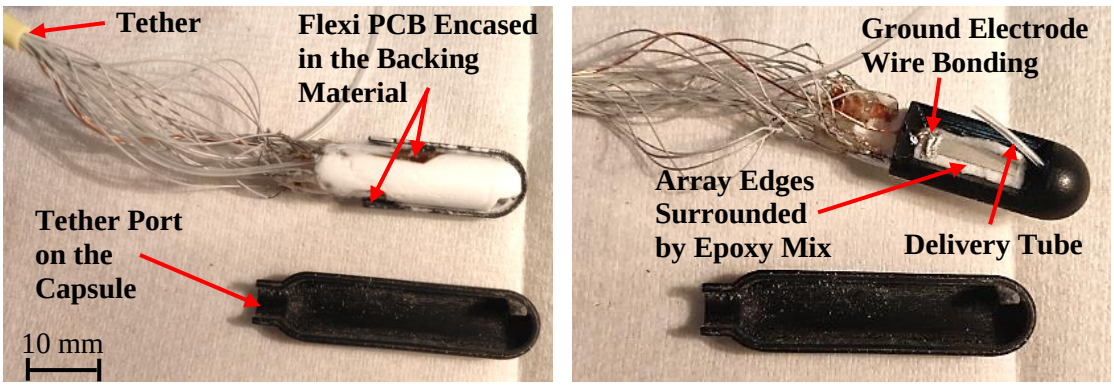

Figure 7-7 Capsule Assembly: a. View of the Cured Backing Layer and Encased Flexi PCB; b. Capsule Top View Showing the Cu Wire Bonded to the Ground Electrode and Array Lateral Edges Surrounded by Epoxy

Following, the bottom part was removed and the PVDC sheet detached from the hardened backing of the transducer. The purpose of this step was to allow more access to the remaining loose components inside the capsule (one suspension delivery tube and the GND cable), and to use a stronger adhesive between the array backing and the bottom part. The Copper wire

was then bonded to the proximal edge of the array top electrode (Figure 7-7 b.) with a two-part Ag conductive epoxy (G3349, Agar Scientific, UK) and then cured in the oven for 30 min at 50°C.

The tether tube was then brought towards the capsule by about 2.5 - 5 cm, in order to fit into the connection port of the casing (Figure 7-7 a.). This step was required due to the lack of space inside the capsule to accommodate the exposed length of cables. Great care was required to slide the tether forward by pulling the bunched cables from the other end. If the pull force was too high, the microcoax cables inside the tether tube could rupture, leading to irreparable damage or the suspension delivery tubes could get blocked or develop leaks. After the tether tube was well positioned, a layer of epoxy was poured inside the bottom capsule part, which was then assembled with the top part holding the transducer. The third part of the capsule was then filled with a flowable mix of microballoon-epoxy and assembled with the other two parts. Any remaining empty space inside the capsule was filled with flowable microballoon-epoxy mix with a 1.0 mm diameter syringe needle, through the tether connection port. Zip ties were used to fasten tightly the assembled capsule which was allowed to cure at room temperature for 12 hr. Afterwards, a layer of varnish was applied on the surface of the array and on the connection with the Copper cable to ensure the assembly was watertight. The locking parts of the capsule and the connection port with the tether tube were further insulated with a thin layer of flowable silicone rubber compound (RS PRO 692-542) applied with a fine brush. Any excess sealant was removed with fine grain sanding paper to avoid any protrusions that could injure the intestine. Figure 7-8 shows the assembled capsule, attached to the tether tube.

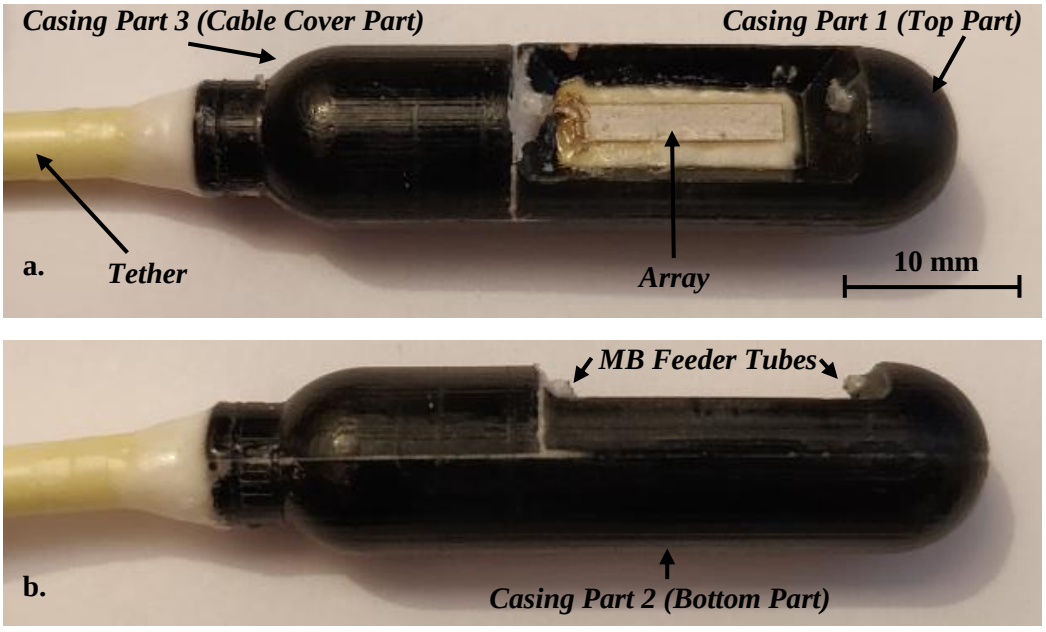

Figure 7-8 Experimental Capsule: a. Top View; b. Side View

A custom rigid PCB was designed and manufactured to allow connection of the microcoaxial cables to the DSL FIToolbox. The inner cores of the microcoaxial cables were exposed with fine tweezers, separated from the ground sheaths, and soldered to the corresponding pads of the PCB. All GND sheaths of the 24 signal microcoax cables were soldered to the DSL connector board, together with the two GND cables from the flexi PCB. The GND sheaths were left unconnected at the capsule side, and were only connected at the FIToolbox plug in order to minimize ground loops that could increase interference.

Finally, the capsule was conformally coated with an 8 μm layer of Parylene C, with a vaporization and condensation process performed under vacuum (SCS Parylene Deposition Equipment, IN, USA). The benefits of Parylene C deposition included biocompatibility, lubricity of the finished layer and added water tightness due to the conformal coating [19]. The finalized capsule assembly, including the tether and silicone tubing and the FIToolbox connector board, is presented in Figure 7-9. A total of three capsules were manufactured as a contingency measure for *in-vivo* experiments, but only the first one was fully characterized.

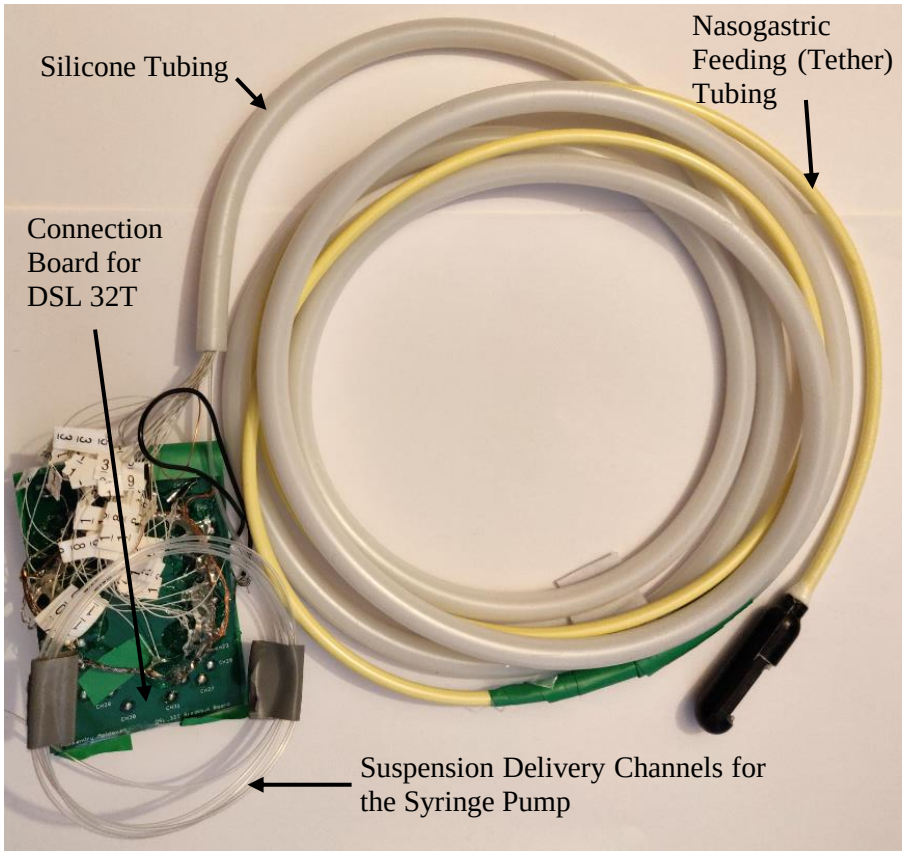

Figure 7-9 Capsule Array with Tubing and Connection Board for the DSL FIToolbox

The manufacturing time per capsule was approximately one month, which was twice than the time required for fabricating the simpler arrays described in Chapter 4. This was due to the

increased complexity of reducing the scale of the device and its associated interconnects, the addition of the microcoaxial cables and the tether tube, as well as, ensuring biocompatibility. Furthermore, the estimated price for manufacturing one capsule was around £1000, including equipment and materials.

7.2.5 FI Toolbox Power Supply Modification

To allow for lower driving voltages and higher currents than the FIToolbox's original capability, as required for better control of the acoustic intensity during therapy, the internal high voltage power supply of the machine was bypassed with two external bench power supplies providing the positive and negative power rails. As the DSL-32T pulsers are powered through the DSL-32R board, the power interface between the two boards was disconnected and the ±Ve pins of the transmitter board were connected directly to the two bench power supplies. A beneficial result from the power supply change was a reduction in noise in the driving signals (Figure 7-10). The noise reduction was associated with a smoother DC voltage applied to the FIToolbox pulsers from the bench power supply, which was equipped with a Cu transformer as opposed to the high voltage supply, which was a switching power supply intended for high voltage output. Being driven at its lower operational range (~ ±10V), the switching power supply introduced ripple in the output DC signal due to larger switch transients associated with slower switching for the low voltage operation. The transients were not efficiently smoothed by the supply's inbuilt filters, which were designed for higher switching rates. Conversely, the bench power supply was operated well within its specification, which led to reduced DC ripple.

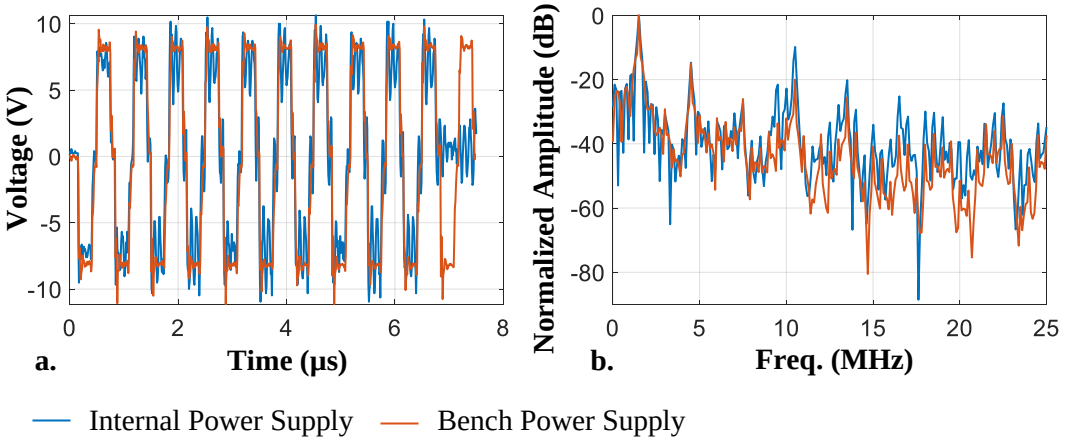

Figure 7-10 Comparison Between the Driving Voltage of the FIToolbox Before and After the Change in Power Supplies for its Pulsers: a. Time Domain Signal; b. Frequency Domain Normalized Amplitude

7.3 Capsule Characterization and Testing

The capsule array was characterized in terms of electrical impedance and beam pattern profiles using the same approach as discussed in Chapter 5. FEA simulations were used to evaluate beamsteering and focusing efficiency of the transducer and were compared with the data obtained with the NH in the scanning tank. The capsule was no longer just dipped in the scanning tank but could be fully submerged due to its water tightness.

7.3.1 Electrical Impedance Analysis

The electrical impedance of each element of the finalized capsule array was measured with an impedance analyser with the probes connected to the corresponding pads of the PCB connector board for the FIToolbox. The data were then compared with the impedances of the array elements measured before the transducer was embedded in the capsule, with only the flexi PCB bonded to the bare array. Figure 7-11 presents a comparison of the electrical impedance magnitude and phase spectra, averaged over all 24 elements for both situations (undamped and damped).

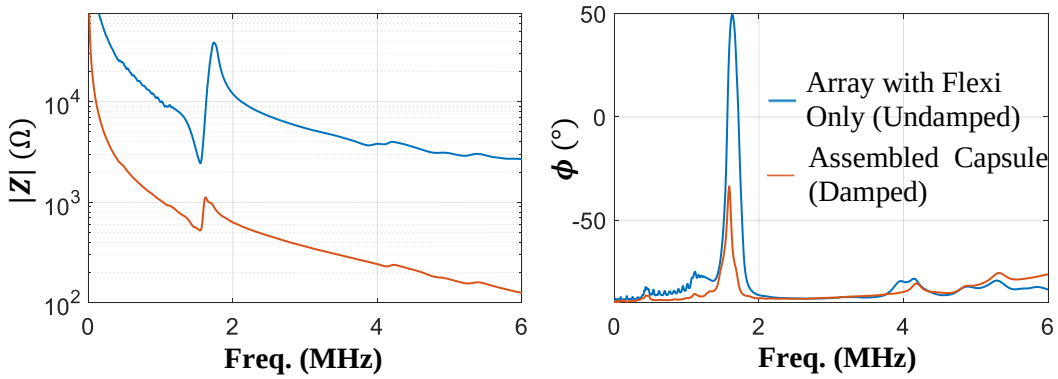

Figure 7-11 Average Impedance Magnitude and Phase Response of All Elements of the Array with Flexi PCB Only vs. the Assembled Capsule Array Including Electrical Interconnects

The average resonance frequency of all elements in the bare array was 1.55 MHz, with a standard deviation of 31.7 kHz, and the average electrical impedance magnitude at resonance was 1940 Ω, with a standard deviation of 540 Ω. The average resonance frequency of all array elements did not change significantly after embedding the transducer in the capsule, with a mean value of 1.54 MHz, and a standard deviation of 21.8 kHz. However, the average impedance magnitude at resonance decreased to 519 Ω due to damping added by the backing layer and capsule casing, and the standard deviation was 146 Ω. The full variation in the measured impedance spectra in relation to the average impedance response of all elements of the array before and after its embedding in the capsule is presented in Figure 7-12.

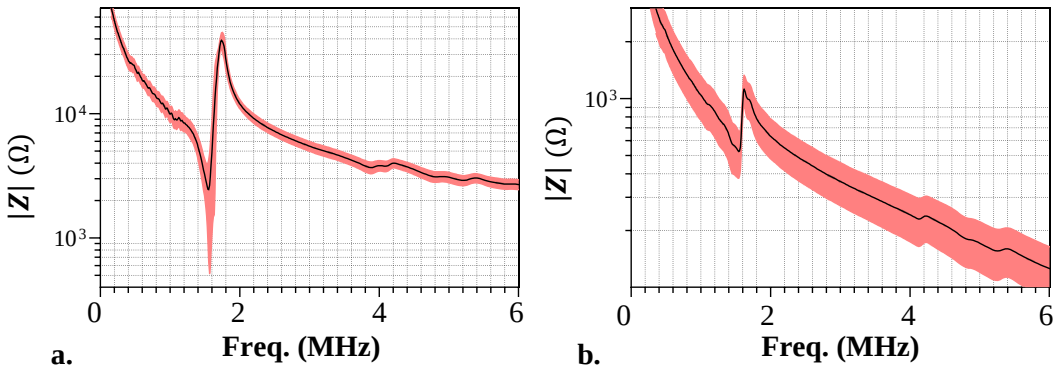

Figure 7-12 Average Impedance Spectra (Black) with Error Intervals (Red) Across all 24 Elements of: a. Bare Array Bonded to the Flexi PCB Only; b. The Fully Assembled Capsule Array

The damped impedance response of the finalized capsule array compared to the bare array with only the flexi PCB bonded to it was caused by the cumulative damping from the backing material, the casing material and from the protective varnish and Parylene-C layers covering the transducer surface. The reduction in the electrical impedance magnitude at f_r , due to the additional cable attached, was beneficial as it led to better electrical matching with the phased array controller. Importantly, no spurious resonance or frequency shift appeared in the impedance of the finished capsule compared to the bare array with flexi only.

7.3.2 Beam Profile Characterization with the Needle Hydrophone

The NH reach along the active aperture of the array was limited by the horizontal clearance of the capsule casing which was only 14.3 mm in length. This restriction did not allow the scanning tank to capture the entire XZ profile of the beam when the array was focused above the 4.26 mm tall capsule walls and steered at angles larger than the clearance. The solution to this issue was to combine two 2-D slice scans fixed in the maximised Y direction (corresponding to the centre of the passive aperture): a shorter and a longer scan along the X direction, depending on the distance (Z) from the array. The first scan started 1.5 mm away from the array surface in the positive Z direction and finished at a distance of 4.3 mm from the array. The length of the scan (X direction) was set to 13.2 mm, allowing for 1.1 mm error margin to avoid the fragile NH colliding with either the capsule angled walls or the protruding suspension delivery tubes (Figure 7-13).

The second scan was performed from a distance of 4.3 mm away from the array surface in the Z direction, which was above the edges of the capsule walls, and it spanned over a distance of 7.5 mm in +Z (Figure 7-13). The length (X direction) of the second scan was increased to 19.5 mm in order to capture the entire steered beam.

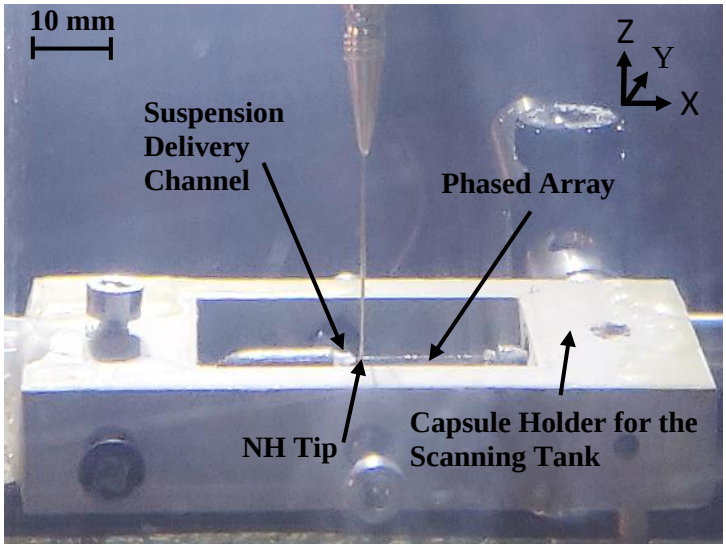

Figure 7-13 Space Restrictions for NH Scanning of the Capsule Array

Subsequently, the data matrices from the two scans were merged and the respective PNP plots were aligned manually to produce the image of the full beam pattern (Figure 7-14) using a custom-designed MATLAB program (Figure B-5, Appendix B). NH scans were performed for the capsule array before and after Parylene coating to evaluate the coating influence on the array's performance. Both XZ and cross section (XY) scans were recorded for various steering angles in the range of {0° - 56°} and focal distances of 4.0 mm, 5.0 mm and 5.7 mm.

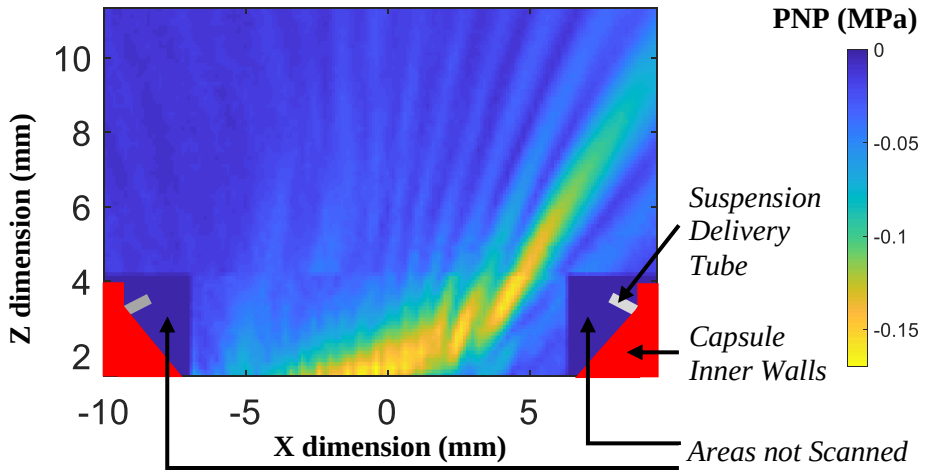

Figure 7-14 Combined NH Scan (Small and Large Reach) of the Beam Pattern Produced by the Capsule Array Focused at 5.7 mm in Depth and Steered at an Angle of 46.4° in Water

7.3.3 Correlation Between the FEA Model and the Experimental Data

The acoustic pressure data acquired with the NH in the scanning tank were compared with the FEA model results in terms of beam shape and average PNP enclosed by the -1dB profile of the beam. Generally, good accordance in terms of beam profiles was obtained between simulations and measurements (Figure 7-15).

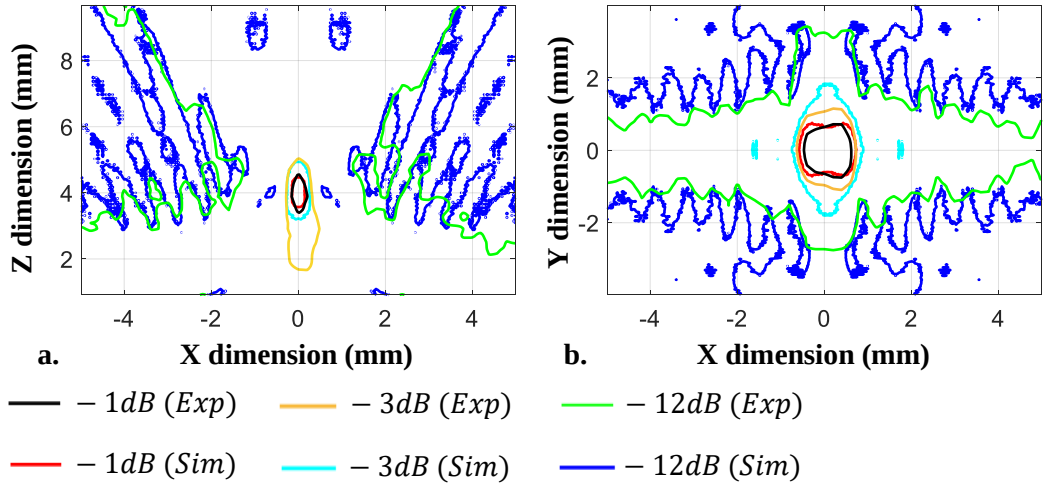

Figure 7-15 Beam Profile Comparison between the NH Measurement with the Scanning Tank and the FEA Simulation for the Capsule Array Focused at 4.0 mm, 0°: a. XZ 2-D Slice; b. Cross Section 2D Plot Measured at a Depth of 3.0 mm from the Array

Slight mismatches in the beam shape and angle between the experimental and the simulated data, especially at steering angles over 35°, were observed after Parylene coating. This was mainly attributed to an imperfect bond between the Parylene layer and the varnish layer previously applied on the array surface. The reason for this is the protective varnish adhered better than Parylene to the array surface due to its chemical bond with the transducer material, whereas Parylene was deposited on top of the varnish layer by evaporation, which has a lower bonding strength. The resulting Parylene layer was also stiffer and less compliant than the varnish.

A comparison of the average -1 dB PNP is presented in Table 7-1. An average 13.1% decrease in the -1 dB PNP fit ($\bar{R}$) between simulation and measurement was obtained for the capsule array without Parylene coating compared to the less complex arrays evaluated in Section 5.4.3. The fit decreased by 21.8% compared to the previous arrays after Parylene coating. The decrease in fit can be partially explained by the mismatch in the backing material shape between the FEA model and the experimental capsule transducer, and the non-inclusion of the part of the capsule casing distal from the array in the model. The manufactured capsule array had a semi-cylindrical backing, attached to the capsule casing with hard epoxy, while the simulation only considered a rectangular backing of similar thickness with the thickest part of the cylindrical backing. Further potential causes for the decrease in the PNP fit were: the lateral clamping from the layer of epoxy with microballoons surrounding the array for water tightness; electrical interference between the closely spaced tracks of the flexible PCB and the solder joints; slight mechanical damage of the active material during manipulation and slight depoling as a result of the heating cycles required during capsule manufacturing and assembly.

The further decrease in the array performance following Parylene coating strengthened the observation of an imperfect bond to the Varnish layer applied on the array surface and added clamping due to material stiffness.

Table 7-1 Average Percentage Ratio and Standard Deviation Between the Measured and the Simulated PNP_{-1dB} for all XZ Beam Profiles Acquired from the Capsule Array

Parylene Coating	No	Yes	
Focal Depth (mm)	5.0	4.0	5.7
Steering Angles	0° | 38.6°	0° | 26.5° | 44.9° | 56.3°	0° | 19.3° | 35° | 46.4°
$\bar{R}^1$	79.0	68.9	71.7
σ^1	5.6	10.1	7.8

[1] $\bar{R}$ and σ expressed in terms of the % ratio between measured and simulated PNP_{-1dB}

7.4 Capsule Preparation for Future in-vivo Trials

7.4.1 Evaluation of the Strength of the Tether Tube and its Bond to Capsule Casing

The tensile strengths of the nasogastric feeding tube and the bond between it and the capsule casing were evaluated in order to ensure the capsule would not break free inside the porcine small bowel when the tether was pulled. The tensile strength evaluation was performed with an Instron Material Testing System (INSTRON, MA, USA) on 9 dummy capsule casings (Figure 7-16). Five casings were bonded to the tether tube with pure Epofix, while the other four were bonded with a more viscous but flowable mixture of Epofix and air-filled microballoons. The latter mixture was used in the manufacturing of the capsule arrays due to its semi-fluid consistency which allowed it to stay in place for the 12 hr hardening period of the epoxy. The tether tube was filled with cables, similar to the real transducer, to maintain its stiffness during bonding.

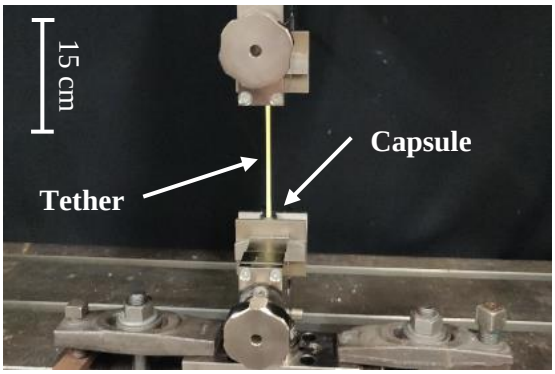

Figure 7-16 Testing the Strength of the Tether Tube and its Bond to the Capsule Casing with a Load Cell

The elongation of the tether tube as function of the tensile force applied by the load cell is presented in Figure 7-17 for both types of bonding materials. The tube elongated for more than 100 mm before it broke in all tests. The breakage point in all samples was at the bond with the capsule and was caused either by the rupture of the tube's silicone material which was softer than the hard epoxy or the detachment of the tube from the capsule joint. The samples bonded with Epofix had an average tensile strength of 459 N, standard deviation 56 N, while the samples bonded with the Epofix and microballoons mix had an average strength of 405 N and standard deviation of 68 N.

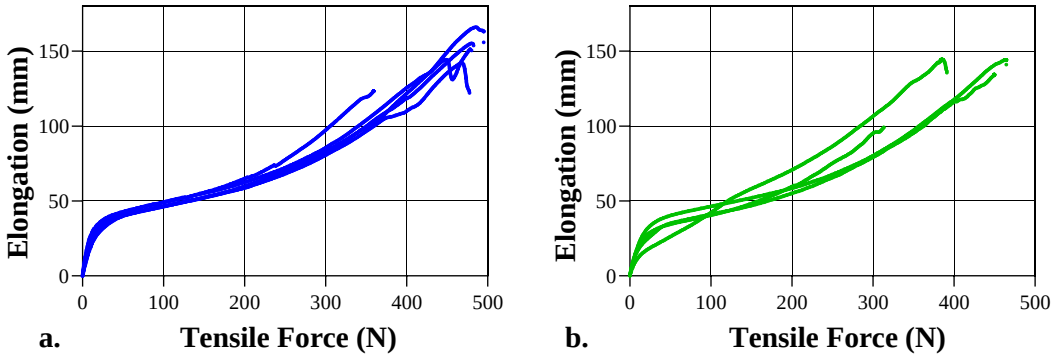

Figure 7-17 Relation Between the Elongation of a 150 mm Long Tether Tube and the Tensile Force Applied Before Rupture. Tether Bonded to the Capsule with: a. Epofix Only; b. Epofix and Microballoons

B. Terry et al. found the mean force required to overcome self-adhesivity of the mucus and friction inside the porcine small intestine was 1.34 ± 0.14 N/cm in the middle region and 1.18 ± 0.22 N/cm in the distal region of the bowel [276]. The reported values are over 300 times less than the measured mechanical strength of the capsule transducer samples. Furthermore, X. Wang et al. measured the resistance force of the small bowel to the passage of an 11 mm diameter by 26 mm length capsule [277], which has the same diameter with the capsule array presented in this chapter, to be 70 mN, which is even lower than the results reported by Terry et al.

7.4.2 Method to Test the Correct Functionality of the Capsule Array During *in-vivo* Experiments

As *in-vivo* sonoporation experiments are expected to be performed in an operating room, a method to ensure the correct functionality of the capsule and the driving system in situ before and after the therapeutic procedure is required in the absence of the NH scanning tank. To accommodate this requirement, a procedure based on pitch-catch was proposed to quickly test the correct functionality of the system while in the operating room. This consisted in sequentially triggering an unfocused, single element transducer (Olympus Corporation, Tokyo, Japan), towards the capsule and monitoring the received acoustic signal by the capsule with the DSL, followed by triggering the capsule array and receiving the US field with the

single element transducer. The two devices were fixed at a separation distance of 15 cm from each other with a custom-made 3-D printed fixture (Figure 7-18) with inserts that guided them into the same position every time.

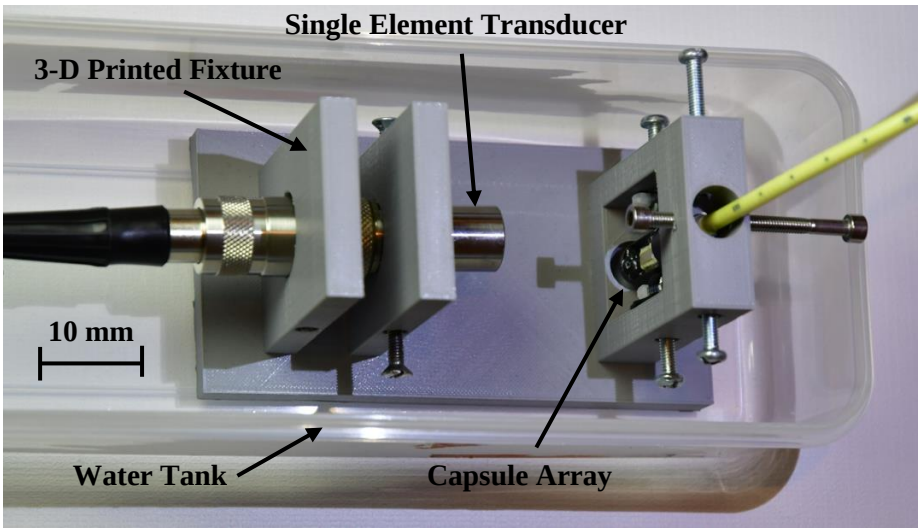

Figure 7-18 Mobile Testing Platform for the Capsule Array

The first part of the testing procedure evaluated the functionality of each array element by firing the single element transducer towards the capsule. The array was connected to the receiver board of the FIToolbox (DSL-32R) and the single element transducer was driven with a signal generator, synced with the FIToolbox. An inspection of the data traces (Figure 7-19) from each channel of the DSL-32R allowed identification of any dead elements of the capsule array. The decreasing voltage amplitude with channel number in Figure 7-19 was caused by the natural focus of the single element transducer being closer to element 1, rather than element 24 of the capsule array. To mitigate this, the 3-D printed fixture was designed to allow modification of the single element transducer height with respect to the capsule array so that its focal zone could be translated to cover the entire aperture of the array.

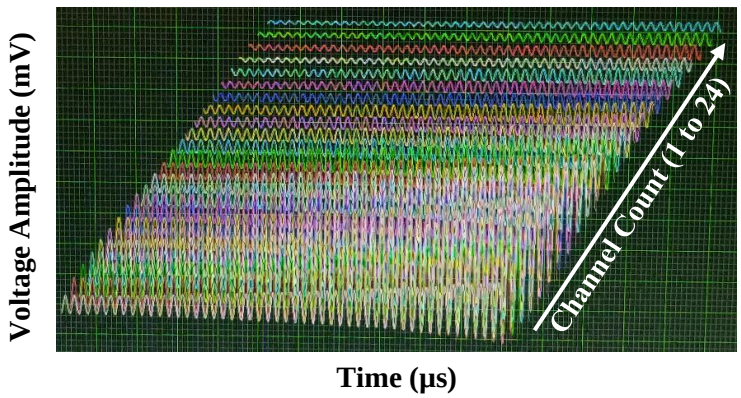

Figure 7-19 Electrical Signals Recorded with the DSL-32R from the Capsule Array, Indicating the Functionality of all Array Elements

The second part of the test will involve connecting the capsule array to the DSL-32T module and focusing it at 15 mm towards the single element transducer. The output voltage from the transducer will be measured before and after the *in-vivo* procedure with an oscilloscope and will be compared with the reference value measured beforehand, during the array characterization. This step ensures the FIToolbox operates correctly, the phased array focuses as expected and the pressure amplitudes obtained at focus are comparable to the ones measured in the laboratory.

7.5 Conclusions

Following the satisfactory *in-vitro* results achieved with the experimental 1D phased arrays, a 24-element capsule array based on the 1.5 MHz, PZT-5H, 1-3 piezocomposite material was designed, manufactured and characterized. The capsule device was intended to perform in-vivo cavitation-enhanced drug delivery in the porcine small bowel. The *in-vivo* experiments are expected to be performed at the University of Edinburgh, Bioresearch & Veterinary Services facility, in early summer 2021, with M. Turcanu responsible of the biological aspects.

The capsule was 40 mm long, had a diameter of 11 mm, and was connected to a nasogastric feeding tube which contained the interconnects for the array and two suspension delivery tubes. Two channels in the capsule situated at the sides of the array were designed to deliver a suspension of MBs and therapeutic agents to facilitate drug delivery during insonation.

The array is separated from the bowel tissue by 4.26 mm tall capsule edges in order to allow efficient beam focusing in the medium between the transducer and the treated region, where cavitation of the delivered MBs is expected. The means to ensure separation was obtained by lowering the array inside the capsule casing and maintaining protruding edges around it. FEA was employed to simulate different edge geometries as an aid to determine the most efficient geometry in terms of space taken, while minimizing reflections from the edges. The capsule casing was 3-D printed with a Polyjet process, which produced high-resolution parts with a smooth, glossy finish. The biocompatibility of the transducer was ensured with an 8 μm thick conformal coating of Parylene-C.

The average electrical resonance frequency of the array elements did not change between the bare array (undamped transducer) and the fully cased array (damped transducer), but the fully cased array had lower average element impedance magnitude.

A comparison between the FEA results and the experimental data acquired with a NH coupled to a scanning tank demonstrated satisfactory correlation between the two approaches in terms of beam shape at different focal distances and steering angles. The Parylene C layer slightly affected the beamsteering ability of the transducer compared to simulation, with the most pronounced effects appearing at high steering angles (above 35°). The fit in terms of PNP between the simulated and the measured datasets was 13.1 % lower than in the case of the simpler array configurations presented in Chapter 5. This is attributed to the more complex geometry of the capsule than of the previous arrays, which was not fully included in the FEA model.

Finally, due to the possibility of transducer failure during transport or during the *in-vivo* experiments, a method was devised to test the correct functionality of the capsule arrays in the operating room, that did not require a NH scanning tank or impedance analyser. A 3-D printed jig is used to hold a single-element transducer at a fixed distance from the array, and by the use of a pitch-catch method, the integrity of the array elements, as well as the functionality of the FIToolbox controller, can be rapidly assessed.

8 Conclusions and Future Work

8.1 Conclusions

Development of the Concept for the Phased Array for Intracorporeal Sonoporation

The main objective of this Thesis was prototyping of an intracorporeal ultrasonic array for sonoporation, based on a simulation approach for designing improved 1-3 piezocomposite 1D phased arrays with high PNP output efficiency.

A review of the literature highlighted that various medical US procedures, such as HIFU ablation, IVUS and endoscopy, employ catheter or capsule US transducers. However, there is limited reporting of research into intracorporeal transducer design for sonoporation, with most sonoporation studies relying on single-element external US transducers. This is partly because sonoporation requires lower centre frequencies than the procedures mentioned beforehand, which is related to larger transducers and because sonoporation is a procedure that is relatively new and emerging.

A subsequent literature review was performed to identify the key US requirements for sonoporation in relation to targeted drug delivery. Most of the studies showed that US centre frequencies associated with cell membrane poration are around 1.0 MHz, with the upper limit being 5.0 MHz. This was generally attributed to the resonance frequency of MBs and to the frequency dependent cavitation threshold. PNP magnitudes between 0.1 MPa and 0.5 MPa are commonly associated with reparable sonoporation throughout the literature when MBs are administered simultaneously with insonation. The sonoporation threshold is reported to increase greatly (> 4.0 MPa) when MBs are not administered during the procedure. As sonoporation is mechanically generated by MB oscillations, US using long pulses has been shown to be efficient in achieving membrane permeabilization, with lower tissue and transducer heating compared to continuous US.

A phased array configuration for the intracorporeal transducer prototype was approached because of the ability to focus and beamsteer, which is useful in reducing catheter motion and thus avoiding vessel damage. Additionally, the depth at which sonoporation takes place can be varied with electronic focusing. The 1D geometry was chosen instead of 1.5D or 2D due to the limited space constraints and due to larger array element size. 1-3 connectivity piezocomposites were employed as the active material for the arrays because of their reduced acoustic impedance, which is required for efficient coupling with tissue, and due to the enhanced coupling coefficient, favourable for the intended therapeutic purpose.

The proximate target of this project was to design therapeutic phased arrays smaller than 2.5 mm in width and 12 mm in length, that could be incorporated in an 8 Fr catheter. This catheter size is compatible with human hepatic arteries and pulmonary vessels, and the device incorporating the prototype arrays could be used for treatment of various pathologies such as solid hepatic tumours. As this work was primarily technical, and not biological, the application by which the arrays were demonstrated was through the development of a smart, 33 Fr capsule for drug administration in the small bowel. The capsule prototype will be used in an *in-vivo* experiment aimed to evaluate insulin delivery through porcine small bowel by means of sonoporation in collaboration with M. Turcanu, University of Glasgow, and the results will be reported in [22].

Design Approach for the Phased Arrays

A cross-platform (MATLAB + OnScale) simulation algorithm based on a combination of FEA and Kirchhoff time domain extrapolation was developed for simulating the 1-3 piezocomposite arrays. The MATLAB code was designed to perform all geometrical and coupling calculations for the piezocomposite material and for the array. The code then called OnScale to simulate the 3-D transducer model with FEA and a water load with extrapolation. The MATLAB program also considered manufacturing and therapeutic limitations for the calculation of the array parameters, which included: lateral size constraints, commercially available dicing blade kerf sizes and protrusions, as well as fixed resonance frequency.

The pressure simulation software was designed with the functionality of performing volume fraction and pillar aspect ratio sweeps in order to relate the 1-3 piezocomposite parameters to the resulting PNP achieved at focus by the simulated arrays. PNP at focus was used as the improvement parameter for the sweeps because it is one of the most important parameters in sonoporation studies. The purpose of the multiparametric sweep was to produce an improved array capable of achieving a high PNP output in the target, with reduced dimensions, that would operate at low driving voltages to avoid self-heating. A subsequent program was developed to evaluate the electrical impedance of the modelled transducers for providing insight into resonance frequency, spurious modes and coupling.

In order to demonstrate the feasibility of the software design approach for prototyping miniature arrays for sonoporation, two different piezoelectric materials were used: PZT-5H and PMN-29%PT, and two resonance frequencies were evaluated: 1.5 MHz and 3.0 MHz.

Phased Array Manufacturing

The four types of arrays developed with the simulation approach were manufactured with the dice and fill technique using the parameters indicated by the multiparametric sweeps. The

piezocomposite bulk materials were then lapped to a thickness corresponding to their designed resonance frequency.

A new method was developed for transducer electrode deposition, which employed a spin coater and Ag ink compound from Creative Materials (Creative Materials Inc., Ayer, MA, USA). Once applied, the ink was cured at a temperature lower than the manufacturer's minimum recommended curing temperature to protect the piezocomposite materials. The proposed method was more cost-effective and required significantly less complex equipment and processing time than thin film deposition, which is normally performed in a cleanroom. Various spin coating parameters were evaluated to minimize the surface electrical resistivity and thickness of electrodes deposited on microscope glass slides. The spin coated electrodes were then compared with a series of electrodes produced with more standard procedures for piezoelectric materials including thin film thermal deposition (Ag, Au, Cu, Al on a Cr base layer), K-bar coating and brush application. The surface resistivity of the respective spin coated electrodes was similar to the thermally evaporated Ag and Cu electrodes, which had the lowest resistivity of all evaporated metals. The electrode smoothness produced by spin coating was similar to the thermally evaporated samples, while both K-bars and brush application produced uneven layers.

Subsequently, the bulk piezocomposite materials were spin coated with Ag ink, elements were then scratch-diced with the dicing machine and the bulk materials were singulated into the designed phased array geometries. Custom-designed flexible PCB interconnections were bonded to the signal electrodes of the arrays and the devices were cased in 3-D printed enclosures. Finally, a custom-designed backing material with low damping and low acoustic impedance was added and the transducers were coated with a thin layer of varnish to ensure waterproofing.

Array Characterisation and Correlation with the Models

The manufactured arrays were driven with a DSL FI Toolbox controller, based on NI FlexRIO hardware, and acoustically characterized with a 3-DOF scanning tank, coupled to a 0.2 mm NH. The electrical impedances of the transducers were measured with an impedance analyser. Two simulation frameworks were developed from the previous multiparametric sweep program to simulate the beam pattern of the arrays in a water load. Both frameworks simulated the transducers with FEA, but the load was either simulated with FEA or with Kirchhoff time integral extrapolation. The beam profiles and PNP magnitudes modelled with the two frameworks were compared to the experimental data for all four types of arrays focused at different distances in the load and steered at several angles. The purpose of this study was to

evaluate the accuracy of simulations in therapeutic planning. The FEA + extrapolation method provided similar results compared to the full-FEA approach, but it was computationally faster and required less memory. The beam shape and steering angle were predicted well by the simulations compared to the experimental data, but the predicted PNP at focus was about twice the measured value. However, the low standard deviation of 3.41% between all evaluated steering angles and focal distances suggested that a simple, proportional correction factor could be enough for aligning the simulated PNP to the measured one.

The lapped thickness of all four piezocomposite materials was thicker than the simulated value by an average of 11.4% to maintain the resonance frequency fixed at either 1.5 MHz or 3.0 MHz. This result highlighted the requirement to update the thickness in the simulation profiles with the real thickness of the manufactured transducers. In order to keep the modelled resonance frequency similar to the experimental materials, the coupling coefficient of the piezocomposites had to be changed to be closer to the experimentally measured one. Therefore, an optimization in the electrical impedance fit between simulation and measurement was performed on the 1.5 MHz materials. The optimization algorithm aimed to minimize the difference in the resonance and antiresonance frequencies between simulation and experimental datasets, by altering the elasto-electric coefficients of the simulated piezoelectric materials. The impedance fit for the 1.5 MHz transducers was very successful. Using the new coefficients for the 3.0 MHz transducers (made of similar piezoelectric materials) improved the fit between the simulated and measured impedance, but not to such an extent as for the lower frequency arrays on which the optimization was performed. This was attributed to manufacturing degradation of the higher frequency materials, especially during the longer lapping processes. The PNP fit between simulation and measurement for the models using the optimized dataset was also enhanced towards 94% for the 1.5 MHz arrays and towards 54.7% for the 3.0 MHz, PZT-5H material (average increase in fit of 20% from the unoptimized case).

***in-vitro* Evaluation of the Phased Arrays**

Both the simulations and the acoustic field data measured with the scanning tank demonstrated that all four types of arrays were able to achieve sufficiently high PNP magnitudes for sonoporation. The PZT-5H arrays were chosen for an *in-vitro* sonoporation study performed on human colorectal cancer cells developed on ThinCert^{TM} porous membranes due to their increased robustness compared to the more sensitive single crystal transducers. The experiments, performed in collaboration with M. Turcanu revealed that both the 1.5 MHz and the 3.0 MHz arrays could control the localization of sonoporation due to focusing and

beamsteering. As most of the sonoporation experiments reported in the literature were performed with single element transducers, the ability to focus at different angles (beams) required consideration of focus sequences and focusing algorithms in addition to the standard duty cycle and pulse repetition frequency parameters. Considering the average width of the focused beam, 13 steering angles were required to insonate the total diameter of the ThinCert^{TM} membrane, measuring 13.65 mm.

Three focusing methods were evaluated in relation to MB reperfusion and sonoporation effectiveness: a continuous sweep between the 13 beams for 11 minutes, a fixed time sweep (50 s insonation of the same spot, then incrementing to the next spot) or a diffuse focus method achieved by assuming the focus of the array was located at a virtual point behind the active aperture. The continuous sweep was the most efficient type. Sonoporation effectiveness was evaluated during the procedure with a TEER meter (which evaluated the barrier function decrease of the cell layer), and post treatment with fluorescence and confocal microscopy, and with a fluorescence plate reader. Decreasing the number of sonicated spots from 13 to 9, 6 or 3, led to lower sonoporation effectiveness, which demonstrated that the arrays could spatially control the amount of tissue permeabilization, not just to produce it in a binary manner. Various MIs, $T_{\%ON}$, PRFs and numbers of cycles were evaluated, and the most favourable set of parameters for tissue permeabilization was identified as: MI=0.2, $T_{\%ON}$=10-15%, PRF=30kHz, 7 cycles per pulse, leading to a barrier function decrease of 59% from the initial value. However, all insonated tissues that manifested barrier function decrease suffered from permanent sonoporation, as the cells exposed to the US field + MBs were lysed. Nonetheless, this study demonstrated that the amount of barrier function decrease could be controlled with the experimental miniature-sized array both spatially and in terms of therapeutic power.

Capsule Array Implementation

Following the *in-vitro* study, the 1.5 MHz, 24 element, PZT-5H array was incorporated into a tethered capsule for future *in-vivo* experiments on porcine small bowel. The capsule casing was designed with two MB + drug delivery channels and with protruding edges that allowed a separation between the array face and the bowel tissue where the beam could be focused and MBs could perfuse. The capsule shape was simulated with FEA to determine the minimum clearance between the array and its walls that did not incur significant reflections. The capsule casing was 3-D printed with biocompatible materials and increased biocompatibility was achieved with a conformal layer of Parylene C. The capsule array was characterized with the scanning tank and the beam profiles were similar to the simulations.

8.2 Future Work

The future work associated with the results obtained and the experimental transducers described in this Thesis can be divided in two main directions: *in-vivo* evaluation of the capsule array for targeted drug delivery and miniaturization towards catheter implementation for intravascular applications.

8.2.1 in-vivo Sonoporation with the Capsule Array

The capsule prototypes described in Chapter 7 were already conformally coated with Parylene C, which conferred biocompatibility, and were acoustically characterized at a series of steering angles and focal distances, rendering them ready for therapeutic use. Furthermore, the satisfactory comparison with the beam profiles obtained with the simulation framework also opened the possibility to use the existing software for predicting beamsteering at other angles than the ones already evaluated with the scanning tank.

Proposed Experimental Setup

At the time of writing, a research team from University of Strathclyde, University of Glasgow and University of Edinburgh was already assembled for evaluating, planning and executing a future experiment involving targeted insulin delivery through porcine small bowel *in vivo* with the capsule array prototype. The *in-vivo* experimental procedure was designed by M. Turcanu and it aims to evaluate insulin absorption in the systemic circulation through the small bowel as a result of sonoporation. Prior to *in-vivo* testing, a control experiment will be performed on *ex-vivo* small bowel tissue sampled from a freshly sacrificed pig. This will allow correlation of the US driving parameters with the bioeffects in the tissue. Subsequently, the capsule will be inserted in the porcine small bowel, *in vivo*, through a stoma. Insulin and MBs will be administered through the two delivery channels in the capsule during insonation. Therapeutic effectiveness will be evaluated both in real time by measurement of glucose levels of the pig and post treatment with histology, fluorescence and confocal microscopy, and other means.

DSL FI Toolbox Modification for Therapeutic Applications

During the *in-vitro* experiments, it was noted that the DSL FI Toolbox presented signal quantization errors for higher duty cycles than 20.7% or higher PRFs than 57%, and the number of cycles per pulse in the current setup was limited to only 10. This was associated with limitations of the software platform for the machine, which was primarily designed for imaging rather than therapeutic purposes, causing overflowing of the machine's available DRAM memory. To solve these issues, a collaboration with David Lines, University of Strathclyde, was established, with the purpose of designing a new program specific for the

purpose of therapeutic US that will allow for higher numbers of pulses and $T_{\%ON}$ than the current software. The new program will be used for the *ex-vivo* and *in-vivo* experiments.

8.2.2 Further Transducer Miniaturization Towards Catheter Implementation

The prototype capsule array (33 Fr diameter) could be miniaturized into an 8 Fr diameter catheter by reducing the backing layer thickness and flexible PCB size, by removing the protruding edges of the capsule casing and by potentially employing other piezoelectric materials in the design of the array.

The software design tools, the array and capsule fabrication methods, the characterization techniques and the programs developed for simulating the acoustic beams developed as part of this Thesis can be employed, with slight modifications, in the future development of the proposed catheter US array for intravascular sonoporation.

Minimization of the Backing Material

A large space of the current capsule is taken by the backing layer. A reduction in the size of this layer will therefore decrease the diameter of the device. However, if the thickness of the microballoon-loaded epoxy backing layer is decreased too much, there may be a risk that it could couple some of the acoustic energy from the array towards the back of the catheter, thus reducing the net power transmitted in the target tissue. A first step is therefore to determine the thinnest possible layer of the present backing material that keeps the stray field sufficiently small.

This can be achieved by using either of the two 3-D beam pattern modelling frameworks described in Chapter 5 to simulate the acoustic pressure at the array focus for various backing layer thicknesses. If that cannot be achieved, one possible approach would be to remove the backing material and replace it with an air backing as in Figure 8-1 a.

Miniaturization of the Flexible PCBs

Also aimed at miniaturisation, the current flexible PCB interconnects bonded to the capsule array were designed with two arms and traces on only one side (Figure 8-1 b.-c.), with a continuous GND plane on the other side (Section 7.2.3). The flexible PCB could be further miniaturized by placing traces on both sides of the PCB and by using micro-vias to pass the traces on the back of the connector board to the array bonding side as in Figure 8-1 d.-e.

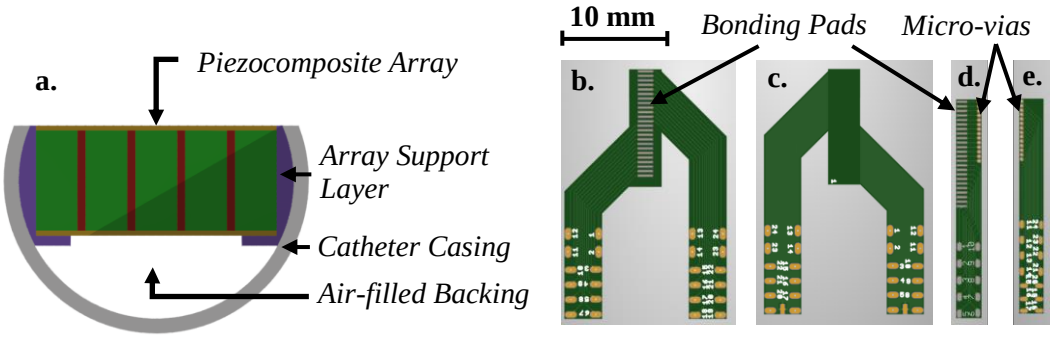

Figure 8-1 a. Proposed Catheter Transducer (Cross Section View); b.-c. Flexible PCB Used in the Capsule Array (Bonding Side, Back Side) ; d.-e. Flexible PCB Proposed for the Catheter Array (Bonding Side, Back Side)

Eliminating the Capsule Protruding Edges

In the current capsule prototype, the protruding edges ensure a 4 - 5 mm clearance between the array surface and the blood vessel epithelial tissue, critical for beam forming and for MB + drug delivery. Removal of the edges will impair drug and MB perfusion to the insonation site and array focusing, which will correlate to a drop in therapeutic effectiveness.

One solution to increase transducer – tissue separation during therapy, while maintaining reduced diameter of the device during insertion would be to equip the catheter transducer with two hollow-centred balloons (Figure 8-2 a.). The two balloons can be fixed at the proximal and distal ends of the array, and be inflated once the catheter is in position for therapy (Figure 8-2 b.), providing a separation of several mm between the array surface and the sonoporated blood vessel epithelium. Figure 8-2 c.-d., reprinted from Ref. [278], presents a possible type of balloon that could be included in the future catheter array prototype.

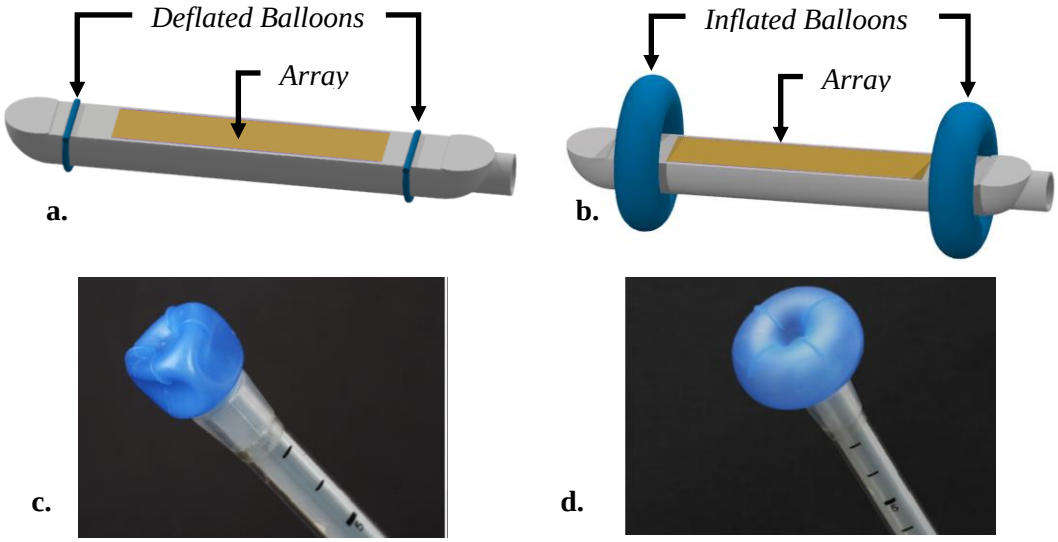

Figure 8-2 Proposed Catheter Array With: a. Deflated Balloons for Intravascular Insertion; b. Inflated Balloons During Therapeutic Procedure to Increase the Separation Between the Array Surface and the Blood Vessel Epithelium; c.-d. Example of Hollow-Centred Balloon Catheter (Reprinted from Ref. [278])

Array Size Reduction and the Use of Other Piezoelectric Materials

Further dimension reduction can be achieved by minimizing the array lateral dimensions and by reduction of the number of elements. This step can be evaluated and performed with the 1-3 piezocomposite phased array design and improvement tool presented in Chapter 3. However, a decrease in the array size will undoubtedly decrease the power output. Finally, a thickness decrease of the active element can be achieved by designing the transducer to operate at lateral resonance [21], but the overall diameter of the device would not be greatly reduced.

Replacing the PZT-5H material with PIN-PMN-PT would allow to obtain higher electromechanical coupling and piezoelectric coefficients. Also, the ternary crystal benefits over PMN-PT from higher Curie temperature and larger mechanical quality factor, which increases its usefulness in high power US transmission [279]. Designing a piezocomposite based on PIN-PMN-PT rather than PZT-5H or PMN-PT will lead to increased power output, which could potentially allow a size reduction for the array.

References

[1] K. Uchino, “Chapter 1 - The Development of Piezoelectric Materials and the New Perspective,” in *Advanced Piezoelectric Materials (Second Edition)*, Second Edition., K. Uchino, Ed. Woodhead Publishing, 2017, pp. 1–92. doi: 10.1016/B978-0-08-102135-4.00001-1.

[2] T. L. Szabo, *Diagnostic ultrasound imaging: inside out*. Academic Press, 2004.

[3] K. Nakamura, *Ultrasonic Transducers: Materials and Design for Sensors, Actuators and Medical Applications*. Elsevier, 2012.

[4] H. E. Elmansy and J. E. Lingeman, “Recent advances in lithotripsy technology and treatment strategies: A systematic review update,” *Int. J. Surg. Lond. Engl.*, vol. 36, no. Pt D, p. 676, Dec. 2016, doi: 10.1016/j.ijsu.2016.11.097.

[5] G. T. Haar and C. Coussios, “High intensity focused ultrasound: Physical principles and devices,” *Int. J. Hyperthermia*, vol. 23, no. 2, pp. 89–104, Jan. 2007, doi: 10.1080/02656730601186138.

[6] I. Lentacker, I. De Cock, R. Deckers, S. C. De Smedt, and C. T. W. Moonen, “Understanding ultrasound induced sonoporation: Definitions and underlying mechanisms,” *Adv. Drug Deliv. Rev.*, vol. 72, pp. 49–64, Jun. 2014, doi: 10.1016/j.addr.2013.11.008.

[7] S. Dhanasekaran and S. Chopra, “Chapter 2 - Getting a Handle on Smart Drug Delivery Systems – A Comprehensive View of Therapeutic Targeting Strategies,” in *Smart Drug Delivery System*, IntechOpen, 2016.

[8] T.-Y. Wang, K. E. Wilson, S. Machtaler, and J. K. Willmann, “Ultrasound and Microbubble Guided Drug Delivery: Mechanistic Understanding and Clinical Implications,” *Curr. Pharm. Biotechnol.*, vol. 14, no. 8, pp. 743–752, Oct. 2014.

[9] J. Lin, X. Liu, X. Gong, Z. Ping, and J. Wu, “Computational study on the propagation of strongly focused nonlinear ultrasound in tissue with rib-like structures,” *J. Acoust. Soc. Am.*, vol. 134, no. 2, pp. 1702–1714, Aug. 2013, doi: 10.1121/1.4812897.

[10] S. Bobkova, L. Gavrilov, V. Khokhlova, A. Shaw, and J. Hand, “Focusing of high intensity ultrasound through the rib cage using a therapeutic random phased array,” *Ultrasound Med. Biol.*, vol. 36, no. 6, Art. no. 6, Jun. 2010, doi: 10.1016/j.ultrasmedbio.2010.03.007.

[11] P. Ramaekers, M. Ries, C. T. W. Moonen, and M. de Greef, “Improved intercostal HIFU ablation using a phased array transducer based on Fermat’s spiral and Voronoi tessellation: A numerical evaluation,” *Med. Phys.*, vol. 44, no. 3, pp. 1071–1088, 2017, doi: 10.1002/mp.12082.

[12] A. Kyriakou, E. Neufeld, B. Werner, M. M. Paulides, G. Szekely, and N. Kuster, “A review of numerical and experimental compensation techniques for skull-induced phase aberrations in transcranial focused ultrasound,” *Int. J. Hyperthermia*, vol. 30, no. 1, pp. 36–46, Feb. 2014, doi: 10.3109/02656736.2013.861519.

[13] G. T. Clement and K. Hynynen, “Correlation of ultrasound phase with physical skull properties,” *Ultrasound Med. Biol.*, vol. 28, no. 5, pp. 617–624, May 2002, doi: 10.1016/s0301-5629(02)00503-3.

[14] M. Andrzejewska and M. Grzymisławski, “The role of intestinal ultrasound in diagnostics of bowel diseases,” *Przegląd Gastroenterol.*, vol. 13, no. 1, pp. 1–5, 2018, doi: 10.5114/pg.2018.74554.

[15] R. Bor, A. Fábián, and Z. Szepes, “Role of ultrasound in colorectal diseases,” *World J. Gastroenterol.*, vol. 22, no. 43, pp. 9477–9487, Nov. 2016, doi: 10.3748/wjg.v22.i43.9477.

[16] J. E. Zimmer, K. Hynynen, D. S. He, and F. Marcus, “The feasibility of using ultrasound for cardiac ablation,” *IEEE Trans. Biomed. Eng.*, vol. 42, no. 9, pp. 891–897, Sep. 1995, doi: 10.1109/10.412655.

[17] R. Seip, M. Biswas, M. Kuznetsov, N. T. Sanghvi, T. A. Gardner, and N. F. Dabhoiwala, “Transurethral high intensity focused ultrasound: catheter based prototypes and experimental results,” in *2000 IEEE Ultrasonics Symposium. Proceedings. An International Symposium (Cat. No.00CH37121)*, Oct. 2000, vol. 2, pp. 1413–1416 vol.2. doi: 10.1109/ULTSYM.2000.921587.

[18] A. Gelet *et al.*, “Transrectal High-Intensity Focused Ultrasound: Minimally Invasive Therapy of Localized Prostate Cancer,” *J. Endourol.*, vol. 14, no. 6, pp. 519–528, Aug. 2000, doi: 10.1089/end.2000.14.519.

[19] J. C. Norton *et al.*, “Intelligent magnetic manipulation for gastrointestinal ultrasound,” *Sci. Robot.*, vol. 4, no. 31, Jun. 2019, doi: 10.1126/scirobotics.aav7725.

[20] F. Stewart *et al.*, “Ultrasound Mediated Delivery of Quantum Dots from a Capsule Endoscope to the Gastrointestinal Wall,” *bioRxiv*, p. 2020.02.24.963066, Feb. 2020, doi: 10.1101/2020.02.24.963066.

[21] J. P. Kilroy, A. V. Patil, J. J. Rychak, and J. A. Hossack, “An IVUS Transducer for Microbubble Therapies,” *IEEE Trans. Ultrason. Ferroelectr. Freq. Control*, vol. 61, no. 3, Art. no. 3, Mar. 2014, doi: 10.1109/TUFFC.2014.2929.

[22] M. V. Turcanu, “Ultrsound Mediated Targeted Drug Delivery in the Small Intestine,” University of Glasgow, Glasgow, UK, “PhD Thesis to be submitted.”

[23] A. Moldovan, “Exploration in Miniature Ultrasound Devices for Therapy with Sonoporation,” presented at the EPSRC Image Guided Therapies Network+ (IGT), University of Dundee, Dundee, UK, Nov. 2018.

[24] A. C. Moldovan, J. Dziewierz, A. Gachagan, S. Cochran, and H. Lay, “Virtual Prototyping of a Catheter Transducer Array for Internal Hepatic Sonoporation,” in *2018 IEEE International Ultrasonics Symposium (IUS)*, Kobe, Oct. 2018, pp. 1–4. doi: 10.1109/ULTSYM.2018.8579783.

[25] A. Moldovan, “Virtual Prototyping of a Catheter Transducer Array for Internal Hepatic Sonoporation,” presented at the 2018 IEEE International Ultrasonics Symposium (IUS), Portopia Hotel, Kobe, Japan, Oct. 2018.

[26] A. Moldovan, “Development of a 1-D Linear Phased Ultrasonic Array for Intravascular Sonoporation,” presented at the The 50th Annual Scientific Meeting of the British Medical Ultrasound Society (BMUS), Emirates Old Trafford, Manchester, UK, Dec. 2018.

[27] A. C. Moldovan, Z. Qiu, D. Lines, A. Gachagan, and S. Cochran, “Development of a 1-D Linear Phased Ultrasonic Array for Intravascular Sonoporation,” in *2019 IEEE International Ultrasonics Symposium (IUS)*, Oct. 2019, pp. 2056–2059. doi: 10.1109/ULTSYM.2019.8925549.

[28] A. Moldovan, “Development of a 1-D Linear Phased Ultrasonic Array for Intravascular Sonoporation,” presented at the 2019 IEEE International Ultrasonics Symposium (IUS), SEC, Glasgow, Scotland, UK, Oct. 2019.

[29] A. C. Moldovan, Z. Qiu, D. Lines, A. Gachagan, and S. Cochran, “Enhanced Modelling of a 1-D Phased Ultrasonic Array for Intracorporeal Sonoporation,” Sep. 2020.

[30] A. Moldovan, “Enhanced Modelling of a 1-D Phased Ultrasonic Array for Intracorporeal Sonoporation,” presented at the 2020 IEEE International Ultrasonics Symposium (IUS), Virtual Symposium, Sep. 2020.

[31] S. Mehier-Humbert, T. Bettinger, F. Yan, and R. H. Guy, “Plasma membrane poration induced by ultrasound exposure: Implication for drug delivery,” *J. Controlled Release*, vol. 104, no. 1, pp. 213–222, May 2005, doi: 10.1016/j.jconrel.2005.01.007.

[32] M. Postema, A. van Wamel, C. T. Lancée, and N. de Jong, “Ultrasound-induced encapsulated microbubble phenomena,” *Ultrasound Med. Biol.*, vol. 30, no. 6, pp. 827–840, Jun. 2004, doi: 10.1016/j.ultrasmedbio.2004.02.010.

[33] Y. Yang, Q. Li, X. Guo, J. Tu, and D. Zhang, “Mechanisms underlying sonoporation: Interaction between microbubbles and cells,” *Ultrason. Sonochem.*, vol. 67, p. 105096, Oct. 2020, doi: 10.1016/j.ultsonch.2020.105096.

[34] C. Li *et al.*, “Recent progress in drug delivery,” *Acta Pharm. Sin. B*, vol. 9, no. 6, pp. 1145–1162, Nov. 2019, doi: 10.1016/j.apsb.2019.08.003.

[35] M. F. Attia, N. Anton, J. Wallyn, Z. Omran, and T. F. Vandamme, “An overview of active and passive targeting strategies to improve the nanocarriers efficiency to tumour sites,” *J. Pharm. Pharmacol.*, vol. 71, no. 8, pp. 1185–1198, 2019, doi: 10.1111/jphp.13098.

[36] G. Tiwari *et al.*, “Drug delivery systems: An updated review,” *Int. J. Pharm. Investig.*, vol. 2, no. 1, pp. 2–11, 2012, doi: 10.4103/2230-973X.96920.

[37] B. W. Stewart and C. P. Wild, *World Cancer Report 2014*. IARC.

[38] S. Senapati, A. K. Mahanta, S. Kumar, and P. Maiti, “Controlled drug delivery vehicles for cancer treatment and their performance,” *Signal Transduct. Target. Ther.*, vol. 3, no. 1, p. 7, Mar. 2018, doi: 10.1038/s41392-017-0004-3.

[39] R. Karshafian, P. D. Bevan, R. Williams, S. Samac, and P. N. Burns, “Sonoporation by Ultrasound-Activated Microbubble Contrast Agents: Effect of Acoustic Exposure Parameters on Cell Membrane Permeability and Cell Viability,” *Ultrasound Med. Biol.*, vol. 35, no. 5, Art. no. 5, May 2009, doi: 10.1016/j.ultrasmedbio.2008.10.013.

[40] D. Miller, N. Smith, M. Bailey, G. Czarnota, K. Hynynen, and I. Makin, "Overview of Therapeutic Ultrasound Applications and Safety Considerations," *J. Ultrasound Med. Off. J. Am. Inst. Ultrasound Med.*, vol. 31, no. 4, pp. 623–634, Apr. 2012.

[41] K. Shung, "Diagnostic Ultrasound: Past, Present, and Future," *J. Med. Biol. Eng.*, vol. 31, pp. 371–374, 2011.

[42] J. Jagannathan *et al.*, "High intensity focused ultrasound surgery (HIFU) of the brain: A historical perspective, with modern applications," *Neurosurgery*, vol. 64, no. 2, pp. 201–211, Feb. 2009, doi: 10.1227/01.NEU.0000336766.18197.8E.

[43] M. Fechheimer, C. Denny, R. F. Murphy, and D. L. Taylor, "Measurement of cytoplasmic pH in Dictyostelium discoideum by using a new method for introducing macromolecules into living cells," *Eur. J. Cell Biol.*, vol. 40, no. 2, pp. 242–247, Apr. 1986.

[44] Tachibana Katsuro and Tachibana Shunro, "Albumin Microbubble Echo-Contrast Material as an Enhancer for Ultrasound Accelerated Thrombolysis," *Circulation*, vol. 92, no. 5, pp. 1148–1150, Sep. 1995, doi: 10.1161/01.CIR.92.5.1148.

[45] H. Nakamura, Ed., *Electroporation and Sonoporation in Developmental Biology*. Springer Japan, 2009. doi: 10.1007/978-4-431-09427-2.

[46] H. Yu and S. Chen, "Analysis of Sonoporation on Cell Membrane by Scanning Electron Microscopy," in *2012 International Conference on Biomedical Engineering and Biotechnology*, May 2012, pp. 968–971. doi: 10.1109/iCBEB.2012.70.

[47] Junru Wu, Joel P. Ross, and Jen-Fu Chiu, "Reparable sonoporation generated by microstreaming," *J. Acoust. Soc. Am.*, vol. 111, no. 3, pp. 1460–1464, Feb. 2002, doi: 10.1121/1.1420389.

[48] C. M. Moran, "CHAPTER 6 - Ultrasonic contrast agents," in *Clinical Ultrasound (Third Edition)*, G. M. Baxter and M. J. Weston, Eds. Edinburgh: Churchill Livingstone, 2011, pp. 77–89. doi: 10.1016/B978-0-7020-3131-1.00006-7.

[49] J. A. Rooney, "Hemolysis Near an Ultrasonically Pulsating Gas Bubble," *Science*, vol. 169, no. 3948, p. 869, Aug. 1970, doi: 10.1126/science.169.3948.869.

[50] W. J. Greenleaf, M. E. Bolander, G. Sarkar, M. B. Goldring, and J. F. Greenleaf, "Artificial Cavitation Nuclei Significantly Enhance Acoustically Induced Cell Transfection," *Ultrasound Med. Biol.*, vol. 24, no. 4, pp. 587–595, May 1998, doi: 10.1016/S0301-5629(98)00003-9.

[51] D. L. Miller, R. A. Gies, and W. B. Chrisler, "Ultrasonically induced hemolysis at high cell and gas body concentrations in a thin-disc exposure chamber," *Ultrasound Med. Biol.*, vol. 23, no. 4, pp. 625–633, Jan. 1997, doi: 10.1016/S0301-5629(97)00042-2.

[52] S. R. Sirsi and M. A. Borden, "Advances in Ultrasound Mediated Gene Therapy Using Microbubble Contrast Agents," *Theranostics*, vol. 2, no. 12, pp. 1208–1222, 2012, doi: 10.7150/thno.4306.

[53] J. A. Rooney, "Shear as a Mechanism for Sonically Induced Biological Effects," *J. Acoust. Soc. Am.*, vol. 52, no. 6B, Art. no. 6B, Dec. 1972, doi: 10.1121/1.1913306.

[54] D. E. Hughes and W. L. Nyborg, “Cell Disruption by Ultrasound,” *Science*, vol. 138, no. 3537, Art. no. 3537, Oct. 1962, doi: 10.1126/science.138.3537.108.

[55] A. R. Williams, D. E. Hughes, and W. L. Nyborg, “Hemolysis Near a Transversely Oscillating Wire,” *Science*, vol. 169, no. 3948, Art. no. 3948, Aug. 1970, doi: 10.1126/science.169.3948.871.

[56] J. P. Ross, X. Cai, J.-F. Chiu, J. Yang, and J. Wu, “Optical and atomic force microscopic studies on sonoporation,” *J. Acoust. Soc. Am.*, vol. 111, no. 3, Art. no. 3, Feb. 2002, doi: 10.1121/1.1448340.

[57] J. Wu, “Shear stress in cells generated by ultrasound,” *Prog. Biophys. Mol. Biol.*, vol. 93, no. 1, pp. 363–373, Jan. 2007, doi: 10.1016/j.pbiomolbio.2006.07.016.

[58] S. Bao, B. D. Thrall, and D. L. Miller, “Transfection of a reporter plasmid into cultured cells by sonoporation in vitro,” *Ultrasound Med. Biol.*, vol. 23, no. 6, Art. no. 6, Jan. 1997, doi: 10.1016/S0301-5629(97)00025-2.

[59] R. P. Holmes, L. D. Yeaman, R. G. Taylor, and D. L. McCullough, “Altered neutrophil permeability following shock wave exposure in vitro.,” *J. Urol.*, vol. 147, no. 3, Art. no. 3, Mar. 1992.

[60] S. Gambihler, M. Delhis, and J. W. Ellwart, “Permeabilization of the plasma membrane of L1210 mouse leukemia cells using lithotripter shock waves,” *J. Membr. Biol.*, vol. 141, no. 3, Art. no. 3, 1994, doi: 10.1007/BF00235136.

[61] D. E. Hughes and W. L. Nyborg, “Cell Disruption by Ultrasound,” *Science*, vol. 138, no. 3537, p. 108, Oct. 1962, doi: 10.1126/science.138.3537.108.

[62] P. Zhong, H. Lin, X. Xi, S. Zhu, and E. S. Bhogte, “Shock wave–inertial microbubble interaction: Methodology, physical characterization, and bioeffect study,” *J. Acoust. Soc. Am.*, vol. 105, no. 3, pp. 1997–2009, Mar. 1999, doi: 10.1121/1.426733.

[63] J. Blakeley, “Drug delivery to brain tumors,” *Curr. Neurol. Neurosci. Rep.*, vol. 8, no. 3, pp. 235–241, 2008.

[64] E. E Konofagou, Y.-S. Tunga, J. Choia, T. Deffieuxa, B. Baseria, and F. Vlachosa, “Ultrasound-induced blood-brain barrier opening,” *Curr. Pharm. Biotechnol.*, vol. 13, no. 7, pp. 1332–1345, 2012.

[65] T. K. Kim and J. H. Eberwine, “Mammalian cell transfection: the present and the future,” *Anal. Bioanal. Chem.*, vol. 397, no. 8, pp. 3173–3178, Aug. 2010, doi: 10.1007/s00216-010-3821-6.

[66] Fowlkes J. Brian and Holland Christy K., Ed., “Section 6—Mechanical Bioeffects in the Presence of Gas-Carrier Ultrasound Contrast Agents,” *J. Ultrasound Med.*, vol. 19, no. 2, Art. no. 2, Feb. 2000.

[67] W. J. Galloway, “An Experimental Study of Acoustically Induced Cavitation in Liquids,” *J. Acoust. Soc. Am.*, vol. 26, no. 5, pp. 849–857, Sep. 1954, doi: 10.1121/1.1907428.

[68] M. Wan, Y. Feng, and G. ter (Gail) Haar, *Cavitation in biomedicine : principles and techniques*. Springer, 2015.

[69] F. Grieser, P. K. Choi, N. Enomoto, H. Harada, K. Okitsu, and K. Yasui, *Sonochemistry and the Acoustic Bubble*. Elsevier Science, 2015.

[70] F. Caupin and E. Herbert, "Cavitation in water: a review," *Comptes Rendus Phys.*, vol. 7, no. 9, pp. 1000–1017, Nov. 2006, doi: 10.1016/j.crhy.2006.10.015.

[71] Y. S. Wei and R. J. Sadus, "Equations of state for the calculation of fluid-phase equilibria," *AIChE J.*, vol. 46, no. 1, pp. 169–196, 2000, doi: 10.1002/aic.690460119.

[72] E. Herbert, S. Balibar, and F. Caupin, "Cavitation pressure in water," *Phys. Rev. E*, vol. 74, no. 4, Art. no. 4, Oct. 2006.

[73] C. E. Brennen, *Cavitation and Bubble Dynamics*. New York: Oxford University Press, 1995.

[74] Q. Zheng, D. J. Durben, G. H. Wolf, and C. A. Angell, "Liquids at large negative pressures: water at the homogeneous nucleation limit," *Science*, vol. 254, no. 5033, pp. 829–832, Nov. 1991, doi: 10.1126/science.254.5033.829.

[75] S J Henderson and R J Speedy, "A Berthelot-Bourdon tube method for studying water under tension," *J. Phys. [E]*, vol. 13, no. 7, Art. no. 7, 1980.

[76] K. Yasui, *Acoustic Cavitation and Bubble Dynamics*. Springer International Publishing, 2018. doi: 10.1007/978-3-319-68237-2.

[77] A. D. Maxwell *et al.*, "Cavitation clouds created by shock scattering from bubbles during histotripsy," *J. Acoust. Soc. Am.*, vol. 130, no. 4, pp. 1888–1898, Oct. 2011, doi: 10.1121/1.3625239.

[78] I. Tzanakis, G. S. B. Lebon, D. G. Eskin, and K. A. Pericleous, "Characterizing the cavitation development and acoustic spectrum in various liquids," *Ultrason. Sonochem.*, vol. 34, pp. 651–662, Jan. 2017, doi: 10.1016/j.ultsonch.2016.06.034.

[79] D. Sunartio, M. Ashokkumar, and F. Grieser, "Study of the Coalescence of Acoustic Bubbles as a Function of Frequency, Power, and Water-Soluble Additives," *J. Am. Chem. Soc.*, vol. 129, no. 18, pp. 6031–6036, May 2007, doi: 10.1021/ja068980w.

[80] C. Guo, "The Relationship between the Collapsing Cavitation Bubble and Its Microjet near a Rigid Wall under an Ultrasound Field," *Cavitation - Sel. Issues*, Nov. 2018, doi: 10.5772/intechopen.79129.

[81] P. Riesz, D. Berdahl, and C. L. Christman, "Free radical generation by ultrasound in aqueous and nonaqueous solutions.," *Environ. Health Perspect.*, vol. 64, pp. 233–252, Dec. 1985.

[82] M. L. Fabiilli, K. J. Haworth, N. H. Fakhri, O. D. Kripfgans, P. L. Carson, and J. B. Fowlkes, "The role of inertial cavitation in acoustic droplet vaporization," *IEEE Trans Ultrason Ferroelectr Freq Control*, vol. 56, 2009, doi: 10.1109/TUFFC.2009.1132.

[83] A. Pain, B. Hui Terence Goh, E. Klaseboer, S.-W. Ohl, and B. Cheong Khoo, "Jets in quiescent bubbles caused by a nearby oscillating bubble," *J. Appl. Phys.*, vol. 111, no. 5, p. 054912, Mar. 2012, doi: 10.1063/1.3692749.

[84] C.-D. Ohl, M. Arora, R. Dijkink, V. Janve, and D. Lohse, "Surface cleaning from laser-induced cavitation bubbles," *Appl. Phys. Lett.*, vol. 89, no. 7, p. 074102, Aug. 2006, doi: 10.1063/1.2337506.

[85] J. E. Chomas, P. A. Dayton, D. J. May, and K. W. Ferrara, "Threshold of fragmentation for ultrasonic contrast agents," *J. Biomed. Opt.*, vol. 6, no. 2, pp. 141–150, Apr. 2001, doi: 10.1117/1.1352752.

[86] S. Sirsi and M. Borden, "Microbubble Compositions, Properties and Biomedical Applications," *Bubble Sci. Eng. Technol.*, vol. 1, no. 1–2, pp. 3–17, Nov. 2009, doi: 10.1179/175889709X446507.

[87] C. Huang, H. Zhang, and R. Bai, "Advances in ultrasound-targeted microbubble-mediated gene therapy for liver fibrosis," *Acta Pharm. Sin. B*, vol. 7, no. 4, pp. 447–452, Jul. 2017, doi: 10.1016/j.apsb.2017.02.004.

[88] V. Paefgen, D. Doleschel, and F. Kiessling, "Evolution of contrast agents for ultrasound imaging and ultrasound-mediated drug delivery," *Front. Pharmacol.*, vol. 6, Sep. 2015, doi: 10.3389/fphar.2015.00197.

[89] V. Sboros, "Response of contrast agents to ultrasound," *Ultrasound Drug Gene Deliv.*, vol. 60, no. 10, pp. 1117–1136, Jun. 2008, doi: 10.1016/j.addr.2008.03.011.

[90] X. Chen and S. Wong, *Cancer Theranostics*. Academic Press, 2014.

[91] L. Hoff, *Acoustic Characterization of Contrast Agents for Medical Ultrasound Imaging*. Springer Netherlands, 2013.

[92] V. Sboros, "Response of contrast agents to ultrasound," *Ultrasound Drug Gene Deliv.*, vol. 60, no. 10, pp. 1117–1136, Jun. 2008, doi: 10.1016/j.addr.2008.03.011.

[93] E. Stride *et al.*, "Microbubble Agents: New Directions," *Ultrasound Med. Biol.*, vol. 46, no. 6, pp. 1326–1343, Jun. 2020, doi: 10.1016/j.ultrasmedbio.2020.01.027.

[94] E. Litau, "Combining Nanoparticles with Colloidal Bubbles: A Short Review," in *Nanoparticles in Biology and Medicine: Methods and Protocols*, E. Ferrari and M. Soloviev, Eds. New York, NY: Springer US, 2020, pp. 383–393. doi: 10.1007/978-1-0716-0319-2_27.

[95] Z. Fan, R. E. Kumon, and C. X. Deng, "Mechanisms of microbubble-facilitated sonoporation for drug and gene delivery," *Ther. Deliv.*, vol. 5, no. 4, pp. 467–486, Apr. 2014, doi: 10.4155/tde.14.10.

[96] J. Wu and W. L. Nyborg, "Ultrasound, cavitation bubbles and their interaction with cells," *Adv. Drug Deliv. Rev.*, vol. 60, pp. 1103–1116, Jun. 2008, doi: 10.1016/j.addr.2008.03.009.

[97] M. Ward, J. Wu, and J.-F. Chiu, "Ultrasound-induced cell lysis and sonoporation enhanced by contrast agents," *J. Acoust. Soc. Am.*, vol. 105, no. 5, Art. no. 5, Apr. 1999, doi: 10.1121/1.426908.

[98] I. Rosenthal, J. Z. Sostaric, and P. Riesz, "Sonodynamic therapy—a review of the synergistic effects of drugs and ultrasound," *Ultrason. Sonochem.*, vol. 11, no. 6, pp. 349–363, Sep. 2004, doi: 10.1016/j.ultsonch.2004.03.004.

[99] J. P. Kilroy, A. V. Patil, J. J. Rychak, and J. A. Hossack, "An IVUS Transducer for Microbubble Therapies," *IEEE Trans. Ultrason. Ferroelectr. Freq. Control*, vol. 61, no. 3, pp. 441–449, Mar. 2014, doi: 10.1109/TUFFC.2014.2929.

[100] J. P. Kilroy, A. L. Klibanov, B. R. Wamhoff, D. K. Bowles, and J. A. Hossack, "Localized In Vivo Model Drug Delivery with Intravascular Ultrasound and Microbubbles," *Ultrasound Med. Biol.*, vol. 40, no. 10, Art. no. 10, Oct. 2014, doi: 10.1016/j.ultrasmedbio.2014.04.007.

[101] K. Okada, N. Kudo, K. Niwa, and K. Yamamoto, "A basic study on sonoporation with microbubbles exposed to pulsed ultrasound," *J. Med. Ultrason.*, vol. 32, no. 1, pp. 3–11, Mar. 2005, doi: 10.1007/s10396-005-0031-5.

[102] D. N. Stephens, D. E. Kruse, A. S. Ergun, S. Barnes, X. Ming Lu, and K. Ferrara, "Efficient Array Design for Sonotherapy," *Phys. Med. Biol.*, vol. 53, no. 14, pp. 3943–3969, Jul. 2008, doi: 10.1088/0031-9155/53/14/014.

[103] AIUM/ NEMA (1992), "Standard for Real-Time Display of Thermal and Mechanical Acoustic Output Indices on Diagnostic Ultrasound Equipment," *AIUM Publications, American Institute of Ultrasound in Medicine*.

[104] "Section 7--discussion of the mechanical index and other exposure parameters. American Institute of Ultrasound in Medicine," *J. Ultrasound Med. Off. J. Am. Inst. Ultrasound Med.*, vol. 19, no. 2, pp. 143–168, Feb. 2000, doi: 10.7863/jum.2000.19.2.143.

[105] H. Pan, Y. Zhou, O. Izadnegahdar, J. Cui, and C. Deng, "Study of sonoporation dynamics affected by ultrasound duty cycle.," *Ultrasound Med. Biol.*, 2005, doi: 10.1016/j.ultrasmedbio.2005.03.014.

[106] Y. Qiu, C. Zhang, J. Tu, and D. Zhang, "Microbubble-induced sonoporation involved in ultrasound-mediated DNA transfection in vitro at low acoustic pressures," *J. Biomech.*, vol. 45, no. 8, pp. 1339–1345, May 2012, doi: 10.1016/j.jbiomech.2012.03.011.

[107] Meijering Bernadet D.M. *et al.*, "Ultrasound and Microbubble-Targeted Delivery of Macromolecules Is Regulated by Induction of Endocytosis and Pore Formation," *Circ. Res.*, vol. 104, no. 5, pp. 679–687, Mar. 2009, doi: 10.1161/CIRCRESAHA.108.183806.

[108] A. van Wamel *et al.*, "Vibrating microbubbles poking individual cells: Drug transfer into cells via sonoporation," *J. Controlled Release*, vol. 112, no. 2, Art. no. 2, May 2006, doi: 10.1016/j.jconrel.2006.02.007.

[109] G. ter Haar, *The safe use of ultrasound in medical diagnosis*. London: British Institute of Radiology, 2012.

[110] M. A. Hanson, *Health effects of exposure to ultrasound and infrasound: report of the independent advisory group on non-ionising radiation*. Health Protection Agency, 2010.

[111] D. M. Rubin, N. Anderton, C. Smalberger, J. Polliack, M. Nathan, and M. Postema, “On the Behaviour of Living Cells under the Influence of Ultrasound,” *Fluids*, vol. 3, no. 4, Art. no. 4, Dec. 2018, doi: 10.3390/fluids3040082.

[112] C.-D. Ohl *et al.*, “Sonoporation from Jetting Cavitation Bubbles,” *Biophys. J.*, vol. 91, no. 11, pp. 4285–4295, Dec. 2006, doi: 10.1529/biophysj.105.075366.

[113] X. Chen, R. S. Leow, Y. Hu, J. M. F. Wan, and A. C. H. Yu, “Single-site sonoporation disrupts actin cytoskeleton organization,” *J. R. Soc. Interface*, vol. 11, no. 95, Jun. 2014, doi: 10.1098/rsif.2014.0071.

[114] F. Prieur *et al.*, “Enhancement of Fluorescent Probe Penetration into Tumors In Vivo Using Unseeded Inertial Cavitation,” *Ultrasound Med. Biol.*, vol. 42, no. 7, pp. 1706–1713, Jul. 2016, doi: 10.1016/j.ultrasmedbio.2016.01.021.

[115] I. Beekers *et al.*, “Opening of endothelial cell–cell contacts due to sonoporation,” *J. Controlled Release*, vol. 322, pp. 426–438, Jun. 2020, doi: 10.1016/j.jconrel.2020.03.038.

[116] H. Inoue *et al.*, “Sonoporation-mediated transduction of siRNA ameliorated experimental arthritis using 3MHz pulsed ultrasound,” *Ultrasonics*, vol. 54, no. 3, pp. 874–881, Mar. 2014, doi: 10.1016/j.ultras.2013.10.021.

[117] X. Chen, J. Wang, J. J. Pacella, and F. S. Villanueva, “The dynamic behavior of microbubbles during long ultrasound tone-burst excitation: mechanistic insights into ultrasound-microbubble mediated therapeutics using high-speed imaging and cavitation detection,” *Ultrasound Med. Biol.*, vol. 42, no. 2, pp. 528–538, Feb. 2016, doi: 10.1016/j.ultrasmedbio.2015.09.017.

[118] S. Bao, B. D. Thrall, and D. L. Miller, “Transfection of a reporter plasmid into cultured cells by sonoporation in vitro,” *Ultrasound Med. Biol.*, vol. 23, no. 6, pp. 953–959, Jan. 1997, doi: 10.1016/S0301-5629(97)00025-2.

[119] A. Vembadi, A. Menachery, and M. A. Qasaimeh, “Cell Cytometry: Review and Perspective on Biotechnological Advances,” *Front. Bioeng. Biotechnol.*, vol. 7, 2019, doi: 10.3389/fbioe.2019.00147.

[120] B. Helfield, X. Chen, S. C. Watkins, and F. S. Villanueva, “Biophysical insight into mechanisms of sonoporation,” *Proc. Natl. Acad. Sci.*, vol. 113, no. 36, Art. no. 36, Sep. 2016, doi: 10.1073/pnas.1606915113.

[121] C. M. St. Croix, S. H. Shand, and S. C. Watkins, “Confocal microscopy: comparisons, applications, and problems,” *BioTechniques*, vol. 39, no. 6S, pp. S2–S5, Dec. 2005, doi: 10.2144/000112089.

[122] G. Linz, S. Djeljadini, L. Steinbeck, G. Köse, F. Kiessling, and M. Wessling, “Cell barrier characterization in transwell inserts by electrical impedance spectroscopy,” *Biosens. Bioelectron.*, vol. 165, p. 112345, Oct. 2020, doi: 10.1016/j.bios.2020.112345.

[123] A. S. Dukhin and P. J. Goetz, “Chapter 3 - Fundamentals of Acoustics in Homogeneous Liquids: Longitudinal Rheology,” in *Studies in Interface Science*, vol. 24, A. S. Dukhin and P. J. Goetz, Eds. Elsevier, 2010, pp. 91–125. doi: 10.1016/S1383-7303(10)23003-X.

[124] R. E. Newnham, *Properties of materials : anisotropy, symmetry, structure*. Oxford; New York: Oxford University Press, 2005.

[125] "Appendix A: Typical Acoustic Properties of Tissues," in *Basics of Biomedical Ultrasound for Engineers*, John Wiley & Sons, Ltd, 2010, pp. 313–314. doi: 10.1002/9780470561478.app1.

[126] "Attenuation and Dispersion," in *Basics of Biomedical Ultrasound for Engineers*, John Wiley & Sons, Ltd, 2010, pp. 93–105. doi: 10.1002/9780470561478.ch5.

[127] "Basic Principles." http://www.usra.ca/regional-anesthesia/introduction/basic.php (accessed Aug. 28, 2020).

[128] W. Heywang, K. Lubitz, and W. Wersing, Eds., *Piezoelectricity: evolution and future of a technology*, vol. 114. New York: Springer Science & Business Media, 2008.

[129] J. G. Smits, "Iterative Method for Accurate Determination of the Real and Imaginary Parts of the Materials Coefficients of Piezoelectric Ceramics," *IEEE Trans. Sonics Ultrason.*, vol. 23, no. 6, pp. 393–401, Nov. 1976, doi: 10.1109/T-SU.1976.30898.

[130] A. Arnau, *Piezoelectric transducers and applications*, vol. 2004. Heidelberg: Springer, 2004.

[131] B. Jaffe, W. R. Cook, and H. L. Jaffe, *Piezoelectric ceramics,*. London; New York: Academic Press, 1971.

[132] T. l. Jordan and Z. Ounaies, "Characterization of Piezoelectric Ceramic Materials," in *Encyclopedia of Smart Materials*, John Wiley & Sons, Inc., 2002. doi: 10.1002/0471216275.esm013.

[133] "IEEE Standard on Piezoelectricity (1987)," *ANSI-IEEE Std 176-1987*, doi: 10.1109/IEEESTD.1988.79638.

[134] Z. Qiu, "Development of MRI-compatible Transducer Arrays for Focused Ultrasound Surgery: The Use of Relaxor-based Piezocrystals," University of Dundee, Dundee, 2014.

[135] "IEEE Standard Definitions and Methods of Measurement for Piezoelectric Vibrators," *IEEE Std No177*, pp. 1-, 1966, doi: 10.1109/IEEESTD.1966.120168.

[136] T. l. Jordan and Z. Ounaies, "Characterization of Piezoelectric Ceramic Materials," in *Encyclopedia of Smart Materials*, John Wiley & Sons, Inc., 2002. doi: 10.1002/0471216275.esm013.

[137] W. Heywang, K. Lubitz, and W. Wersing, Eds., *Piezoelectricity: evolution and future of a technology*, vol. 114. New York: Springer Science & Business Media, 2008.

[138] H. N. Shekhani and K. Uchino, "Evaluation of the mechanical quality factor under high power conditions in piezoelectric ceramics from electrical power," *J. Eur. Ceram. Soc.*, vol. 35, no. 2, pp. 541–544, Feb. 2015, doi: 10.1016/j.jeurceramsoc.2014.08.038.

[139] Z. Butt, Z. Anjum, A. Sultan, F. Qayyum, H. M. Khurram Ali, and S. Mehmood, "Investigation of Electrical Properties & Mechanical Quality Factor of Piezoelectric

Material (PZT-4A)," *J. Electr. Eng. Technol.*, vol. 12, no. 2, pp. 846–851, 2017, doi: 10.5370/JEET.2017.12.2.846.

[140] S. Zhang, F. Li, X. Jiang, J. Kim, J. Luo, and X. Geng, "Advantages and challenges of relaxor-PbTiO3 ferroelectric crystals for electroacoustic transducers – A review," *Prog. Mater. Sci.*, vol. 68, pp. 1–66, Mar. 2015, doi: 10.1016/j.pmatsci.2014.10.002.

[141] S. Priya *et al.*, "A Review on Piezoelectric Energy Harvesting: Materials, Methods, and Circuits," 2017, doi: 10.1515/ehs-2016-0028.

[142] R. G. Ballas, *Piezoelectric multilayer beam bending actuators: Static and dynamic behavior and aspects of sensor integration*. Springer Science & Business Media, 2007.

[143] L. Pardo, "5 - Piezoelectric ceramic materials for power ultrasonic transducers," in *Power Ultrasonics*, Oxford: Woodhead Publishing, 2015, pp. 101–125.

[144] P. K. Khanna, S. Ahmad, and R. Grimme, "Molecular Weiss domain polarization in piezoceramics to diaphragm, cantilever and channel construction in low-temperature-cofired ceramics for micro-fluidic applications," *Mater. Chem. Phys.*, vol. 89, no. 1, pp. 56–63, Jan. 2005, doi: 10.1016/j.matchemphys.2004.08.023.

[145] Y.-K. An, M. K. Kim, and H. Sohn, "4 - Piezoelectric transducers for assessing and monitoring civil infrastructures," in *Sensor Technologies for Civil Infrastructures*, vol. 55, M. L. Wang, J. P. Lynch, and H. Sohn, Eds. Woodhead Publishing, 2014, pp. 86–120. doi: 10.1533/9780857099136.86.

[146] W. A. Smith and B. A. Auld, "Modeling 1-3 composite piezoelectrics: thickness-mode oscillations," *IEEE Trans. Ultrason. Ferroelectr. Freq. Control*, vol. 38, no. 1, Art. no. 1, 1991.

[147] E. K. Akdogan, M. Allahverdi, and A. Safari, "Piezoelectric composites for sensor and actuator applications," *IEEE Trans. Ultrason. Ferroelectr. Freq. Control*, vol. 52, no. 5, pp. 746–775, May 2005, doi: 10.1109/TUFFC.2005.1503962.

[148] R. Banks, R. L. O'Leary, and G. Hayward, "Enhancing the bandwidth of piezoelectric composite transducers for air-coupled non-destructive evaluation," *Ultrasonics*, vol. 75, pp. 132–144, Mar. 2017, doi: 10.1016/j.ultras.2016.10.007.

[149] S. Walter *et al.*, "Manufacturing and electrical interconnection of piezoelectric 1-3 composite materials for phased array ultrasonic transducers," in *2008 31st International Spring Seminar on Electronics Technology*, May 2008, pp. 255–260. doi: 10.1109/ISSE.2008.5276575.

[150] N. Chubachi and H. Kamata, "Various equivalent circuits for thickness mode piezoelectric transducers," *Electron. Commun. Jpn. Part II Electron.*, vol. 79, no. 6, pp. 50–59, 1996, doi: 10.1002/ecjb.4420790606.

[151] M. Redwood, "Transient Performance of a Piezoelectric Transducer," *J. Acoust. Soc. Am.*, vol. 33, no. 4, pp. 527–536, Apr. 1961, doi: 10.1121/1.1908709.

[152] P. Maréchal, F. Levassort, L.-P. Tran-Huu-Hue, and M. Lethiecq, "Lens-focused transducer modeling using an extended KLM model," *Ultrasonics*, vol. 46, no. 2, pp. 155–167, May 2007, doi: 10.1016/j.ultras.2007.01.006.

[153] K. F. Graff, “6 - Power ultrasonic transducers: principles and design,” in *Power Ultrasonics*, Oxford: Woodhead Publishing, 2015, pp. 127–158.

[154] N. Abboud, G. Wojcik, D. Vaughan, J. Mould, D. Powell, and L. Nikodym, “Finite Element Modeling for Ultrasonic Transducers (Preprint),” *Proc SPIE Int Symp Med. Imaging*, vol. 3341, 1998, doi: 10.1117/12.308015.

[155] G. R. Liu and S. S. Quek, “Computational modelling,” in Finite Element Method: A Practical Course, Butterworth-Heinemann, Oxford, UK, 2003, pp. 1–11. doi: 10.1016/B978-075065866-9/50002-5.

[156] C. V. Nielsen, W. Zhang, L. M. Alves, N. Bay, and P. Martins, *Modeling of Thermo-Electro-Mechanical Manufacturing Processes: Applications in Metal Forming and Resistance Welding*. London: Springer-Verlag, 2013. doi: 10.1007/978-1-4471-4643-8.

[157] “The Basics,” *OnScale*. http://support.onscale.com/hc/en-us/articles/360015653612 (accessed Sep. 17, 2020).

[158] J. M. Dobson, “An integrated framework for finite element modelling of ultrasonic inspections of carbon fibre reinforced polymer components,” University of Strathclyde, Glasgow, United Kingdom.

[159] G. L. Wojcik, D. K. Vaughan, N. Abboud, and . J. Mould J., “Electromechanical modeling using explicit time-domain finite elements,” in *1993 Proceedings IEEE Ultrasonics Symposium*, Oct. 1993, pp. 1107–1112 vol.2. doi: 10.1109/ULTSYM.1993.339594.

[160] W. Lee and Y. Roh, “Ultrasonic transducers for medical diagnostic imaging,” *Biomed. Eng. Lett.*, vol. 7, no. 2, pp. 91–97, Mar. 2017, doi: 10.1007/s13534-017-0021-8.

[161] V. T. Rathod, “A Review of Acoustic Impedance Matching Techniques for Piezoelectric Sensors and Transducers,” *Sensors*, vol. 20, no. 14, Jul. 2020, doi: 10.3390/s20144051.

[162] C. Fei *et al.*, “Design of matching layers for high-frequency ultrasonic transducers,” *Appl. Phys. Lett.*, vol. 107, no. 12, Sep. 2015, doi: 10.1063/1.4931703.

[163] Y. Yamashita, Y. Hosono, and K. Itsumi, “Low-Attenuation Acoustic Silicone Lens for Medical Ultrasonic Array Probes,” in *Piezoelectric and Acoustic Materials for Transducer Applications*, A. Safari and E. K. Akdoğan, Eds. Boston, MA: Springer US, 2008, pp. 161–177. doi: 10.1007/978-0-387-76540-2_8.

[164] S. Umemura, “Focused ultrasound transducer for thermal treatment,” *Int. J. Hyperthermia*, vol. 31, no. 2, pp. 216–221, Feb. 2015, doi: 10.3109/02656736.2015.1008059.

[165] H. S. Lay *et al.*, “In-Vivo Evaluation of Microultrasound and Thermometric Capsule Endoscopes,” *IEEE Trans. Biomed. Eng.*, vol. 66, no. 3, pp. 632–639, Mar. 2019, doi: 10.1109/TBME.2018.2852715.

[166] P. Bour, V. Ozenne, F. Marquet, B. Denis de Senneville, E. Dumont, and B. Quesson, “Real-time 3D ultrasound based motion tracking for the treatment of mobile organs with

MR-guided high-intensity focused ultrasound," *Int. J. Hyperthermia*, vol. 34, no. 8, pp. 1225–1235, Nov. 2018, doi: 10.1080/02656736.2018.1433879.

[167] J.-L. Li, X.-Z. Liu, D. Zhang, and X.-F. Gong, "Influence of Ribs on the Nonlinear Sound Field of Therapeutic Ultrasound," *Ultrasound Med. Biol.*, vol. 33, no. 9, Art. no. 9, Sep. 2007, doi: 10.1016/j.ultrasmedbio.2007.05.001.

[168] K. Shapoori, J. Sadler, A. Wydra, E. V. Malyarenko, A. N. Sinclair, and R. Gr. Maev, "An Ultrasonic-Adaptive Beamforming Method and Its Application for Trans-skull Imaging of Certain Types of Head Injuries; Part I: Transmission Mode," *IEEE Trans. Biomed. Eng.*, vol. 62, no. 5, pp. 1253–1264, May 2015, doi: 10.1109/TBME.2014.2371752.

[169] C. Minonzio, "A step towards aberration corrections for transcranial ultrasound - Estimation of skull thickness and speed of sound," 2019.

[170] F. Marquet, Y.-S. Tung, T. Teichert, V. P. Ferrera, and E. E. Konofagou, "Noninvasive, Transient and Selective Blood-Brain Barrier Opening in Non-Human Primates In Vivo," *PLOS ONE*, vol. 6, no. 7, p. e22598, Jul. 2011, doi: 10.1371/journal.pone.0022598.

[171] "Conversion Tables," *SAI Infusion Technologies*. https://www.sai-infusion.com/pages/conversion-tables (accessed Aug. 22, 2020).

[172] H.-L. Liu, C.-H. Fan, C.-Y. Ting, and C.-K. Yeh, "Combining microbubbles and ultrasound for drug delivery to brain tumors: current progress and overview," *Theranostics*, vol. 4, no. 4, Art. no. 4, 2014, doi: 10.7150/thno.8074.

[173] A. Burgess, K. Shah, O. Hough, and K. Hynynen, "Focused ultrasound-mediated drug delivery through the blood-brain barrier," *Expert Rev. Neurother.*, vol. 15, no. 5, pp. 477–491, May 2015, doi: 10.1586/14737175.2015.1028369.

[174] E. E. Konofagou, Y.-S. Tung, J. Choi, T. Deffieux, B. Baseri, and F. Vlachos, "Ultrasound-Induced Blood-Brain Barrier Opening," *Curr. Pharm. Biotechnol.*, vol. 13, no. 7, pp. 1332–1345, Jun. 2012.

[175] J. H. Lee *et al.*, "Towards wireless capsule endoscopic ultrasound (WCEU)," in *2014 IEEE International Ultrasonics Symposium*, Sep. 2014, pp. 734–737. doi: 10.1109/ULTSYM.2014.0181.

[176] A. Blana *et al.*, "First Analysis of the Long-Term Results with Transrectal HIFU in Patients with Localised Prostate Cancer," *Eur. Urol.*, vol. 53, no. 6, pp. 1194–1203, Jun. 2008, doi: 10.1016/j.eururo.2007.10.062.

[177] L. Poissonnier *et al.*, "Control of Prostate Cancer by Transrectal HIFU in 227 Patients," *Eur. Urol.*, vol. 51, no. 2, pp. 381–387, Feb. 2007, doi: 10.1016/j.eururo.2006.04.012.

[178] K. Stephens, "Novel MRI-Guided Ultrasound Treatment Destroys Prostate Cancer," *AXIS Imaging News*, Dec. 2019.

[179] Y. Liu *et al.*, “Effect of Microbubble-enhanced Ultrasound on Prostate Permeability: A Potential Therapeutic Method for Prostate Disease,” *Urology*, vol. 81, no. 4, p. 921.e1-921.e7, Apr. 2013, doi: 10.1016/j.urology.2012.12.022.

[180] O. Zolochevska, X. Xia, B. J. Williams, A. Ramsay, S. Li, and M. L. Figueiredo, “Sonoporation Delivery of Interleukin-27 Gene Therapy Efficiently Reduces Prostate Tumor Cell Growth In Vivo,” *Hum. Gene Ther.*, vol. 22, no. 12, pp. 1537–1550, Dec. 2011, doi: 10.1089/hum.2011.076.

[181] X. Chen, D. Cvetkovic, C.-M. Ma, and L. Chen, “Quantitative study of focused ultrasound enhanced doxorubicin delivery to prostate tumor in vivo with MRI guidance,” *Med. Phys.*, vol. 39, no. 5, pp. 2780–2786, 2012, doi: 10.1118/1.4705346.

[182] S. K. S. Huang and M. A. Wood, *Catheter Ablation of Cardiac Arrhythmias*. Elsevier Health Sciences, 2014.

[183] K. L. Gentry and S. W. Smith, “Integrated catheter for 3-d intracardiac echo cardiography and ultrasound ablation,” *IEEE Trans. Ultrason. Ferroelectr. Freq. Control*, vol. 51, no. 7, pp. 800–808, Jul. 2004, doi: 10.1109/TUFFC.2004.1320739.

[184] J. Werner, E.-J. Park, H. Lee, D. Francischelli, and N. B. Smith, “Feasibility of in vivo Transesophageal Cardiac Ablation Using a Phased Ultrasound Array,” *Ultrasound Med. Biol.*, vol. 36, no. 5, pp. 752–760, May 2010, doi: 10.1016/j.ultrasmedbio.2010.02.002.

[185] V. A. Salgaonkar and C. J. Diederich, “Catheter-based ultrasound technology for image-guided thermal therapy: Current technology and applications,” *Int. J. Hyperth. Off. J. Eur. Soc. Hyperthermic Oncol. North Am. Hyperth. Group*, vol. 31, no. 2, pp. 203–215, Mar. 2015, doi: 10.3109/02656736.2015.1006269.

[186] T. Ma, B. Zhou, T. K. Hsiai, and K. K. Shung, “A Review of Intravascular Ultrasound–Based Multimodal Intravascular Imaging: The Synergistic Approach to Characterizing Vulnerable Plaques,” *Ultrason. Imaging*, vol. 38, no. 5, pp. 314–331, Sep. 2016, doi: 10.1177/0161734615604829.

[187] A. Vasquez, N. Mistry, and J. Singh, “Impact of Intravascular Ultrasound in Clinical Practice,” *Interv. Cardiol. Rev.*, vol. 9, no. 3, pp. 156–163, Aug. 2014, doi: 10.15420/icr.2014.9.3.156.

[188] J. P. Kilroy, A. L. Klibanov, B. R. Wamhoff, and J. A. Hossack, “Intravascular Ultrasound Catheter to Enhance Microbubble-Based Drug Delivery via Acoustic Radiation Force,” *IEEE Trans. Ultrason. Ferroelectr. Freq. Control*, vol. 59, no. 10, pp. 2156–2166, Oct. 2012, doi: 10.1109/TUFFC.2012.2442.

[189] L. C. Phillips, A. L. Klibanov, D. K. Bowles, M. Ragosta, J. A. Hossack, and B. R. Wamhoff, “Focused in vivo Delivery of Plasmid DNA to the Porcine Vascular Wall via Intravascular Ultrasound Destruction of Microbubbles,” *J. Vasc. Res.*, vol. 47, no. 3, Art. no. 3, Apr. 2010, doi: 10.1159/000258905.

[190] L. A. da Silveira, F. B. C. Silveira, and V. P. S. Fazan, “Arterial diameter of the celiac trunk and its branches: anatomical study,” *Acta Cir. Bras.*, vol. 24, no. 1, pp. 43–47, Feb. 2009, doi: 10.1590/S0102-86502009000100009.

[191] J. Kim *et al.*, “Intravascular forward-looking ultrasound transducers for microbubble-mediated sonothrombolysis,” *Sci. Rep.*, vol. 7, p. 3454, 2017, doi: 10.1038/s41598-017-03492-4.

[192] M. Komiyama, H. Nakajima, M. Nishikawa, K. Yamanaka, Y. Iwai, and T. Yasui, “A 3.2-French Cerebral Diagnostic Catheter for All Ages: Technical Note,” *Am. J. Neuroradiol.*, vol. 22, no. 8, Art. no. 8, Sep. 2001.

[193] C. D. Herickhoff, G. A. Grant, G. W. Britz, and S. W. Smith, “Dual-Mode IVUS Catheter for Intracranial Image-Guided Hyperthermia: Feasibility Study,” *IEEE Trans. Ultrason. Ferroelectr. Freq. Control*, vol. 57, no. 11, Art. no. 11, Nov. 2010, doi: 10.1109/TUFFC.2010.1723.

[194] P. Morris, *Practical Neuroangiography*. Lippincott Williams & Wilkins, 2007.

[195] P. A. Willette and S. Coffield, “Current Trends in the Management of Difficult Urinary Catheterizations,” *West. J. Emerg. Med.*, vol. 13, no. 6, pp. 472–478, Dec. 2012, doi: 10.5811/westjem.2011.11.6810.

[196] G. Cummins *et al.*, “Gastrointestinal diagnosis using non-white light imaging capsule endoscopy,” *Nat. Rev. Gastroenterol. Hepatol.*, vol. 16, no. 7, Art. no. 7, Jul. 2019, doi: 10.1038/s41575-019-0140-z.

[197] Y. Kim, H. Rhim, M. J. Choi, H. K. Lim, and D. Choi, “High-Intensity Focused Ultrasound Therapy: an Overview for Radiologists,” *Korean J. Radiol.*, vol. 9, no. 4, pp. 291–302, Aug. 2008, doi: 10.3348/kjr.2008.9.4.291.

[198] “3. Boundary Conditions & Loading,” *OnScale*. http://support.onscale.com/hc/en-us/articles/360015370591 (accessed Jun. 02, 2020).

[199] N. Y. Gnedin, V. A. Semenov, and A. V. Kravtsov, “Enforcing the Courant–Friedrichs–Lewy condition in explicitly conservative local time stepping schemes,” *J. Comput. Phys.*, vol. 359, pp. 93–105, Apr. 2018, doi: 10.1016/j.jcp.2018.01.008.

[200] K. Uchino, “3 - Piezoelectric ceramics for transducers,” in *Ultrasonic Transducers*, K. Nakamura, Ed. Woodhead Publishing, 2012, pp. 70–116. doi: 10.1533/9780857096302.1.70.

[201] M. Kim, J. Kim, and W. Cao, “Electromechanical coupling coefficient of an ultrasonic array element,” *J. Appl. Phys.*, vol. 99, no. 7, p. 074102, Apr. 2006, doi: 10.1063/1.2180487.

[202] “Publication and Proposed Revision of ANSI/IEEE Standard 176-1987 ‘ANSI/IEEE Standard on Piezoelectricity,’” *IEEE Trans. Ultrason. Ferroelectr. Freq. Control*, vol. 43, no. 5, pp. 717-, Sep. 1996, doi: 10.1109/TUFFC.1996.535477.

[203] R. Sun, L. Wang, Y. Zhang, and C. Zhong, “Characterization of 1-3 Piezoelectric Composite with a 3-Tier Polymer Structure,” *Materials*, vol. 13, no. 2, Jan. 2020, doi: 10.3390/ma13020397.

[204] H. J. Lee and S. Zhang, “Design of Low-Loss 1–3 Piezoelectric Composites for High-Power Transducer Applications,” *IEEE Trans. Ultrason. Ferroelectr. Freq. Control*, vol. 59, no. 9, Art. no. 9, Sep. 2012, doi: 10.1109/TUFFC.2012.2415.

[205] G. Hayward and J. Bennett, “Assessing the influence of pillar aspect ratio on the behavior of 1-3 connectivity composite transducers,” *IEEE Trans. Ultrason. Ferroelectr. Freq. Control*, vol. 43, no. 1, pp. 98–108, Jan. 1996, doi: 10.1109/58.484469.

[206] S. Torkamani, S. Roy, M. E. Barkey, E. Sazonov, S. Burkett, and S. Kotru, “A novel damage index for damage identification using guided waves with application in laminated composites,” *Smart Mater. Struct.*, vol. 23, no. 9, p. 095015, Aug. 2014, doi: 10.1088/0964-1726/23/9/095015.

[207] P. Reynolds, J. Hyslop, and G. Hayward, “Analysis of spurious resonances in single and multi-element piezocomposite ultrasonic transducers,” in *IEEE Symposium on Ultrasonics, 2003*, Oct. 2003, vol. 2, pp. 1650-1653 Vol.2. doi: 10.1109/ULTSYM.2003.1293227.

[208] P. Reynolds, “Analysis and Design of Piezocomposite Ultrasonic Transducers Using Finite Element Technique and Surface Displacement Profiles,” University of Strathclyde, Glasgow, United Kingdom, 1998.

[209] J. A. Hossack and G. Hayward, “Finite-element analysis of 1-3 composite transducers,” *IEEE Trans. Ultrason. Ferroelectr. Freq. Control*, vol. 38, no. 6, pp. 618–629, Nov. 1991, doi: 10.1109/58.108860.

[210] I. Trots, A. Nowicki, M. Lewandowski, and Y. Tasinkevych, “Synthetic Aperture Method in Ultrasound Imaging,” 2011. doi: 10.5772/15986.

[211] B. E. Anderson, W. J. Hughes, and S. A. Hambric, “Grating lobe reduction in transducer arrays through structural filtering of supercritical plates,” *J. Acoust. Soc. Am.*, vol. 126, no. 2, pp. 612–619, Jul. 2009, doi: 10.1121/1.3159366.

[212] L. W. Schmerr, *Fundamentals of Ultrasonic Phased Arrays*, vol. 215. Cham: Springer International Publishing, 2015. doi: 10.1007/978-3-319-07272-2.

[213] T. L. Szabo, “Chapter 7 - Array Beamforming,” in *Diagnostic Ultrasound Imaging: Inside Out (Second Edition)*, Second Edition., T. L. Szabo, Ed. Boston: Academic Press, 2014, pp. 209–255. doi: 10.1016/B978-0-12-396487-8.00007-0.

[214] T. L. Szabo, “Chapter 6 - Beamforming,” in *Diagnostic Ultrasound Imaging: Inside Out (Second Edition)*, Second Edition., T. L. Szabo, Ed. Boston: Academic Press, 2014, pp. 167–207. doi: 10.1016/B978-0-12-396487-8.00006-9.

[215] J. Jang and J. H. Chang, “Design and Fabrication of Double-Focused Ultrasound Transducers to Achieve Tight Focusing,” *Sensors*, vol. 16, no. 8, Aug. 2016, doi: 10.3390/s16081248.

[216] E. Brilakis, “Chapter 9 - Complex Lesion Subsets,” in *Manual of Chronic Total Occlusion Interventions (Second Edition)*, E. Brilakis, Ed. Academic Press, 2018, pp. 289–339. doi: 10.1016/B978-0-12-809929-2.00009-0.

[217] Z. F. Issa, J. M. Miller, and D. P. Zipes, “6 - Advanced Mapping and Navigation Modalities,” in *Clinical Arrhythmology and Electrophysiology (Third Edition)*, Z. F. Issa, J. M. Miller, and D. P. Zipes, Eds. Philadelphia: Elsevier, 2019, pp. 155–205. doi: 10.1016/B978-0-323-52356-1.00006-2.

[218] J. Brizuela, J. Camacho, G. Cosarinsky, J. M. Iriarte, and J. F. Cruza, “Improving elevation resolution in phased-array inspections for NDT,” *NDT E Int.*, vol. 101, pp. 1–16, Jan. 2019, doi: 10.1016/j.ndteint.2018.09.002.

[219] S. M. van der Meer, M. Versluis, D. Lohse, C. T. Chin, A. Bouakaz, and N. de Jong, “The resonance frequency of SonoVue trade; as observed by high-speed optical imaging,” in *IEEE Ultrasonics Symposium, 2004*, Aug. 2004, vol. 1, pp. 343-345 Vol.1. doi: 10.1109/ULTSYM.2004.1417735.

[220] C. Lazarus, A. N. Pouliopoulos, M. Tinguely, V. Garbin, and J. J. Choi, “Clustering dynamics of microbubbles exposed to low-pressure 1-MHz ultrasound,” *J. Acoust. Soc. Am.*, vol. 142, no. 5, Art. no. 5, Nov. 2017, doi: 10.1121/1.5010170.

[221] F. A. Jolesz and K. H. Hynynen, Eds., *MRI-Guided Focused Ultrasound Surgery*, 0 ed. CRC Press, 2007. doi: 10.3109/9781420019933.

[222] G. Chen, H. Liu, Y. Lin, and Y. Lin, “Experimental Analysis of 1-3 Piezocomposites for High-Intensity Focused Ultrasound Transducer Applications,” *IEEE Trans. Biomed. Eng.*, vol. 60, no. 1, pp. 128–134, Jan. 2013, doi: 10.1109/TBME.2012.2226881.

[223] M. A. B. Andrade, N. P. Alvarez, F. Buiochi, C. Negreira, and J. C. Adamowski, “Analysis of 1-3 piezocomposite and homogeneous piezoelectric rings for power ultrasonic transducers,” *J. Braz. Soc. Mech. Sci. Eng.*, vol. 31, no. 4, pp. 312–318, Dec. 2009, doi: 10.1590/S1678-58782009000400005.

[224] C. Liu, F. T. Djuth, Q. Zhou, and K. K. Shung, “Micromachining Techniques in Developing High-Frequency Piezoelectric Composite Ultrasonic Array Transducers,” *IEEE Trans. Ultrason. Ferroelectr. Freq. Control*, vol. 60, no. 12, pp. 2615–2625, Dec. 2013, doi: 10.1109/TUFFC.2013.2860.

[225] H. P. Savakus, K. A. Klicker, and R. E. Newnham, “PZT-epoxy piezoelectric transducers: A simplified fabrication procedure,” *Mater. Res. Bull.*, vol. 16, no. 6, pp. 677–680, Jun. 1981, doi: 10.1016/0025-5408(81)90267-1.

[226] A. Safari, V. F. Janas, and A. Bandyopadhyay, “Development of fine-scale piezoelectric composites for transducers,” *AIChE J.*, vol. 43, no. S11, pp. 2849–2856, 1997, doi: 10.1002/aic.690431334.

[227] R. McPhillips, “Fabrication of Ultrasound Transducers and Arrays Integrated within Needles for Imaging Guidance and Diagnosis,” University of Dundee, Dundee, United Kingdom, 2017.

[228] Y. Q. Fu *et al.*, “Advances in piezoelectric thin films for acoustic biosensors, acoustofluidics and lab-on-chip applications,” *Prog. Mater. Sci.*, vol. 89, pp. 31–91, Aug. 2017, doi: 10.1016/j.pmatsci.2017.04.006.

[229] T. Kerdcharoen and C. Wongchoosuk, “11 - Carbon nanotube and metal oxide hybrid materials for gas sensing,” in *Semiconductor Gas Sensors*, R. Jaaniso and O. K. Tan, Eds. Woodhead Publishing, 2013, pp. 386–407. doi: 10.1533/9780857098665.3.386.

[230] K. Wasa, M. Kitabatake, and H. Adachi, *Thin Films Material Technology: Sputtering of Compound Materials*. Berlin Heidelberg: Springer-Verlag, 2004.

[231] P. Naulleau, “2.17 - Optical Lithography,” in *Comprehensive Nanoscience and Nanotechnology (Second Edition)*, D. L. Andrews, R. H. Lipson, and T. Nann, Eds. Oxford: Academic Press, 2019, pp. 387–398. doi: 10.1016/B978-0-12-803581-8.10433-3.

[232] A. S. H. Makhlouf, “1 - Current and advanced coating technologies for industrial applications,” in *Nanocoatings and Ultra-Thin Films*, A. S. H. Makhlouf and I. Tiginyanu, Eds. Woodhead Publishing, 2011, pp. 3–23. doi: 10.1533/9780857094902.1.3.

[233] S. Arulkumar, S. Parthiban, A. Goswami, R. S. Varma, M. Naushad, and M. B. Gawande, “Low temperature processed titanium oxide thin-film using scalable wire-bar coating,” *Mater. Res. Express*, vol. 6, no. 12, p. 126427, Dec. 2019, doi: 10.1088/2053-1591/ab5eed.

[234] S. Merilampi, T. Laine-Ma, and P. Ruuskanen, “The characterization of electrically conductive silver ink patterns on flexible substrates,” *Microelectron. Reliab.*, vol. 49, no. 7, pp. 782–790, Jul. 2009, doi: 10.1016/j.microrel.2009.04.004.

[235] “Creative Materials 118-09A/B119-44 Silver Ink Datasheet [Online].” https://server.creativematerials.com/datasheets/DS_118_09.pdf (accessed Feb. 01, 2018).

[236] D09 Committee, “Test Method for D-C Resistance or Conductance of Moderately Conductive Materials,” ASTM International. doi: 10.1520/D4496-13.

[237] K. Chen, H.-S. Lee, A. P. Chandrakasan, and C. G. Sodini, “Ultrasonic Imaging Transceiver Design for CMUT: A Three-Level 30-Vpp Pulse-Shaping Pulser With Improved Efficiency and a Noise-Optimized Receiver,” *IEEE J. Solid-State Circuits*, vol. 48, no. 11, pp. 2734–2745, Nov. 2013, doi: 10.1109/JSSC.2013.2274895.

[238] J. Liu and M. F. Insana, “Coded Pulse Excitation for Ultrasonic Strain Imaging,” *IEEE Trans. Ultrason. Ferroelectr. Freq. Control*, vol. 52, no. 2, pp. 231–240, Feb. 2005.

[239] K. A. Wear, P. M. Gammell, S. Maruvada, Y. Liu, and G. R. Harris, “Improved measurement of acoustic output using complex deconvolution of hydrophone sensitivity,” *IEEE Trans. Ultrason. Ferroelectr. Freq. Control*, vol. 61, no. 1, pp. 62–75, Jan. 2014, doi: 10.1109/TUFFC.2014.6689776.

[240] “Ultrasonics. Field characterization. Specification and measurement of field parameters for high intensity therapeutic ultrasound (HITU) transducers and systems,” *BSI Stand. Publ.*, no. PD IEC TS 62556:2014, May 2014.

[241] J. Lubbers and R. Graaff, “A simple and accurate formula for the sound velocity in water,” *Ultrasound Med. Biol.*, vol. 24, no. 7, pp. 1065–1068, Sep. 1998, doi: 10.1016/S0301-5629(98)00091-X.

[242] A. M. Hurrell and S. Rajagopal, “The Practicalities of Obtaining and Using Hydrophone Calibration Data to Derive Pressure Waveforms,” *IEEE Trans. Ultrason. Ferroelectr. Freq. Control*, vol. 64, no. 1, pp. 126–140, 2017, doi: 10.1109/TUFFC.2016.2594770.

[243] K. A. Wear, P. M. Gammell, S. Maruvada, Y. Liu, and G. R. Harris, “Time-delay spectrometry measurement of magnitude and phase of hydrophone response,” *IEEE*

Trans. Ultrason. Ferroelectr. Freq. Control, vol. 58, no. 11, pp. 2325–2333, Nov. 2011, doi: 10.1109/TUFFC.2011.2090.

[244] "5. Shell Elements," *OnScale*. http://support.onscale.com/hc/en-us/articles/360020423632 (accessed Sep. 30, 2020).

[245] A. L. Bernassau, D. Hutson, C. E. M. Demore, and S. Cochran, "Characterization of an epoxy filler for piezocomposites compatible with microfabrication processes [Correspondence]," *IEEE Trans. Ultrason. Ferroelectr. Freq. Control*, vol. 58, no. 12, pp. 2743–2748, Dec. 2011, doi: 10.1109/TUFFC.2011.2137.

[246] "Calculating Piezoelectric Material Properties from Material Datasheet," *OnScale*. http://support.onscale.com/hc/en-us/articles/360002073378 (accessed Jun. 15, 2020).

[247] D. ROYER and E. Dieulesaint, *Elastic Waves in Solids I: Free and Guided Propagation*. Berlin Heidelberg: Springer-Verlag, 2000.

[248] J. F. Nye and P. P. L. J. F. Nye, *Physical Properties of Crystals: Their Representation by Tensors and Matrices*. Clarendon Press, 1985.

[249] P. Dineva, D. Gross, R. Müller, and T. Rangelov, *Dynamic Fracture of Piezoelectric Materials*, vol. 212. Cham: Springer International Publishing, 2014. doi: 10.1007/978-3-319-03961-9.

[250] S. V. Bogdanov, "Acoustical method for the determination of the elastic and piezoelectric constants of crystals of classes 6mm and 4mm," *Acoust. Phys.*, vol. 46, no. 5, pp. 530–533, Sep. 2000, doi: 10.1134/1.1310376.

[251] H. J. Lee, S. Zhang, and T. R. Shrout, "Scaling effects of relaxor-PbTiO3 crystals and composites for high frequency ultrasound," *J. Appl. Phys.*, vol. 107, no. 12, Jun. 2010, doi: 10.1063/1.3437068.

[252] M. Cain, M. Stewart, and M. Gee, "Degradation of Piezoelectric Materials," *NPL Rep. CMMTA 148*, pp. 1–42, 1999.

[253] X. Yan *et al.*, "Lead-Free Intravascular Ultrasound Transducer Using BZT-50BCT Ceramics," *IEEE Trans. Ultrason. Ferroelectr. Freq. Control*, vol. 60, no. 6, pp. 1272–1276, Jun. 2013, doi: 10.1109/TUFFC.2013.2692.

[254] "ThinCert™ Cell Culture Inserts - Greiner Bio-One." https://www.gbo.com (accessed Jun. 30, 2020).

[255] G. Linz, S. Djeljadini, L. Steinbeck, G. Köse, F. Kiessling, and M. Wessling, "Cell barrier characterization in transwell inserts by electrical impedance spectroscopy," *Biosens. Bioelectron.*, vol. 165, p. 112345, Oct. 2020, doi: 10.1016/j.bios.2020.112345.

[256] S. M. van der Meer *et al.*, "Microbubble spectroscopy of ultrasound contrast agents," *J. Acoust. Soc. Am.*, vol. 121, no. 1, Art. no. 1, Jan. 2007, doi: 10.1121/1.2390673.

[257] F. E. Shamout *et al.*, "Enhancement of Non-Invasive Trans-Membrane Drug Delivery Using Ultrasound and Microbubbles During Physiologically Relevant Flow," *Ultrasound Med. Biol.*, vol. 41, no. 9, Art. no. 9, Sep. 2015, doi: 10.1016/j.ultrasmedbio.2015.05.003.

[258] M. Turcanu *et al.*, “An Organoid derived Cell Layer as an in vitro Model for US-mediated Drug Delivery Studies,” 2020 IEEE International Ultrasonics Symposium (IUS), Sep. 2020.

[259] T. van Rooij *et al.*, “Viability of endothelial cells after ultrasound-mediated sonoporation: Influence of targeting, oscillation, and displacement of microbubbles,” *J. Controlled Release*, vol. 238, pp. 197–211, Sep. 2016, doi: 10.1016/j.jconrel.2016.07.037.

[260] V. Pereno *et al.*, “Layered acoustofluidic resonators for the simultaneous optical and acoustic characterisation of cavitation dynamics, microstreaming, and biological effects,” *Biomicrofluidics*, vol. 12, no. 3, p. 034109, May 2018, doi: 10.1063/1.5023729.

[261] I. Skachkov, Y. Luan, A. F. W. van der Steen, N. de Jong, and K. Kooiman, “Targeted microbubble mediated sonoporation of endothelial cells in vivo,” *IEEE Trans. Ultrason. Ferroelectr. Freq. Control*, vol. 61, no. 10, Art. no. 10, Oct. 2014, doi: 10.1109/TUFFC.2014.006440.

[262] B. D. M. Meijering, R. H. Henning, W. H. Van Gilst, I. Gavrilović, A. Van Wamel, and L. E. Deelman, “Optimization of ultrasound and microbubbles targeted gene delivery to cultured primary endothelial cells,” *J. Drug Target.*, vol. 15, no. 10, pp. 664–671, Jan. 2007, doi: 10.1080/10611860701605088.

[263] Z. Fan, D. Chen, and C. X. Deng, “Characterization of the Dynamic Activities of a Population of Microbubbles Driven by Pulsed Ultrasound Exposure in Sonoporation,” *Ultrasound Med. Biol.*, vol. 40, no. 6, pp. 1260–1272, Jun. 2014, doi: 10.1016/j.ultrasmedbio.2013.12.002.

[264] P. S. Yarmolenko *et al.*, “Thresholds for thermal damage to normal tissues: An update,” *Int. J. Hyperth. Off. J. Eur. Soc. Hyperthermic Oncol. North Am. Hyperth. Group*, vol. 27, no. 4, pp. 320–343, 2011, doi: 10.3109/02656736.2010.534527.

[265] R. E. Decker, Z. E. Lamantia, T. S. Emrick, and M. L. Figueiredo, “Sonodelivery in Skeletal Muscle: Current Approaches and Future Potential,” *Bioengineering*, vol. 7, no. 3, Sep. 2020, doi: 10.3390/bioengineering7030107.

[266] W. G. Pond, *Encyclopedia of Animal Science (Print)*. CRC Press, 2004.

[267] L. M. Gonzalez, A. J. Moeser, and A. T. Blikslager, “Porcine models of digestive disease: the future of large animal translational research,” *Transl. Res. J. Lab. Clin. Med.*, vol. 166, no. 1, pp. 12–27, Jul. 2015, doi: 10.1016/j.trsl.2015.01.004.

[268] T. T. Kararli, “Comparison of the gastrointestinal anatomy, physiology, and biochemistry of humans and commonly used laboratory animals,” *Biopharm. Drug Dispos.*, vol. 16, no. 5, pp. 351–380, Jul. 1995, doi: 10.1002/bdd.2510160502.

[269] C. N. Beale, L. A. Reyelt, C. A. Bogins, N. Y. Chan, and S. E. Perkins, “Duodenal Cannulation in Pigs (Sus scrofa) as a Drug Delivery Method,” *Comp. Med.*, vol. 68, no. 1, pp. 48–55, Feb. 2018.

[270] Y. Qiu *et al.*, “Ultrasound Capsule Endoscopy With a Mechanically Scanning Micro-ultrasound: A Porcine Study,” *Ultrasound Med. Biol.*, vol. 46, no. 3, pp. 796–804, Mar. 2020, doi: 10.1016/j.ultrasmedbio.2019.12.003.

[271] M. Kopáčová *et al.*, "Wireless Video Capsule Enteroscopy in Preclinical Studies: Methodical Design of Its Applicability in Experimental Pigs," *Dig. Dis. Sci.*, vol. 55, no. 3, pp. 626–630, Mar. 2010, doi: 10.1007/s10620-009-0779-3.

[272] B. Tiller *et al.*, "Piezoelectric microphone via a digital light processing 3D printing process," *Mater. Des.*, vol. 165, p. 107593, 2019, doi: https://doi.org/10.1016/j.matdes.2019.107593.

[273] M. Stiborová, V. Martínek, H. Rýdlová, P. Hodek, and E. Frei, "Sudan I Is a Potential Carcinogen for Humans: Evidence for Its Metabolic Activation and Detoxication by Human Recombinant Cytochrome P450 1A1 and Liver Microsomes," *Cancer Res.*, vol. 62, no. 20, pp. 5678–5684, Oct. 2002.

[274] J.-R. Riba, "Analysis of formulas to calculate the AC resistance of different conductors' configurations," *Electr. Power Syst. Res.*, vol. 127, pp. 93–100, Oct. 2015, doi: 10.1016/j.epsr.2015.05.023.

[275] "NFPA 79, Electrical Standard for Industrial Machinery, 2007 Edition," *NFPA June Assoc. Tech. Meet.*, Jul. 2006.

[276] B. S. Terry, A. B. Lyle, J. A. Schoen, and M. E. Rentschler, "Preliminary Mechanical Characterization of the Small Bowel for In Vivo Robotic Mobility," *J. Biomech. Eng.*, vol. 133, no. 9, pp. 0910101–0910107, Sep. 2011, doi: 10.1115/1.4005168.

[277] X. Wang and M. Q.-H. Meng, "An experimental study of resistant properties of the small intestine for an active capsule endoscope," *Proc. Inst. Mech. Eng. [H]*, vol. 224, no. 1, pp. 107–118, Sep. 2009, doi: 10.1243/09544119JEIM540.

[278] G.-H. Son, K. H.-J. Chang, J.-E. Song, and K.-Y. Lee, "Use of a uniconcave balloon in emergency cerclage," *Am. J. Obstet. Gynecol.*, vol. 212, no. 1, p. 114.e1-114.e4, Jan. 2015, doi: 10.1016/j.ajog.2014.07.022.

[279] G. Li *et al.*, "Investigation of High-Power Properties of PIN-PMN-PT Relaxor-Based Ferroelectric Single Crystals and PZT-4 Piezoelectric Ceramics," *IEEE Trans. Ultrason. Ferroelectr. Freq. Control*, vol. 67, no. 8, pp. 1641–1646, Aug. 2020, doi: 10.1109/TUFFC.2020.2979217.

Appendix

Appendix A: Material Constants of the Kerf Filler

The material constants used for modelling the kerf filler of the piezocomposites are detailed in Table A-1.

Table A-1 Material Constants of the Kerf Filler

Frequency	$\rho\ (Kg/m^3)$	$^1v_l(m/s)$	$^2v_s(m/s)$	$^3\alpha_{long}(dB/cm)$	$^4\alpha_{shear}\ (dB/cm)$
1.0 MHz	1149	2536	1179	2.87	7.38

^1v_l = longitudinal velocity, ^2v_s = shear velocity, $^3\alpha_{long}$ = longitudinal attenuation, $^4\alpha_{shear}$ = shear attenuation

Appendix B: Screenshots of Programs Developed as Part of this Thesis

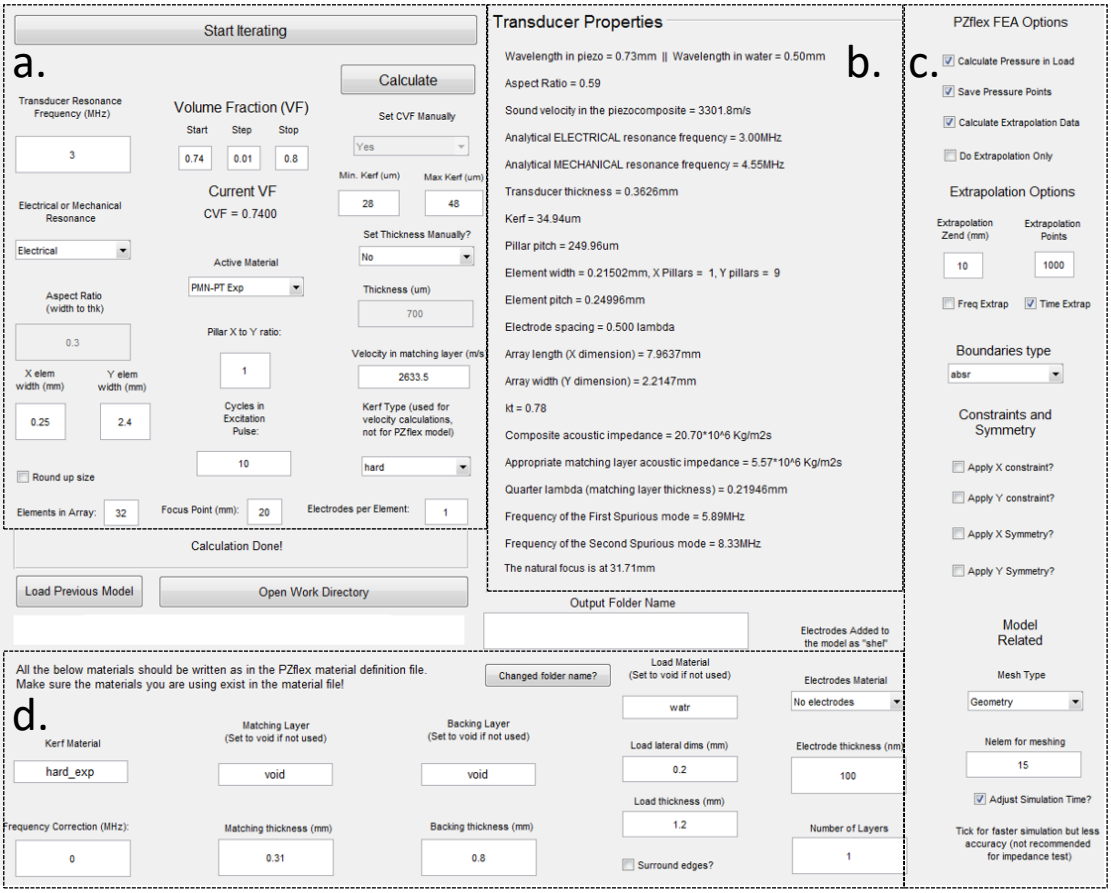

Figure B-1 Screenshot of the Volume Fraction Sweep GUI Developed in MATLAB with its Constituent Parts: a. 1-3 Piezocomposite Parameter Selection; b. Analytically Determined Transducer Properties; c. OnScale Commands; d. Materials Selection

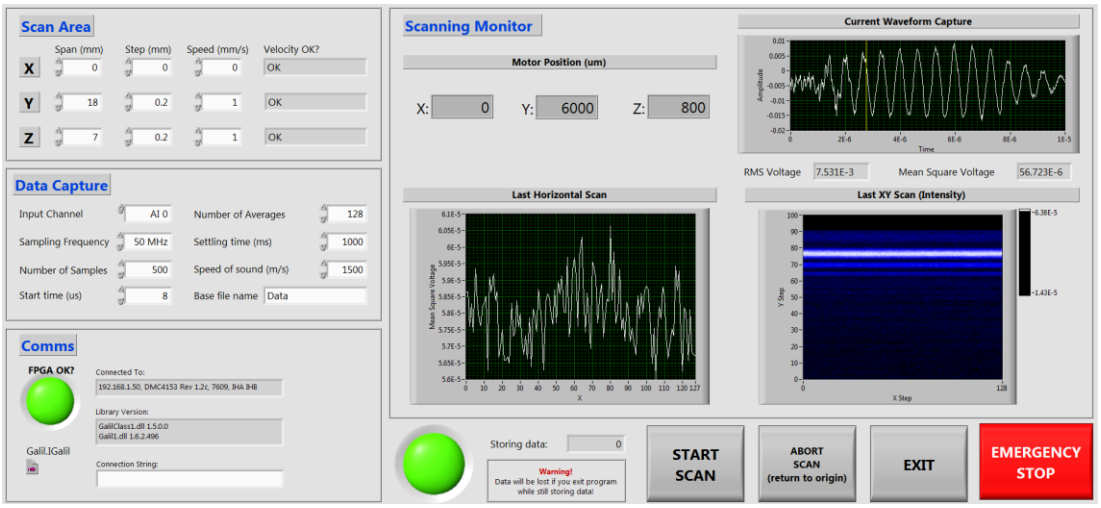

Figure B-2 Screenshot of the NI LabView Program Developed for Experimental Beam Pattern Characterization

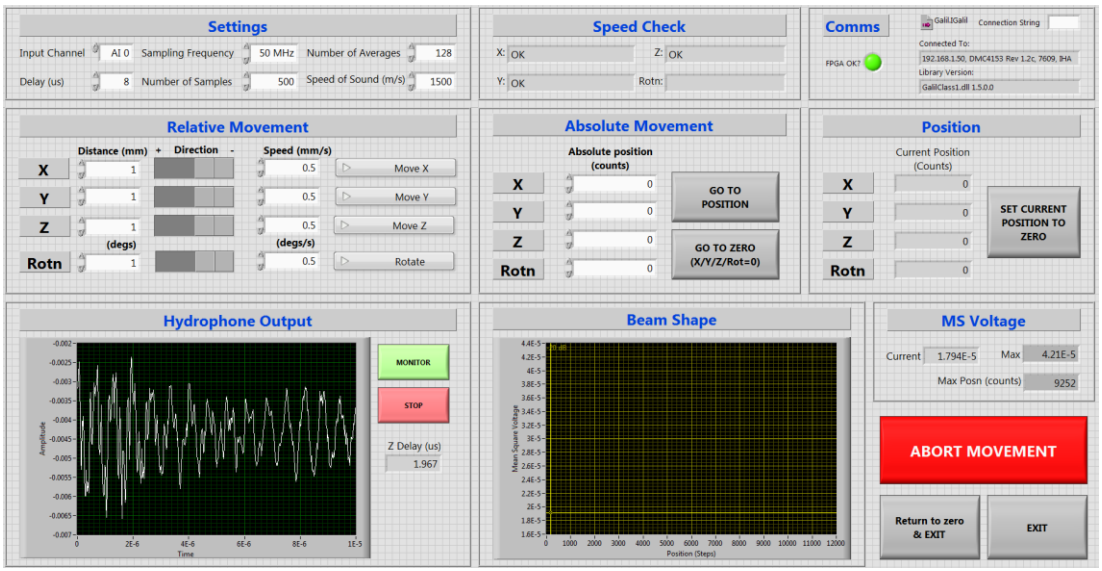

Figure B-3 Screenshot of the NI LabView Program Developed for NH Alignment with Respect to the Characterized Transducer

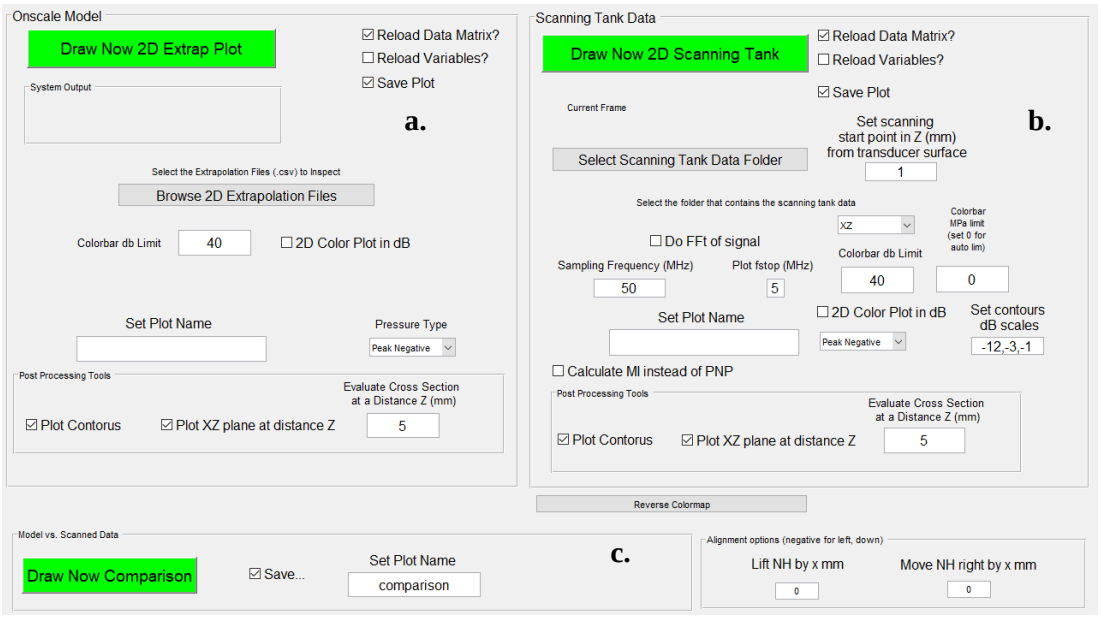

Figure B-4 Screenshot of the MATLAB GUI Designed for Plotting the Beam Pattern from: a. The OnScale Model; b. The Scanning Tank Measurement, and c. The Comparison Tools

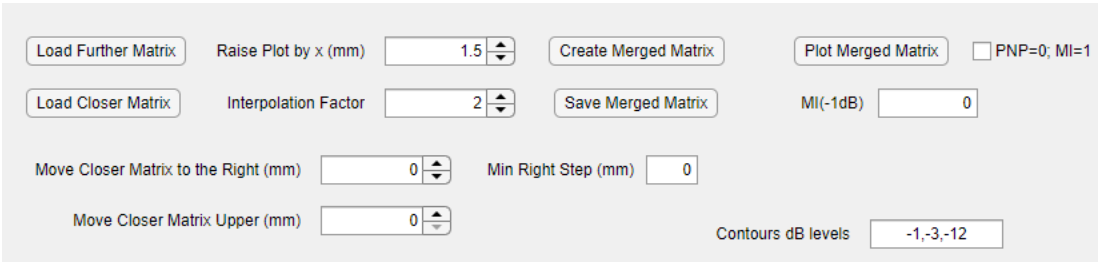

Figure B-5 Screenshot of the MATLAB GUI Designed for Merging the Shorter and longer Scans Recorded with the NH to form One Image of the Beam Profile Achieved by the Capsule Array

Appendix C: Octagonal Single Element Transducer

Design and Simulation of a Single Element Octagonal Transducer for Sonoporation

An octagonal, flat surface, single element, piezocomposite transducer resonating at 1.0 MHz was designed and optimized with the VF sweep procedure detailed in Section 3.4. The device was then manufactured and characterized with a similar approach as for the 1D phased arrays described in Chapters 4 and 5. The piezoelectric material was PZT-5H and the kerf filler was Epofix.

The octagonal transducer was designed for studying *in-vitro* MB-facilitated sonoporation of Caco-2 cells developed on ThinCert™ porous PET membranes [258]. As part of the procedure, the device had to be inserted into cell wells with an inner diameter of 13.65 mm (Section 6.1.2). The outer transducer diameter was restricted to 10 mm to allow access for a microbubble (MB) delivery channel, a suction tube, a TEER probe, and a thermocouple in the same well Figure C-1 (Ref. [258]). The cross section of the piezoelectric element was limited to 8 mm in order to account for the extra width added by a waterproof 3-D printed casing.

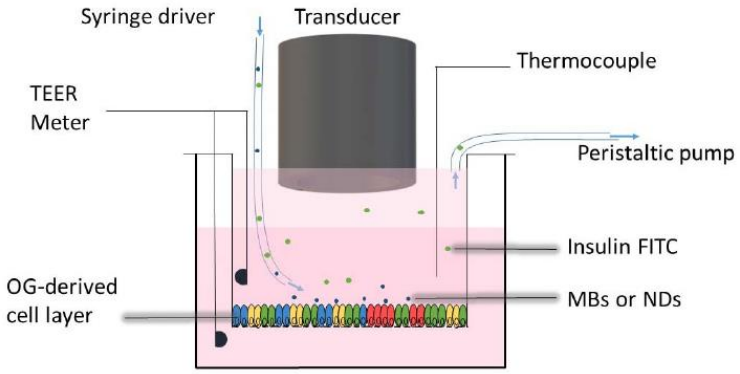

Figure C-1 Schematic Diagram of the in-vitro Experimental Procedure with the Octagonal Single Element Transducer, (Reprinted from Ref. [258])

The octagonal shape of the active element (Figure C-2 a.) was chosen instead of a square geometry because it has a larger area for the same diagonal length (i.e. an octagon fills a greater area of a disc than a square), which leads to higher power output. In order to evaluate the effect of lateral modes generated by the symmetry in the geometry of the transducer on the impedance response and PNP output, an irregular octagonal transducer (Figure C-2 b.) was additionally developed and compared with the regular one. The irregular octagonal element was designed by cutting four of its sides at 15° inwards from the parallel sides of the regular octagon and the other four sides at 10° as in Figure C-2 b.

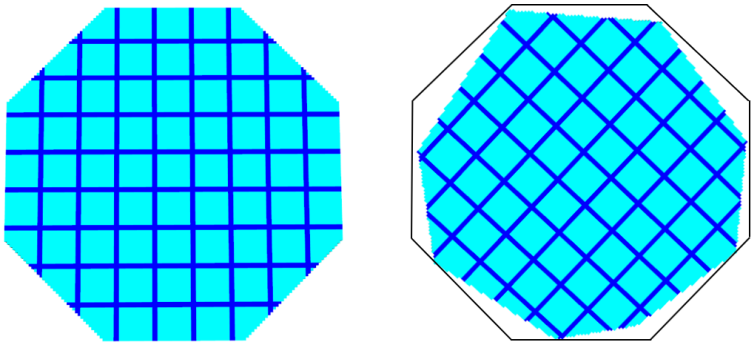

Figure C-2 Cross Section View of the FEA Models for the Octagonal Transducer Designs: a. Regular Octagon; b. Irregular Octagon

The VF sweep was performed only for the regular octagonal transducer and simulated with FEA the active piezocomposite element coupled to a 3.0 mm deep water load. The acoustic pressure in the bulk depth of the load (3.0 mm to 30 mm) was evaluated along the line perpendicular to the centre of the element with time extrapolation, similarly with the methodology described in Section 3.4.1. The results of the sweep (Figure C-3) show the highest PNP at focus was obtained for a VF of 0.78, and that VF values in the interval {0.66; 0.72 - 0.76} led to PNP magnitudes less than 5% lower than the maximum PNP.

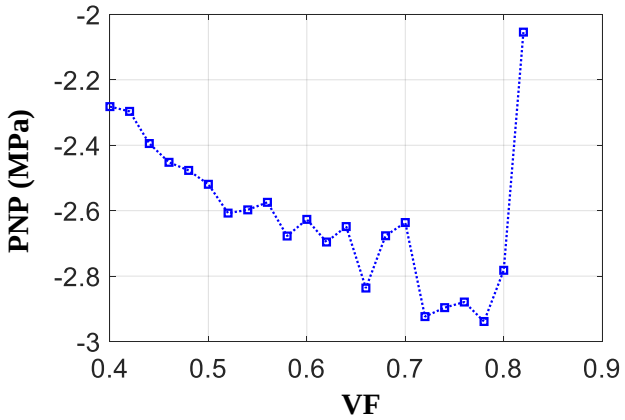

Figure C-3 VF Sweep Results for the Regular Octagonal Transducer Driven with a 10-cycle, 100 V Peak Voltage, 1.0 MHz Ideal Sine Wave

The piezocomposite configuration corresponding to VF = 0.74 was implemented for manufacturing because the calculated kerf width was the closest to the width of the available dicing blades. The parameter set used in the development of both the regular and the irregular octagonal transducers is detailed in Table C-1.

Table C-1 Parameter Set for the Octagonal Transducer Determined from the VF Sweep

Piezocomposite Properties	
Resonance Frequency (MHz)	1.0
Active Material	PZT-5H
Kerf Material	Epofix
VF	0.74
PAR	0.43
$thk\ (\mu m)$	1491
Ideal $W_{ke}\ (\mu m)$	104.9
$PP\ (\mu m)$	750.6
Transducer Parameters	
Regular Octagon Diagonal (mm)	7.37
Natural Focus Distance (mm)	9.05

Manufacturing of the Octagonal Transducers

The piezocomposite material for the octagonal transducers was manufactured with the dice and fill process described in Section 4.3.1 and then lapped to the required thickness. The resulting material was then electroded with a 400 nm layer of Au deposited on a 20 nm base layer of Cr through thermal evaporation, under vacuum, with an Edwards E306 Thin Film Deposition System (Edwards, West Sussex, UK).

The array casing was designed by M. Turcanu and 3-D printed with an Objet Eden (Stratasys, MN, USA) polyjet printer using VeroGrey photopolymer. A 10 mm thick low acoustic impedance, low damping backing layer was added to confer mechanical support for the active element. The backing material was a mixture of Epofix and air filled microballoons, and was manufactured with the procedure described in Section 4.6.2. A straight edge mount SMA connector was inserted into the 3-D printed case to allow interfacing the active element of the transducer with the driving electronics. Subsequently, the device was waterproofed with a thin layer of varnish applied with a brush. The finalized transducer is presented in Figure C-4 a.

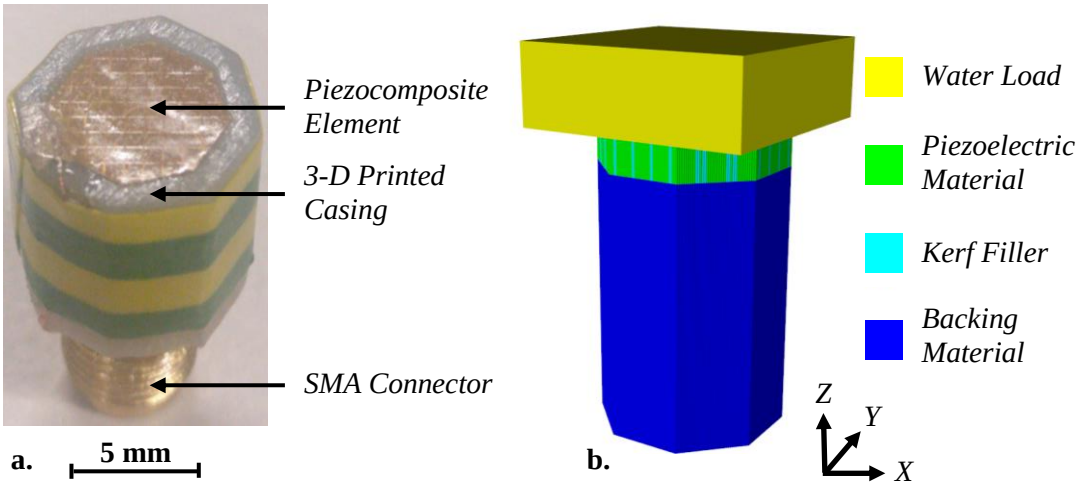

Figure C-4 a. Manufactured Octagonal Transducer; b. Model of the Octagonal Transducer with Backing Layer and Coupled to a Water Load

Acoustic Characterization of the Transducer and Pressure Modelling

2-D pressure profiles from the octagonal transducers were acquired with the scanning tank coupled to a 0.5 mm needle hydrophone (NH, Figure C-5), following the procedure described in Section 5.2.3. The transducer was excited with a 10-cycle sine wave burst, with a frequency of 1.0 MHz from a signal generator (Rigol DG4162 - RIGOL Technology Co., Suzhou, China) connected to a 50 dB linear power amplifier (ENI 2100L - Bell Electronics NW, Inc., WA, USA).

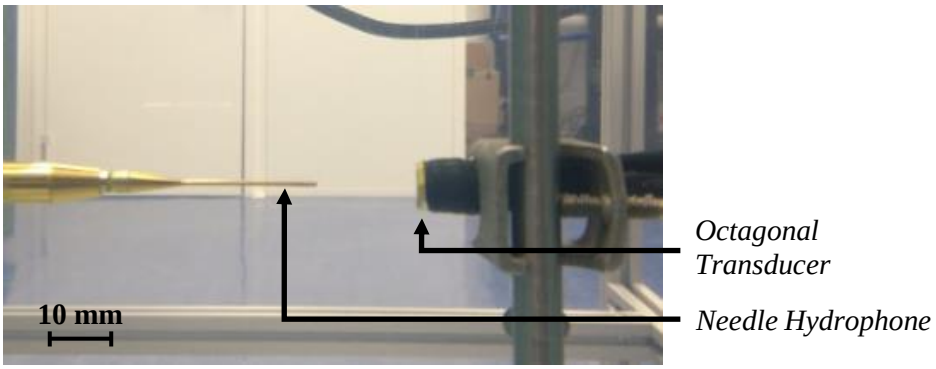

Figure C-5 Beam Pattern Characterization of the Octagonal Transducer

FEA was used to simulate the single element transducer, its backing layer and a water load with a reduced depth of 3.0 mm (Figure C-4 b.). The acoustic propagation in the majority of the water depth (3.0 mm – 25 mm) was simulated with 2-D time extrapolation, similar to the method described in Section 5.3.1. Figure C-6 shows good correlation was obtained between the simulated beam profiles and the beam profiles measured with the scanning tank for both types of octagonal transducers.

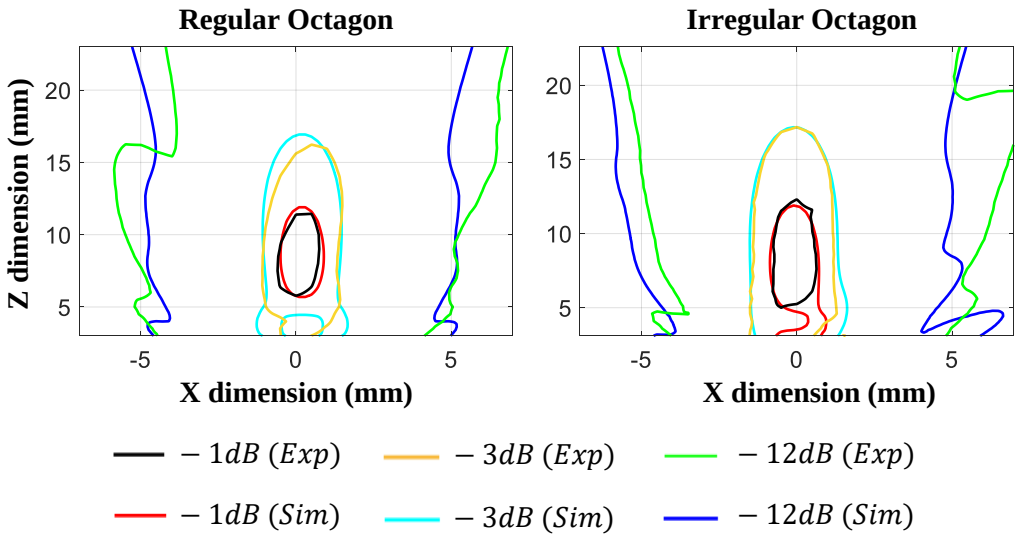

Figure C-6 dB Profile Comparison Between the Simulated (Sim) and the Experimentally (Exp) Measured Acoustic Beam Profiles for the Octagonal, Single Element Transducers

In order to control therapeutic dosage, the output voltage of the signal generator was related to the PNP magnitude achieved by the transducers in the vicinity of the target cell layer. Therefore, PNP was measured at an axial distance of 7.0 mm away from the element surface, into the water load, for various driving signal amplitudes (Figure C-7). The 7.0 mm separation was chosen in order to minimize MB destruction through cavitation in the pre-target region by placing the beginning of the transducer's focal zone (enclosed by the -1dB profile in Figure C-6) close to the cell layer.

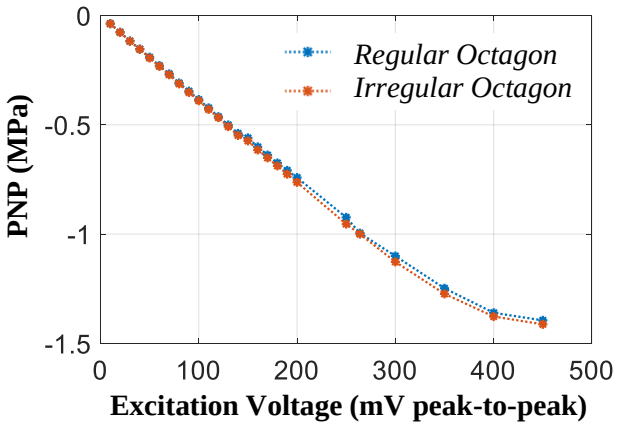

Figure C-7 Variation of PNP at 7.0 mm in the Load as Function of Signal Generator Output Voltage for Both Octagonal Transducers

Figure C-7 shows both transducers achieve similar PNP magnitudes at 7.0 mm into the water load even if the irregular octagonal element has a slightly smaller cross section. The reason for this is probably because the NH was better aligned with the NH in the case of the irregular octagon, and not because of reduced spurious modes due to the asymmetric geometry. The electrical impedance spectrum of the two transducers depicted in Figure C-8 shows the two

devices have very similar electrical impedances. Therefore, the irregular octagon is not better than the regular one. Furthermore, the coupling coefficient of the real transducers is lower than the FEA simulation results, which is similar to the results reported in Section 5.4.1 for the phased arrays.

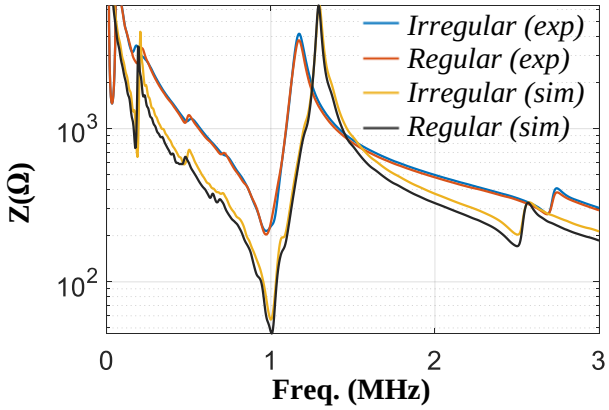

Figure C-8 Experimentally (Exp) Measured and Simulated (Sim) Electrical Impedance of the Regular and Irregular Octagonal, Single Element Transducers with Backing Layer

Conclusions

Two octagonal, single element, 1.0 MHz, piezocomposite transducers aimed for *in-vitro* sonoporation were designed using the VF sweep program based on FEA + time extrapolation developed as part of this Thesis (Section 3.4.1). The two transducers were then manufactured and acoustically characterized with a scanning tank coupled to a NH. The simulated and the measured beam profiles had a good degree of similarity, which was in accordance with the results obtained from the phased arrays (Section 5.4.2). The driving voltage of the experimental transducers was then correlated with the PNP magnitude achieved by the devices in the region where the cell layer was expected to be situated as part of the *in-vitro* experiments, which are reported by M. Turcanu in Ref. [258]. Both transducers were able to achieve PNP magnitudes well above 1.0 MPa, which is larger than the threshold required for sonoporation enhanced by MBs (Table 2-1).